”Modelling and characterization of deformation and damage mechanisms in high manganese alloyed steels”

Von der Fakultät für Georessourcen und Materialtechnik der
Rheinisch -Westfälischen Technischen Hochschule Aachen

zur Erlangung des akademischen Grades eines

Doktors der Ingenieurwissenschaften

genehmigte Dissertation

vorgelegt von **M.Sc.**

Manjunatha Madivala Venkateshappa

aus Madivala Kolar, Karnataka, Indien

Berichter: Univ.-Prof. Dr.-Ing. Wolfgang Bleck
Univ.-Prof. Dr.-Ing. Ulrich Prahl

Tag der mündlichen Prüfung: 15. Juli 2019

Diese Dissertation ist auf den Internetseiten der Universitätsbibliothek online verfügbar

This cumulative dissertation consists of four journal publications

Manjunatha Madivala, Alexander Schwedt, Su Leen Wong, Franz Roters, Ulrich Prahl, and Wolfgang Bleck. Temperature dependent strain hardening and fracture behavior of twip steel. *International Journal of Plasticity*, 104:80 – 103, 2018. ISSN 0749-6419. doi: https://doi.org/10.1016/j.ijplas.2018.02.001
© 2018 Elsevier Ltd. Reprinted with permission from Elsevier. The original publication is available at science direct.

Manjunatha Madivala, Alexander Schwedt, Ulrich Prahl, and Wolfgang Bleck. Anisotropy and strain rate effects on the failure behavior of twip steel: A multiscale experimental study. *International Journal of Plasticity*, 2018. ISSN 0749-6419. doi: https://doi.org/10.1016/j.ijplas.2018.11.015
© 2018 Elsevier Ltd. Reprinted with permission from Elsevier. The original publication is available at science direct.

Manjunatha Madivala, Alexander Schwedt, Ulrich Prahl, and Wolfgang Bleck. Strain hardening, damage and fracture behavior of al added high mn twip steels. *Metals*, 8(12), 2019. ISSN 2075-4701. doi: 10.3390/met8121014. URL http://www.mdpi.com/2075-4701/8/12/1014
© 2018 MDPI. Reprinted with permission from MDPI. The original publication is available at Metals–Open Access Journal.

Manjunatha Madivala and Wolfgang Bleck. Strain rate dependent mechanical properties of twip steel. *JOM*, Sep 2018. ISSN 1543-1851. doi: https://doi.org/10.1007/s11837-018-3137-0
© 2018 The Minerals, Metals & Materials Society. Reprinted with permission from Springer Nature. The original publication is available at SpringerLink.

D 82 (Diss. RWTH Aachen University, 2019)

Acknowledgments

I would like to express my sincere thanks and gratitude to my revered supervisors Prof. Dr.-Ing. Wolfgang Bleck, Professor & Head, Steel Institute, RWTH Aachen University, Aachen & Prof. Dr.-Ing. Ulrich Prahl, Professor & Head, Institue of Metal Forming, TU Bergakademie Freiberg, Freiberg for their invaluable guidance and sustained encouragement throughout the duration of the project. The support and cooperation that I received were overwhelming. My sincere thanks to them for all the help rendered to me during the dissertation work.

I would like to express my sincere regards and gratitude to my project partners PD Dr. Franz Roters, Group Head, Theory and Simulation & Dr. Su Leen Wong, Max-Planck Institut für Eisenforschung, Düsseldorf & Dr. Alexander Schwedt, Central Facility for Electron Microscopy (GFE), RWTH Aachen University, for their guidance, support, and encouragement throughout the dissertation work. I would like to thank all my project colleagues of SFB761 "Steel-ab initio" for their extraordinary support, guidance and cooperation.

I would like to thank my colleagues Aniruddha Dutta, Abhay Gaurav, Krishna Komerla, Konstantin Schacht, Mingxuan Lin, Patrick Fayek, Sebastian Wesselmecking, Tobias Ingendhal & Xiaofei Guo for their invaluable suggestions and extended help.

I would like to thank all my colleagues at IEHK for their extraordinary help and cooperation. Finally, I would like to thank my friends, family members, my wife Mayuri and son Chakrit for their encouragement, strong support and inspiration all these years.

Aachen, March 2019 *Manjunatha Madivala*

Abstract

High manganese twinning induced plasticity (TWIP) steels have exceptional mechanical properties such as strength and ductility, but the abrupt fracture is encountered in these steels with complex and yet poorly known fracture mechanisms. The mechanical behavior of TWIP steels under dynamic loading conditions is quite important for their application in high-performance structural components in the automotive industry. Hence the influence of strain rate, anisotropy, and adiabatic heating on the mechanical properties was studied by quasi-static and dynamic tensile tests with synchronous temperature and strain measurements. To study the local deformation behavior and failure initiation uni-axial tensile tests in conjunction with digital image correlation were carried out. Interrupted micro tensile test samples were analyzed in the scanning electron microscope (SEM) combined with the electron backscatter diffraction measurements (EBSD) to study the evolution of microstructure, deformation mechanisms and microcracks development with increasing macroscopic strain.

The deformation mechanisms of TWIP steel strongly depend on their chemical composition, microstructure, and deformation temperature. Thus in this work, three alloys containing different C, Mn, and Al contents with stacking fault energy (SFE) values of 24 mJ/m^2, 27 mJ/m^2, and 29 mJ/m^2 were studied in detail. The strain-hardening and fracture behavior of X60Mn22 TWIP steel at temperatures ranging from 123 K to 773 K were investigated. Tensile tests were combined with EBSD and synchrotron X-ray diffraction (XRD) to study the evolution of microstructure during deformation. In order to predict the occurrence of either TWIP or transformation-induced plasticity (TRIP) effect and their influence on the work hardening, it is necessary to develop models that are able to predict the SFE accurately based on composition and temperature. Furthermore, to design TWIP/TRIP steels with enhanced properties, the deformation mechanisms along with the influencing variables must be investigated separately. A physically based dislocation density and temperature dependent crystal plasticity constitutive model incorporating SLIP, TWIP and TRIP effects is developed for the prediction of the strain hardening behavior and evolution of deformation mechanisms.

TWIP steel showed high strength of $\geq$1100 MPa in combination with excellent ductility of $\geq$45 %, but slight variation in yield strength and elongation values were observed when tested along rolling, transverse and shear (45°) directions. It exhibited excellent energy absorption (EA) capacity of above 55 kJ/Kg at all strain rates compared to dual phase (DP) steels, TRIP steel, and ferritic steels. However, EA of TWIP steel is slightly lower compared to austenitic stainless steels 1.4301 and 1.4318. Temperature rise due to adiabatic heating has led to an increase of SFE, thereby resulting in a change of twinning behavior or the promotion of dislocation glide under dynamic loading. Twinning was identified as the most predominant deformation mode in all the alloys, which occurred along with dislocation glide at room temperature. The addition of Al has increased SFE thereby delaying the nucleation of deformation twins and prolonged saturation of twinning. Dislocation glide, mechanical twinning, and strain induced ε-martensite transformation were identified as the governing strain hardening mechanisms at different temperatures. The temperature dependent SFE plays a crucial role in determining the prevailing deformation mode. At temperatures below 298 K, the $\gamma \rightarrow \varepsilon$-martensite transformation occurred and its volume fraction increased as the temperature decreased. Twinning was the dominant deformation mechanism at 298 K and the twin fraction increased with temperature until a transition temperature of about 473 K, above which, the deformation mode changed

from twinning and dislocation glide to only dislocation glide. The very good correspondence of simulation and experimental $\sigma - \varepsilon$ curves along with the predicted twin and ε-martensite fractions with the experimental observations suggest that the proposed modeling strategy can aid in designing new TWIP/TRIP steels.

The serrations on the σ–ε curves were the main characteristic behavior of TWIP steel observed under quasi-static loading, which starts to disappear with increasing $\dot{\varepsilon}$ and vanishes completely under dynamic loading. Serrated flow behavior was caused due to dynamic strain aging (DSA), which include the dynamic interaction of solute atoms with dislocations and the Mn-C short-range ordering. The plastic instability caused due to DSA has led to inhomogeneous behavior in the form of nucleation and propagation of shear bands during deformation known as Portevin-Le Chatelier (PLC) effect. Al-addition has led to the decrease of C diffusivity and reduction in tendency for Mn-C short-range ordering resulting in the suppression of serrated flow caused due to dynamic strain aging (DSA) in an alloy with 0.3 wt.% C at room temperature and quasi-static testing, while DSA was delayed in an alloy with 0.6 wt.% C. However, an alloy with 0.6 wt.% C showing DSA effect exhibited enhanced strain hardening and ductility compared to an alloy with 0.3 wt.% C without DSA effect. Failure at macro-level occurred at the intersection of two shear bands close to the edge of the specimen with the negligible amount of strain localization. At the micro-level, cracks originated mainly at grain boundaries (GB) and triple junctions due to increased stress concentration caused by the intercepting deformation twins and the slip band extrusions at GB. Micro-cracks that developed at manganese sulfide and aluminum nitride inclusions showed no tendency for growth even after large deformation indicating the minimal detrimental effect on the mechanical properties.

The high manganese TWIP steels not only exhibited extraordinary mechanical properties but also showed excellent damage tolerance. Hence TWIP steel sheets are highly suitable for the safety-relevant automobile components and other applications.

Zusammenfassung

Hochmanganhaltige TWIP-Stähle (TWinning Induced Plasticity) haben außergewöhnliche mechanische Eigenschaften wie Festigkeit und Duktilität, jedoch kommt es bei diesen Stählen zu abrupten Brüchen mit komplexen und bisher kaum bekannten Bruchmechanismen. Das mechanische Verhalten von TWIP-Stählen unter dynamischen Beanspruchungsbedingungen ist für ihre Anwendung in Hochleistungsstrukturbauteilen in der Automobilindustrie sehr wichtig. Daher wurde der Einfluss von Dehnungsgeschwindigkeit, Anisotropie und der adiabatischen Erwärmung auf die mechanischen Eigenschaften durch quasistatische und dynamische Zugversuche, mit kombinierter lokaler Dehnungsmessung und Infrarot-Thermographie, untersucht. Damit war es möglich lokale Verformungstemperaturen und -Geschwindigkeiten zu quantifizieren. Zur Untersuchung des lokalen Verformungsverhaltens und des Versagens wurden einachsige Zugversuche in Verbindung mit einer digitalen Bildkorrelation durchgeführt. Unterbrochene Mikrozugversuchsproben wurden im Rasterelektronenmikroskop (SEM) mittels Elektronenrückstreubeugung (EBSD) analysiert, um die Entwicklung der Mikrostruktur, der Deformationsmechanismen und die Entwicklung von Mikrorissen mit zunehmender makroskopischer Dehnung zu untersuchen.

Die Verformungsmechanismen von TWIP- Stählen hängen stark von ihrer chemischen Zusammensetzung, Mikrostruktur und Verformungstemperatur ab. Daher wurden in dieser Arbeit drei Legierungen mit unterschiedlichen Gehalten an C, Mn und Al mit Stapelfehlerenergien (SFE) von 24 mJ/m2, 27 mJ/m2 und 29 mJ/m2 detailliert untersucht. Untersucht wurden das Kaltverfestigungs- und Bruchverhalten des X60Mn22 TWIP-Stahl im Temperaturbereich von 123 K bis 773 K. Zugversuche wurden mit EBSD und Synchrotronröntgenbeugung (XRD) kombiniert, um die Entwicklung der Mikrostruktur während der Verformung zu untersuchen. Um das Auftreten des TWIP- oder TRIP-Effektes (TRansformation Induced Plasticity) und deren Einfluss auf die Verfestigungsrate vorherzusagen, müssen Modelle entwickelt werden, die in der Lage sind, die SFE basierend auf der Zusammensetzung und der Temperatur genau vorherzusagen. Um TWIP / TRIP-Stähle mit verbesserten Eigenschaften zu entwickeln, müssen außerdem die Verformungsmechanismen zusammen mit den Einflussgrößen separat untersucht werden. Dazu wurde ein physikalisch basiertes Versetzungsdichte- und temperaturabhängiges Kristallplastizitätsmodell entwickelt, welches die SLIP-, TWIP- und TRIP-Effekte berücksichtigt und für die Vorhersage des Verfestigungsverhaltens und der Entwicklung der Verformungsmechanismen genutzt werden kann.

Der TWIP-Stahl X60Mn22 zeigte eine hohe Festigkeit von $>$1100 MPa in Kombination mit einer ausgezeichneten Duktilität von $>$45 %, jedoch wurden Schwankungen der Streckgrenze und der Dehnungswerte beobachtet, wenn entlang der Walz-, Quer- und Scherrichtung (45°) getestet wurde. Verglichen mit Zweiphasenstählen (DP-Stählen), TRIP-Stählen und ferritischen Stählen zeigte sich ein ausgezeichnetes Energieabsorptionsvermögen (EA) von über 55 kJ/kg bei allen Dehnungsraten. Das EA von TWIP-Stählen ist jedoch etwas niedriger als z.B. bei den austenitischen rostfreien Stählen 1.4301 und 1.4318. Ein Temperaturanstieg aufgrund adiabatischer Erwärmung führt zu einem Anstieg der SFE, was zu einer änderung des Zwillingsverhaltens oder der Förderung von Versetzungsgleiten unter dynamischer Belastung führt. Deformationszwillingsbildung wurde als der vorherrschende Verformungsmodus in allen Legierungen identifiziert, der zusammen mit Versetzungsgleiten bei Raumtemperatur auftrat. Die Zugabe von Al erhöht die SFE, wodurch die Keimbildung von Deformationszwillingen verzögert

wird und die Sättigung der Zwillingsbildung zu größeren Dehnungen verschoben wird. Versetzungsgleiten, mechanische Zwillingsbildung und durch Dehnung induzierte Epsilon-Martensit-Transformation wurden als die bestimmenden Verfestigungsmechanismen bei verschiedenen Temperaturen identifiziert. Die temperaturabhängige SFE spielt eine entscheidende Rolle bei der Bestimmung des vorherrschenden Verformungsmodus. Bei Temperaturen unter 298 K trat die Epsilon-Martensit-Umwandlung auf und ihr Volumenanteil nahm mit abnehmender Temperatur zu. Die Zwillingsbildung war der dominante Verformungsmechanismus bei 298 K und der Zwillingsvolumenanteil stieg mit der Temperatur bis zu einer übergangstemperatur von etwa 473 K, oberhalb derer sich der Verformungsmodus von Zwillingsbildung und Versetzungsgleiten auf nur Versetzungsgleiten änderte. Die sehr gute übereinstimmung von simulierten und experimentellen Spannungs-Dehnungs-Kurven hinsichtlich der Zwillings- und Epsilon-Martensit-Anteile lässt vermuten, dass die vorgeschlagene Modellierungsstrategie bei der Entwicklung neuer TWIP / TRIP-Stähle hilfreich sein kann. Der sägezahnartige Verlauf der Fließkurven im Spannungs-Dehnungs-Diagramm aufgrund ausgeprägter lokaler Verformung ist ein weiteres besonderes Merkmal der TWIP-Stähle. Bei einigen Legierungen kann dieser Effekt bereits bei Raumtemperatur beobachtet werden. Mit zunehmender Dehnungsgeschwindigkeit nimmt die Sägezahnform ab und verschwindet bei dynamischer Belastung vollständig. Das gezackte Fließverhalten resultiert aus einer dynamischen Dehnungsalterung (DSA), die durch die dynamische Wechselwirkung von gelösten Atomen mit Versetzungen und durch die Mn-C Anordnung im Nahbereich verursacht wird. Die durch DSA verursachte plastische Instabilität führt zu inhomogenem Verhalten bei der Bildung und Ausbreitung von Scherbändern während der Verformung. Dies wird als Portevin-Le Chatelier (PLC) -Effekt bezeichnet.

Eine Al-Zugabe führte zu einer verringerte C Diffusivität und einer Reduktion der Mn-C Nahordnungs-Neigung. Dies resultierte in einer zu einer Unterdrückung der dynamischen Dehnungsalterung (DSA) in einer Legierung mit 0,3 Gew.-% C bei Raumtemperatur. Die DSA wurde in einer Legierung mit 0,6 Gew.-% C verzögert und hatte im Vergleich zu einer Legierung mit 0,3 Gew.-% eine verbesserte Verformungshärtung und Duktilität. Ein Versagen auf Makroebene trat am Schnittpunkt zweier Scherbänder nahe dem Rand der Probe bei einem vernachlässigbaren Ausmaß an Dehnungslokalisierung auf. Auf der Mikro-ebene entstanden Risse haupt-sächlich an Korngrenzen (GB) und Tripel-Punkten, aufgrund einer erhöhten Spannungskonzentration, welche durch die überlappung von von Verformungszwillingen und Gleitbandextrusionen an GB verursacht wurde. Mikrorisse, die an Mangansulfid- und Aluminiumnitrid-Einschlüssen auftraten, zeigten auch nach starker Verformung keine Tendenz zum Wachstum, sodass davon auszugehen ist, dass sich diese Art von Einschlüssen nur minimal auf die mechanischen Eigenschaften auswirkt.

Die hochmanganhaltigen TWIP-Stähle zeigten nicht nur außergewöhnliche mechanische Eigenschaften, sondern auch eine hervorragende Schadenstoleranz. Somit eignen sich TWIP-Stahl Bleche hervorragend für die sicherheitsrelevanten Automobilkomponenten und andere Anwendungen.

Contents

1 Introduction **1**

2 State of the art **3**

2.1 High Manganese Steels . . . 3
2.2 Serrated flow and dynamic strain aging . . . 4
2.3 Temperature and strain rate dependence . . . 4
2.4 Role of alloying elements . . . 6
2.5 Constitutive modeling . . . 6
2.6 Damage development and failure behavior . . . 7

3 Research papers **9**

3.1 Research Paper 1 . . . 9
3.2 Research Paper 2 . . . 34
3.3 Research Paper 3 . . . 57
3.4 Research Paper 4 . . . 81

4 General discussion **94**

4.1 Serrated flow and dynamic strain aging . . . 94
4.1.1 Influence of temperature, strain rate and anisotropy . . . 94
4.1.2 Influence of C and Al alloying . . . 95
4.2 Strain hardening . . . 96
4.2.1 Effect of temperature . . . 96
4.2.2 Effect of strain rate . . . 98
4.2.3 Effect of Al-addition . . . 99
4.3 Damage and failure . . . 101
4.3.1 Role of extrinsic parameters . . . 101
4.3.2 Role of deformation bands . . . 101
4.3.3 Role of inclusions . . . 102
4.3.4 Role of deformation mechanisms . . . 102

5 Conclusions **104**

1 Introduction

Through many years of development and application, advanced high strength steels (AHSS) and metallic materials have proved themselves to be versatile and effective materials for automotive parts [5–9]. However, the demand for safety, durability and cost-effectiveness of the structural components used in modern automobiles has increased tremendously over the years. This has driven steel producers and engineers to develop new grades that are lighter, stronger and better formable with improved mechanical properties. These applications have ranged from increased strength for performance and weight reduction to zinc coatings for improved corrosion resistance to bake hardenable grades for closure panel dent resistance [10]. Steels for automotive applications in general require greater formability for styling body panels to great strength for crash performance. The components not only have to be stronger to resist crushing in the passenger compartment, but should also provide energy absorption in the front and rear crumple zones [11]. Thus it is necessary to develop new materials focusing on the special requirements. Through careful control of chemistry and processing, materials can be tailored to provide optimum performance, keeping an aim on specific applications. By choosing different alloying elements and careful processing, the required microstructural constituents with unique mechanical behavior can be obtained resulting in many types of materials for automotive applications [12]. Thus variations in chemistry, microstructure, and deformation mechanisms are crucial aspects in the design and performance of metallic materials. The main goal of the current work is to investigate the mechanical behavior of high Mn twinning induced plasticity (TWIP) steels suitable for safety-relevant automotive parts and other applications.

TWIP steels exhibit exceptional strength and ductility, which enables their use in the production of high performance structural parts for automotive, defense, cryogenic, and other applications [13, 14]. Many such parts are operated under varying conditions of temperature. Therefore, it is of paramount importance to understand the influence of temperature on the deformation and fracture behavior of such components. TWIP/TRIP steels are low stacking fault energy face centered cubic (FCC) alloys with excellent work hardening behavior, which originates from their deformation mechanisms such as dislocation glide, deformation twinning (TWIP) and ε- or α'-martensite transformation (TRIP) [15–17]. The activation of these deformation mechanisms is mainly controlled by the stacking fault energy [18, 19]. Thus the aim of this study is to investigate the influence of extrinsic parameters such as temperature and strain rate on the deformation mechanisms.

TWIP steels are such class of steels characterized by high work hardening capacity along with exceptional strength and ductility [13, 20, 21]. The high energy absorption capacity enables their use in the production of high performance structural parts in automobiles with superior crash performance and light weight structural reinforcements [22]. To describe the overall performance of steels combining both strength and elongation, the most commonly used material characteristic parameter is the ECO-index, expressed as the product of ultimate tensile strength (UTS) and uniform elongation (UE). The ECO-index value for conventional AHSS is limited to about 20 GPa %, but for high Mn TWIP steels, it can go beyond 50 GPa % [23]. However, evaluating the material performance solely based on quasi-static tensile test properties such as strength and ductility and judging their suitability for structural parts may be inadequate since during the crash of automobiles, the parts are not deformed until failure and the deformation rates are much larger [24]. The most commonly used techniques to characterize dynamic tensile

properties are servo-hydraulic (SH) system, split Hopkinson pressure bar (SHB) system, single bar (SB) system and drop weight system, with each test method providing a specific strain rate ($\dot{\varepsilon}$) range. The bar systems (SBH and SB) are able offer very high $\dot{\varepsilon}$ range (>1000 /s) than the SH system, yet SH system is more reliable for relatively lower $\dot{\varepsilon}$ (<500 /s) [25]. Thus the goal of this work is to investigate the crash-worthiness of TWIP steel and to determine its mechanical properties and energy absorption capacity under dynamic loading conditions. Besides, this study also compares TWIP steels properties with other AHSS steel grades to check its suitability for different components.

2 State of the art

2.1 High Manganese Steels

High manganese twinning induced plasticity (TWIP) steels are second generation advanced high strength steels characterized by high work hardening capacity along with exceptional strength and ductility [20, 26]. The sustained and high strain hardening rate (SHR) of TWIP steels can be ascribed to their deformation mechanisms such as dislocation glide, deformation twinning, and ε-martensite transformation [27, 28]. TWIP steels with different chemical compositions such as Fe-18Mn-0.6C, Fe-28Mn-0.3C, Fe-22Mn-0.6C and Fe-18Mn-0.6C-1.5Al, exhibit extraordinary mechanical properties such as ultimate tensile strength >1000 MPa, uniform elongation >50% and excellent energy absorption capacity >55 kJ/kg making them highly suitable for automotive applications [2, 4, 13, 20, 22, 26, 29].

The materials behavior strongly dependent on their chemical composition, microstructure and deformation conditions [1, 4, 27, 28, 30]. The plastic deformation mechanisms such as mechanical twinning and ε-martensite phase transformation can occur besides dislocation slip in these steels [30–32]. Deformation twins and ε-martensite plates increase the work hardening by acting as obstacles to dislocation motion [33, 34]. At different temperatures, the deformation mode changes from ε-martensite formation to mechanical twinning, indicating close relationship with different kinds of planar defects involved in their nucleation and growth process. The activation barriers for these partially competing mechanisms are strongly dependent on the stacking fault energy (SFE) [32]. Thus, the SFE plays a crucial role in regulating a change from dislocation glide at high temperatures, to either dislocation glide in conjunction with twinning at ambient temperatures or dislocation glide in conjunction with ε-martensite phase transformation at low temperatures [35]. In general, ε-martensite transformation is observed when the SFE is below 20 mJ/m^2, while twinning is observed in the range of SFE from 20–60 mJ/m^2. When the SFE exceeds 60 mJ/m^2, dislocation glide becomes the predominant mode of plastic deformation [29, 31, 36]. In order to predict the occurrence of either TWIP or TRIP effect and their influence on the work hardening, it is necessary to develop models that are able to predict the SFE accurately based on composition and temperature. Furthermore, to design TWIP/TRIP steels with enhanced properties, the deformation mechanisms along with the influencing variables must be investigated separately.

The unique characteristic behavior of these steels is the nucleation and propagation of deformation bands during deformation, which results in serrations on the $\sigma - \varepsilon$ curves, known as Portevin-Le Chatelier (PLC) effect [37–39]. The serrations in TWIP steels are classified as Type A, depending on their morphology. They are known as locking serrations because of repeated locking and unlocking of dislocations by solute atoms commonly known as dynamic strain aging (DSA) [30, 39–41]. It was stated that DSA effectively modified the SHR but its influence on the SHR is limited due to the lower activation energy attained in these steels [38]. Many authors stated that mechanical twinning and its associated dynamic Hall-Petch effect remain the only mechanisms that can be responsible for sustained and high SHR of TWIP steels [13, 22, 38, 42]. However, the influence of DSA on the deformation behavior and its role in manifesting the SHR cannot be ignored.

2.2 Serrated flow and dynamic strain aging

Chen et al. observed serrated stress-strain curves in X60Mn18 TWIP steel, which was due to the formation and propagation of Portevin-Le Chatelier (PLC) bands during deformation [43]. This effect was mainly due to DSA associated with the negative strain rate sensitivity (SRS). For type A bands, the stress-strain curve will not be flat during band propagation but, shows a continuous increase in the plateau region. In contrast multiple uncorrelated discontinuities in the stress-strain curve are observed for type B bands. Type A bands were observed at lower strains and type B bands at higher strains, which are specific to these steels. Similar observations were also made by [38] and it was found that the activation energy attained was quite low in TWIP steel, hence the contribution of DSA to work-hardening was limited. DSA results in inhomogeneous flow behavior of the material, which can lead to surface defects in the formed parts. However, due to the high strain rate involved during forming operations, DSA was suppressed which results in good surface quality of the stamped parts. [44] investigated the nucleation, propagation, and morphology of PLC bands quantitatively in TWIP steel by considering straight and tapered geometries, to study the influence of stress concentration on the band nucleation. In straight gauge specimens, type A bands nucleated at the gripping ends or in the gauge section center and the band propagation commenced at the end of each nucleation event with inhomogeneous strain distribution. Whereas, in tapered specimens the bands nucleated between the gauge center and the gripping end, indicating that band nucleation is not limited to geometry induced stress concentrators. [45] suggested that plastic instability may be triggered due to twinning along with other effects. A low twin fraction was observed in the investigated steels, hence twinning alone cannot support the entire strain accumulation required for strain jumps. [39] investigated TWIP steel with and without Al and stated that DSA is the result of an interaction between C-Mn point defect complexes and stacking faults. [46] observed the plastic instability before and after its onset using high resolution optical extensometry and stated that PLC bands and the deformation bands observed in TWIP steel are not identical in nature, which implies that the classical DSA theory cannot be applied. The deformation bands in TWIP steel begin with small strain heterogeneities and develop into pronounced deformation bands accompanied with stress serrations. [47] investigated a TWIP steel with 1.2 wt.% C and stated that DSA and ε-martensite transformation were found to accelerate the premature fracture due to localized deformation. [48] studied the SRS of TWIP steels by varying the Al content and found that there is a negative to positive transition of SRS with increasing Al content. The twin density decreased with increasing strain rate and negative SRS was observed in TWIP steels with 0 wt.% Al and 1.5 wt.% Al whereas, the 6 wt.% Al alloy exhibited positive SRS. The experimental observations indicated that the SRS of TWIP steels was strongly influenced by deformation twins and dislocations. [49] investigated the influence of strain rate on the occurrence of PLC bands. DSA was suppressed with increasing strain rate and the local strain concentration within the PLC band was more severe at higher strain rates. [50] compared the local deformation behavior of TWIP steel under quasi-static and dynamic tensile loading and reported that twinning in the early stage of deformation resulted in higher strength and ductility along with similar local strain at failure even under dynamic loading. The uncertainty in failure behavior due to the initiation and propagation of PLC bands at different temperatures needs to be understood.

2.3 Temperature and strain rate dependence

Curtze and Kuokkala investigated TWIP steels with different chemical compositions to study the influence of the SFE on the hardening behavior at different temperatures and strain rates

[35]. It was reported that alloys with SFE in the range of 21–27 mJ/m^2, showed enhanced strength and ductility compared to alloys with SFE above 42 mJ/m^2. The alloys where twinning occurred, showed better work hardening compared to alloys where deformation occurred only via dislocation glide. [47] reported that this increase in work hardening was due to the increase in deformation twin density, however, with increase in plastic strain the deformation twin density saturated resulting in a sudden drop of work hardening leading to failure. [51] also studied the influence of C on the SFE in TWIP steels at low temperatures. It was observed that with increasing fraction of C in the alloy the SFE increased and as a result, the strain induced ε-martensite transformation was suppressed even at low temperatures. Dynamic strain aging (DSA) was observed above room temperature, where twinning occurred along with dislocation glide. High work hardening in these alloys was solely due to ε-martensite transformation at low temperatures and twinning along with DSA above room temperature. [30] investigated the influence of Al addition on DSA phenomena at different temperatures. Addition of Al suppressed the DSA phenomena by increasing the activation energy for C diffusion and reducing the time for the interaction between stacking faults and C-Mn point defect complexes. At elevated temperature DSA is enhanced due to the increased defect mobility. [36] investigated the influence of temperature on work-hardening in TWIP steel and presented that the mechanical twins had a limited effect on the work-hardening behavior and that their influence significantly reduced with the temperature. This contradicts the observations made by many researchers [13, 14, 29]. On the other hand it was also stated that development of stacking faults and their interactions with the dislocation glide contributed to the enhancement of work-hardening in TWIP steel.

Dynamic tensile tests was carried out on Fe-25Mn-3Al-3Si TWIP/TRIP steel by [52] showed an increase in yield strength (YS), UTS and elongation with increase in $\dot{\varepsilon}$. The material mainly deformed by dislocation glide along with TWIP and TRIP effect. The specimen temperature increased by about 60 °C due to adiabatic heating, which resulted in a change of SFE from 21 to $\sim$23 mJ/m^2. It was stated that, $\dot{\varepsilon}$ did not influence the microstructure morphology such as thickness and spacing of deformation twins or ε-martensite laths. In a similar study on Fe-15Mn-0.6C-1.2Al TWIP steel by [50], serrated flow behavior was observed under quasi-static tests and homogenous flow behavior without serrations under dynamic tests. Dynamic loading resulted in increase of UTS, slight reduction of elongation and profuse necking. This is mainly due to the adiabatic heating during deformation which led to increase in SFE resulting in decrease of twinning rate. [53] studied the same alloy and found differences in slip characteristics and twin formation due to variation of $\dot{\varepsilon}$. Under quasi-static loading, dislocation cell structures formation showed a transition from combined planar and wavy slip to wavy slip, whereas under dynamic loading combined planar and wavy slip was activated from the early stages of deformation. In the initial stages of deformation, stacking faults were observed and after deforming to 20 %, 30 % strain primary twins could be seen under quasi-static test, while in dynamic tests both primary and secondary twinning were quite active in the later stages of deformation. [54] has investigated the influence of grain size and strain rate on the hardening behavior in Fe-20Mn-0.6C steel. For all the investigated grain sizes in the range from 3.5–25 µm, YS increased with increase in $\dot{\varepsilon}$, whereas UTS and elongation decreased with increase in $\dot{\varepsilon}$. It was reported that strain localization within the shear bands and adiabatic heating has led to the reduction of mechanical properties. Microstructure investigations has revealed dislocation slip along with primary twins in the early and middle stages of deformation, whereas in the later stages of deformation rapid nucleation of twins was observed at high $\dot{\varepsilon}$. [55] has investigated Fe-15Mn-0.7C-2Al-2Si steel at various $\dot{\varepsilon}$ and observed a positive SRS of YS and decrease in deformation twinning rate at high $\dot{\varepsilon}$. At low $\dot{\varepsilon}$, activation of multiple twin systems and large intergranular misorientations was observed in contrast to high $\dot{\varepsilon}$. In the current study,

the influence of adiabatic heating at different $\dot{\varepsilon}$ on the activation of deformation mechanisms is investigated. The $\dot{\varepsilon}$ influence on the deformation behavior and mechanical properties is studied in detail, with a special emphasis on strain localization and failure.

2.4 Role of alloying elements

The appearance of serrations on the σ–ε curves requires the material to be plastically deformed to a certain deformation known as critical strain (ε_c). A detailed study on the X60Mn22 alloy revealed repeated serrations on the σ–ε curves at different strain rates and temperatures. With an increase in temperature or grain size, the ε_c for the initiation of serrations decreased and with the increase of strain rate ($\dot{\varepsilon}$), the ε_c increased [1, 2]. In Fe-Mn-C alloys, it was shown that with the increase in C content from 0.0 wt.% to 1.1 wt.% C, the ε_c for triggering serrations has decreased [56]. A comparative study on Fe-Mn-C-x alloys with and without Al showed that with Al-addition the ε_c has increased [57]. It was also shown that with increasing Al content from 0.0 to 3.0 wt.%, the initiation of serrated flow shifted to higher strains or completely suppressed [19]. A similar study also revealed severe serrated flow in an X60Mn22 alloy at different $\dot{\varepsilon}$, whereas in an X60MnAl22-1.5 alloy serrations appeared only at quasi-static $\dot{\varepsilon}$ and the initiation of serrations shifted to high strains [58]. It was shown in X60MnAl18-x alloys with 0.0, 1.5 and 2.5 wt.% Al contents, that severe serrated flow also occurred in Al-containing alloys at elevated temperatures [30]. Thus, it can be clearly understood that ε_c for the initiation of the serrations in Fe-Mn-C-Al alloys is mainly influenced by stacking fault energy (SFE), the alloying elements such as C and Al, deformation temperature, $\dot{\varepsilon}$ and microstructure of the material. From the experimental observations in the literature, it can be stated that in the alloys of Fe-Mn-C and Fe-Mn-C-Al with different chemical compositions the serrated σ–ε behavior can be observed but the range of temperature, $\dot{\varepsilon}$ regimes, microstructure states and the strain ε_c at which serrations appears could be different. In the current study, an X60Mn22, an X60MnAl17-1 and X30MnAl23-1 alloys were investigated in detail to study the influence of alloying elements such as C and Al on the serrated flow behavior.

2.5 Constitutive modeling

Physically based models for strain hardening and twinning evolution have been developed over many years. [59] introduced a dislocation density based model, which accounts for the interaction between twinning and dislocation motion by incorporating the characteristic spacing of twins into the dislocation storage term. In the model developed by [60], the evolution function of the twin volume fraction is a mathematical description of the twin nucleation, which captured the experimental observations of the microstructure. The twin–slip interactions were based on the evolution of the dislocation mean free path accounting for the three-dimensional spatial arrangement of twins within a grain. In the model proposed by [61], dislocations were classified into mobile and forest dislocations and the strain hardening was related to the evolution of these two coupled dislocation densities. The grains were classified into twinned and untwinned type, and each type had a separate formulation for the evolution of the dislocation density based on the Kubin-Estrin model. [62] developed an isotropic TWIP model by combining the three internal variable model (3IVM) of [63] and the twin nucleation model of [64]. The model considered the dislocation cell structure and divided the dislocations into three types: mobile dislocation in the cell, in the cell walls, and immobile dislocation dipoles. The model was able to predict flow stress and evolution of twinning at different temperatures. [65, 66] proposed crystal plasticity-based models to simulate the combined effect of slip and twinning. These models have the capability to model strain hardening and texture evolution associated

with deformation twinning at the grain scale. [67] used the visco-plastic self-consistent (VPSC) approach for modeling the deformation behavior of hadfield steel, considering twinning and slip effects to predict the stress-strain response and texture evolution. [68] extended the classical crystal plasticity model to include deformation twinning and used it to predict strain hardening and deformation textures in low SFE FCC metals. [69] also proposed a model for strain hardening of TWIP steel involving crystallographic slip and twinning, considering both the slip-twin and twin-twin interactions. [70] combined different approaches and proposed a dislocation-density-based description for work hardening, by relating it to the mean free path (MFP) of dislocations measured along each slip system. Different homogenization schemes were applied to predict the texture evolution and strain hardening of TWIP steel. [71] proposed a crystal plasticity model with combined slip, twinning, and transformation induced plasticity using a micromechanics based approach. The simulation results of single crystals were compared with the experimental data from literature for its validation. These models have only considered either the effect of slip and twinning or the effect of slip and transformation. However, a comprehensive model incorporating the combined effect of slip, deformation twinning and martensitic transformation considering both the microstructural aspects and temperature was not available and is of great interest in the current study.

The isotropic TWIP model by [62], though developed for polycrystalline materials does not take individual grain orientations and grain boundary interactions into account. [72] included the dislocation slip and shear band formation in the crystal plasticity framework [73]. The TWIP model was further extended by [74] to consider the $\gamma \rightarrow \varepsilon$ martensitic transformation (TRIP), so that, the constitutive model has the capability to simulate the concurrent evolution of dislocation densities, twin and ε-martensite volume fractions. The onset of twinning or martensite transformation in the model was determined by two separate expressions based on the critical stress for twin and ε-martensite growth. However, the model does not explicitly account for the precise distribution and arrangement of twins and martensite plates/lathes but rather the volume fraction of twins and ε-martensite at each material point.

2.6 Damage development and failure behavior

TWIP steels showed characteristic differences in the failure behavior when the material deformed by only SLIP or SLIP in combination with TWIP or SLIP in combination with TRIP [1]. Fracture surface analysis depicted the formation of fine dimples with quasi-brittle islands where ε-martensite was present, fine or shallow dimples where twinning was the dominant deformation mode and larger dimples along with coalescence of voids at MnS inclusions where deformation occurred by dislocation glide. Fracture surfaces with coarse and finer dimples at 673 K and finer dimples at 298 K were observed under tensile loading [75]. Macroscopic observations revealed an abrupt failure in TWIP steels without any strain localization or necking, which occurred at the intersection of two deformation bands close to the specimen edges. It was claimed that the increased stress concentration caused by the intercepting deformation twins and the slip band extrusions at grain boundary (GB) has led to micro-crack formation. Inter-granular micro-crack initiation and propagation events were observed in the microstructure at GBs and triple junctions along with the rapid nucleation of minute voids [2]. A similar study also showed micro-cracks at the intersection of deformation bands mainly at the edge and side surfaces of the tensile specimen. The cracks were observed at GB junctions and the mechanical twin boundaries [76]. It was claimed that the exponential increase of the macroscopic void volume fraction led to the sudden failure or decrease of SHR in TWIP steels [77]. In general, fracture in ductile materials is preceded by necking, which occurs when the stress-

strain response satisfies the plastic instability criterion described as

$$\sigma \geq d\sigma/d\varepsilon \tag{2.1}$$

where σ is the true stress, and ε is the true strain. Even though, ductile fracture was found in TWIP steels, Eq. 2.1 cannot be applied, because the homogenous deformation condition necessary was not satisfied due to the propagation of localized PLC bands. A detailed study on the evolution of damage in TWIP steel by 3D X-ray tomography experiments has shown that the average void diameter and the stress triaxiality remained constant throughout the deformation until failure. It was claimed that the damage development process involved rapid nucleation of minute voids combined with substantial growth of the largest voids [78]. [79] examined the void size distribution close to the fracture surface in a sheared specimen. Most of the voids found were tiny secondary dimples with few elongated cavities, indicating localized failure. The factors such as temperature, strain rate and stress state have a direct influence on the active deformation modes, which in turn influence the damage and failure in TWIP steels. The TWIP steels which show DSA effect, the failure occurs abruptly. However, the addition of Al not only increases ductility but also changes the local deformation and fracture behavior. It is also important to understand the relationship between the deformation mechanisms and the mechanism of micro-crack formation. The study should be carried out in TWIP steels with and without Al-addition both at the micro- and macro-scale.

3 Research papers

3.1 Research Paper 1

Title: Temperature dependent strain hardening and fracture behavior of TWIP Steel

Manjunatha Madivala, Alexander Schwedt, Su Leen Wong, Franz Roters, Ulrich Prahl, and Wolfgang Bleck. Temperature dependent strain hardening and fracture behavior of twip steel. *International Journal of Plasticity*, 104:80 – 103, 2018. ISSN 0749-6419. doi: https://doi.org/10.1016/j.ijplas.2018.02.001
© 2018 Elsevier Ltd. Reprinted with permission. The original publication is available at science direct.

Highlights:

- Strain hardening and fracture behaviour of X60Mn22 TWIP steel is co-related with the active deformation mechanisms as a function temperature and stacking fault energy (SFE).
- XRD and EBSD measurements to Identify the temperature limits at which deformation mode changes as a function of SFE. ε-martensite and twin volume fractions at different temperatures and strains were quantified.
- Demonstrated modeling strategy for predicting the σ–ε curves, strain hardening behavior and elongation by virtual tensile tests using the advanced crystal plasticity framework taking into account the influence of temperature, deformation rate, microstructure, and anisotropy.
- FFT-based crystal plasticity simulations predicts the evolution of twinning, ε-martensite at different temperatures along with stress-strain curves and the work hardening behavior.

International Journal of Plasticity 104 (2018) 80–103

Contents lists available at ScienceDirect

International Journal of Plasticity

journal homepage: www.elsevier.com/locate/ijplas

Temperature dependent strain hardening and fracture behavior of TWIP steel

Manjunatha Madivala[a,*], Alexander Schwedt[b], Su Leen Wong[c], Franz Roters[c], Ulrich Prahl[a], Wolfgang Bleck[a]

[a] Institut für Eisenhüttenkunde (IEHK), RWTH Aachen University, Aachen, Germany
[b] Gemeinschaftslabor für Elektronenmikroskopie (GFE), RWTH Aachen University, Aachen, Germany
[c] Max-Planck-Institut für Eisenforschung GmbH, Düsseldorf, Germany

ARTICLE INFO

Keywords:
TWIP steel
Deformation twinning
ε-Martensite transformation
Fracture
Crystal plasticity

ABSTRACT

In this study, the strain-hardening and fracture behavior of high manganese austenitic twinning induced plasticity (TWIP) steel at temperatures ranging from 123 K to 773 K were investigated. Tensile tests were combined with electron backscatter diffraction (EBSD) and synchrotron X-ray diffraction (XRD) to study the evolution of microstructure during deformation. Twinning and strain induced ε-martensite transformation were identified as the governing strain hardening mechanisms. The temperature dependent stacking fault energy (SFE) plays a crucial role in determining the prevailing deformation mode. At temperatures below 298 K, the γ → ε-martensite transformation occurred and its volume fraction increased as the temperature decreased. Twinning was the dominant deformation mechanism at 298 K and the twin fraction increased with temperature until a transition temperature of about 473 K, above which, the deformation mode changed from twinning and dislocation glide to only dislocation glide. Serrated flow was observed at temperatures above 233 K and below 473 K, due to a dynamic strain aging (DSA) mechanism specific to TWIP steels, that include the interaction of solute atoms with both dislocations and twins. This plastic instability was related to the propagation of Portevin-Le Chatelier (PLC) bands during deformation. Furthermore, scanning electron microscopy (SEM) of the fractured specimens gave an insight into the change in dimple size and the presence of quasi-brittle islands which were a direct consequence of the various active deformation mechanisms. A dislocation density and temperature dependent crystal plasticity model incorporating both twinning-induced plasticity and transformation-induced plasticity (TRIP) was used to predict the strain hardening and deformation behavior. The predicted twin and ε-martensite fractions are in good agreement with the experimental observations. Furthermore, the proposed modeling strategy can aid in designing new TWIP/TRIP steels.

1. Introduction

High manganese twinning induced plasticity (TWIP) steels exhibit exceptional strength and ductility, which enables their use in the production of high performance structural parts for automotive, defense, cryogenic, and other applications (Bouaziz et al., 2011; De Cooman et al., 2017). Many such parts are operated under varying conditions of temperature. Therefore, it is of paramount importance to understand the influence of temperature on the deformation and fracture behavior of such components. TWIP/TRIP

* Corresponding author. Institut für Eisenhüttenkunde (IEHK), RWTH Aachen University, Intzestraße 1, 52072, Aachen, Germany.
E-mail address: Manjunatha.Madivala@iehk.rwth-aachen.de (M. Madivala).

https://doi.org/10.1016/j.ijplas.2018.02.001
Received 30 September 2017; Received in revised form 18 January 2018; Accepted 4 February 2018
Available online 08 February 2018
0749-6419/ © 2018 Elsevier Ltd. All rights reserved.

steels are low stacking fault energy face centered cubic (FCC) alloys with excellent work hardening behavior, which originates from their deformation mechanisms such as dislocation glide, deformation twinning (TWIP) and ε- or α'-martensite transformation (TRIP) (Linderov et al., 2014; Martin et al., 2016; Kim et al., 2017). The activation of these deformation mechanisms is mainly controlled by the stacking fault energy (Pierce et al., 2014; Kim and De Cooman, 2016).

Grässel et al. (2000) developed Fe-(15–30) wt.% Mn-3Al-3Si steels, that showed large uniform elongation (UE) between 60 and 95% and exhibited ultimate tensile strength (UTS) between 650 and 1100 MPa. These alloys derived their enhanced mechanical properties through TWIP/TRIP deformation mechanisms. Many researchers later studied TWIP steels (X60Mn18, X30Mn28, X60Mn22 and X60MnAl18–1.5) by varying C, Mn and Al contents that showed a UE of more than 50% and a UTS of above 1000 MPa (Bouaziz et al., 2011; Saeed-Akbari et al., 2012; De Cooman et al., 2017). The superior tensile properties of these steels were attributed to the sustained high work hardening rates. Depending on the chemical composition and temperature, plastic deformation mechanisms such as mechanical twinning and ε-martensite phase transformation can occur besides dislocation slip in these steels (Allain et al., 2004a; Idrissi et al., 2009; Jung and De Cooman, 2013). Deformation twins and ε-martensite plates increase the work hardening by acting as obstacles to dislocation motion (Renard and Jacques, 2012; Pierce et al., 2015). At different temperatures, the deformation mode changes from ε-martensite formation to mechanical twinning, indicating close relationship with different kinds of planar defects involved in their nucleation and growth process. The activation barriers for these partially competing mechanisms are strongly dependent on the stacking fault energy (SFE) (Idrissi et al., 2009). Thus, the SFE plays a crucial role in regulating a change from dislocation glide at high temperatures, to either dislocation glide in conjunction with twinning at ambient temperatures or dislocation glide in conjunction with ε-martensite phase transformation at low temperatures (Curtze and Kuokkala, 2010). In general, ε-martensite transformation is observed when the SFE is below 20 mJ/m^2, while twinning is observed in the range of SFE from 20 to 60 mJ/m^2. When the SFE exceeds 60 mJ/m^2, dislocation glide becomes the predominant mode of plastic deformation (Allain et al., 2004a; Saeed-Akbari et al., 2012; Shterner et al., 2016). In order to predict the occurrence of either TWIP or TRIP effect and their influence on the work hardening, it is necessary to develop models that are able to predict the SFE accurately based on composition and temperature. Furthermore, to design TWIP/TRIP steels with enhanced properties, the deformation mechanisms along with the influencing variables must be investigated separately.

Curtze and Kuokkala (2010) investigated TWIP steels with different chemical compositions to study the influence of the SFE on the hardening behavior at different temperatures and strain rates. It was reported that alloys with SFE in the range of 21–27 mJ/m^2, showed enhanced strength and ductility compared to alloys with SFE above 42 mJ/m^2. The alloys where twinning occurred, showed better work hardening compared to alloys where deformation occurred only via dislocation glide. Koyama et al. (2013) reported that this increase in work hardening was due to the increase in deformation twin density, however, with increase in plastic strain the deformation twin density saturated resulting in a sudden drop of work hardening leading to failure. Koyama et al. (2011) also studied the influence of C on the SFE in TWIP steels at low temperatures. It was observed that with increasing fraction of C in the alloy the SFE increased and as a result, the strain induced ε-martensite transformation was suppressed even at low temperatures. Dynamic strain aging (DSA) was observed above room temperature, where twinning occurred along with dislocation glide. High work hardening in these alloys was solely due to ε-martensite transformation at low temperatures and twinning along with DSA above room temperature. Jung and De Cooman (2013) investigated the influence of Al addition on DSA phenomena at different temperatures. Addition of Al suppressed the DSA phenomena by increasing the activation energy for C diffusion and reducing the time for the interaction between stacking faults and C-Mn point defect complexes. At elevated temperature DSA is enhanced due to the increased defect mobility. Shterner et al. (2016) investigated the influence of temperature on work-hardening in TWIP steel and presented that the mechanical twins had a limited effect on the work-hardening behavior and that their influence significantly reduced with the temperature. This contradicts the observations made by many researchers (Bouaziz et al., 2011; Saeed-Akbari et al., 2012; De Cooman et al., 2017). On the other hand it was also stated that development of stacking faults and their interactions with the dislocation glide contributed to the enhancement of work-hardening in TWIP steel. A comprehensive study involving a change in deformation modes due to SFE over a wide range of temperatures has not yet been carried out.

Chen et al. (2007) observed serrated stress-strain curves in X60Mn18 TWIP steel, which was due to the formation and propagation of Portevin–Le Chatelier (PLC) bands during deformation. This effect was mainly due to DSA associated with the negative strain rate sensitivity (SRS). For type A bands, the stress-strain curve will not be flat during band propagation but, shows a continuous increase in the plateau region. In contrast multiple uncorrelated discontinuities in the stress-strain curve are observed for type B bands. Type A bands were observed at lower strains and type B bands at higher strains, which are specific to these steels. Similar observations were also made by Allain et al. (2008) and it was found that the activation energy attained was quite low in TWIP steel, hence the contribution of DSA to work-hardening was limited. DSA results in inhomogeneous flow behavior of the material, which can lead to surface defects in the formed parts. However, due to the high strain rate involved during forming operations, DSA was suppressed which results in good surface quality of the stamped parts. Zavattieri et al. (2009) investigated the nucleation, propagation, and morphology of PLC bands quantitatively in TWIP steel by considering straight and tapered geometries, to study the influence of stress concentration on the band nucleation. In straight gauge specimens, type A bands nucleated at the gripping ends or in the gauge section center and the band propagation commenced at the end of each nucleation event with inhomogeneous strain distribution. Whereas, in tapered specimens the bands nucleated between the gauge center and the gripping end, indicating that band nucleation is not limited to geometry induced stress concentrators. Lebedkina et al. (2009) suggested that plastic instability may be triggered due to twinning along with other effects. A low twin fraction was observed in the investigated steels, hence twinning alone cannot support the entire strain accumulation required for strain jumps. Lee et al. (2011) investigated TWIP steel with and without Al and stated that DSA is the result of an interaction between C-Mn point defect complexes and stacking faults. Roth et al. (2012) observed the plastic instability before and after its onset using high resolution optical extensometry and stated that PLC bands and the deformation bands

observed in TWIP steel are not identical in nature, which implies that the classical DSA theory cannot be applied. The deformation bands in TWIP steel begin with small strain heterogeneities and develop into pronounced deformation bands accompanied with stress serrations. Koyama et al. (2013) investigated a TWIP steel with 1.2 wt.% C and stated that DSA and ε-martensite transformation were found to accelerate the premature fracture due to localized deformation. Yang et al. (2017a) studied the SRS of TWIP steels by varying the Al content and found that there is a negative to positive transition of SRS with increasing Al content. The twin density decreased with increasing strain rate and negative SRS was observed in TWIP steels with 0 wt.% Al and 1.5 wt.% Al whereas, the 6 wt. % Al alloy exhibited positive SRS. The experimental observations indicated that the SRS of TWIP steels was strongly influenced by deformation twins and dislocations. Bian et al. (2017) investigated the influence of strain rate on the occurrence of PLC bands. DSA was suppressed with increasing strain rate and the local strain concentration within the PLC band was more severe at higher strain rates. Kang et al. (2017) compared the local deformation behavior of TWIP steel under quasi-static and dynamic tensile loading and reported that twinning in the early stage of deformation resulted in higher strength and ductility along with similar local strain at failure even under dynamic loading. The uncertainty in failure behavior due to the initiation and propagation of PLC bands at different temperatures needs to be understood.

In general, fracture in ductile materials is preceded by necking, which occurs when the stress-strain response satisfies the plastic instability criterion described as

$$\sigma \geq d\sigma/d\varepsilon \tag{1}$$

where σ is the true stress, and ε is the true strain. Even though, ductile fracture was found in TWIP steels, Eq. (1) cannot be applied, because the homogenous deformation condition necessary was not satisfied due to the propagation of localized PLC bands. To investigate the damage evolution in TWIP steel, Fabrègue et al. (2013) carried out 3D X-ray tomography experiments, which showed that average void diameter and triaxility remained constant throughout the deformation. The damage process involved intense nucleation of tiny voids combined with significant growth of the biggest cavities. Lorthios et al. (2010) examined the void size distribution close to the fracture surface in a sheared specimen. Most of the voids found were tiny secondary dimples with few elongated cavities, indicating localized failure. Fracture surfaces with coarse and finer dimples at 673 K and finer dimples at 298 K were observed under tensile loading (Lorthios et al., 2015). The sudden failure or drop of strain hardening in TWIP steels was due to exponential increase of the macroscopic void volume fraction (Yang et al., 2017b). Recently, Yu et al. (2017) showed that edge and side cracks occurred along the grain boundary junctions and the mechanical twin boundaries. These cracks were mainly found at the edge and side surfaces where local deformation bands met. Factors such as temperature, strain rate and stress state have a direct influence on the active deformation modes, which in turn influence the damage and failure in TWIP steels.

Physically based models for strain hardening and twinning evolution have been developed over many years. Bouaziz and Guelton (2001) introduced a dislocation density based model, which accounts for the interaction between twinning and dislocation motion by incorporating the characteristic spacing of twins into the dislocation storage term. In the model developed by Allain et al. (2004b), the evolution function of the twin volume fraction is a mathematical description of the twin nucleation, which captured the experimental observations of the microstructure. The twin–slip interactions were based on the evolution of the dislocation mean free path accounting for the three-dimensional spatial arrangement of twins within a grain. In the model proposed by Kim et al. (2012), dislocations were classified into mobile and forest dislocations and the strain hardening was related to the evolution of these two coupled dislocation densities. The grains were classified into twinned and untwinned type, and each type had a separate formulation for the evolution of the dislocation density based on the Kubin-Estrin model. Steinmetz et al. (2013) developed an isotropic TWIP model by combining the three internal variable model (3IVM) of Roters et al. (2000) and the twin nucleation model of Mahajan and Chin (1973). The model considered the dislocation cell structure and divided the dislocations into three types: mobile dislocation in the cell, in the cell walls, and immobile dislocation dipoles. The model was able to predict flow stress and evolution of twinning at different temperatures. Kalidindi (1998a), Staroselsky and Anand (1998) proposed crystal plasticity-based models to simulate the combined effect of slip and twinning. These models have the capability to model strain hardening and texture evolution associated with deformation twinning at the grain scale. Karaman et al. (2000) used the visco-plastic self-consistent (VPSC) approach for modeling the deformation behavior of hadfield steel, considering twinning and slip effects to predict the stress-strain response and texture evolution. Kalidindi (2001) extended the classical crystal plasticity model to include deformation twinning and used it to predict strain hardening and deformation textures in low SFE FCC metals. Shiekhelsouk et al. (2009) also proposed a model for strain hardening of TWIP steel involving crystallographic slip and twinning, considering both the slip-twin and twin-twin interactions. Dancette et al. (2012) combined different approaches and proposed a dislocation-density-based description for work hardening, by relating it to the mean free path (MFP) of dislocations measured along each slip system. Different homogenization schemes were applied to predict the texture evolution and strain hardening of TWIP steel. Sun et al. (2016) proposed a crystal plasticity model with combined slip, twinning, and transformation induced plasticity using a micromechanics based approach. The simulation results of single crystals were compared with the experimental data from literature for its validation. These models have only considered either the effect of slip and twinning or the effect of slip and transformation. However, a comprehensive model incorporating the combined effect of slip, deformation twinning and martensitic transformation considering both the microstructural aspects and temperature was for a long time not available to the best knowledge of the authors and is of great interest in the current study.

The isotropic TWIP model by Steinmetz et al. (2013), though developed for polycrystalline materials does not take individual grain orientations and grain boundary interactions into account. Jia et al. (2012) included the dislocation slip and shear band formation in the crystal plasticity framework (Roters et al., 2012). The TWIP model was further extended by Wong et al. (2016) to consider the $\gamma \rightarrow \varepsilon$ martensitic transformation (TRIP), so that, the constitutive model has the capability to simulate the concurrent evolution of dislocation densities, twin and ε-martensite volume fractions. The onset of twinning or martensite transformation in the

model was determined by two separate expressions based on the critical stress for twin and ε-martensite growth. However, the model does not explicitly account for the precise distribution and arrangement of twins and martensite plates/lathes but rather the volume fraction of twins and ε-martensite at each material point.

The first objective of this work, was to provide a detailed description of the influence of temperature and SFE on the deformation mechanisms, strain hardening and fracture behavior of X60Mn22 TWIP steel. Electron back scatter diffraction (EBSD) and synchrotron X-ray diffraction (XRD) were used to study the evolution of microstructure and change in active deformation mechanisms at different temperatures. The strain hardening behavior was assessed by uniaxial tensile tests conducted at different temperatures ranging from 123 K to 773 K. The material properties were correlated with the stacking fault energy (SFE) dependent deformation mechanisms such as dislocation glide, twinning and ε-martensite transformation, to explain the strain hardening and fracture behavior. The second objective of this work, was to apply the TWIP/TRIP model of Wong et al. (2016) for predicting the strain-hardening behavior of TWIP steel for a wide range of temperatures. The microstructural parameters such as grain size and its distribution were considered for the generation of a representative volume element (RVE). In order to account for the anisotropy, the grain orientations measured using EBSD were assigned to the grains of the RVE. The model parameters were calibrated and optimized to predict the evolution of the microstructure and the deformation mechanisms at different temperatures using RVE simulations. Additionally the results were validated with the experimentally measured values. Considére's plastic instability criterion described in Eq. (1) was applied to predict the uniform elongation and necking in the simulations. The proposed modeling approach enabled the prediction of the onset of different deformation mechanisms based on the SFE and the effect of these competing deformation mechanisms on the hardening behavior of the material.

This paper is structured as follows: first, the experimental methods for characterizing the microstructure, deformation mechanisms, and mechanical properties are described. Next, the thermodynamic approach used for the prediction of the SFE as a function of temperature is reviewed, followed by a detailed description of the constitutive model used for predicting the material behavior. The simulation procedure including the virtual microstructure generation together with boundary conditions and optimization of constitutive model parameters is described next. Finally, the experimental and simulation results are presented.

2. Materials and experimental methods

The material investigated in this study was a high manganese austenitic TWIP steel. EBSD was used to analyze the texture and microstructure of the material. Tensile tests in conjunction with digital image correlation (DIC) were performed in a furnace. XRD was used to study the evolution of ε-martensite and EBSD for qualitative description of the twin evolution. The EBSD measurements were carried out to investigate the trend in the evolution of twinning or ε-martensite transformation and the phase changes with respect to temperature. Finally, fracture behavior was analyzed using scanning electron microscopy (SEM).

2.1. Chemical composition

The material considered was a industrially produced X60Mn22 TWIP steel with 0.27 wt.% Vanadium. The chemical composition was determined by optical emission spectroscopy (OES), as presented in Table 1. In the as delivered state, the material was cold rolled and annealed with a sheet thickness of 1.4 mm.

2.2. Microstructure

The microstructure consisted of fine equiaxed austenitic grains (γ) with an average grain size of 3.0 µm. Fig. 1(a) shows the inverse pole figure (IPF) with respect to the rolling direction depicting the grain sizes and the crystal orientation distribution. The initial texture was rather weak with a texture index of 1.18. Fig. 1(b) provides the grain size distribution function, where it can be observed that the grain size varied from 0.5 to 10 µm, with a very small fraction of grains larger than 5 µm. The fine grained microstructure and the addition of Vanadium helped in improving the yield strength of the material (Chateau et al., 2010; Scott et al., 2011). The detailed procedure for evaluation of grain size is explained in Section 2.6.

2.3. Tensile tests

Tensile specimens with A30 geometry (gauge length 20 mm and width 6 mm) as shown in Fig. 2 were cut along the rolling direction and the edges were polished up to a surface roughness of 0.125 µm. Tensile tests at different temperatures were carried out using a Zwick/Roell Z250 machine equipped with a furnace, along with an electrical resistance heating system and liquid nitrogen for cooling to lower temperatures. Thermocouple and a fan were installed in the furnace to determine the temperature and uniformly distribute temperature. An additional thermocouple was directly attached to the specimen's surface within the gauge length, for

Table 1
Chemical composition of the X60Mn22 TWIP steel in wt.%.

C	Si	Mn	P	S	Cr	Ni	Cu	Al	V	N	Fe
0.59	0.21	22.26	0.013	<0.001	0.08	0.02	0.02	0.01	0.27	0.019	Bal.

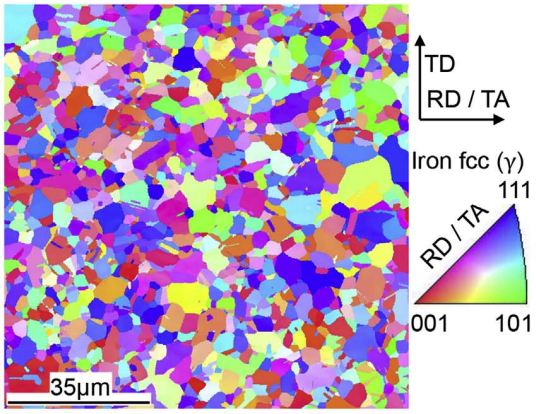

(a) EBSD map of undeformed sample showing variation in grain size and orientation; microstructure is fully Austenitic (γ); RD: rolling direction; TD: transverse direction; TA: tensile axis.

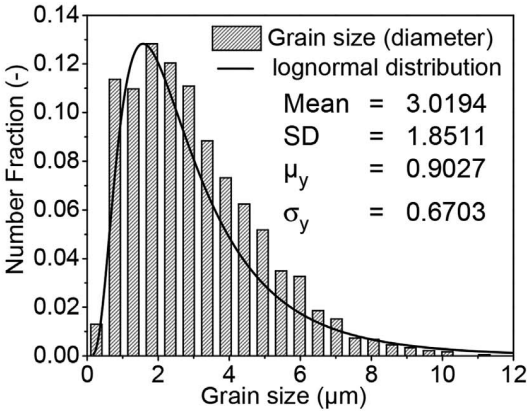

(b) Grain size distribution obtained from EBSD measurements fitted with a lognormal distribution function; average/mean grain size is 3.0 μm and standard deviation (SD) is 2 μm; μ_y and σ_y are the lognormal distribution function parameters.

Fig. 1. Microstructure of X60Mn22 TWIP steel.

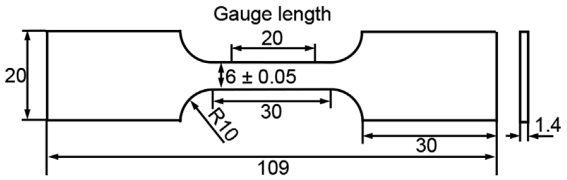

Fig. 2. Geometry of the tensile samples used in the experiments. All dimensions are given in mm.

precise control of temperature with a tolerance of ±1 °C. The tests were carried out with a cross head displacement rate of 1.8 mm/min, which corresponds to a quasi-static strain rate of about 0.001 s^{-1}. An extensometer was used to measure the change in length of the samples, which facilitates the recording of the actual elongation. A black and white speckle pattern was prepared for the digital image correlation (DIC) measurements. The ARAMIS DIC system was used for investigating the initiation and propagation of PLC bands during deformation.

2.4. Synchrotron X-ray diffraction

The ε-martensite fraction was determined by synchrotron XRD measurements on tensile samples interrupted at a true strain of 0.05, 0.10, 0.20, 0.30, 0.40 and after fracture. A diffractometer with Bragg-Brentano (θ-2θ) para focusing geometry was used for the measurements to increase intensity and angular resolution. A MAR345 image plate detector with a resolution of 3450 pixels was used to record the diffraction pattern. Initial calibration was done to calibrate the center of the 2D-detector and the exact sample to detector distance. The specimen holder was slightly inclined with a reflection angle of about 2° and the goniometer radius (i.e the sample to detector distance) was adjusted to 339 mm. The calibration was done for silicon and samples were measured with an exposure time of about 90 s. The synchrotron radiation passed through a silicon monochromator which produced monochromatic X-rays with an energy of 27 keV (wavelength of $\lambda = 0.46$ A°).

The diffraction pattern was then transformed by integrating the intensity of each detection point on a ring into a 1D diagram using the fit2D program (Hammersley, 2016). The fit2D program, enables to prescribe the calibrated tilt angle for further calculation. During the evaluation of the measurement results, the intensity of the individual pixels of the MAR345 detector lying on a ring was summed up in a first step. As a result, the program provides a table in which the integrated intensities are plotted over the 2θ angle. In a second step, the area under the respective peaks was determined. Using the Rietveld analysis, the corresponding volume fraction of the individual phases could be derived by integrating the intensities of the individual peaks of γ(200) and ε(101) (Rietveld, 1969; Choi et al., 1999). The open source program Materials Analysis Using Diffraction (MAUD) (Matthies et al., 1997) was used for the analysis of the data. According to B. C. De Cooman et al. (2011), in FCC metals the ε-martensite exhibits a complete hcp structure and mechanical twins show a local hcp arrangement only on their boundaries. Therefore the ε-martensite volume fraction can be deduced directly from the integrated intensities of the ε-martensite peaks. The lattice parameter proposed by Gebhardt et al. (2010) was used as a reference for further quantification of the austenite and ε-martensite phase fractions. More details on the experimental and evaluation procedure can be found in Twardowski (2013).

2.5. Scanning electron microscopy (SEM)

Fracture surface analysis of tensile samples was carried out using a field emission SEM from the Zeiss Σigma family. Three samples were investigated at each temperature in the range from 123 K–773 K to identify differences in the fracture behavior. Images were taken at different locations such as the middle of the specimen, close to the edges and at corners to calculate dimple size with good statistics. SEM images were processed using the ImageJ software (Schindelin et al., 2015) to determine the dimple size. Images in binary format were imported into the software, then the image scale was calibrated and dimple boundaries were identified. The images were further segmented to distinguish the dimples from their background by manual thresholding. Overlapping dimples in the images were separated by using a watershed function and the resulting images were analyzed using a Matlab program developed by Lehto et al. (2016) to determine the volume weighted average dimple size. For better statistics eight images were analyzed for each temperature and the average dimple size was determined.

2.6. Electron back scatter diffraction (EBSD)

EBSD measurements were carried out using a JEOL JSM 7000F FEG-SEM equipped with an EDAX-TSL Hikari camera to observe the initial microstructure and the orientation of grains. A voltage of 20 kV with a probe current of about 20–30 nA and a step size of 100 nm were used for the initial microstructural investigation. OIM® Data Collection 6.2/OIM® Analysis 6.2 software was used to analyze the data. For the estimation of grain size, two EBSD measurements were performed, with each mapped area containing more than 2500 grains. Grain boundaries were identified as boundaries where the misorientation angle was above 5°. Twin boundaries were ignored during the grain detection procedure and regions with at least five pixels were counted as grains. A moderate grain confidence index (CI) standardization clean-up procedure, which removes the low CI pixels at grain boundaries was applied. The number-weighted average grain diameter (D) was used to quantify the average grain size (equivalent diameter) in the microstructure.

To study the evolution of phases and twinning with temperature, EBSD measurements were performed on the test sample close to the fracture surface along the rolling direction as shown in Fig. 6. The samples were embedded in a non-conductive epoxy resin, ground and electropolished. The interface between the sample and the resin was coated with silver paint to ensure conduction. To investigate evolution of twinning with increasing strain, EBSD measurements were also carried out on the electropolished micro tensile samples interrupted at a true strain of 0.05, 0.12, 0.22, 0.32 and after fracture. A step size of 50 nm was used for the fractured samples and 100 nm for the interrupted micro tensile samples. Twins have the same crystal structure as the matrix, differing only by their crystallographic orientation. Thus twin boundaries can be identified by inspecting the misorientation between the neighboring measurement points (Wright and Larsen, 2002). If the misorientation was within a given tolerance of the specified twin misorientation, the boundary separating the two points may be identified as a potential twin or twin boundary. In addition, for a coherent twin detection, the twinning planes must be coincident with the grain boundary plane. However, most of the deformation twins detected by EBSD were incoherent. Hence the criterion used for the identification of twin boundaries was 60° misorientation angle about the <111> axis, along with an angular tolerance of 5° within the γ_{fcc}-matrix (Saeed-Akbari et al., 2012). The quality of the EBSD measurement is given by the Confidence Index (CI) value. The unindexed points were excluded from the evaluation of the twin fraction by neglecting all points with CI < 0.1.

The extraction of twins or twin bundles from EBSD maps containing grains with twins was carried out using a MATLAB® based program (MTEX toolbox) (Bachmann et al., 2011). Unindexed points as shown in Fig. 3(a) (pixels in red), were not considered for the twin evaluation. For quantitative evaluation of the twin fraction, the number of pixels indexed as twins or twin bundles were compared with the total number of pixels. The detected twins and grains can be seen in Fig. 3(a) and the separated twins in Fig. 3(b). The ratio of twin bundles area in the grain to the total grain area provides the twin fraction per grain. A numerical average of twins in all grains represents the total twin fraction of the sample. The detection of twins based on orientation, depends on the density of the twin lamellae within the interaction volume. Twins were indexed by observing the most intensive bands obtained from the superposition of two identified patterns. If enough twins were found then the indexing resulted in the twin orientation, otherwise the indexing yielded the parent orientation. Because of such limitations in twin detection, the smallest twins could not be identified.

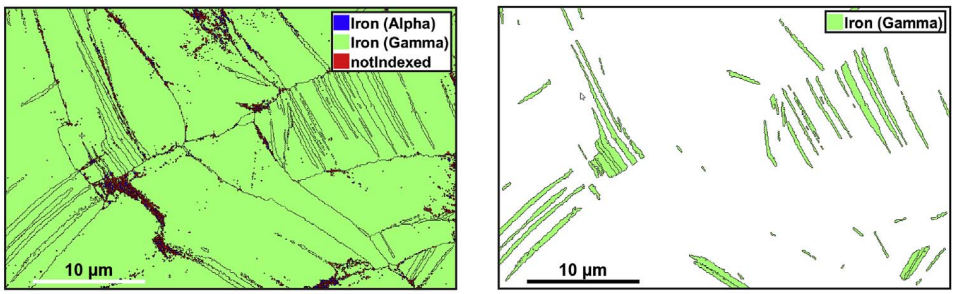

(a) Imported EBSD map using the MTEX Toolbox showing the identified grain and twin boundaries; the pixels in red are the unindexed points.

(b) Twins or twin bundles separated from the grains using the twin orientation relationship criterion.

Fig. 3. Extraction of twins from grains and the evaluation of twin fraction.

Furthermore, the deformation in the sample resulted in a large proportion of unindexed pixels. Hence the approach used is only semi-quantitative measure for the evolution of twinning.

3. Modeling and simulations

3.1. Thermodynamic stacking fault energy (SFE) calculations

The active deformation mechanisms in TWIP steels are determined by the SFE. There are several models to calculate the SFE based on the thermodynamic approach (Saeed-Akbari et al., 2009, 2012; Pierce et al., 2014; Zambrano, 2016). The main difference in these models is the expression to calculate the austenite Ne′el temperature which depends largely on different alloying elements present in the material and the additional term of Gibbs free energy, ΔG_{excess} which considers the influence of austenite grain size on the SFE. In this work, the SFE was calculated using the thermodynamic model of Allain et al. (2004c), which was further extended by Dumay et al. (2008) to consider the influence of the alloying elements Al, Cr, Si and Cu. The model takes into account the variation of Gibbs free energy for each alloying element and their interactions during $\gamma \rightarrow \varepsilon$ transformation. The expressions used for the austenite and ε-martensite Ne′el temperature as presented in Eq. (2) and Eq. (3), respectively, take into account the influence of different alloying elements (Dumay et al., 2008; Allain et al., 2004c).

$$T^{\gamma}_{Ne'el} = 250ln(x_{Mn}) - 4750x_C x_{Mn} - 222x_{Cu} - 2.6x_{Cr} - 6.2x_{Al} - 13x_{Si} + 720(K) \quad (2)$$

$$T^{\varepsilon}_{Ne'el} = 580x_{Mn}(K) \quad (3)$$

The SFE is defined as (Hirth, 1970; Olson and Cohen, 1976):

$$\Gamma_{sf} = 2\rho\Delta G^{\gamma\rightarrow\varepsilon} + 2\sigma^{\gamma/\varepsilon} \quad (4)$$

where $\Delta G^{\gamma\rightarrow\varepsilon}$ is the Gibbs free energy difference and $\sigma^{\gamma/\varepsilon}$ is the interfacial energy between the austenite and ε-martensite phases. ρ is the molar surface density of the {111} plane which is given by:

$$\rho = \frac{4}{\sqrt{3}a^2}\frac{1}{N_A} \quad (5)$$

where a is the FCC lattice parameter of the austenite phase and N_A is Avogadro's number.

Plots of calculated values of the SFE and $\Delta G^{\gamma\rightarrow\varepsilon}$ as a function of temperature and composition (ref. Table 1) are shown in Fig. 4(a) and (b) respectively. It can be seen that at lower temperatures the chemical contribution to SFE was negative and the magnetic contribution was quite large. Similar effects can also be observed in the contribution of the $\Delta G^{\gamma\rightarrow\varepsilon}_{chemical}$ (chemical) and $\Delta G^{\gamma\rightarrow\varepsilon}_{magnetic}$ (magnetic) parts of change in Gibbs free energy as shown in Fig. 4(b). The Gibbs free energy variation due to the transition from antiferromagnetic to paramagnetic was taken into account in the current thermodynamic model (Allain et al., 2004c). However, the large discrepancy in SFE due to contributions of chemical or magnetic parts shown in Fig. 4(a) and (b), indicated that magnetic interactions and/or chemical ordering exist and play a crucial role along with lattice stability in Fe-Mn alloys at these temperatures (Vitos et al., 2006; Music et al., 2007; Dick et al., 2009). The computed values of Ne′el temperature of austenite from Eq. (2) and the Ne′el temperature of ε-martensite from Eq. (3) were 314 K and 128 K respectively. The SFE should be in the range of 22–26 mJ/m^2 for TWIP steels at 298 K. The transition between TWIP and ε-martensite phase transformation typically occurs when the SFE is between 18 and 20 mJ/m^2. However when the SFE is below 12 mJ/m^2 the formation of α'-martensite is preferred (Dumay et al., 2008). Since

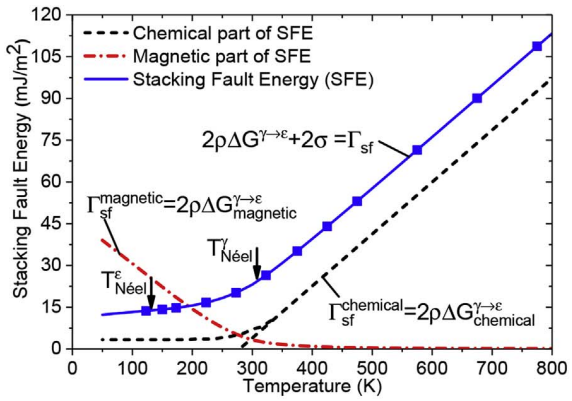

(a) Variation of SFE (Γ_{sf}) with temperature; $\Gamma^{magnetic}_{sf}$: Magnetic Contribution to SFE; $\Gamma^{chemical}_{sf}$: Chemical contribution to SFE; $T^{\gamma}_{Néel}$: Néel temperature for γ and $T^{\varepsilon}_{Néel}$: Néel temperature for ε-martensite.

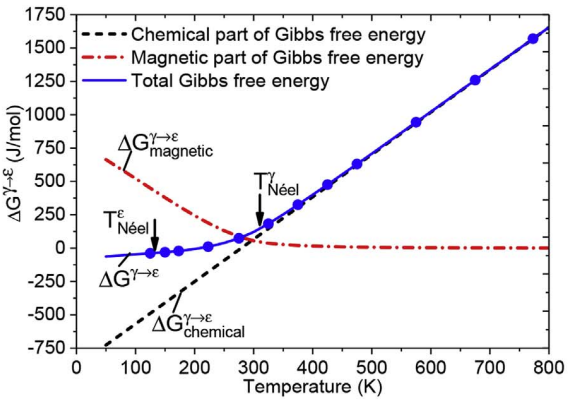

(b) Variation of Gibbs free energy ($\Delta G^{\gamma\rightarrow\varepsilon}$) with temperature; $\Delta G^{\gamma\rightarrow\varepsilon}_{magnetic}$: Magnetic part of Gibbs free energy; $\Delta G^{\gamma\rightarrow\varepsilon}_{chemical}$: Chemical part of Gibbs free energy.

Fig. 4. Stacking fault energy and Gibbs free energy as a function of temperature calculated based on the thermodynamic approach for X60Mn22 TWIP steel.

ε-martensite was found only in the X60Mn22 TWIP steel as described in Section 4.1, the SFE at lower temperatures should be adjusted to be larger than 12 mJ/m^2 by controlling the interface energy parameter. The interface energy value of $\sigma^{\gamma/\varepsilon} = 8$ mJ/m^2 as proposed by Allain et al. (2004c), Dumay et al. (2008), Saeed-Akbari et al. (2009) satisfies this criterion.

3.2. Constitutive model

A detailed description of the constitutive model used in the current study has been published in the author's previous work (Wong et al., 2016). In this study, only a brief summary of the model is presented in this section. Twin formation in FCC metals is associated with the dissociation of a perfect dislocation on the {111} plane into two Shockley partial dislocations as presented in Teutonico (1963), Hirth and Lothe (1982):

$$\frac{a}{2}\left\langle 01\bar{1}\right\rangle + \frac{a}{2}\left\langle 10\bar{1}\right\rangle = 3 \times \frac{a}{6}\left\langle 11\bar{2}\right\rangle \tag{6}$$

where a is the lattice parameter.

Twin formation involves the passage of $\frac{1}{6}\langle 11\bar{2}\rangle$ Shockley partials on every {111} plane (Mahajan and Chin, 1973; Christian and Mahajan, 1995), while the formation of ε-martensite ($\gamma \rightarrow \varepsilon$ transformation) is achieved through the passage of $\frac{1}{6}\langle 11\bar{2}\rangle$ Shockley partials on every second {111} plane (Christian, 1951; Olson and Cohen, 1972). For low SFE FCC metals, mechanical twinning, and ε-martensite nucleation mechanisms are very similar in terms of the dislocation reactions which form the twin and ε-martensite nuclei.

The twin nucleus model used to describe deformation twinning was first proposed by Mahajan and Chin (1973). Further work on the twin nucleus model was presented by Roters (2011), Steinmetz et al. (2013), Wong et al. (2016). The critical condition for growth of the twin nucleus is determined by the overall energy of the system which is the sum of the energy supplied by the applied shear stress, Q_{work}, the energy required to create two interfaces between the twin and the parent phase, Q_{sf} and the energy required to extend the dislocation line, Q_{line}. The expression for the total energy of the system is given by

$$Q_{\text{total}} = \underbrace{-3b\tau A(r, L)}_{\mathbf{Q_{work}}} + \underbrace{\Gamma_{\text{sf}} A(r, L)}_{\mathbf{Q_{sf}}} + \underbrace{\frac{9}{2} G b^2 B(r, L)}_{\mathbf{Q_{line}}} \tag{7}$$

where the term Γ_{sf} is the stacking fault energy (SFE) and b is the magnitude of the Burgers vector of the Shockley partial. For the term Q_{sf}, the SFE is assumed to be approximately twice the twin interface energy Γ_{sf}. The term $A(r, L)$ is the area function and $B(r, L)$ is the line length function for a twin nucleus with dimensions r and L.

The critical stress for the growth of the twin nucleus is then given by Steinmetz et al. (2013):

$$\hat{\tau}_{\text{tw}} = \frac{\Gamma_{\text{sf}}}{3b_{\text{tw}}} + \frac{3Gb_{\text{tw}}}{L_{\text{tw}}} \tag{8}$$

The hcp nucleus model proposed by Mahajan et al. (1977) and further extended by Wong et al. (2016) was used to describe the $\gamma \rightarrow \varepsilon$ martensitic phase transformation. The critical condition for the growth of a hcp nucleus is also determined by the overall energy of the system similar to the twin nucleation model. The expression for the overall energy of the system is similar to Eq. (7), but an additional term Q_{trans} is added to account for the release of energy due to a change in phase as shown in Eq. (9). For the interface energy term, Q_{int}, the previous assumption that the SFE is approximately twice the twin interface energy Γ_{sf} as used in the twinning case in Eq. (7) is not valid for low SFE. The expression for the total energy of the system is given by Wong et al. (2016):

$$Q_{\text{total}} = \underbrace{-3b\tau A(r, L)}_{\mathbf{Q_{work}}} + \underbrace{2\sigma^{\gamma/\varepsilon} A(r, L)}_{\mathbf{Q_{int}}} + \underbrace{\frac{9}{2} G b^2 B(r, L)}_{\mathbf{Q_{line}}} + \underbrace{hA(r, L)\Delta G^{\gamma\rightarrow\varepsilon}}_{\mathbf{Q_{trans}}} \tag{9}$$

where $\sigma^{\gamma/\varepsilon}$ is the interface energy, h is the height of the hcp nucleus, $L = L_{\text{tr}}$, and $\Delta G^{\gamma\rightarrow\varepsilon}$ is the change in Gibbs free energy per unit volume for the austenite to martensite transformation.

The critical stress for growth of the hcp nucleus is given by

$$\hat{\tau}_{\text{tr}} = \frac{\Gamma_{\text{sf}}}{3b_{\text{tr}}} + \frac{3Gb_{\text{tr}}}{L_{\text{tr}}} + \frac{h\Delta G^{\gamma\rightarrow\varepsilon}}{3b_{\text{tr}}} \tag{10}$$

where b_{tr} is the magnitude of the Burgers vector for transformation.

In the crystal plasticity simulations, both deformation twinning and ε-martensite transformation was considered in addition to crystallographic slip. Following the approach of Kalidindi (1998b), the contributions of mechanical twinning and phase transformation were taken into account as additional terms in the plastic velocity gradient. The total plastic deformation gradient can thus be calculated as the sum of all three, crystallographic slip, deformation twinning, and phase transformation according to

$$\mathbf{L}_{\text{p}} = \left(1 - \sum_{\beta=1}^{N_{\text{tw}}} f^{\beta} - \sum_{\chi=1}^{N_{\text{tr}}} f^{\chi}\right) \sum_{\alpha=1}^{N_{\text{s}}} \dot{\gamma}^{\alpha} \boldsymbol{m}^{\alpha} \otimes \boldsymbol{n}^{\alpha} + \sum_{\beta=1}^{N_{\text{tw}}} \dot{\gamma}^{\beta} \boldsymbol{m}_{\text{tw}}^{\beta} \otimes \boldsymbol{n}_{\text{tw}}^{\beta} + \sum_{\chi=1}^{N_{\text{tr}}} \dot{\gamma}^{\chi} \boldsymbol{m}_{\text{tr}}^{\chi} \otimes \boldsymbol{n}_{\text{tr}}^{\chi} \tag{11}$$

where f^{β} is the volume fraction of twins for the twin system β and f^{χ} is the volume fraction of martensite for the transformation system χ. The vectors $\boldsymbol{m}$ and $\boldsymbol{n}$ denote the directions and plane normals of the deformation systems on which shear occurs at a rate of $\dot{\gamma}$.

The microstructure is parametrized in terms of the edge dislocation density ρ_e, the dipole dislocation density ρ_d, the twin volume fraction f_{tw} and ε-martensite volume fraction f_{tr}. In a dislocation-based model, the Orowan (1934) equation gives the shear rate on the slip system α as

$$\dot{\gamma}^{\alpha} = \rho_e b_s v_0 \exp\left[-\frac{Q_s}{k_B T}\left\{1 - \left(\frac{|\tau_{eff}^{\alpha}|}{\tau_{sol}}\right)^{p}\right\}^{q}\right] \mathrm{sign}(\tau^{\alpha}) \tag{12}$$

where τ_{eff}^{α} is the effective resolved shear stress on the slip system α, τ_{sol} is the solid solution strength, b_s is the magnitude of the Burgers vector for slip, v_0 is the prefactor for calculating dislocation glide velocity, Q_s is the activation energy for dislocation slip, k_B is the Boltzmann constant, T is the temperature, and p and q are fitting parameters.

The shear rate for each twin system β is given by

$$\dot{\gamma}^{\beta} = \gamma_{tw} \dot{f}^{\beta} \tag{13}$$

where γ_{tw} is the characteristic twin shear.

The shearing rate for each transformation system χ is given by

$$\dot{\gamma}^{\chi} = \gamma_{tr} \dot{f}^{\chi} \tag{14}$$

where γ_{tr} is a characteristic shear for transformation.

Strain hardening in the model is described in terms of a dislocation mean free path (MFP) approach, which is denoted by the symbol λ. The MFP for slip has contributions due to dislocations λ_{slip}^{α}, the formation of twins $\lambda_{sliptwin}^{\alpha}$ and the formation of ε-martensite $\lambda_{sliptrans}^{\alpha}$. The MFP between two obstacles seen by a growing twin is given by λ_{tw}^{β} and the MFP between two obstacles seen by a growing ε-martensite lath is given by λ_{tr}^{χ}.

The evolution of the twin volume fraction is given by

$$\dot{f}^{\beta} = (1 - f_{tw} - f_{tr}) V^{\beta} \dot{N}_{tw}^{\beta} \tag{15}$$

where $\dot{N}_{tw}^{\beta}$ is the twin nucleation rate for the twin system β and V^{β} is the volume of a new twin.

The volume of a new twin is given by

$$V^{\beta} = \frac{\pi}{4} \Lambda_{tw}^{2} t_{tw} \tag{16}$$

where Λ_{tw} is the MFP for twins and t_{tw} is the average twin thickness.

The twin nucleation rate for the twin system β is given as

$$\dot{N}_{tw}^{\beta} = \dot{N}_0 p_{ncs} p_{tw} \tag{17}$$

where $\dot{N}_0$ is the number density of potential twin nuclei per unit time.

The probability that cross-slip does not occur, which would allow a sufficient number of dislocations to pile up and form the stress concentration necessary to form a twin nucleus, is given as

$$p_{ncs} = 1 - \exp\left[-\frac{V_{cs}}{k_B T}(\tau_r - \tau^{\beta})\right] \tag{18}$$

where V_{cs} is the cross-slip activation volume and τ_r is the stress needed to bring two partials to the critical distance needed to form the twin nucleus.

The probability that the twin nucleus bows out to form a twin is

$$p_{tw} = \exp\left[-\left(\frac{\hat{\tau}_{tw}}{\tau^{\beta}}\right)^{A}\right] \tag{19}$$

where the critical stress for twinning, $\hat{\tau}_{tw}$, is given in Eq. (8), τ^{β} is the resolved shear stress on the twin system β and A is a fitting parameter which determines the sharpness of the transition between the non-twinning to the twinning regime.

The evolution of the volume fraction of ε-martensite is given by

$$\dot{f}^{\chi} = (1 - f_{tw} - f_{tr}) V^{\chi} \dot{N}_{tr}^{\chi} \tag{20}$$

where $\dot{N}_{tr}^{\chi}$ is the total nucleation rate of ε-martensite and V^{χ} is the volume of the new ε-martensite lath.

The volume of the new ε-martensite lath is given by

$$V^{\chi} = \frac{\pi}{4} \Lambda_{tr}^{2} t_{tr} \tag{21}$$

where Λ_{tr} is the MFP for ε-martensite and t_{tr} is the ε-martensite mean thickness.

The probability that the six layer hcp nucleus bows out to form an ε-martensite lath is

$$p_{\mathrm{tr}} = \exp\left[-\left(\frac{\hat{\tau}_{\mathrm{tr}}}{\tau^{\chi}}\right)^{B}\right] \tag{22}$$

where the critical stress for transformation, $\hat{\tau}_{\mathrm{tr}}$ is given in Eq. (10), τ^{χ} is the resolved shear stress on the transformation system χ and B is a fitting parameter.

The total nucleation rate of ε-martensite is given as

$$\dot{N}_{\mathrm{tr}}^{\chi} = \dot{N}_0 p_{\mathrm{tr}} \tag{23}$$

The expression for $\dot{N}_0$ in Eq. (23) is assumed to be the same as that in Eq. (17) because the dislocation reactions are assumed to be equally likely to form twin nuclei or ε-martensite nuclei.

3.3. RVE generation and simulation approach

The simulations were performed using the spectral solver implemented in the open source crystal plasticity simulation framework DAMASK (Roters et al., 2012). Lebensohn et al. (2012) proposed the usage of the Fast Fourier Transform (FFT) approach for modeling and prediction of micromechanical fields in polycrystalline materials. Eisenlohr et al. (2013) extended the DAMASK framework to solve elasto-viscoplastic boundary value problems using the spectral solver in combination with various constitutive models. The spectral methods were developed further to predict the micro-mechanical behavior of plastically deforming heterogeneous materials by Shanthraj et al. (2015). In the current work, the constitutive model developed within the framework of DAMASK incorporating the dislocation glide, twinning and ε-martensite phase transformation effects was used for the simulations. A brief description of the constitutive law is outlined in Section 3.2 and a more detailed theoretical discussion is given elsewhere (Wong et al., 2016).

A periodic representative volume element (RVE) with physical dimensions of $12\times12\times12\,\mu m^3$ was constructed from a Voronoi tessellations on a grid consisting of 32×32×32 voxels and 500 random seed points. The seed points were generated using a lognormal distribution function parameters, $\mu_y = 0.9027$ and $\sigma_y = 0.6703$ (as shown in Section 2.2) to take into account the grain size distribution (Quey et al., 2011). All voxels belonging to a Voronoi grain were assigned the same crystal orientation. From the EBSD measurement encompassing more than 2500 grains, as shown in Fig. 1, an orientation distribution function (ODF) was determined. Using this ODF, 500 grain orientations were assigned to the individual grains of the RVE.

The boundary conditions were chosen to represent uniaxial tension along the x-direction. The uniaxial tension was prescribed through mixed boundary conditions as presented below

$$\frac{\dot{\overline{F}}}{10^{-3}s^{-1}} = \begin{bmatrix} 1 & 0 & 0 \\ 0 & * & 0 \\ 0 & 0 & * \end{bmatrix} \quad \text{and} \quad \frac{\overline{P}}{Pa} = \begin{bmatrix} * & * & * \\ * & 0 & * \\ * & * & 0 \end{bmatrix} \tag{24}$$

where $\dot{\overline{F}}$ is the rate of deformation gradient, $\overline{P}$ First-Piola-Kirchoff stress and '*' denotes the components for which complementary conditions were prescribed. These conditions were applied in 4800 increments over 600 s for a final deformation of $\overline{F}_{11} = 1.6$ which corresponds to a uniaxial tensile strain of 0.6. The boundary conditions imposed on the RVE were approximately same as those for the mechanical loading in the uniaxial tension experiments with the strain rate of $0.001\,s^{-1}$ as explained in Section 2.3.

The averaged stress and strain values at each increment obtained from the RVE simulations were compared with the experimental stress–strain (σ–ε) and the strain-hardening ($d\sigma/d\varepsilon$–ε) behavior. The procedure for obtaining optimized constitutive model parameters for dislocation glide, twinning and ε-martensite transformation will be explained in Section 3.4 and the list of model parameters finally used in the simulations is given in Table 4. The single crystal elastic moduli used for the austenite phase and the ε-martensite phase are given in Table 2. The remaining model parameters, which are temperature dependent input parameters such as the solid solution strength (τ_{sol}), the stacking fault energy (Γ_{sf}), and the Gibbs free energy difference for the $\gamma \rightarrow \varepsilon$ transformation ($\Delta G^{\gamma\rightarrow\varepsilon}$) are given in Table 3. Since the yield strength of the material varies with temperature, the solid solution strength (τ_{sol}) was varied to achieve this difference in the simulated flow curves. The approach for determining SFE and Gibbs free energy was described in Section 3.1.

3.4. Constitutive model parameters

Music et al. calculated elastic properties of the Fe-Mn alloys using ab initio methods and deduced the elastic constants for the austenite phase as a function of Mn (Music et al., 2007). For the Mn composition given in Table 1, the single crystal elastic constants for austenite phase were obtained. The single crystal elastic constants for the ε-martensite phase were calculated from the FCC elastic constants using the procedure described by Wong et al. (2016). The elastic constants for the γ-phase and the ε-martensite phase are given in Table 2.

The SFE at different temperatures is the controlling parameter for switching between the deformation mechanisms dislocation glide, twinning and ε-martensite transformation. The Gibbs free energy difference, $\Delta G^{\gamma\rightarrow\varepsilon}$, controls the triggering of the ε-martensite transformation in the model. The procedure for the evaluation of the SFE and Gibbs free energy difference, $\Delta G^{\gamma\rightarrow\varepsilon}$ was explained in Section 3.1. The computed values of SFE and $\Delta G^{\gamma\rightarrow\varepsilon}$ at different temperatures are given in Table 3.

The constitutive model parameters for the crystal plasticity model were determined by fitting the macroscopic stress–strain (σ–ε)

Table 2
Single crystal elastic constants for Austenite (fcc) and ε-martensite (hcp) used in the model (Music et al., 2007; Wong et al., 2016).

Austenite (fcc)	ε-martensite (hcp)	units
$C_{11}^{fcc} = 175.0$	$C_{11}^{hcp} = 242.3$	GPa
$C_{12}^{fcc} = 115.0$	$C_{12}^{hcp} = 117.7$	GPa
$C_{44}^{fcc} = 135.0$	$C_{13}^{hcp} = 45.0$	GPa
	$C_{33}^{hcp} = 315.0$	GPa
	$C_{44}^{hcp} = 40.5$	GPa

Table 3
Temperature-dependent input parameters for the investigated TWIP steel. The solid solution strength, τ_{sol}, is determined by fitting the experimental flow curves shown in Fig. 10. The SFE, Γ_{sf}, and the Gibbs free energy difference, $\Delta G^{\gamma\rightarrow\varepsilon}$, are calculated using the thermodynamic approach of Dumay et al. (2008), assuming an interface energy ($\sigma^{\gamma/\varepsilon}$) value of 8 mJ/m^2 for all temperatures as explained in Section 3.1.

Temperature(K)	τ_{sol}(MPa)	Γ_{sf}(mJ/m^2)	$\Delta G^{\gamma\rightarrow\varepsilon}$(J/mol)
123	262	13.69	−39.29
153	213	14.17	−30.98
173	188	14.72	−21.76
233	146	17.18	20.06
298	127	22.86	116.71
323	123	26.45	177.69
373	116	34.78	319.40
423	109	43.63	469.85
473	101	52.70	624.07
573	87	71.11	937.27
673	82	89.67	1253.00
773	65	108.3	1569.67

and the strain-hardening ($d\sigma/d\varepsilon$–ε) curves obtained from the uniaxial tension experiments shown in Figs. 10 and 11. The dislocation glide parameters of the model were determined from inverse analysis of the experimental flow curves at 673 K and 773 K as shown in Fig. 10, where dislocation glide is the only active deformation mechanism. The dislocation glide parameters were fixed, after obtaining a set of parameters with which both σ–ε and $d\sigma/d\varepsilon$–ε behavior can be fitted for 673 K and 773 K as shown in Fig. 14(a) and (b).

The TWIP parameters were optimized in a similar approach by fitting the flow curves from 298 K to 473 K as shown in Fig. 14(a) and the maximum twin fraction shown in Fig. 18(a) at 298 K. The fitted $\sigma - \varepsilon$ curves for temperatures between 298 K and 473 K are also shown in Fig. 14(a). However since the hardening behavior for the low-temperature flow curves was quite different in comparison to the high-temperature curves, it was found that a different value of i_{slip} was required for low temperature flow curves exhibiting dislocation glide in combination with TWIP and TRIP effects (123 K–473 K).

The change in Gibbs free energy, $\Delta G^{\gamma\rightarrow\varepsilon}$, required for the activation of the TRIP effect was calculated using the approach mentioned in Section 3.1 and other ε-martensite transformation parameters were obtained by fitting both the $\sigma - \varepsilon$ curves at 123 K as shown in Fig. 14(a) and the evolution of the ε-martensite fraction as shown in Fig. 18(b). With the Gibbs free energy difference predicted at 123 K by the thermodynamic model, the constitutive model predicts the ε-martensite volume fraction satisfactorily as observed in experiments. The optimized constitutive model parameters used for X60Mn22 TWIP steel are presented in Table 4.

4. Results

4.1. Temperature dependence of deformation mechanisms

Temperature has a significant influence on the SFE, which controls the activation of various deformation mechanisms at different temperatures. Therefore, it plays a crucial role in the evolution of microstructure and phase fractions. The diffraction intensity over the diffraction angle (2-θ) plot in Fig. 5(a) shows the peaks of austenite (γ) and the ε-martensite phases for the deformation temperature of 123 K. In the enlarged view in Fig. 5(a) large peaks of ε-martensite phase can be observed at a true strain of 0.1. The EBSD image in Fig. 5(a) also indicates the presence of a large fraction of ε-martensite. The diffraction intensity over the diffraction angle (2-θ) plot in Fig. 6 shows the peaks of austenite (γ) and the ε-martensite phases for the deformation temperature of 298 K. In the enlarged view of Fig. 6 the small peak of ε-martensite can be observed for the strains starting from 0.05 until failure ($\varepsilon \approx 0.4$). The EBSD measurement in Fig. 6 shows the microstructure and its constituent phases and the enlarged views of the small regions a-c confirm the presence of a small fraction of ε-martensite phase even at 298 K. Similarly Fig. 5(b) presents only the peaks of austenite (γ) phase for the deformation temperature of 423 K and an enlarged view is also shown. The EBSD measurement at this temperature also confirms the presence of only austenite (γ) phase. As explained in Section 3.1, the SFE decreases to about 13 mJ/m^2 leading to ε-martensite phase transformation at a temperature of 123 K and the SFE increases to about 44 mJ/m^2 at 423 K, leading to complete

Table 4
Optimized constitutive model parameters for X60Mn22 TWIP steel.

	Symbol	Description	Value	Unit
Dislocation glide parameters	b_s	Burgers vector for slip	2.56×10^{-10}	m
	Q_s	Activation energy for slip	3.5×10^{-19}	J
	Q_c	Activation energy for climb	3.0×10^{-19}	J
	Ω	Activation volume for climb	$1.5b_s^3$	m^3
	p	Obstacle profile top	1.15	
	q	Obstacle profile bottom	1.0	
	i_s	Mean free path in multiples of dislocation spacing	30.0 ($\leq$ 473 K) 12.0 (> 473 K)	
	v_0	Dislocation glide velocity prefactor	1.0×10^{-4}	m/s
	D_0	Self-diffusion coefficient for FCC Fe	4.0×10^{-5}	m^2/s
	C_{anni}	Coefficient for minimum dipole height	2.0	
	d	Grain size	3.0	μm
Twinning parameters	b_{tw}	Burgers vector for twinning	1.20×10^{-10}	m
	L_{tw}	Width of twin nucleus	9.0×10^{-8}	m
	i_{tw}	Mean free path in multiples of twin spacing	2.0	
	t_{tw}	Average twin thickness	5.0×10^{-8}	m
	A	Twinning transition profile width exponent	2.0	
	V_{cs}	Cross-slip activation volume	1.67×10^{-29}	m^3
ε-martensite phase transformation parameters	b_{tr}	Burgers vector for transformation	1.20×10^{-10}	m
	L_{tr}	Width of martensite nucleus	9.0×10^{-8}	m
	i_{tr}	Mean free path in multiples of martensite spacing	2.0	
	t_{tr}	Average martensite thickness	1.0×10^{-7}	m
	B	Transformation transition profile width exponent	15.0	

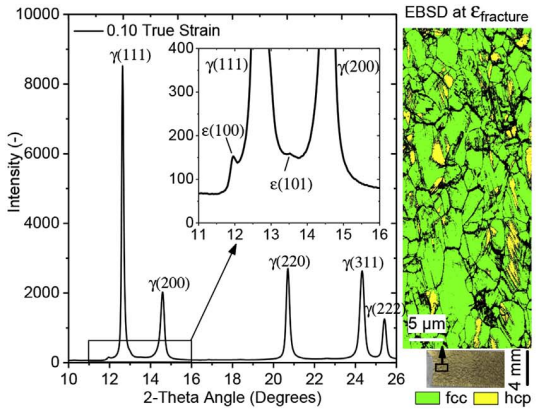

(a) Phases in a sample deformed at a temperature of 123 K; left: XRD peaks of γ and ε-martensite phases strained to 0.1 true strain; right: EBSD phase map of the fractured sample showing γ and ε-martensite phases.

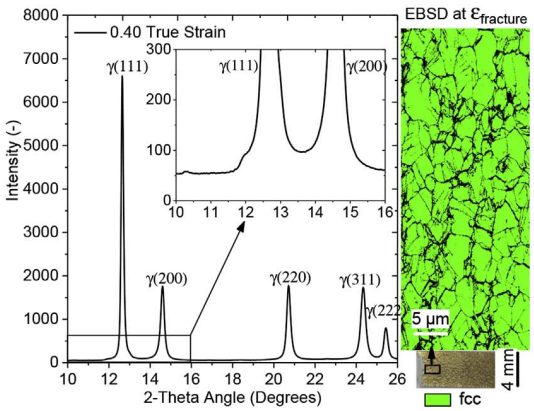

(b) Phases in a sample deformed at a temperature of 423 K; left: XRD peaks of γ phase at 423 K, strained to 0.4 true strain; right: EBSD phase map of the fractured sample showing γ phase.

Fig. 5. Phases at 123 K and 423 K.

suppression of ε-martensite transformation. Thus due to the increase in SFE, XRD experiments at 423 K do not show any ε-martensite transformation throughout the deformation until failure. Even though the SFE is 23 mJ/m^2 at 298 K, a small fraction of ε-martensite transformation is present, which could be due to a variation of local manganese content and with that the SFE.

In Fig. 7, Inverse Pole Figure (IPF) and Image Quality (IQ) maps are shown for different temperatures in the range from 123 K to 773 K. Due to very similar appearance the EBSD maps for 153 K, 173 K, 233 K, 323 K, 573 K and 773 K are not shown. The IQ map at 123 K indicates the presence of a large fraction of ε-martensite (yellow color) and also few $\Sigma 3$ twin boundaries (blue color). The $\Sigma 3$ twin boundary fraction is quite low in the sample deformed to failure at 123 K in comparison to other temperatures. In the IQ maps shown in Fig. 7, a high number of $\Sigma 3$ twin boundaries (blue color) was determined by EBSD, which reveals intense mechanical twinning between 298 K and 473 K. $\Sigma 3$ twins or twin bundles are indicated by the white arrows in Fig. 7 (IQ maps between 298 K and 473 K). The $\Sigma 3$ twin boundary fraction drops drastically in the sample deformed to failure at 673 K. With increasing temperature from 123 K to 298 K, the ε-martensite fraction decreases and the $\Sigma 3$ boundary fraction increases. With further increase in temperature above 298 K the ε-martensite vanishes completely and the $\Sigma 3$ boundary fraction increases gradually up to a temperature of 473 K. At

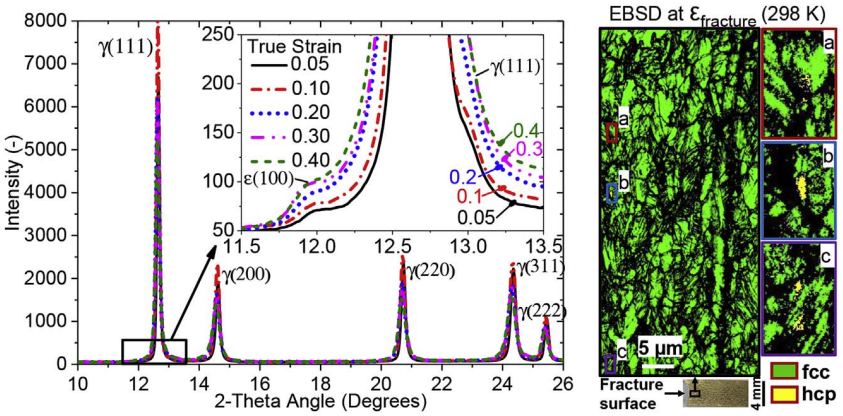

Fig. 6. Evolution of deformation mechanisms in X60Mn22 TWIP steel at 298 K; left: XRD peaks of γ and ε-martensite phases at different strains; right: EBSD phase map of the fractured sample showing γ and ε-martensite phases; position of the EBSD measurement on fractured sample is shown; pixels in black are unindexed points.

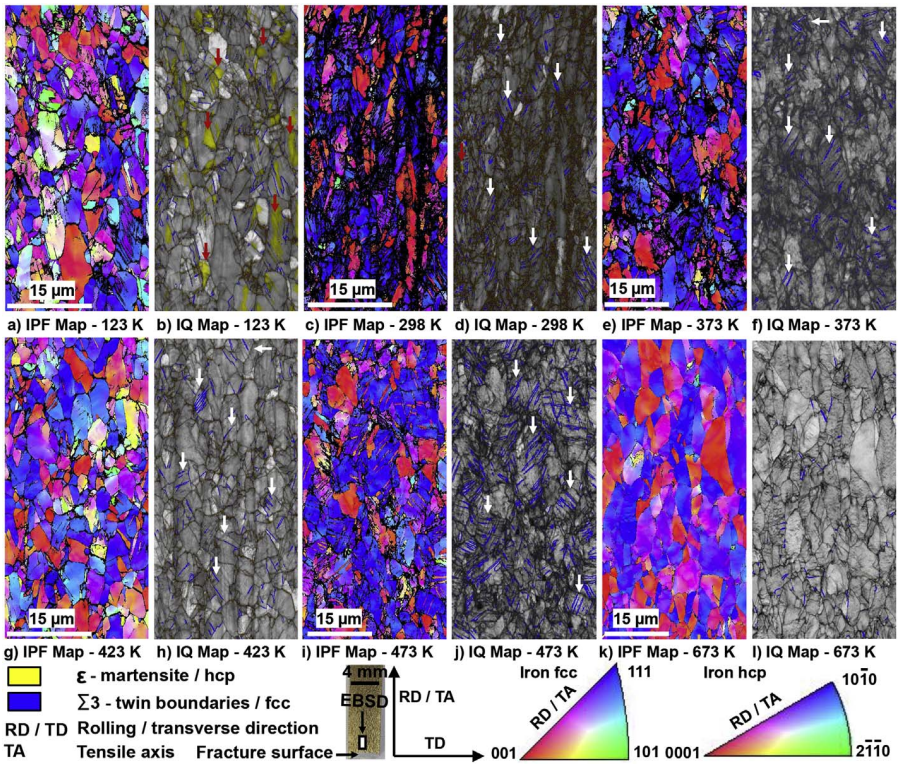

Fig. 7. RD-IPF maps of fractured samples at a temperature of: a) 123 K, c) 298 K, e) 373 K, g) 423 K, i) 473 K and k) 673 K; IQ maps of fractured samples showing γ and ε-martensite phases at a temperature of: b) 123 K, d) 298 K, f) 373 K, h) 423 K, j) 473 K and l) 673 K; blue color in IQ maps indicates Σ3 twin boundaries pointed by white arrows and yellow colored regions indicate the ε-martensite phase pointed by red arrows. The EBSD maps for temperatures 153 K, 173 K, 233 K, 323 K, 573 K and 773 K were not included in the picture due to similar appearance; position of the EBSD measurement on fractured sample is shown; pixels in black are unindexed points. (For interpretation of the references to color in this figure legend, the reader is referred to the Web version of this article.)

573 K, twinning still occurs, but the Σ3 boundary fraction decreases again. For all temperatures above 573 K, due to the large increase of the SFE (about 80 mJ/m^2), twinning is suppressed completely and deformation occurs by dislocation glide only (IQ map at 673 K).

The crystal orientation of grains has an influence on whether they preferentially undergo twinning or dislocation glide. The grains oriented along <111> will prefer twinning and the grains oriented along <001> dislocation glide as can be seen in Fig. 7 and Fig. 8 (Gutierrez-Urrutia and Raabe, 2011). Grains which are oriented along the <101> direction reorient toward the <111> direction during deformation and twins initiate in these grains as shown in Fig. 8(b) and (c). In Fig. 8(d) and (e) large heterogeneous deformation within the grains and their neighbors can be observed and all grains are either oriented along the <111> or the <001> direction.

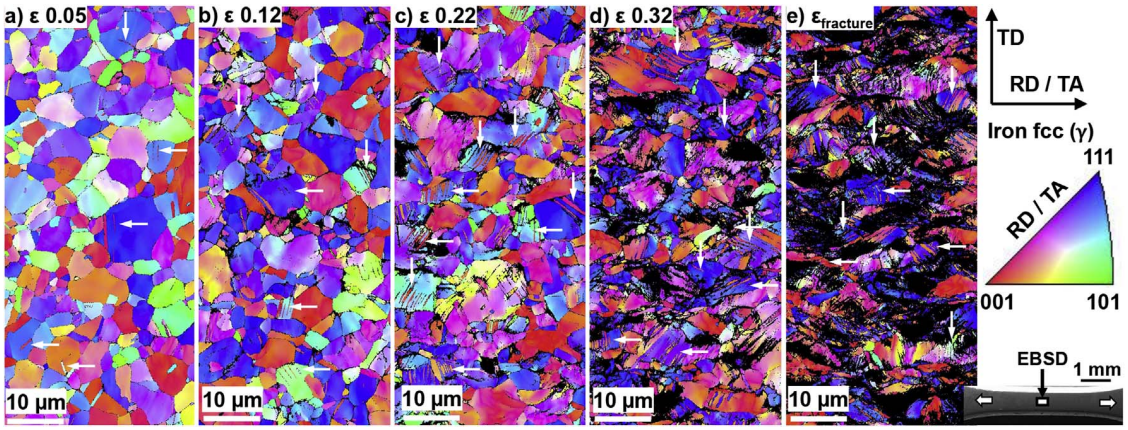

Fig. 8. EBSD maps of interrupted tensile samples showing the evolution of microstructure, orientation of grains and twins at different strains in X60Mn22 TWIP steel at 298 K; RD-IPF maps of interrupted tensile samples strained to a) 0.05 true strain, b) 0.12 true strain, c) 0.22 true strain, d) 0.32 true strain, e) failure; few twins are indicated by arrows in white color; position of the EBSD measurement on micro tensile sample is shown; pixels in black are unindexed points. (For interpretation of the references to color in this figure legend, the reader is referred to the Web version of this article.)

4.2. Temperature dependence of mechanical properties

Mechanical properties of TWIP steel depend primarily on the active deformation mechanisms, which vary with temperature due to the change in SFE. The variation of the mechanical properties such as yield strength (YS), ultimate tensile strength (UTS), uniform elongation (UE) and total elongation (TE), plotted as a function of temperature and SFE are shown in Fig. 9. At 298 K, the material has a YS of 480 MPa and an UTS of 1100 MPa. The material has a YS of 600 MPa at 123 K, which decreases to 250 MPa at 773 K. The YS of the material decreases almost linearly with increasing temperature. Between 123 K and 473 K, the UTS remains almost constant and is above 1050 MPa with a variation of about 200 MPa. Thus the temperature has a negligible influence on the UTS below 473 K. At temperatures between 673 K and 773 K, the UTS is in the range of 480–580 MPa, which is approximately half of the UTS at 298 K. The TE of the material is about 48–50% and almost constant for the temperatures between 233 K and 373 K. The TE increases above 60% for temperatures above 423 K. However, the UE decreases to almost 40% for temperature above 673 K. Temperature does not influence the TE above 233 K. The temperature ranges, where different deformation mechanisms such as dislocation glide, twinning and ε-martensite transformation are active and the range of temperature at which DSA or serrated flow occurs (as discussed in Section 4.1) are indicated in Fig. 9. The fracture mode transition temperature from completely ductile to ductile plus quasi-brittle fracture and the temperature range where necking is observed are also shown in Fig. 9.

The stress-strain behavior of the material at different temperatures is shown in Fig. 10. It can be seen that as temperature increases from 123 K to 473 K, the flow stress decreases slightly and above 473 K the flow stress drops drastically. It is known that in high

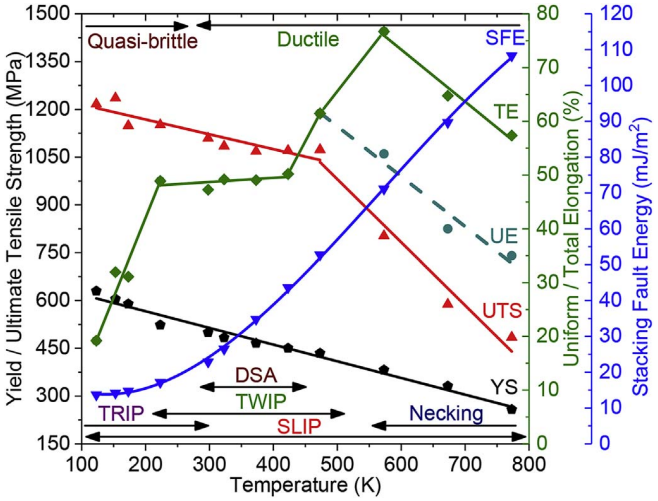

Fig. 9. Temperature influence on yield/tensile strength, uniform/total elongation and stacking fault energy for X60Mn22 TWIP steel; UE and TE are identical for temperatures between 123 K and 473 K, at which no necking occurs; the UE is plotted for temperatures between 573 K and 773 K, at which necking occurs; different SFE dependent deformation modes and the range of temperatures at which necking occurs are indicated at the bottom; the range of temperatures where ductile and quasi-brittle fracture can be observed is indicated at the top.

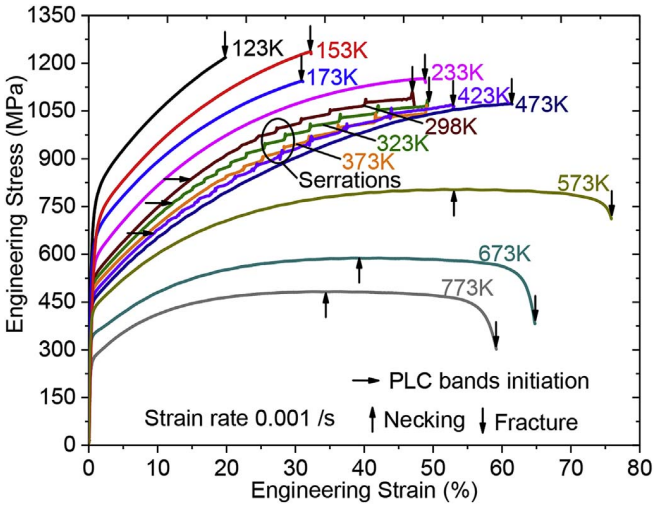

Fig. 10. Stress-strain curves at different deformation temperatures for X60Mn22 TWIP steel; serrations are observed in a temperature range from 298 K to 473 K; diffuse necking is observed for temperatures between 573 K and 773 K, which is indicated by upward arrows; downward arrows indicate fracture of the specimen.

manganese TWIP steels serrated flow occurs. It has been interpreted as a result of DSA mechanism or as Portevin-Le Chatelier effect (PLC) (Dastur and Leslie, 1981; De Almeida et al., 1994; Barbier et al., 2009). For the temperatures between 123 K and 233 K no serrations are observed on the flow curves. For temperatures in the range from 298 K to 423 K serrated flow behavior is observed, at 473 K the serrations start to disappear and with further increase of temperature serrations are completely suppressed. For all temperatures below 473 K failure occurs suddenly with very little or no necking. However, the TE at 423 K and 473 K in comparison to other temperatures is slightly higher and the samples show slight necking before failure. For the temperatures between 573 K and 773 K, diffuse necking occurs before failure.

The strain hardening rate (SHR) as a function of strain for different deformation temperatures is plotted in Fig. 11. For temperatures below 473 K remarkably high strain hardening is observed. The SHR is above 2500 MPa for all temperatures below 473 K until a strain of 0.3. For all temperatures initially, hardening is characterized by a sharp drop of the SHR. With a small increase in deformation, for the temperatures between 298 K and 473 K, the SHR increases to reach a constant value, decreasing with increasing temperature. For temperatures in the range of 298 K–373 K, where severe PLC bands are formed, the SHR decreases slightly after reaching a constant value at first and then rupture occurs causing a further drop in SHR. At 423 K, the SHR increases continuously until a strain of 0.35 and finally decreases upon failure. At 473 K, the SHR remains almost constant from the beginning, where no serrations can be observed, and then finally decreases slowly before rupture. At temperatures below 233 K and at temperatures above 473 K, where DSA does not occur and dislocation glide is the primary deformation mechanism, the SHR decreases steadily until rupture. The change in the strain hardening behavior in the X60Mn22 TWIP steel can be attributed to the temperatures at which DSA is active and the activation of different deformation mechanisms at different temperatures due to the change in SFE.

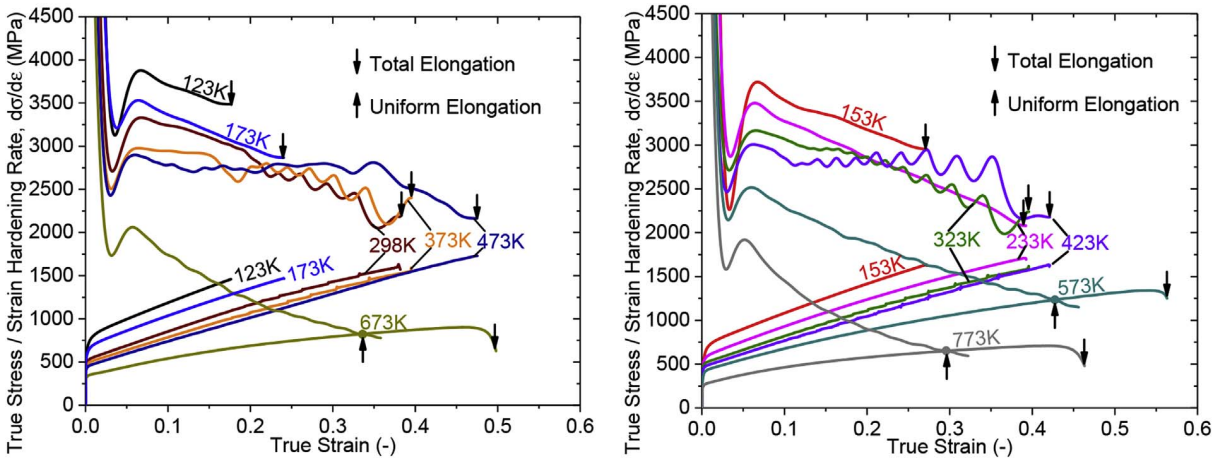

Fig. 11. Strain hardening behavior of X60Mn22 TWIP steel at different deformation temperatures in the range from 123 K–773 K; the downward arrows indicate total elongation and the upward arrows indicate uniform elongation.

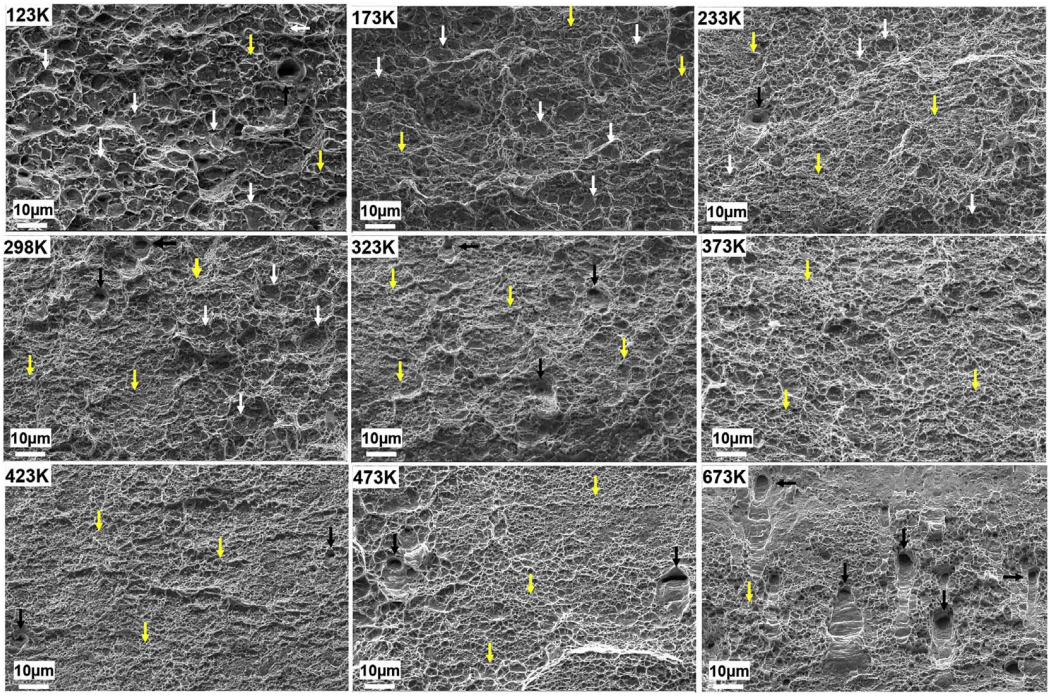

Fig. 12. Fracture surfaces of X60Mn22 TWIP steel at different deformation temperatures between 123 K and 673 K; the fracture surface at 153 K is similar to that at 173 K; the fracture surface at 573 K and 773 K is similar to that at 673 K; yellow arrows indicate regions of fine dimples, white arrows indicate quasi-brittle islands and black arrows indicate large elliptical voids formed at MnS inclusions. (For interpretation of the references to color in this figure legend, the reader is referred to the Web version of this article.)

4.3. Fracture

The activation of different deformation mechanisms at different temperatures leads to different fracture surface characteristics and failure behavior. The influence of temperature on the fracture behavior of TWIP steel is shown in Fig. 12. Quasi-brittle islands are observed on the fractured surface at temperatures below 298 K (indicated by white arrows). The area fraction of such islands increases as the temperature decreases below 298 K, which can be correlated to the increase in ε-martensite volume fraction. At all temperatures above 233 K ductile fracture with the formation of fine dimples is observed on the fractured surfaces. Fine dimples are present at almost all temperatures (indicated by yellow arrows). Bigger voids of elliptical shape are formed due to the presence of manganese sulphide (MnS) inclusions in the material, where coalescence of smaller voids takes place during the deformation (indicated by black arrows). Fine and shallow dimples are observed only at temperatures where twinning is the dominant deformation mechanism. Shallow dimples are observed on the fractured surfaces at 423 K, where severe serrations (Fig. 10) and bundles of micro twins are found in the microstructure (Fig. 7). At higher temperatures, 673 K and 773 K, many bigger voids are observed, along with mixed fine and large dimples around them. For temperatures where dislocation glide is more dominant than other deformation mechanisms, larger voids are observed.

The evolution of dimple size as a function of temperature is shown in Fig. 13. It is observed, that for temperatures in the range from 298 K to 473 K the average dimple size is approximately 1 μm. The fraction of dimples in this range of temperature is approximately 85–90%. For temperatures below 298 K and above 473 K, the average dimple size increases to about 2–2.5 μm and the dimple density drops drastically. For all temperatures below 473 K, no necking is observed in the samples and for the temperatures above 473 K, diffuse necking is observed. For temperatures between 123 K and 233 K, the reduction of area (RoA) is small, which is due to the ε-martensite transformation at lower temperatures which leads to quasi-brittle fracture as shown in Fig. 12. The RoA of the tensile samples is about 35% and it remained almost constant for temperatures in the range from 298 K to 473 K. Due to diffuse necking, RoA increases for all temperatures above 573 K.

4.4. Modeling

Investigating the strain hardening behavior of TWIP steels along with the active deformation mechanisms experimentally is both time consuming and challenging. Under such circumstances, modeling can be a useful tool for the prediction of mechanical properties.

The flow curves shown in Fig. 10 exhibit two different types of strain hardening behavior (see Fig. 11) depending on the temperature range. The flow curves in the temperature range from 123 K to 473 K have the same slope in the plastic regime and differ

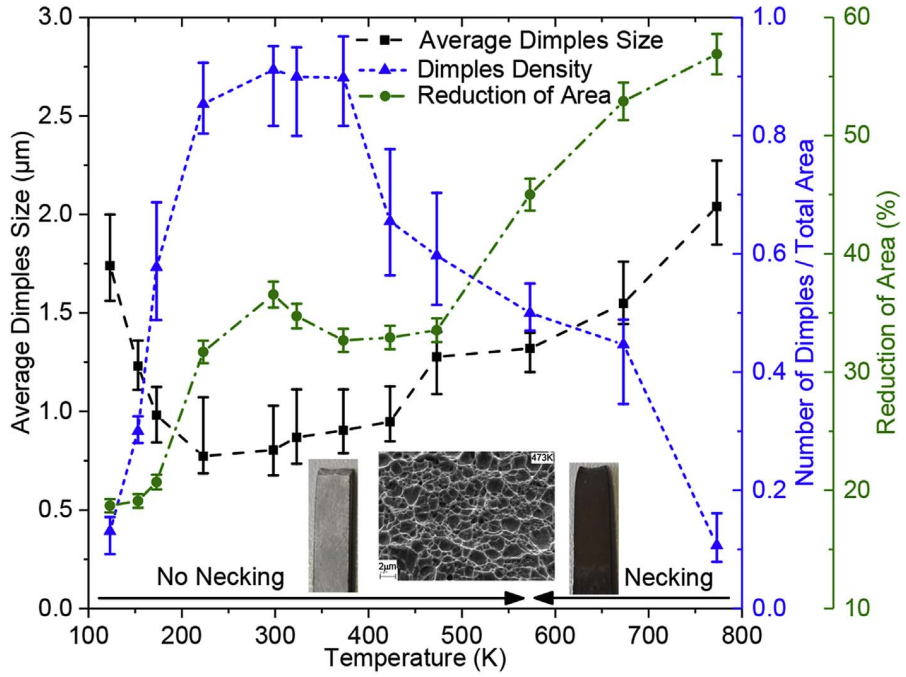

Fig. 13. Dimple size and density on the fracture surface, reduction of area at fracture in X60Mn22 TWIP steel tested at different temperatures; the transition temperature between necking and no necking regions is shown at the bottom.

only in the yield stress, where the yield stress increases with decreasing temperature (Grässel et al., 2000; Frommeyer et al., 2003; Curtze and Kuokkala, 2010). While the high-temperature flow curves (573 K–773 K) posses a smaller slope compared to the lower temperature curves (123 K–473 K) i.e. they exhibit less strain hardening. Dislocation glide is the only active deformation mechanism at temperatures between 573 K and 773 K. Additional activation of the TWIP and/or TRIP effect at lower temperatures leads to increased strain hardening.

The comparison between the experimental and simulated flow curves is shown in Fig. 14(a), while the comparison between the experimental and simulated hardening curves is shown in Fig. 14(b). The hardening curves were calculated as the slope of the flow curves. The simulated flow curves fit very well to the experimental data. Also the simulated and experimental strain hardening curves are in good agreement. Considére's plastic instability criterion described in Eq. (1) was applied to predict the uniform elongation and necking in the simulations. The difference between the predicted and experimental UE is shown in Fig. 14(b). For temperatures below 473 K, due to the activation of different deformation mechanisms along with PLC bands depending on temperature, failure occurred before necking in the experiments. To predict the UE more accurately, therefore it is necessary to consider the influence of competing deformation mechanisms on damage initiation and failure.

The comparison of the measured and simulated twin fraction at different temperatures is shown in Fig. 15(a) and the evolution

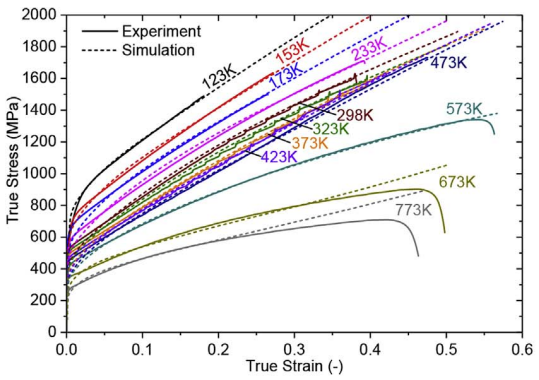

(a) Comparison of simulated stress-strain curves with experiments.

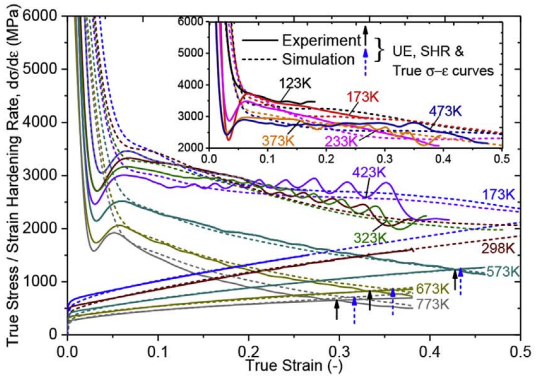

(b) Comparison of simulated strain hardening curves with experiments; exp UE: black arrows on continuous lines; sim UE: blue arrows on dotted lines.

Fig. 14. Comparison of stress-strain curves and strain hardening behavior between experiments and simulations at deformation temperatures from 123 K to 773 K.

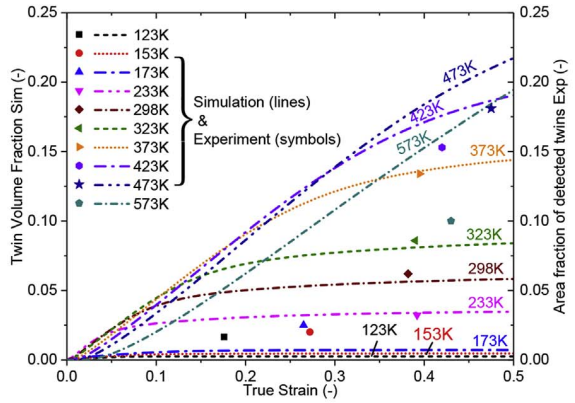

(a) Evolution of twin fraction during straining at different temperatures.

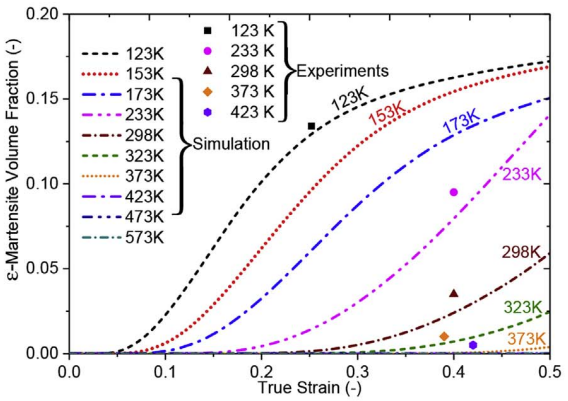

(b) Evolution of ε-martensite volume fraction during straining at different temperatures.

Fig. 15. Evolution of deformation mechanisms in simulation at deformation temperatures from 123 K to 573 K; in simulations at a temperature of 673 K and 773 K twin fraction is zero and at temperatures above 373 K ε-martensite fraction is zero; whereas minute fraction of twins can be observed at 673 K and 773 K in the experiments as shown in Fig. 7; EBSD was carried out only after failure at different temperatures, therefore only one point of twin fraction is plotted for each temperature (Fig. 15(a)); ε-martensite fraction was measured only at 123 K, 233 K, 298 K, 323 K and 423 K, therefore only at these temperatures and at the point of failure ε-martensite fraction is plotted (Fig. 15(b)).

with strain at 298 K is shown in Fig. 18(a). It can be seen in Fig. 15(a) that twinning initiates after a strain of about 0.05. For temperatures above 298 K, the initiation of twinning is delayed and the twin fraction increases gradually up to 473 K above which it decreases again (see Fig. 15(a)). There is a qualitative agreement between the measured and computed twin fraction, where the twin fraction increases with increase in deformation at 298 K (see Fig. 18(a)). The predicted twin fraction is slightly higher than the values obtained from the EBSD for temperatures above 373 K. The EBSD measurements obtained, from the interrupted tensile samples deformed to different strains at 298 K, yielded high quality measurements with very few unindexed points as shown in Fig. 8. The EBSD measurements carried out on the fractured samples for temperatures between 123 K and 773 K show the evolution of twinning (see Fig. 7). Twins were not detected at temperatures above 673 K as shown in Fig. 7(i) and the model also predicted that twinning does not occur at these temperatures. Thus the model is able to predict not only twin fraction at different temperatures, but also the change in deformation mode with temperature. The comparison of the measured and simulated ε-martensite fraction at different temperatures is shown in Fig. 15(b) and the evolution with strain is shown in Fig. 18(b). The measured and computed ε-martensite volume fraction decreases with increasing temperature. The ε-martensite volume fraction in experiments at 298 K is about 0.05 and it drops to zero at temperatures above 323 K. The ε-martensite transformation is active at lower temperatures because of the low SFE and does not occur at higher temperatures as the SFE and Gibbs free energy differences increase.

5. Discussion

5.1. Dynamic strain aging (DSA)

Serrations are observed in the experimental flow curves (see Fig. 10) at temperatures above 298 K, however they begin to diminish with increasing temperatures up to 473 K. This behavior in the flow curves has also been observed in other TWIP steels (Zavattieri et al., 2009; Kim et al., 2009; Bouaziz et al., 2011). It has been primarily attributed to the Portevin–Le Chatelier effect, a type of dynamic strain aging mechanism, which describes the dynamic interaction between mobile dislocations and the obstacles in the form of twin boundaries. When dislocations meet obstacles (twins) they are temporarily arrested. During this time solutes such as interstitial atoms diffuse to the dislocations further strengthening the obstacles. Eventually, when the applied stress is sufficiently high, dislocations will overcome these obstacles and will quickly move to the next obstacle, where they are stopped again and the process is repeated. With increasing temperature the SFE increases, leading to the suppression of twinning in the material, thereby reducing the number of twin boundaries resulting in the suppression of serrations. Serrations are completely suppressed above 473 K, due to the change in deformation mode from twinning along with dislocation glide to only dislocation glide. The diffusivity of the solute atoms decreases with decreasing temperature, which suppresses the DSA below 298 K (Idrissi et al., 2009). The predicted stress-strain behavior (see Fig. 14(a)) does not capture the serrated flow, as the DSA effect is not considered in the current constitutive model. The DSA effect could be incorporated into the model following the approaches proposed by Kubin and Estrin (1990), Kok et al. (2003).

5.2. Strain hardening and elongation

TWIP steel exhibit high strain hardening (see Fig. 11) at all temperatures below 473 K and the failure occurs abruptly without necking. The excellent strain hardening behavior is mainly due to dislocation glide in combination with twinning and ε-martensite

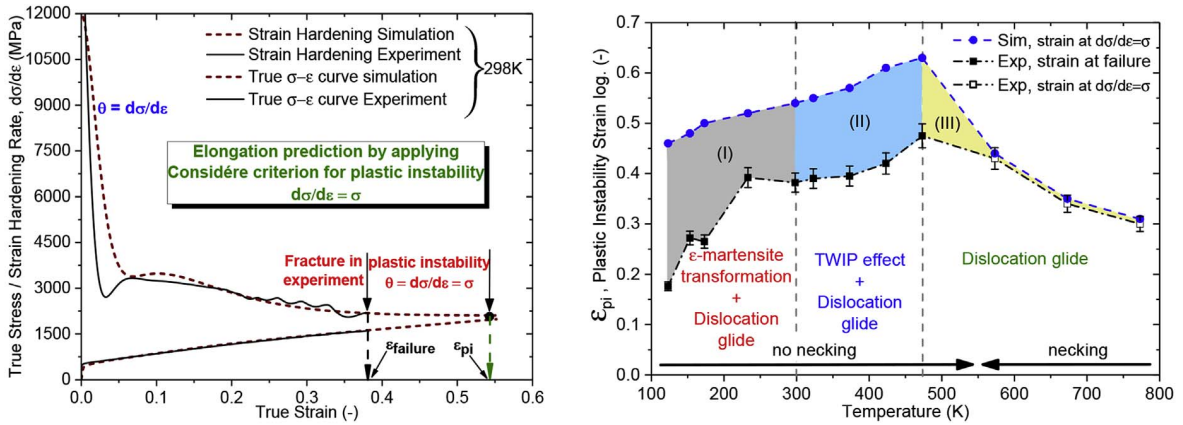

(a) Comparison of strain hardening behavior. $\varepsilon_{failure}$, strain at failure in experiment; ε_{pi}, strain at which Considére's plastic instability criterion is satisfied in the simulation.

(b) Comparison of strain at fracture, $\varepsilon_{failure}$, in experiments with plastic instability strain, ε_{pi}, obtained by applying Considére's criterion to the simulated $\sigma - \varepsilon$ and hardening curves at different temperatures; temperature ranges for changes in active deformation mechanisms are indicated by dotted lines.

Fig. 16. Comparison of simulated strain hardening behavior with experiment at 298 K and strain at fracture at different deformation temperatures for X60Mn22 TWIP steel.

transformation (Koyama et al., 2011; Gutierrez-Urrutia and Raabe, 2011; Kim and De Cooman, 2016). The strain hardening behavior of the TWIP steel at 298 K is shown in Fig. 11, the EBSD measurements carried out at different strains are shown in Fig. 8 and the evolution of twinning with strain can be seen in Fig. 17. It is observed from Fig. 18(a) that the volume fraction of Σ3 twin boundaries increases steadily from 0.015 to 0.05, for a true strain of 0.3 and then remains almost constant until failure, which can be directly correlated with the strain hardening behavior of the material. The strain hardening remains almost constant when the twinning starts and thereafter decreases steadily until failure. At a strain of about 0.22, in almost all of the grains (see Fig. 17), twins are observed which act as obstacles to dislocation motion leading to large strain hardening. At this stage, deformation within the grains already shows large heterogeneity and a further increase in deformation can lead to the initiation of damage in the material, mainly due to large stress concentrations at the twin and grain boundary intersections. This can lead to failure at any stage of deformation.

The serrated flow in the material due to DSA leads to local plastic instability due to strain localization in the bands (Zavattieri et al., 2009). After some deformation, PLC bands nucleate and propagate from one shoulder end to the other during the entire deformation, leading to inhomogeneous deformation. Hence, Considére's criterion cannot be applied when DSA is active, since the homogeneous deformation condition is not satisfied. In the experimental $\sigma - \varepsilon$ curves, as shown in Fig. 10, the serrated flow behavior is observed for all the temperatures between 298 K and 473 K. It can be seen from Fig. 11 that the strain hardening rate ($d\sigma/d\varepsilon$) and the $\sigma - \varepsilon$ curve do not intersect and failure occurs without necking for all the temperatures below 473 K. So the elongation plotted for the experiments in Fig. 9 corresponds to the total elongation (TE) or the elongation at failure for temperatures up to 473 K. However, between 573 K and 773 K, homogeneous $\sigma - \varepsilon$ behavior was observed and hence Considére's plastic instability criterion was applied at these temperatures to calculate the UE as shown in Fig. 11 and the point of $d\sigma/d\varepsilon = \sigma$ is also plotted.

The RVE simulations satisfy the homogeneous deformation conditions throughout and hence a smooth $\sigma - \varepsilon$ behavior is obtained as shown in Fig. 14(a). The approach for elongation prediction at 298 K in experiments and simulation is illustrated in Fig. 16(a). The predicted values of elongation for different temperatures according to Considére's plastic instability criterion are compared with experiments in Fig. 16(b). The error in prediction of elongation above 473 K, is smaller when compared to the lower temperatures. For the temperatures between 298 K and 473 K, twinning in combination with dislocation glide helps in improving the strain hardening behavior, but reduces the ductility or elongation due to initiation of micro-cracks. At temperatures below 298 K, the ε-martensite fraction increases with a decrease in temperature, which results in drastic reduction of ductility. The large difference in prediction of elongation can be seen at lower temperatures in Fig. 16(b). For the accurate prediction of the elongation, damage initiation criteria at the micro scale have to be taken into account in the constitutive model, which will be considered by the authors in the future.

5.3. Evolution of twinning and ε-martensite phase transformation

The prediction of the ε-martensite and twin fraction is dependent on accurate determination of the SFE and Gibbs free energy difference. At higher temperatures the thermodynamic model predicts a slightly higher SFE than expected, which leads to larger twin fractions as shown in Fig. 15(a). The evolution of twinning predicted at 298 K is compared with also the experimentally obtained values for different strains in Fig. 18(a). Barbier et al. (2009) reported a twin fraction of 0.09 at a true strain of 0.55 in a X60Mn22 alloy. Jung et al. (2014) investigated a X60Mn18 alloy to study the evolution of twinning with strain at different temperatures. The twin fraction reported in their study was 0.3 at 298 K and 398 K, and reduced to 0.15 at 573 K. This indicated that the transition

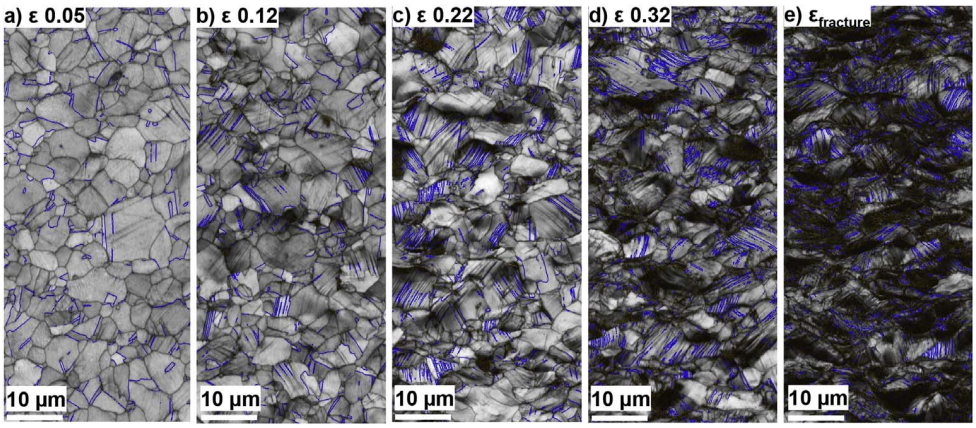

Fig. 17. Evolution of twinning during straining at 298 K; IQ maps showing Σ3 twin boundaries (blue) in the samples deformed to a) 0.05 true strain, b) 0.12 true strain, c) 0.22 true strain, d) 0.32 true strain and e) failure. (For interpretation of the references to color in this figure legend, the reader is referred to the Web version of this article.)

temperature, at which twinning started to decrease, was lower than 573 K. The study by Shterner et al. (2016) on X60MnAl18-1 steel reported a twin fraction of 0.15 at a true strain of 0.5 at 298 K and a decrease in twin fraction with increasing temperature. This trend in the evolution of twin fraction is also observed in the current study (see Fig. 15(a)). At lower temperatures the calculation of SFE and Gibbs free energy difference using the thermodynamic approach is challenging due to complex magnetic or chemical interactions which can result in slight variations in the prediction of the ε-martensite volume fraction as seen in Fig. 18(b). At 323 K and 423 K no ε-martensite is present as seen in Fig. 5(b). It should be noted that determining the SFE more accurately will improve the prediction of the evolution of deformation mechanisms.

The determination of twin fraction based on the fraction of pixel areas relative to measurement areas depends on the EBSD interaction volume/spatial resolution along with the degree of the deformation. The Σ3 twins or twin bundles which satisfy the twin detection criterion at different strains are shown in Fig. 17. It can be observed from Fig. 17 that the percentage of unindexed points increases beyond 30% macroscopic strain. However, below ≤25% macroscopic strain the percentage of indexed points is above 90% and the CI value is above 0.85 for all measurements indicating a high accuracy. Still many twins smaller than 50 nm were detected as twin bundles using the EBSD technique because of the limited spatial resolution. Hence it is clear that the twin fraction of the material determined using EBSD is only semi-quantitative and can only be used to show the trends. The XRD measurements on the interrupted tensile samples at different temperatures produced reliable results for all samples including the samples deformed at lower temperatures (see Figs. 15(b) and 18(b)). However, performing in-situ tensile tests at different temperatures should give even better results. Due to the complex experimental setup requiring a chamber incorporating both heating and cooling systems to perform tensile tests, investigations were carried out using an ex-situ approach in this study.

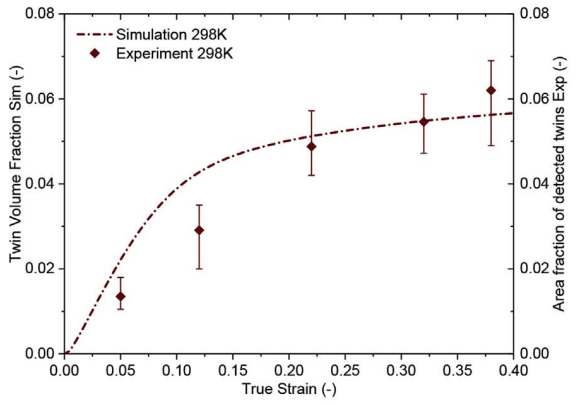

(a) Evolution of twin fraction with strain evaluated from EBSD measurements at 298 K; Evolution of twin fraction in the simulation at 298 K.

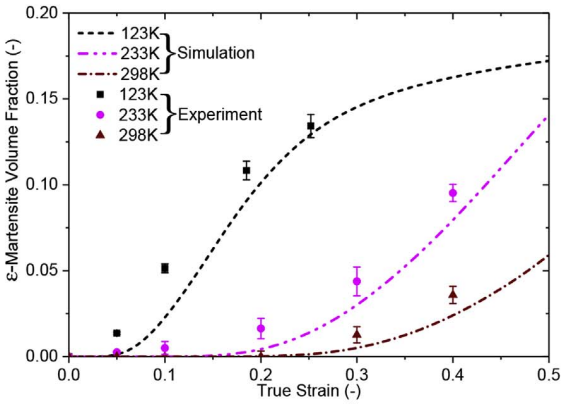

(b) Evolution of ε-martensite volume fraction during straining at 123 K, 233 K and 298 K, evaluated from Synchrotron XRD measurements; Evolution of ε-martensite volume fraction in the simulation at the same temperatures.

Fig. 18. Evolution of twinning and ε-martensite volume fraction in X60Mn22 TWIP steel during deformation in simulation and experiments.

Table 5
Relationship between deformation mechanisms and fracture behavior at different temperatures for X60Mn22 TWIP steel.

Temperature K	SLIP	TRIP	TWIP	DSA	Necking	Observations
< 173	✓	✓	-	-	-	large dimples, some quasi-brittle islands
233	✓	✓	✓	-	-	fine dimples, few quasi-brittle islands
298	✓	✓	✓	✓	-	fine dimples, very few quasi-brittle islands
323–423	✓	-	✓	✓	-	few large voids and shallow dimples
473	✓	-	✓	-	-	shallow dimples
573–773	✓	-	-	-	✓	large voids with coalescence at inclusions

5.4. Fracture behavior as a function of intrinsic material properties

The change in fracture surface characteristics shown in Fig. 12 at different temperatures is mainly due to the various active deformation mechanisms as presented in Fig. 7. The relationship between the deformation mechanisms and the fracture behavior expressed as a function of temperature is presented in Table 5. For temperatures above 573 K, plastic deformation occurs only by dislocation glide which results in a continuous decrease in strain hardening finally leading to diffuse necking and failure due to strain localization. Failure at these temperatures occurs by void coalescence, growth and decohesion at MnS inclusions. Therefore, ductile failure with large dimples along with few large elliptical voids close to MnS inclusions are observed on the fracture surface. Twinning along with dislocation glide and DSA occurs at temperatures between 298 K and 473 K. Several twin bundles in the size range of 10–50 nm are observed in many grains after deformation (see Fig. 17). Twin formation involves the creation of new boundaries, which progressively reduce the effective mean free path of dislocations and increases the flow stress. Such dynamic Hall-Petch effect results in high strain hardening. Experimental observations such as a flat fracture surface (see Fig. 13) and the fine dimples (see Fig. 12) clearly indicate rapid nucleation of voids leading to failure (Fabrègue et al., 2013). Since there is no prior necking before failure, there are no indications of localization of plastic strain except in the PLC bands. Microcracks initiate at the surface defects or edges of the tensile specimen where the PLC bands are located (Yu et al., 2017), and propagate rapidly resulting in transgranular ductile fracture (see Fig. 12). Activation of the ε-martensite phase transformation in the material due to low SFE at temperatures below 298 K leads to a reduction of ductility and abrupt failure. Micro-cracks initiate at grain boundaries mainly due to stress concentrations caused by ε-martensite/twin boundary intersections (Koyama et al., 2012). The presence of quasi-brittle islands on the fracture surfaces at and below 298 K is a direct consequence of the ε-martensite phase.

6. Conclusions

The deformation mechanisms of X60Mn22 TWIP steel strongly depend on temperature. At temperatures below 298 K, the $\gamma \rightarrow \varepsilon$-martensite transformation occurs and its volume fraction increases as the temperature decreases. A small fraction of twins is present even at these low temperatures. Twinning and dislocation glide are the dominant deformation mechanisms at 298 K and the twin fraction increases with temperature up to the transition temperature of 473 K, above which the deformation mode changes from both deformation twinning and dislocation glide to only dislocation glide due to the increasing SFE.

The change in the strain hardening behavior in the material is attributed to the temperatures at which DSA is active and the activation of different deformation mechanisms due to the change in the SFE. For temperatures below 298 K, abrupt failure occurs because of the ε-martensite transformation. DSA or serrated $\sigma - \varepsilon$ behavior is observed at temperatures above 233 K and below 473 K. For temperatures above 298 K and below 473 K, sudden failure occurs without any prior necking due to the activation of DSA and twinning. DSA is completely suppressed for temperatures above 473 K and diffuse necking is observed before failure. This is due to deformation by dislocation glide only.

Temperature has a negligible influence on the total elongation and tensile strength of the material above 233 K and below 473 K, where twinning in combination with DSA and dislocation glide occur simultaneously. The tensile strength decreases steadily above 473 K, where dislocation glide plays a predominant role. However, at temperatures below 233 K, the elongation drops drastically when ε-martensite phase transformation in combination with dislocation glide occurs.

TWIP steel exhibits a unique characteristic fracture behavior showing ductile fracture with the formation of fine dimples at all temperatures, but additionally, quasi-brittle islands are observed at temperatures where ε-martensite is present. A fracture surface with fine or shallow dimples is seen at temperatures where twinning is the dominant deformation mechanism. Large elliptical voids are observed at locations where MnS inclusions were present in the material and their fraction increases above 473 K.

A dislocation density based crystal plasticity model incorporating dislocation glide, twinning and ε-martensite phase transformation was calibrated for the X60Mn22 TWIP steel and used for the modeling of the flow behavior and the evolution of twin and ε-martensite volume fraction. Based on the temperature dependent stacking fault energy and Gibbs free energy, the model predicts the activation of ε-martensite transformation at low temperatures, twinning at intermediate temperatures and dislocation glide only at high temperatures. Quantitative comparisons were made between the experiments and simulations based on the RVE simulations using the FFT-based solver implemented in the DAMASK framework.

The very good correspondence of simulation and experimental results suggest that, this technique can be applied to the design and testing of new advanced high strength steels (AHSS) and in particular austenitic TWIP/TRIP steels of Fe-Mn-C, Fe-Mn-C-Al, Fe-Mn-C-Al-Cr, and Cr-Mn-Ni alloys.

Acknowledgments

The authors gratefully acknowledge the financial support of the German Research Foundation (DFG) within the Collaborative Research Center (SFB 761) “steel-ab initio”. The authors thank ThyssenKrupp steel Europe AG for the material supply. The authors would also like to acknowledge the DELTA machine group of TU Dortmund for providing synchrotron radiation and technical support. Simulations were performed with computing resources granted by RWTH Aachen University under project rwth0167.

Appendix A. Supplementary data

Supplementary data related to this article can be found at http://dx.doi.org/10.1016/j.ijplas.2018.02.001.

References

Allain, S., Chateau, J.P., Bouaziz, O., Migot, S., Guelton, N., 2004a. Correlations between the calculated stacking fault energy and the plasticity mechanisms in Fe–Mn–C alloys. Mater. Sci. Eng. A 387–389, 158–162. https://doi.org/10.1016/j.msea.2004.01.059.

Allain, S., Chateau, J.P., Bouaziz, O., 2004b. A physical model of the twinning-induced plasticity effect in a high manganese austenitic steel. Mater. Sci. Eng. A 387–389, 143–147. http://www.sciencedirect.com/science/article/pii/S0921509304004368 https://doi.org/10.1016/j.msea.2004.01.060 13th International Conference on the Strength of Materials.

Allain, S., Chateau, J.P., Dahmoun, D., Bouaziz, O., 2004c. Modeling of mechanical twinning in a high manganese content austenitic steel. Mater. Sci. Eng. A 387–389, 272–276. http://www.sciencedirect.com/science/article/pii/S092150930400601X https://doi.org/10.1016/j.msea.2004.05.038 13th International Conference on the Strength of Materials.

Allain, S., Cugy, P., Scott, C., Chateau, J.P., Rusinek, A., Deschamps, A., 2008. The influence of plastic instabilities on the mechanical properties of a high-manganese austenitic femnc steel. Int. J. Mater. Res. 99 (7), 734–738. https://doi.org/10.3139/146.101693.

Bachmann, F., Hielscher, R., Schaeben, H., 2011. Grain detection from 2d and 3d EBSD data–specification of the MTEX algorithm. Ultramicroscopy 111 (12), 1720–1733. http://doi.org/10.1016/j.ultramic.2011.08.002.

Barbier, D., Gey, N., Bozzolo, N., Allain, S., Humbert, M., 2009. Ebsd for analysing the twinning microstructure in fine-grained twip steels and its influence on work hardening. J. Microsc. 235 (1), 67–78. https://doi.org/10.1111/j.1365-2818.2009.03182.x.

Bian, X., Yuan, F., Wu, X., 2017. Correlation between strain rate sensitivity and characteristics of Portevin-LeChátelier bands in a twinning-induced plasticity steel. Mater. Sci. Eng. A 696, 220–227. https://doi.org/10.1016/j.msea.2017.04.078.

Bouaziz, O., Guelton, N., 2001. Modelling of twip effect on work-hardening. Mater. Sci. Eng. A 319–321, 246–249. http://www.sciencedirect.com/science/article/pii/S0921509300020190 https://doi.org/10.1016/S0921-5093(00)02019-0.

Bouaziz, O., Allain, S., Scott, C., Cugy, P., Barbier, D., 2011. High manganese austenitic twinning induced plasticity steels: a review of the microstructure properties relationships. Curr. Opin. Solid State Mater. Sci. 15 (4), 141–168. http://www.sciencedirect.com/science/article/pii/S1359028611000179 https://doi.org/10.1016/j.cossms.2011.04.002.

Chateau, J.P., Dumay, A., Allain, S., Jacques, A., 2010. Precipitation hardening of a FeMnC TWIP steel by vanadium carbides. J. Phys. Conf. Series. 240, 012023. http://iopscience.iop.org/1742-6596/240/1/012023.

Chen, L., Kim, H.S., Kim, S.K., de Cooman, B.C., 2007. Localized deformation due to Portevin–LeChatelier effect in 18Mn–0.6C TWIP austenitic steel. ISIJ Int. 47 (12), 1804–1812. https://doi.org/10.2355/isijinternational.47.1804.

Choi, H.C., Ha, T.K., Shin, H.C., Chang, Y.W., 1999. The formation kinetics of deformation twin and deformation induced ?-martensite in an austenitic fe-c-mn steel. Scripta Mater. 40 (10), 1171–1177. http://www.sciencedirect.com/science/article/pii/S1359646299000172 https://doi.org/10.1016/S1359-6462(99)00017-2.

Christian, J.W., 1951. A theory of the transformation in pure cobalt. Proc. Roy. Soc. Lond. A Math. Phys. Eng. Sci. 206 (1084), 51–64. http://dx.doi.org/10.1098/rspa.1951.0055.

Christian, J., Mahajan, S., 1995. Deformation twinning. Prog. Mater. Sci. 39 (1–2), 1–157. http://www.sciencedirect.com/science/article/pii/0079642594000077 https://doi.org/10.1016/0079-6425(94)00007-7.

Curtze, S., Kuokkala, V.T., 2010. Dependence of tensile deformation behavior of TWIP steels on stacking fault energy, temperature and strain rate. Acta Mater. 58 (15), 5129–5141. http://www.sciencedirect.com/science/article/pii/S1359645410003344 https://doi.org/10.1016/j.actamat.2010.05.049.

Dancette, S., Delannay, L., Renard, K., Melchior, M.A., Jacques, P.J., 2012. Crystal plasticity modeling of texture development and hardening in TWIP steels. Acta Mater. 60 (5), 2135–2145. http://doi.org/10.1016/j.actamat.2012.01.015.

Dastur, Y.N., Leslie, W.C., 1981. Mechanism of work hardening in Hadfield manganese steel. Metall. Trans. A 12 (5), 749–759. https://doi.org/10.1007/BF02648339.

De Almeida, L.H., Emygdio, P., Le May, I., 1994. Activation energy calculation and dynamic strain aging in austenitic stainless steel. Scripta Metall. Mater. 31 (5), 505–510. https://doi.org/10.1016/0956-716X(94)90134-1.

De Cooman, B.C., Chin, K.G., Kim, J., 2011. High mn twip steels for automotive applications. InTech. http://dx.doi.org/10.5772/14086.

De Cooman, B.C., Estrin, Y., Kim, S.K., 2017. Twinning-induced plasticity (TWIP) steels. Acta Mater. https://doi.org/10.1016/j.actamat.2017.06.046.

Dick, A., Hickel, T., Neugebauer, J., 2009. The effect of disorder on the concentration-dependence of stacking fault energies in $Fe_{1-x}Mn_x$ – a first principles study. Steel Res. Int. 80 (9), 603–608. https://doi.org/10.2374/SRI09SP015.

Dumay, A., Chateau, J.P., Allain, S., Migot, S., Bouaziz, O., 2008. Influence of addition elements on the stacking-fault energy and mechanical properties of an austenitic Fe–Mn–C steel. Mater. Sci. Eng. A 483–484, 184–187. http://www.sciencedirect.com/science/article/pii/S0921509307009525 https://doi.org/10.1016/j.msea.2006.12.170 14th International Conference on the Strength of Materials.

Eisenlohr, P., Diehl, M., Lebensohn, R.A., Roters, F., 2013. A spectral method solution to crystal elasto-viscoplasticity at finite strains. Int. J. Plast. 46, 37–53. https://doi.org/10.1016/j.ijplas.2012.09.012.

Fabrègue, D., Landron, C., Bouaziz, O., Maire, E., 2013. Damage evolution in TWIP and standard austenitic steel by means of 3D X ray tomography. Mater. Sci. Eng. A 579, 92–98. https://doi.org/10.1016/j.msea.2013.05.013.

Frommeyer, G., Brüx, U., Neumann, P., 2003. Supra-ductile and high-strength manganese-TRIP/TWIP steels for high energy absorption purposes. ISIJ Int. 43 (3), 438–446. https://doi.org/10.2355/isijinternational.43.438.

Gebhardt, T., Music, D., Hallstedt, B., Ekholm, M., Abrikosov, I.A., Vitos, L., Schneider, J.M., 2010. Ab initio lattice stability of fcc and hcp femn random alloys. J. Phys. Condens. Matter 22 (29), 295402. http://stacks.iop.org/0953-8984/22/i=29/a=295402.

Grässel, O., Krüger, L., Frommeyer, G., Meyer, L., 2000. High strength Fe–Mn–(Al, Si) TRIP/TWIP steels development — properties — application. Int. J. Plast. 16 (10–11), 1391–1409. http://www.sciencedirect.com/science/article/pii/S0749641900000152 https://doi.org/10.1016/S0749-6419(00)00015-2.

Gutierrez-Urrutia, I., Raabe, D., 2011. Dislocation and twin substructure evolution during strain hardening of an Fe–22wt.% Mn–0.6wt.% C TWIP steel observed by electron channeling contrast imaging. Acta Mater. 59 (16), 6449–6462. https://doi.org/10.1016/j.actamat.2011.07.009.

Hammersley, A.P., 2016. FIT2D: a multi-purpose data reduction, analysis and visualization program. J. Appl. Crystallogr. 49 (2), 646–652. https://doi.org/10.1107/S1600576716000455.

Hirth, J., 1970. Thermodynamics of stacking faults. Metall. Trans. 1 (9), 2367–2374. https://doi.org/10.1007/BF03038365.

Hirth, J.P., Lothe, J., 1982. Theory of Dislocations. John Wiley & Sons, New York.

Idrissi, H., Ryelandt, L., Veron, M., Schryvers, D., Jacques, P., 2009. Is there a relationship between the stacking fault character and the activated mode of plasticity of

Fe–Mn-based austenitic steels? Scripta Mater. 60 (11), 941–944. http://www.sciencedirect.com/science/article/pii/S1359646209000761 https://doi.org/10.1016/j.scriptamat.2009.01.040.
Jia, N., Roters, F., Eisenlohr, P., Kords, C., Raabe, D., 2012. Non-crystallographic shear banding in crystal plasticity FEM simulations: example of texture evolution in α-brass. Acta Mater. 60 (3), 1099–1115. http://www.sciencedirect.com/science/article/pii/S1359645411007622 https://doi.org/10.1016/j.actamat.2011.10.047.
Jung, I.C., De Cooman, B.C., 2013. Temperature dependence of the flow stress of Fe–18Mn–0.6C–xAl twinning-induced plasticity steel. Acta Mater. 61 (18), 6724–6735. https://doi.org/10.1007/s12540-014-1008-y.
Jung, J.E., Park, J., Kim, J.S., Jeon, J.B., Kim, S.K., Chang, Y.W., 2014. Temperature effect on twin formation kinetics and deformation behavior of Fe-18Mn-0.6C TWIP steel. Met. Mater. Int. 20 (1), 27–34. https://doi.org/10.1007/s12540-014-1008-y.
Kalidindi, S.R., 1998a. Modeling the strain hardening response of low {SFE} {FCC} alloys. Int. J. Plast. 14 (12), 1265–1277. http://www.sciencedirect.com/science/article/pii/S0749641998000540 https://doi.org/10.1016/S0749-6419(98)00054-0.
Kalidindi, S.R., 1998b. Incorporation of deformation twinning in crystal plasticity models. J. Mech. Phys. Solid. 46 (2), 267–290. http://www.sciencedirect.com/science/article/pii/S0022509697000513 https://doi.org/10.1016/S0022-5096(97)00051-3.
Kalidindi, S.R., 2001. Modeling anisotropic strain hardening and deformation textures in low stacking fault energy fcc metals. Int. J. Plast. 17 (6), 837–860. http://www.sciencedirect.com/science/article/pii/S0749641900000711 https://doi.org/10.1016/S0749-6419(00)00071-1.
Kang, M., Park, J., Sohn, S.S., Kim, H.S., Kim, N.J., Lee, S., 2017. Interpretation of quasi-static and dynamic tensile behavior by digital image correlation technique in TWinning Induced Plasticity (TWIP) and low-carbon steel sheets. Mater. Sci. Eng. A 693, 170–177. https://doi.org/10.1016/j.msea.2017.03.076.
Karaman, I., Sehitoglu, H., Beaudoin, A., Chumlyakov, Y., Maier, H., Tomé, C., 2000. Modeling the deformation behavior of hadfield steel single and polycrystals due to twinning and slip. Acta Mater. 48 (9), 2031–2047. http://www.sciencedirect.com/science/article/pii/S1359645400000513 https://doi.org/10.1016/S1359-6454(00)00051-3.
Kim, J.K., De Cooman, B.C., 2016. Stacking fault energy and deformation mechanisms in Fe-xMn-0.6C-yAl TWIP steel. Mater. Sci. Eng. A 676, 216–231. https://doi.org/10.1016/j.msea.2016.08.106.
Kim, J.K., Chen, L., Kim, H.S., Kim, S.K., Estrin, Y., Cooman, B.C., 2009. On the tensile behavior of high-manganese twinning-induced plasticity steel. Metall. Mater. Trans. A 40 (13), 3147–3158. https://doi.org/10.1007/s11661-009-9992-0.
Kim, J., Estrin, Y., Beladi, H., Timokhina, I., Chin, K.G., Kim, S.K., De Cooman, B.C., 2012. Constitutive modeling of the tensile behavior of Al-TWIP steel. Metall. Mater. Trans. A 43 (2), 479–490. https://doi.org/10.1007/s11661-011-0898-2.
Kim, J.K., Kwon, M.H., De Cooman, B.C., 2017. On the deformation twinning mechanisms in twinning-induced plasticity steel. Acta Mater. 141, 444–455. https://doi.org/10.1016/j.actamat.2017.09.043.
Kok, S., Bharathi, M.S., Beaudoin, A.J., Fressengeas, C., Ananthakrishna, G., Kubin, L.P., Lebyodkin, M., 2003. Spatial coupling in jerky flow using polycrystal plasticity. Acta Mater. 51 (13), 3651–3662. https://doi.org/10.1016/S1359-6454(03)00114-9.
Koyama, M., Sawaguchi, T., Lee, T., Lee, C.S., Tsuzaki, K., 2011. Work hardening associated with -martensitic transformation, deformation twinning and dynamic strain aging in fe–17mn–0.6c and fe–17mn–0.8c twip steels. Mater. Sci. Eng. A 528 (24), 7310–7316. https://doi.org/10.1016/j.msea.2011.06.011.
Koyama, M., Sawaguchi, T., Tsuzaki, K., 2012. Quasi-cleavage fracture along annealing twin boundaries in a Fe–Mn–C austenitic steel. ISIJ Int. 52, 161–163. http://www.jstage.jst.go.jp/article/isijinternational/52/1/52_1_161/_pdf.
Koyama, M., Sawaguchi, T., Tsuzaki, K., 2013. TWIP effect and plastic instability condition in an Feˆ—ˆ–Mnˆ—ˆ–C austenitic steel. ISIJ Int. 53 (2), 323–329. https://doi.org/10.2355/isijinternational.53.323.
Kubin, L.P., Estrin, Y., 1990. Evolution of dislocation densities and the critical conditions for the Portevin-Le Châtelier effect. Acta Metall. Mater. 38 (5), 697–708. https://doi.org/10.1016/0956-7151(90)90021-8.
Lebedkina, T.A., Lebyodkin, M.A., Chateau, J.P., Jacques, A., Allain, S., 2009. On the mechanism of unstable plastic flow in an austenitic FeMnC TWIP steel. Mater. Sci. Eng. A 519 (1–2), 147–154. https://doi.org/10.1016/j.msea.2009.04.067.
Lebensohn, R.A., Kanjarla, A.K., Eisenlohr, P., 2012. An elasto-viscoplastic formulation based on fast Fourier transforms for the prediction of micromechanical fields in polycrystalline materials. Int. J. Plast. 32–33, 59–69. https://doi.org/10.1016/j.ijplas.2011.12.005.
Lee, S.J., Kim, J., Kane, S.N., de Cooman, B.C., 2011. On the origin of dynamic strain aging in twinning-induced plasticity steels. Acta Mater. 59 (17), 6809–6819. https://doi.org/10.1016/j.actamat.2011.07.040.
Lehto, P., Romanoff, J., Remes, H., Sarikka, T., 2016. Characterisation of local grain size variation of welded structural steel. Weld. World 60 (4), 673–688. https://doi.org/10.1007/s40194-016-0318-8.
Linderov, M., Segel, C., Weidner, A., Biermann, H., Vinogradov, A., 2014. Deformation mechanisms in austenitic TRIP/TWIP steels at room and elevated temperature investigated by acoustic emission and scanning electron microscopy. Mater. Sci. Eng. A 597, 183–193. https://doi.org/10.1016/j.msea.2013.12.094.
Lorthios, J., Nguyen, F., Gourgues, A.F., Morgeneyer, T.F., Cugy, P., 2010. Damage observation in a high-manganese austenitic TWIP steel by synchrotron radiation computed tomography. Scripta Mater. 63 (12), 1220–1223. https://doi.org/10.1016/j.scriptamat.2010.08.042.
Lorthios, J., Mazière, M., Lemoine, X., Cugy, P., Besson, J., Gourgues-Lorenzon, A.F., 2015. Fracture behaviour of a Fe–22Mn–0.6C–0.2V austenitic TWIP steel. Int. J. Mech. Sci. 101–102, 99–113. https://doi.org/10.1016/j.ijmecsci.2015.07.029.
Mahajan, S., Chin, G., 1973. Formation of deformation twins in f.c.c. crystals. Acta Metall. 21 (10), 1353–1363. http://www.sciencedirect.com/science/article/pii/0001616073900850 https://doi.org/10.1016/0001-6160(73)90085-0.
Mahajan, S., Green, M., Brasen, D., 1977. A model for the FCC → HCP transformation, its applications, and experimental evidence. Metall. Trans. A 8 (2), 283–293. https://doi.org/10.1007/BF02661642.
Martin, S., Wolf, S., Martin, U., Krüger, L., Rafaja, D., 2016. Deformation mechanisms in austenitic TRIP/TWIP steel as a function of temperature. Metall. Mater. Trans. A 47 (1), 49–58. https://doi.org/10.1007/s11661-014-2684-4.
Matthies, S., Lutteroti, L., Wenk, H.R., 1997. Advances in texture analysis from diffraction spectra. J. Appl. Crystallogr. 30 (1), 31–42. http://journals.iucr.org/j/issues/1997/01/00/vi0049/vi0049.pdf.
Music, D., Takahashi, T., Vitos, L., Asker, C., Abrikosov, I.A., Schneider, J.M., 2007. Elastic properties of Fe–Mn random alloys studied by ab initio calculations. Appl. Phys. Lett. 91 (19). https://doi.org/10.1063/1.2807677.
Olson, G., Cohen, M., 1972. A mechanism for the strain-induced nucleation of martensitic transformations. J. Less Common Met. 28 (1), 107–118. http://www.sciencedirect.com/science/article/pii/0022508872901737 https://doi.org/10.1016/0022-5088(72)90173-7.
Olson, G.B., Cohen, M., 1976. A general mechanism of martensitic nucleation: Part I. General concepts and the FCC → HCP transformation. Metall. Trans. A 7 (12), 1897–1904. https://doi.org/10.1007/BF02659822.
Orowan, E., 1934. Zur Kristallplastizität. I–III. Z. Phys. 89 (9–10), 605–613. https://doi.org/10.1007/BF01341478.
Pierce, D., Jiménez, J., Bentley, J., Raabe, D., Oskay, C., Wittig, J., 2014. The influence of manganese content on the stacking fault and austenite/-martensite interfacial energies in Fe–Mn–(Al–Si) steels investigated by experiment and theory. Acta Mater. 68, 238–253. http://www.sciencedirect.com/science/article/pii/S135964541400010X https://doi.org/10.1016/j.actamat.2014.01.001.
Pierce, D.T., Jiménez, J.A., Bentley, J., Raabe, D., Wittig, J.E., 2015. The influence of stacking fault energy on the microstructural and strain-hardening evolution of Fe–Mn–Al–Si steels during tensile deformation. Acta Mater. 100, 178–190. https://doi.org/10.1016/j.actamat.2015.08.030.
Quey, R., Dawson, P.R., Barbe, F., 2011. Large-scale 3D random polycrystals for the finite element method: generation, meshing and remeshing. Comput. Meth. Appl. Mech. Eng. 200 (17–20), 1729–1745. https://doi.org/10.1016/j.cma.2011.01.002.
Renard, K., Jacques, P.J., 2012. On the relationship between work hardening and twinning rate in TWIP steels. Mater. Sci. Eng. A 542, 8–14. https://doi.org/10.1016/j.msea.2012.01.123.
Rietveld, H.M., 1969. A profile refinement method for nuclear and magnetic structures. J. Appl. Crystallogr. 2 (2), 65–71. https://doi.org/10.1107/S0021889869006558.
Roters, F., 2011. Advanced Material Models for the Crystal Plasticity Finite Element Method – Development of a General CPFEM Framework. Habilitation thesis. . http://darwin.bth.rwth-aachen.de/opus3/volltexte/2011/3874/.

Roters, F., Raabe, D., Gottstein, G., 2000. Work hardening in heterogeneous alloys—a microstructural approach based on three internal state variables. Acta Mater. 48 (17), 4181–4189. https://doi.org/10.1016/S1359-6454(00)00289-5.
Roters, F., Eisenlohr, P., Kords, C., Tjahjanto, D., Diehl, M., Raabe, D., 2012. Damask: the düsseldorf advanced MAterial simulation kit for studying crystal plasticity using an FE based or a spectral numerical solver. Procedia IUTAM 3, 3–10. http://www.sciencedirect.com/science/article/pii/S2210983812000028 https://doi.org/10.1016/j.piutam.2012.03.001.
Roth, A., Lebedkina, T.A., Lebyodkin, M.A., 2012. On the critical strain for the onset of plastic instability in an austenitic FeMnC steel. Mater. Sci. Eng. A 539, 280–284. https://doi.org/10.1016/j.msea.2012.01.094.
Saeed-Akbari, A., Imlau, J., Prahl, U., Bleck, W., 2009. Derivation and variation in composition-dependent stacking fault energy maps based on subregular solution model in high-manganese steels. Metall. Mater. Trans. A 40 (13), 3076–3090. https://doi.org/10.1007/s11661-009-0050-8.
Saeed-Akbari, A., Mosecker, L., Schwedt, A., Bleck, W., 2012. Characterization and prediction of flow behavior in high-manganese twinning induced plasticity steels: Part i. mechanism maps and work-hardening behavior. Metall. Mater. Trans. A 43 (5), 1688–1704. https://doi.org/10.1007/s11661-011-0993-4.
Schindelin, J., Rueden, C.T., Hiner, M.C., Eliceiri, K.W., 2015. The ImageJ ecosystem: an open platform for biomedical image analysis. Mol. Reprod. Dev. 82 (7–8), 518–529. http://onlinelibrary.wiley.com/doi/10.1002/mrd.22489/epdf.
Scott, Colin, Remy, Blandine, Collet, Jean-Louis, Cael, Aurelie, Bao, Cuimin, Danoix, Frederic, Malard, Benoît, Curfs, Caroline, 2011. Precipitation strengthening in high manganese austenitic TWIP steels. Int. J. Mater. Res. http://www.hanser-elibrary.com/doi/pdf/10.3139/146.110508.
Shanthraj, P., Eisenlohr, P., Diehl, M., Roters, F., 2015. Numerically robust spectral methods for crystal plasticity simulations of heterogeneous materials. Int. J. Plast. 66, 31–45. https://doi.org/10.1016/j.ijplas.2014.02.006.
Shiekhelsouk, M., Favier, V., Inal, K., Cherkaoui, M., 2009. Modelling the behaviour of polycrystalline austenitic steel with twinning-induced plasticity effect. Int. J. Plast. 25 (1), 105–133. http://doi.org/10.1016/j.ijplas.2007.11.004.
Shterner, V., Timokhina, I.B., Beladi, H., 2016. On the work-hardening behaviour of a high manganese TWIP steel at different deformation temperatures. Mater. Sci. Eng. A 669, 437–446. https://doi.org/10.1016/j.msea.2016.05.104.
Staroselsky, A., Anand, L., 1998. Inelastic deformation of polycrystalline face centered cubic materials by slip and twinning. J. Mech. Phys. Solid. 46 (4), 671–696. http://www.sciencedirect.com/science/article/pii/S0022509697000719 https://doi.org/10.1016/S0022-5096(97)00071-9.
Steinmetz, D.R., Jäpel, T., Wietbrock, B., Eisenlohr, P., Gutierrez-Urrutia, I., Saeed-Akbari, A., Hickel, T., Roters, F., Raabe, D., 2013. Revealing the strain-hardening behavior of twinning-induced plasticity steels: theory, simulations, experiments. Acta Mater. 61 (2), 494–510. https://doi.org/10.1016/j.actamat.2012.09.064.
Sun, C., Guo, N., Fu, M., Wang, S., 2016. Modeling of slip, twinning and transformation induced plastic deformation for TWIP steel based on crystal plasticity. Int. J. Plast. 76, 186–212. http://www.sciencedirect.com/science/article/pii/S0749641915001400 https://doi.org/10.1016/j.ijplas.2015.08.003.
Teutonico, L.J., 1963. The dissociation of dislocations in the face-centered cubic structure. Acta Metall. 11 (12), 1283–1289. http://www.sciencedirect.com/science/article/pii/0001616063900233 https://doi.org/10.1016/0001-6160(63)90023-3.
Twardowski, R., 2013. Mikrostrukturelle beschreibung von verformung und schädigung hochmanganhaltiger stähle mit trip und twip-effekt. Ph.D. thesis. RWTH Aachen University, Aachen. http://publications.rwth-aachen.de/record/229452/files/4900.pdf.
Vitos, L., Nilsson, J.O., Johansson, B., 2006. Alloying effects on the stacking fault energy in austenitic stainless steels from first-principles theory. Acta Mater. 54 (14), 3821–3826. http://www.sciencedirect.com/science/article/pii/S1359645406002989 https://doi.org/10.1016/j.actamat.2006.04.013.
Wong, S.L., Madivala, M., Prahl, U., Roters, F., Raabe, D., 2016. A crystal plasticity model for twinning- and transformation-induced plasticity. Acta Mater. 118, 140–151. https://doi.org/10.1016/j.actamat.2016.07.032.
Wright, S.I., Larsen, R.J., 2002. Extracting twins from orientation imaging microscopy scan data. J. Microsc. 205 (3), 245–252. http://onlinelibrary.wiley.com/doi/10.1046/j.1365-2818.2002.00992.x/epdf.
Yang, H.K., Zhang, Z.J., Tian, Y.Z., Zhang, Z.F., 2017a. Negative to positive transition of strain rate sensitivity in Fe-22Mn-0.6C-x(Al) twinning-induced plasticity steels. Mater. Sci. Eng. A 690, 146–157. https://doi.org/10.1016/j.msea.2017.02.014.
Yang, C.L., Zhang, Z.J., Zhang, P., Zhang, Z.F., 2017b. The premature necking of twinning-induced plasticity steels. Acta Mater. 136, 1–10. https://doi.org/10.1016/j.actamat.2017.06.042.
Yu, H.Y., Lee, S.M., Nam, J.H., Lee, S.J., Fabrègue, D., Park, M.h., Tsuji, N., Lee, Y.K., 2017. Post-uniform elongation and tensile fracture mechanisms of Fe-18Mn-0.6C-xAl twinning-induced plasticity steels. Acta Mater. 131, 435–444. https://doi.org/0.1016/j.actamat.2017.04.011.
Zambrano, O.A., 2016. Stacking fault energy maps of Fe–Mn–Al–C–Si steels: effect of temperature, grain size, and variations in compositions. J. Eng. Mater. Technol. 138 (4), 041010. https://doi.org/10.1115/1.4033632.
Zavattieri, P.D., Savic, V., Hector Jr., L.G., Fekete, J.R., Tong, W., Xuan, Y., 2009. Spatio-temporal characteristics of the Portevin–Le Châtelier effect in austenitic steel with twinning induced plasticity. Int. J. Plast. 25 (12), 2298–2330. http://www.sciencedirect.com/science/article/pii/S0749641909000266 https://doi.org/10.1016/j.ijplas.2009.02.008.

3.2 Research Paper 2

Title: Anisotropy and strain rate effects on the failure behavior of TWIP steel: A multiscale experimental study

Manjunatha Madivala, Alexander Schwedt, Ulrich Prahl, and Wolfgang Bleck. Anisotropy and strain rate effects on the failure behavior of twip steel: A multiscale experimental study. *International Journal of Plasticity*, 2018. ISSN 0749-6419. doi: https://doi.org/10.1016/j.ijplas.2018.11.015
© 2018 Elsevier Ltd. Reprinted with permission. The original publication is available at science direct.

Highlights:

- Anisotropy and strain rate influence on the mechanical behavior.
- Energy absorption capacity of TWIP steel compared with AHSS.
- Local strain distribution and its evolution during deformation.
- Adiabatic heating and its effect on deformation mechanisms.
- Mechanism of micro-crack formation in X60Mn22 TWIP steel.

International Journal of Plasticity 115 (2019) 178–199

Contents lists available at ScienceDirect

International Journal of Plasticity

journal homepage: www.elsevier.com/locate/ijplas

Anisotropy and strain rate effects on the failure behavior of TWIP steel: A multiscale experimental study

Manjunatha Madivala[a,*,1], Alexander Schwedt[b], Ulrich Prahl[a], Wolfgang Bleck[a]

[a] Institut für Eisenhüttenkunde (IEHK), RWTH Aachen University, Aachen, Germany
[b] Gemeinschaftslabor für Elektronenmikroskopie (GFE), RWTH Aachen University, Aachen, Germany

ARTICLE INFO

Keywords:
TWIP steel
Deformation twinning
Damage
Fracture
Strain rate
Energy absorption

ABSTRACT

The effect of anisotropy and strain rate on the work hardening and fracture behavior of high manganese twinning induced plasticity (TWIP) steel was investigated. Uni-axial tensile tests in conjunction with digital image correlation were carried out to study the local deformation behavior and failure initiation. The influence of adiabatic heating on the mechanical behavior was studied by performing quasi-static and dynamic tensile tests with synchronous temperature and strain measurements. Interrupted micro tensile test samples were analyzed in the scanning electron microscope combined with the electron backscatter diffraction measurements to study the evolution of microstructure, twinning, and micro-cracking mechanisms. TWIP steel showed high strength of $\geq$1100 MPa in combination with excellent ductility of $\geq$45%, but slight variation in yield strength and elongation values was observed when tested along rolling, transverse and shear (45°) directions. The material exhibited excellent energy absorption capacity of above 55 kJ/kg at different strain rates. The serrations on the σ–ε curves was the main characteristic behavior of TWIP steel observed under quasi-static loading, which start to disappear with increasing $\dot{\varepsilon}$ and vanishes completely under dynamic loading. Serrated flow behavior was caused due to dynamic strain aging (DSA), which include the dynamic interaction of solute atoms with dislocations and the Mn-C short-range ordering. The plastic instability caused due to DSA has led to inhomogeneous behavior in the form of nucleation and propagation of shear bands during deformation known as Portevin-Le Chatelier (PLC) effect. Temperature rise due to adiabatic heating at high $\dot{\varepsilon}$ has led to increase of SFE, thereby resulting in a change of twinning behavior or the promotion of dislocation glide. Failure at macro-level occurred at the intersection of two shear bands close to the edge of the specimen with the negligible amount of strain localization. At the micro-level, cracks originated mainly at grain boundaries (GB) and triple junctions due to increased stress concentration caused by the intercepting deformation twins and the slip band extrusions at GB. Intergranular crack initiation and propagation instances were evident in the microstructure along with the rapid nucleation of minute voids. Even though few micro-cracks have appeared at lower strains, their growth was rather limited. Thus, TWIP steel exhibited enhanced resistance to damage resulting in superior ductility.

* Corresponding author.
E-mail address: Manjunatha.Madivala@iehk.rwth-aachen.de (M. Madivala).
[1] Institut für Eisenhüttenkunde (IEHK), RWTH Aachen University, Intzestraße 1, 52072, Aachen, Germany.

https://doi.org/10.1016/j.ijplas.2018.11.015
Received 23 July 2018; Received in revised form 23 November 2018; Accepted 25 November 2018
Available online 30 November 2018
0749-6419/ © 2018 Elsevier Ltd. All rights reserved.

1. Introduction

The demand for safety, durability and cost effectiveness of structural parts used in modern automobiles has increased tremendously over the years. To achieve superior crash performance, the major requirement is high strength and ductility. Steels widely used in automobiles require greater formability for the fabrication of complex body parts. High manganese twinning induced plasticity (TWIP) steels are such class of steels characterized by high work hardening capacity along with exceptional strength and ductility (Grässel et al., 2000; Lee et al., 2017). The excellent strain hardening rate (SHR) of TWIP steels originates from their deformation mechanisms such as dislocation glide, deformation twinning and ε-martensite transformation (TRIP) (Pierce et al., 2015; Kim et al., 2017). TWIP steels with different chemical compositions such as Fe-18Mn-0.6C, Fe-28Mn-0.3C, Fe-22Mn-0.6C and Fe-18Mn-0.6C-1.5Al, showed a uniform elongation (UE) of more than 50% and a ultimate tensile strength (UTS) of above 1000 MPa (Saeed-Akbari et al., 2012; De Cooman et al., 2018). Evaluation of the material performance solely based on quasi-static tensile tests and judging their suitability for safety critical parts may be inadequate. Since during the crash of automobiles, the parts are not deformed until failure and the deformation rates are very high (Bleck and Schael, 2000). Thus to check the crash-worthiness of TWIP steel, the mechanical properties and energy absorption (EA) capacity is investigated under both quasi-static and dynamic loading conditions.

The superior tensile properties of TWIP steels were attributed to the sustained high work hardening rates. Plastic deformation mechanisms such as deformation twinning and strain induced ε-martensite transformation occurred beside dislocation slip in these steels depending on the chemical composition, strain rate and temperature (Idrissi et al., 2009). Deformation twins and ε-martensite platelets increase the SHR by acting as obstacles to dislocation motion thereby reducing the effective dislocation mean free path (Renard and Jacques, 2012). Fe-Mn-C-Al alloys with stacking fault energy (SFE) in the range of 21–27 mJ/m^2, exhibited enhanced strength and ductility compared to alloys with SFE above 42 mJ/m^2. Thus in alloys where twinning prevailed over dislocation glide, displayed better SHR compared to the alloys where deformation occurred only via dislocation glide (Curtze and Kuokkala, 2010). The increase in SHR was due to increase in deformation twin density. However, with increase in plastic strain the twin density saturated resulting in a sudden drop of SHR leading to failure. The dynamic strain aging (DSA) occurred above room temperature, where twinning along with dislocation glide were the active deformation modes (Koyama et al., 2013). The DSA effectively modified the SHR but its contribution to SHR is rather limited, since the activation energy attained in Fe-22Mn-0.6C TWIP steel was quite low (Allain et al., 2008). Thus the high SHR in TWIP steels was solely due to the occurrence of deformation twinning along with dislocation glide at intermediate temperatures. The $\dot{\varepsilon}$ influence on the activation of different deformation mechanisms during deformation and its relation with the SHR is not very well understood. Thus in this study, the evolution of twinning with increasing macroscopic strain is studied and correlated with the SHR.

High Mn steels show a unique characteristic behavior in the form of nucleation and propagation of narrow deformation shear bands during tensile loading. This results in serrated/jerky flow known as Portevin-Le Chatelier (PLC) effect. The formation and propagation of shear bands during deformation was mainly due to DSA associated with the negative strain rate sensitivity (SRS) (Chen et al., 2007). The shear bands traverse the gage length of deforming tensile specimen between the successive serrations and the shape of the serrations is related to the mode of band propagation. The serrations of type A are known to be associated with repetitive nucleation of deformation bands from one end of the gage length and their continuous propagation to the other end. Each of the load drop/increase corresponds to the initiation/disappearance of the shear band and the plateau between the two consecutive serrations peaks corresponds to the nucleation and propagation of shear band within the gage length (Gopinath et al., 2009). The type A bands nucleated at the gripping ends or in the gage section center and the band propagation commenced at the end of each nucleation event with inhomogeneous strain distribution (Zavattieri et al., 2009). The deformation bands in TWIP steel begin with small strain heterogeneity and develop into pronounced deformation bands accompanied with serrated flow. Lee et al. (2011) investigated TWIP steel with and without Al and stated that DSA is the result of an interaction between Mn-C point defect complexes and stacking faults. It was stated that DSA can occur by a single diffusive jump of C atom in the stacking fault region. DSA occurs after deforming the material to critical strain ($\boldsymbol{\varepsilon_c}$), when the C atom of the Mn-C complex has enough time to interact with a stacking fault irrespective of the Mn-C reorientation time. The presence of Mn-C octahedral short range order (SRO) or short range clusters (SRC) was proved experimentally by small-angle neutron scattering (SANS) technique (Kang et al., 2014; Song and Houston, 2018). Both the studies investigated Fe-18Mn-0.6C alloy and it was stated that the size of the Mn-C clusters decreased and the number density of the Mn-C clusters increased with increasing macroscopic strain. Seol et al. (2017) has used multiscale characterization techniques to understand DSA and showed that SRO caused by SRC was responsible for DSA and also claimed that high $\dot{\varepsilon}$ deformation resulted in increase in C concentration of SRC, which led to the suppression of DSA. Kang et al. (2017) compared the local deformation behavior of TWIP steel under quasi-static and dynamic tensile loading and reported that twinning in the early stage of deformation resulted in higher strength and ductility along with similar local strain at failure even under dynamic loading. Bian et al. (2017) investigated the influence of $\dot{\varepsilon}$ on the occurrence of DSA. DSA was suppressed with increasing $\dot{\varepsilon}$ and the local strain concentration within the shear band was more severe at higher $\dot{\varepsilon}$. The $\boldsymbol{\varepsilon_c}$ for the onset of DSA increased with increase in $\dot{\varepsilon}$ showing negative SRS and the velocity of bands propagation ($\mathbf{V_b}$) decreased with increasing macroscopic strain. It is important to understand the role of DSA on the plastic strain localization and failure initiation to use TWIP steel for automotive applications. Hence this study focuses on elucidating the failure initiation mechanism due to the propagation of shear bands.

Dynamic tensile tests was carried out on Fe-25Mn-3Al-3Si TWIP/TRIP steel by Benzing et al. (2018) showed an increase in yield strength (YS), UTS and elongation with increase in $\dot{\varepsilon}$. The material mainly deformed by dislocation glide along with TWIP and TRIP effect. The specimen temperature increased by about 60 °C due to adiabatic heating, which resulted in a change of SFE from 21 to ~23 mJ/m^2. It was stated that, $\dot{\varepsilon}$ did not influence the microstructure morphology such as thickness and spacing of deformation twins

or ε-martensite laths. In a similar study on Fe-15Mn-0.6C-1.2Al TWIP steel by Kang et al. (2017), serrated flow behavior was observed under quasi-static tests and homogenous flow behavior without serrations under dynamic tests. Dynamic loading resulted in increase of UTS, slight reduction of elongation and profuse necking. This is mainly due to the adiabatic heating during deformation which led to increase in SFE resulting in decrease of twinning rate. Park et al. (2017) studied the same alloy and found differences in slip characteristics and twin formation due to variation of $\dot{\varepsilon}$. Under quasi-static loading, dislocation cell structures formation showed a transition from combined planar and wavy slip to wavy slip, whereas under dynamic loading combined planar and wavy slip was activated from the early stages of deformation. In the initial stages of deformation, stacking faults were observed and after deforming to 20%, 30% strain, primary twins could be seen under quasi-static test, while in dynamic tests both primary and secondary twinning were quite active in the later stages of deformation. Shen et al. (2016) has investigated the influence of grain size and strain rate on the hardening behavior in Fe-20Mn-0.6C steel. For all the investigated grain sizes in the range from 3.5 to 25 μm, YS increased with increase in $\dot{\varepsilon}$, whereas UTS and elongation decreased with increase in $\dot{\varepsilon}$. It was reported that strain localization within the shear bands and adiabatic heating has led to the reduction of mechanical properties. Microstructure investigations has revealed dislocation slip along with primary twins in the early and middle stages of deformation, whereas in the later stages of deformation rapid nucleation of twins was observed at high $\dot{\varepsilon}$. Rahman et al. (2014) has investigated Fe-15Mn-0.7C-2Al-2Si steel at various $\dot{\varepsilon}$ and observed a positive SRS of YS and decrease in deformation twinning rate at high $\dot{\varepsilon}$. At low $\dot{\varepsilon}$, activation of multiple twin systems and large intergranular misorientations was observed in contrast to high $\dot{\varepsilon}$. In the current study, the influence of adiabatic heating at different $\dot{\varepsilon}$ on the activation of deformation mechanisms is investigated. The $\dot{\varepsilon}$ influence on the deformation behavior and mechanical properties is studied in detail, with a special emphasis on strain localization and failure.

TWIP showed characteristic differences in the failure behavior when the material deformed by only SLIP or SLIP in combination with TWIP or SLIP in combination with TRIP (Madivala et al., 2018). Fracture surface analysis depicted the formation of fine dimples with quasi-brittle islands where ε-martensite was present, fine or shallow dimples where twinning was the dominant deformation mode and larger dimples along with coalescence of voids at MnS inclusions where deformation occurred by only dislocation glide . Yu et al. (2017) showed the formation of micro-cracks at the grain boundary junctions and the mechanical twin boundaries. These cracks were mainly found at the edge and side surfaces of tensile specimen where local deformation shear bands met. Yang et al. (2017) has reported that sudden failure or drop of strain hardening in TWIP steels was due to exponential increase of the macroscopic void volume fraction. Fabrègue et al. (2013) investigated the damage evolution in TWIP steel by 3D X-ray tomography experiments and showed that average void diameter and triaxility remained constant throughout the deformation. The damage process involved intense nucleation of tiny voids combined with significant growth of the biggest cavities. Lorthios et al. (2010) examined the void size distribution close to the fracture surface in a sheared specimen. Most of the voids found were tiny secondary dimples with few elongated cavities, indicating localized failure. The factors such as temperature, strain rate and stress state have a direct influence on the active deformation modes, which in turn influence the damage and failure in TWIP steels. This work focuses on the mechanism of micro-crack formation in TWIP steel and its relation with deformation mechanisms.

This paper discuses the influence of anisotropy and strain rate on the strain hardening and fracture behavior of X60Mn22 TWIP steel. Uni-axial tensile tests were carried out at different strain rates ranging from 0.00001 to 250/s for investigating the mechanical behavior under both quasi-static and dynamic conditions. The serrated flow caused due to the DSA was studied by carrying out tensile tests in conjunction with digital image correlation (DIC) over the entire deformation range until failure. Analyzing local plastic strain evolution during deformation using DIC measurements assisted in understanding the inhomogeneous flow behavior resulted due to the propagation of shear bands and their subsequent influence on the failure initiation. Synchronous temperature measurements during deformation at various strain rates aid in the accurate estimation of SFE at different elongations, enabling the prediction of different active deformation mechanisms. The correlation of predicted mechanisms with microstructure evolution processes was verified by electron back scatter diffraction (EBSD) measurements. Detailed deformation mechanisms were examined by analyzing how twinning and dislocation glide were varied under the quasi-static and dynamic loading conditions. The role of inclusions present on the mechanical properties and failure initiation along rolling, transverse and shear (45°) directions was investigated in detail. The mechanism of micro-cracks formation and their evolution at different stages of deformation was studied by interrupted micro tensile tests in the scanning electron microscope (SEM).

2. Material and experimental methods

The material investigated in this study is a high manganese TWIP steel, produced by industrial processing route, designated as X60Mn22 (Fe-22Mn-0.6C). Initial microstructure analysis such as the grain size or morphology and the evolution of twinning with increasing macroscopic strain was characterized by using EBSD technique. The qualitative and quantitative analysis of inclusions type, size and their distribution was investigated by techniques such as optical and field-emission SEM with energy dispersive X-ray spectroscopy (EDS/EDX). The evolution of microstructure and micro-cracks development during deformation was studied by carrying out interrupted micro tensile tests in SEM. The mechanical behavior of the material was investigated by quasi-static tensile tests in conjunction with DIC and dynamic tests along with synchronous temperature measurements using thermocamera. Finally fracture behavior of the macroscopic tensile specimens were analyzed by SEM.

2.1. Material

The material studied was a cold rolled and annealed steel with a sheet thickness of 1.4 mm. The chemical composition of the alloy was determined by using optical emission spectroscopy and the SFE of the material was calculated using the sub-regular solution

Table 1
Chemical composition (in wt.%) and the SFE value (in mJ/m^2) of the investigated X60Mn22 TWIP steel.

C	Si	Mn	P	S	Cr	Ni	Cu	Al	V	N	Fe	SFE
0.59	0.21	22.26	0.013	< 0.001	0.08	0.02	0.02	0.01	0.27	0.019	Bal.	27

thermodynamic model as described in Madivala et al. (2018), is shown in Table 1. The interface energy ($\sigma^{\gamma/\varepsilon}$) value of 10 mJ/m^2 was assumed for calculating the SFE.

The microstructure of the material consisted of fine equiaxed austenitic grains (γ) with an average grain size of 3.0 μm. Fig. 1(a) shows the inverse pole figure map (IPF) with respect to the rolling direction, depicting the grain sizes and the crystal orientation distribution. Fig. 1(b) provides the grain size distribution function, where it can be observed that the grain size varied from 0.5 to 10 μm, with only a small fraction of grains, being larger than 5 μm.

The estimated area fraction and size of the inclusions present in the material are given in Fig. 2. The measured area fraction of inclusions is ~0.03 and the average size of inclusions is ~1.5 μm. The size of the smallest inclusions was estimated to be about ~0.5 μm. EDS analysis performed on almost all of the inclusions found indicate manganese sulphides (MnS) and aluminum oxides (Al_2O_3) in elongated and globular shapes respectively as shown in Fig. 2. The MnS inclusions are usually elongated along rolling direction (RD) and their shape can be visualized along the RD-TD plane (TD: transverse direction) as seen in Fig. 2. Small fraction of tiny round inclusions were also present with small amounts of S and slightly larger amounts of C and Mn compared to the base material. The material was tested in the as delivered condition as explained in Section 2.3.

2.2. Microscopy

SEM analysis was carried out on the broken samples obtained from the macroscopic tensile tests to investigate the differences in fracture behavior. The fracture surface images were taken at different locations to observe the changes in fracture morphology and behavior at the inclusions. SEM images were processed using the ImageJ software and analyzed using a Matlab program to determine the average dimple size.

Quantitative analysis of inclusions was carried out by optical microscopy in conjunction with an image-analysis software to measure the size and area fraction according to DIN EN 10247/ASTM E45 standard. SEM/EDS technique was applied to analyze the inclusions qualitatively based on their chemical composition. The specimens of size 20 × 20 mm^2 (RD x TD) were embedded in a epoxy resin, ground and mechanically polished with a diamond pastes of 3 μm and 1 μm, followed by electro-polishing.

The EBSD measurements were performed on the micro tensile samples and fractured specimens with a scan area containing more than 2500 grains using a field-emission JEOL JSM-7000F SEM equipped with an EDAX-TSL Hikari detector. The step size of 100 nm was set along with an operating voltage of 20 kV and a probe current of about 20–30 nA. The TSL OIM® Analysis 7 software was used to analyze the data. All the scanned points with a confidence index (CI) value between 0.1 and 1.0 were considered for the analysis. The micro tensile specimens (gage length 2 mm and width 1 mm) were cut along the RD from the cold-rolled and annealed sheets using the wire erosion cutting. The specimens were initially mechanically ground with 800, 1200, 2400, and 4000 silicon carbide grit paper on both sides including the edges followed by mechanical polishing using 3 μm and 1 μm diamond suspension on one side. To remove the remaining artifacts the samples were further electro-polished at room temperature by applying a voltage potential of 35 V for 15 s using an electrolyte consisting of 95% acetic acid and 5% perchloric acid. The microstructures of both undeformed and deformed specimens were analyzed by EBSD on the RD-TD planes. The evolution of twinning with increasing strain was investigated by carrying out EBSD measurements on the electro-polished micro tensile samples interrupted at a true strain of 0.0, 0.1, 0.2, 0.3, 0.4

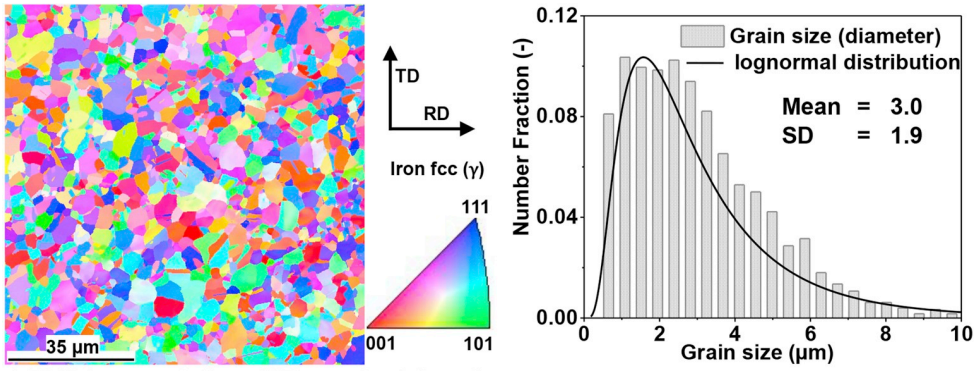

a) EBSD inverse pole figure (IPF) map of undeformed sample showing variation in grain size and orientation.

b) Grain size distribution fitted with a log-normal distribution function.

Fig. 1. Microstructure and grain size distribution of the investigated X60Mn22 TWIP steel. a) microstructure is fully austenitic (γ); RD: rolling direction; TD: transverse direction. b) average grain size is 3.0 μm and standard deviation (SD) is 1.9 μm.

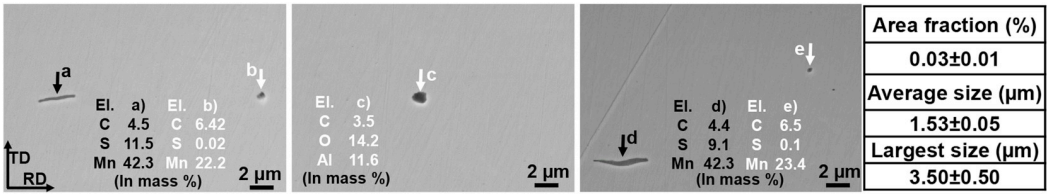

Fig. 2. Cleanliness analysis of inclusions. SEM micro-graphs depicting non-metallic inclusions present: MnS (a,d), Al_2O_3 (c) and small fraction of tiny inclusions with small amount of S, slightly larger amounts of C and Mn (b,e); major alloying elements found in the inclusions is also presented.The area fraction, average and largest size of inclusions present was estimated by analyzing 4–5 optical microscopy images taken at different locations.

and just before fracture (see Fig. 8). Measurements were carried out in the middle of the specimen with an area containing more than 2500 grains as shown in Fig. 8. Grain boundaries in the undeformed microstructure were identified with the misorientation criteria of 5° by applying a cleaning procedure consisting of moderate grain confidence index standardization. Twin boundaries were ignored during the grain detection procedure and the regions with at least five pixels were counted as grains. The number-weighted average grain diameter was used to quantify the grain size. Twin boundaries in the deformed microstructures were identified with a criterion of 60° misorientation angle about the $< 111 >$ axis, along with an angular tolerance of 5° within the γ_{FCC}-matrix (FCC: face centered cubic). The twin fraction was calculated based on the relative fraction of the pixel areas of **Σ**-3 twins to the measured areas as a function of macroscopic strain as described in Madivala et al. (2018).

2.3. Mechanical tests

To investigate the micro-cracking mechanisms, interrupted micro tensile tests were carried out in the field emission SEM from Zeiss **Σ**igma family. The tests were interrupted at different strains to observe the crack initiation and their development over the entire gage length. The tests were carried out at room temperature in SEM using a micro tensile testing device with the adjusted cross head displacement rate of 0.4 mm/min which correspond to a quasi-static $\dot{\varepsilon}$ of $0.003\,s^{-1}$. The micro tensile sample is shown in Fig. 3(d) and the region of measurement is shown in Fig. 8.

Macroscopic tensile tests were carried out according to DIN EN ISO 6892 standard with a sample geometry consisting of a gage length of 75 mm and a width of 12.5 mm as shown in Fig. 3(c). The samples were obtained using water-jet cutting along RD, TD and shear (45°) directions (SD). The cut edges of the samples were polished up to a surface roughness of 0.125 µm. Tensile tests in

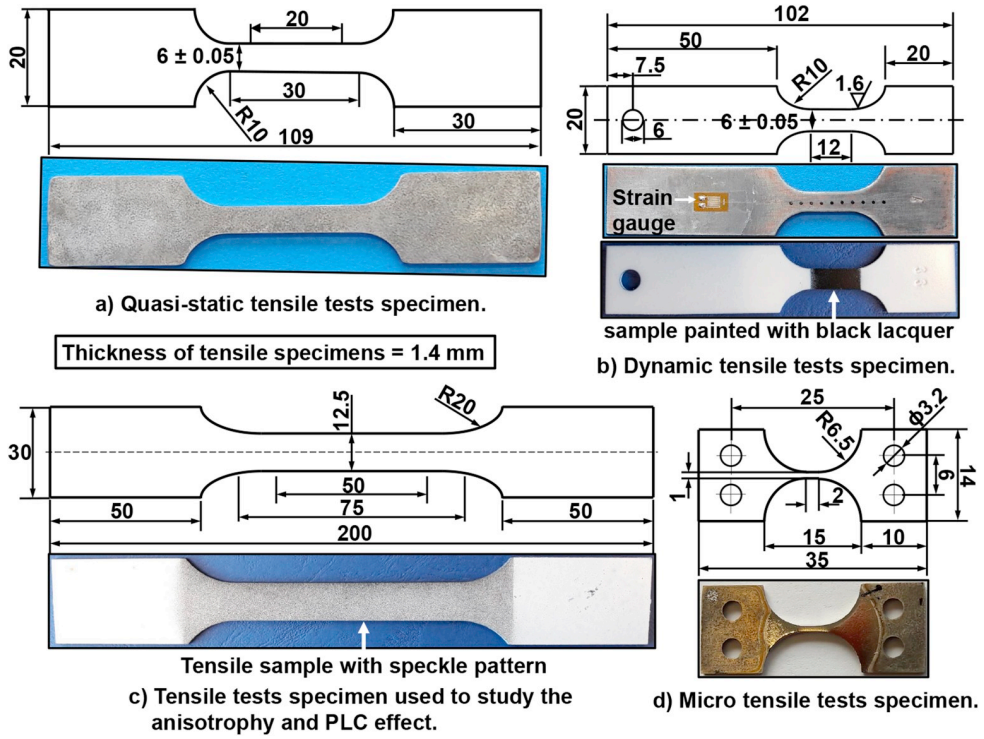

Fig. 3. Geometries used for the quasi-static and dynamic tensile tests.

conjunction with the DIC were performed at room temperature using a Zwick/Roell Z100 machine with a cross head displacement rate of 1.8 mm/min, which corresponds to a quasi-static $\dot{\varepsilon}$ of about 0.001 s^{-1}. A high contrast black and white stochastic pattern was prepared on the sample surface for the DIC measurements as shown in Fig. 3(c). The GOM Aramis 12M 2D DIC system was applied for analyzing the local strain distribution and to study the shear bands propagation during deformation. The images were captured at a rate of 1 Hz throughout the test. The ARAMIS DIC® software was used for the analysis of the tensile tests data. A facet size of 100 µm was set for the local strain calculation. Young's modulus, shear modulus and Poisson's ratio of the material were determined by ultrasonic method, as described in Mosecker et al. (2015). To study the influence of strain rate ($\dot{\varepsilon}$) under quasi-static loading a specimen geometry as shown in Fig. 3(a) was tested using a Zwick100 machine. The different cross head displacement rates such as 0.018, 0.18, 1.8, 18, 180 and 900 mm/min was set to achieve strain rates of 0.00001, 0.0001, 0.001, 0.01, 0.1 and 0.5/s respectively. A videoextensometer was used to measure the change in length of the samples, which facilitates the recording of the actual elongation.

To investigate the TWIP steel behavior under crash loading conditions, dynamic tensile tests were carried out at room temperature using a servo-hydraulic 100 KN high speed tensile testing machine (Roell/Amsler HTM2012) equipped with an electro-optical extensometer and a thermocamera. Tensile tests with the ram speeds in the range from 0.01 to 5000 mm/s can be performed with the geometry shown in Fig. 3(b). The speeds used in current work are 12, 120, 1200 and 3000 mm/s, which correspond to strain rates of 1, 10, 100 and 250/s respectively. The tensile force was measured by a standard piezo-electric load cell up to a $\dot{\varepsilon}$ of 10/s and at high $\dot{\varepsilon}$ using a titanium load cell with strain gages attached to the sample shoulder (as shown in Fig. 3(b)). The strain was measured by an inductive displacement sensor for the piston stroke and the results were verified by using an electro-optical extensometer. The storage of test data was carried out using a 4-channel transient recorder. The sample was painted with black lacquer to achieve the optimum contrast for the elongation measurements using an extensometer of type 200x from Zimmer KG.

Temperature variation in the specimen during deformation was investigated by carrying out tensile tests in conjunction with high speed infrared thermography camera JADE III MWIR S MTC (InfraTec GmbH). A sample geometry shown in Fig. 3(b) was used for all $\dot{\varepsilon}$ tests. A Zwick/Roell Z100 machine was used for quasi-static tests and Roell/Amsler HTM2012 for dynamic tests. Each specimen was coated with a black lacquer to minimize the reflections from the surroundings. The degree of emissivity for the sample tested was determined using a pyrometer with emissivity adjustment. A sample of the material is heated to a known temperature which can be determined very accurately using a thermocouple. At the same time, the sample temperature is measured with the infrared thermography camera and the degree of emission in the camera software is varied until the temperature displayed corresponds to that of the thermocouple. The temperature measurement range of camera is from −40 °C to 600 °C. The temperature measurement was carried out as a function of strain rate and maximum image acquisition rate in different photography modes. The data was acquired and analyzed using IRBIS® online software (from InfraTec GmbH) to extract the temperature variation within the gage length of the specimen. The temperature data were correlated with the strain measured from the videoextensometer. For all quasi-static tests, images were acquired at a frame rate of 1 Hz in full-frame-mode with a maximum of 384x288 pixels resolution and with a T calibration range from 30 to 130 °C. At the strain rates of 1 and 10/s, images were acquired in quarter-frame-mode at a frame rate of 888 Hz with a maximum of 80x60 pixels resolution and a calibration range from 30 to 170 °C. For strain rates above 10/s, images were captured using line-mode at a frame rate of 6578 Hz with a maximum of 320x1 pixels resolution and a calibration range from 30 to 150 °C. The major difference between line-mode and others is that only a single line in the center of sample over the entire gauge length will be scanned during deformation, whereas full/half/quarter images will be captured in other modes. The overall accuracy of temperature measurements within the range of calibration was ± 1 °C.

3. Results

3.1. Macroscopic response

The influence of anisotropy and strain rate dependency on work hardening behavior are of crucial importance for the crash performance of the material and also play a large role in selecting the optimal forming processes for manufacturing of components. Understanding tensile properties under quasi-static and dynamic loading conditions will aid in choosing TWIP steel for a specific application.

3.1.1. Effect of anisotropy

The σ–ε curves and the strain hardening rate curves (SHR, $d\sigma/d\varepsilon$) obtained by uni-axial tensile tests at room temperature (23 °C) along RD, TD and SD (45°) are shown in Fig. 4. In the σ–ε curves shown in Fig. 4(a), periodic serrations of type A can be observed, caused mainly due to DSA. These serrations appear quite similar in characteristics along RD, TD and SD in terms of distance between the two serrations and stress jump at the serrations with increasing deformation. The distance between two serrations is smaller at the beginning of serrations and became larger with increasing strain. Similarly, the stress jump at the serration at 18% strain is about 12–15 MPa, whose magnitude increased to about 20–25 MPa at 40% strain. The material shows almost linear flow behavior throughout the deformation and an abrupt failure in the end. Initially, at all directions hardening is characterized by a sharp drop of the SHR and with small increase in deformation, SHR increases to reach a constant value. The SHRs in all directions is above 3000 MPa at the beginning of the deformation and decreases to about 2000 MPa at failure. The first marked inflexion in SHRs occurs at ~0.05 true strain, where it started to decrease steadily. Thereafter, SHR shows a general drop until the final failure indicating no additional active deformation mechanisms.

The mechanical properties of the material vary slightly along RD, TD and SD. The variation in properties such as yield/ultimate

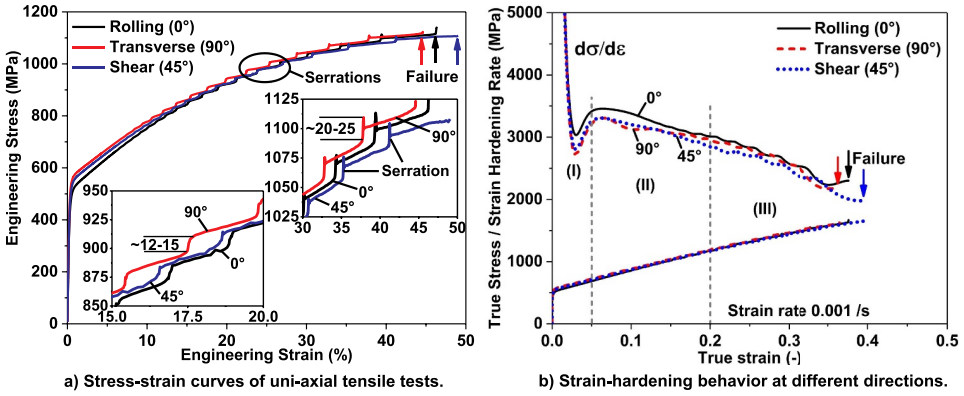

Fig. 4. Anisotropy effect on the mechanical behavior of the investigated X60Mn22 TWIP steel.

tensile strength (YS/UTS), uniform/total elongation (UE/TE), Lankford coefficient (r-value), strain hardening exponent (n-value), density (ρ), Young's modulus (E), shear modulus (G), Poisson's ratio (ν) and ECO-index are presented in Table 2. The material has a YS of 500 MPa along RD, whereas in TD and SD, YS is slightly higher by ~20 MPa. UTS of the material is above 1100 MPa in all three directions and it is slightly high along RD and TD. TE of the material is about 45% and it is marginally high along SD. The macroscopic failure strain ($\boldsymbol{\varepsilon_f}$) in all three directions is ≥ 45%. The ECO-index of TWIP steel in all three directions is above 50 GPa %, indicate that material shows uniform behavior in all directions. The material has a Young's modulus of 165 GPa, shear modulus of 63 GPa and a Poisson's ratio of 0.31. The strain-hardening coefficient in all three directions is ~0.3. The average r-value of ~1.07 and R_{45} value of 1.05 suggest that the material is quite close to isotropic. The presence of MnS and Al_2O_3 inclusions in the material did not affect the mechanical properties to large extent, but led to slight reduction of the UE/TE along TD.

3.1.2. *Effect of strain rate*

The σ–ε curves of quasi-static and dynamic tensile tests are shown in Fig. 5(a). With decrease in $\dot{\varepsilon}$, tensile strength and ductility of the material has increased. Periodic serrations of type A can be observed on the σ–ε curves for all $\dot{\varepsilon}$ up to 0.5/s. With further increase in $\dot{\varepsilon}$ above 0.5/s, the serrations start to disappear and the failure behavior changes from abrupt failure to classical necking and failure. Under dynamic loading conditions, flow behavior without any serrations can be observed at all $\dot{\varepsilon}$ between 1/s and 250/s along with large strain localization due to pronounced necking. Serrations observed on the σ–ε curves for the $\dot{\varepsilon}$ of 100/s and 250/s are not due to DSA, but due to the force measurement.

The strain hardening rates (SHR, $d\sigma/d\varepsilon$) plotted for both quasi-static and dynamic $\dot{\varepsilon}$ is shown in Fig. 5(b). With increase in $\dot{\varepsilon}$, SHR of the material has decreased. Hardening for all $\dot{\varepsilon}$ is characterized by a sharp drop of the SHR at the beginning, followed by its increase to a constant value with further slight increase in deformation. The first inflexion in SHR occurs at ~0.05 true strain for a $\dot{\varepsilon}$ of 0.0001/s and it shifts to the right with increasing $\dot{\varepsilon}$. The inflexion in SHR for $\dot{\varepsilon}$ above 0.5/s occurs at ~0.1 true strain, where it started to decrease steadily. The SHR for a $\dot{\varepsilon}$ of 0.0001/s is about 3500 MPa at the beginning of the deformation and decreases to about 2000 MPa at failure. With the increase in $\dot{\varepsilon}$ from 0.0001/s to 0.5/s, the SHR decreases from 3500 MPa to 2800 MPa at the beginning of the deformation. The SHR is above 2500 MPa for all dynamic tests up to a true strain of ~0.2 and it decreases to about 1400 MPa at failure. In general, the SHR of TWIP steel decreases with increasing $\dot{\varepsilon}$ and shows a general drop for all quasi-static tests until the final failure indicating no additional active deformation mechanisms. However, the SHR decreases quite steadily for all dynamic tests after a true strain of ~0.2 suggesting a slight change in deformation behavior of the material.

The variation of mechanical properties with increasing $\dot{\varepsilon}$ is plotted in Fig. 5(c). The YS of the material remains almost constant for all quasi-static tests and it starts to increase linearly when the $\dot{\varepsilon}$ changed to dynamic. The UTS of the material is above 1000 MPa until a $\dot{\boldsymbol{\varepsilon}}$ of 0.5/s and it started to decrease slightly by about 50 MPa with further increase in $\dot{\varepsilon}$. The UE/TE of material is almost same for quasi-static tests, but with increasing $\dot{\varepsilon}$ the UE decreased almost linearly, where as the TE is almost constant at high $\dot{\varepsilon}$ as well. The

Table 2
Mechanical properties of X60Mn22 TWIP steel: yield/ultimate tensile strength (YS/UTS), uniform/total elongation (UE/TE), Lankford coefficient (r-value), strain hardening exponent (n-value), Young's modulus (E), shear modulus (G), Poisson's ratio (ν) and ECO-index; RD/0°: rolling direction, TD/90°: transverse direction, SD/45°: shear direction, specimen cut along 45° to RD/TD; All data are average values determined from at least three parallel experiments.

Direction	YS	UTS	UE	TE	r-value	n-value	E	G	ν	ECO-index
	MPa	MPa	%	%	–	–	GPa	GPa	–	GPa %
RD/0°	501	1139	45.7	45.7	0.81	0.33	165.7	62.9	0.316	52
SD/45°	517	1108	48.4	48.4	1.05	0.31	165.9	63.4	0.309	54
TD/90°	524	1132	44.6	44.6	1.38	0.30	170.9	65.2	0.311	51

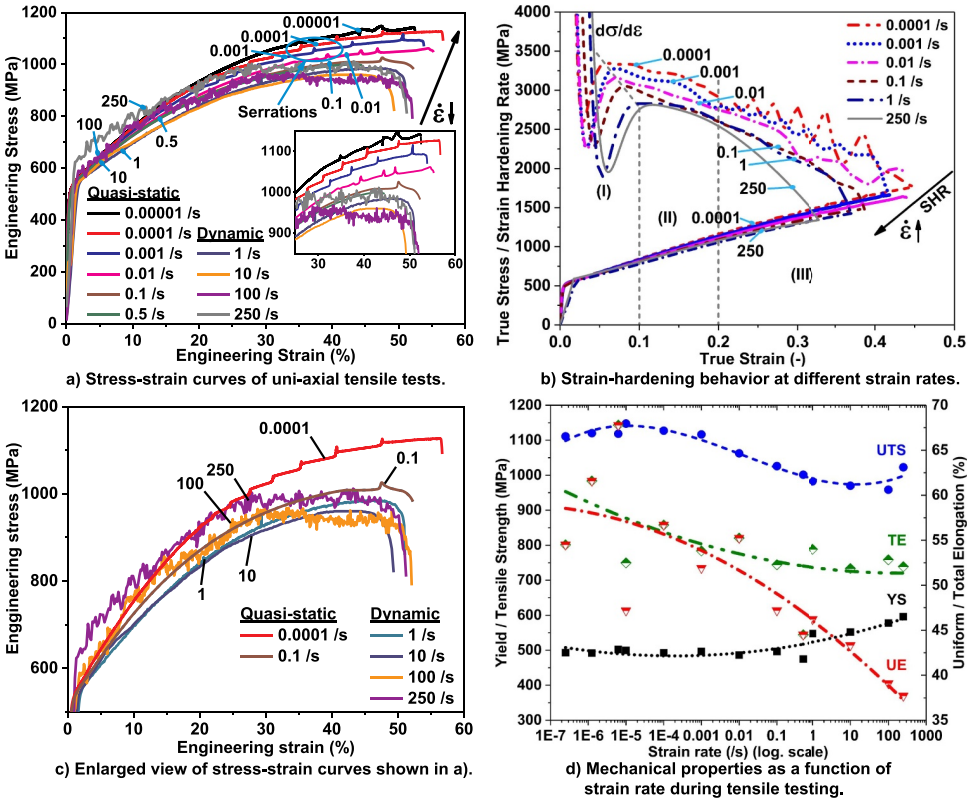

Fig. 5. Strain rate effect on the mechanical behavior of the investigated X60Mn22 TWIP steel. At least three repeatable tests were performed for each condition. All data are average values determined from at least three parallel experiments. YS: yield strength, UTS: ultimate tensile strength, UE: uniform elongation and TE: total elongation.

elongation values at high strain rates are lower compared to that of quasi-static conditions. This change in behavior of the material can be correlated to adiabatic heating.

The local temperature increase in the material due to adiabatic heating is shown in Fig. 6. For tensile tests at different $\dot{\varepsilon}$, the temperature distribution over the entire gage length of the specimen with increasing strain is shown in Fig. 6(a) and the temperature variation in the middle of the specimen is shown in Fig. 6(b). It can be observed from Fig. 6(a) that with increase in macroscopic strain, the temperature in the specimen rises due to adiabatic heating. As the $\dot{\varepsilon}$ increases from quasi-static to dynamic, the temperature raises quite rapidly in the specimen during deformation. The localized deformation in the material after reaching uniform elongation will also lead to rise in temperature locally. At the $\dot{\varepsilon}$ of 0.01/s and 0.5/s, the maximum localized temperature just before the failure is ~120 °C, whereas under dynamic tests, temperature rises to 180 °C and above. However at the point before the uniform elongation the average temperature is between 60 °C and 100 °C. At ~30% strain, the temperature distribution in the specimen is uniform through out and the average values are about 40, 80, 90, 100, 110 °C at a $\dot{\varepsilon}$ of 0.01, 0.5, 1, 10 and 100/s respectively. After 30% strain, the temperature distribution is localized and increases further close to necking. Just before failure, the temperature raises above 200 °C locally, which is also beyond the range of temperature measurements at high speed testing. It can be seen from Fig. 6(b) that as the $\dot{\varepsilon}$ is increased from quasi-static to dynamic, localization of temperature increases due to pronounced necking at high $\dot{\varepsilon}$, whereas temperature distribution is more uniform over the gage length until failure at low $\dot{\varepsilon}$. The rise in temperature above 180 °C due to adiabatic heating could influence the active deformation mechanisms at different $\dot{\varepsilon}$ leading to change in the material failure behavior.

3.1.3. Energy absorption

The important property which characterize the behavior of material under crash loading conditions is the specific energy absorption, defined as the deformation energy per unit volume at a given temperature (23 °C) and at the $\dot{\varepsilon}$ of 100/s to 1000/s, determined by high speed tensile tests. Similarly, ECO-index parameter defined as the product of UTS and UE is also an indicator of the overall performance of material.

Energy absorption (EA) values for different steels are determined by integrating the area under the σ–ε curve until the start of decrease in stress as shown in Fig. 7(a) and alternatively until 10% elongation. The area under the σ–ε curve for TWIP steel is quite larger compared to all other AHSS, indicating high energy absorbed per volume (W). In order to exclude the influence of specimen geometry, particularly the different thickness values, the total energy values were converted to mass-specific values. Higher total

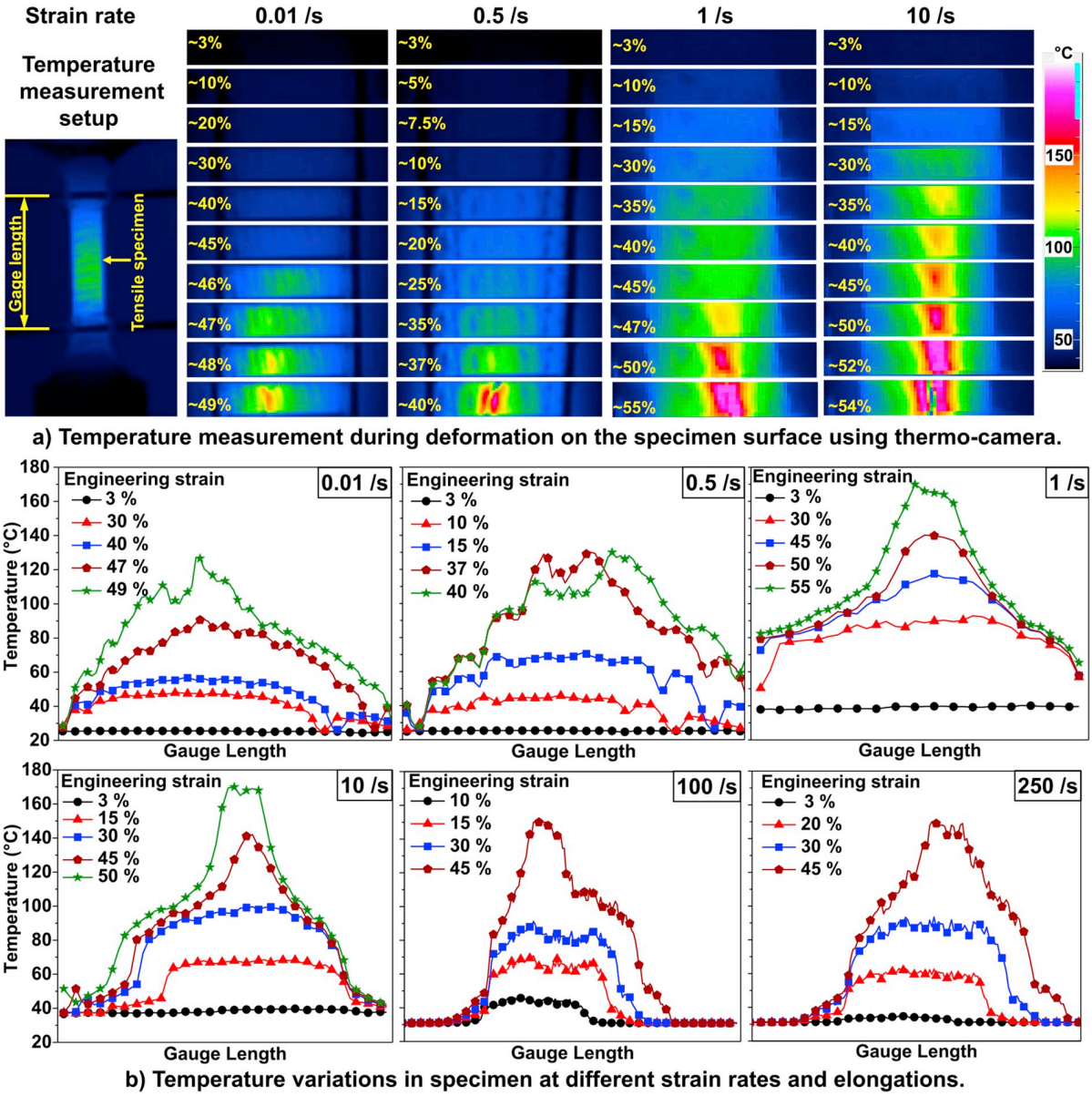

Fig. 6. Strain rate influence on the adiabatic heating during deformation. a) left: setup illustration; middle: temperature distribution at different strain rates and macroscopic strains over the entire gage length; right: legend for local temperature distribution. b) Temperature calibration range for the thermocamera: for strain rates of 0.01/s and 0.5/s – 30 °C to 130 °C; 1/s and 10/s – 30 °C to 170 °C; 100/s and 250/s – 30 °C to 150 °C.

mass specific energy absorption is achieved by the TWIP steel as shown in Fig. 7(c) at a $\dot{\varepsilon}$ of 100/s. The bar diagram of Fig. 7(c) shows the total mass specific energy absorption capacity of the TWIP steel in comparison with other AHSS (DP steels and TRIP steel), ferritic steels (DC04 and ZStE340) and austenitic steels (1.4301 and 1.4318) (Bleck and Schael, 2000). Total EA value of TWIP steel is double or even higher than that of dual phase steels (DP600, DP800 and DP1000) and ferritic steels. TWIP steel absorbs 1.5 times more energy than that of the TRIP steel and also more than twice that of DP1000 at a $\dot{\varepsilon}$ of 100/s. However both austenitic stainless steels (1.4301 and 1.4318) show slightly higher EA compared to TWIP steel under crash conditions. At a $\dot{\varepsilon}$ of 100/s, mass specific EA value of TWIP steel is above 55 kJ/kg and all other AHSS and ferritic steels possess energy values between $22 \leq W \leq 40$ kJ/kg, which absorb 60%–30% less energy compared to that of the crash resistant TWIP steel.

Similarly, EA up to 10% elongation of TWIP steel is compared with other steels at a strain rate of 100/s tested under same conditions as shown in Fig. 7(d). It is evident that even for up to 10% elongation TWIP steel absorbs larger energy compared to AHSS and ferritic steels, but slightly less energy than austenitic steels. It can be observed that TWIP steel absorbs only slight high energy value compared to DP1000 for up to 10% elongation. However at a fixed elongation of 10%, EA values of ferritic steel ZStE340,

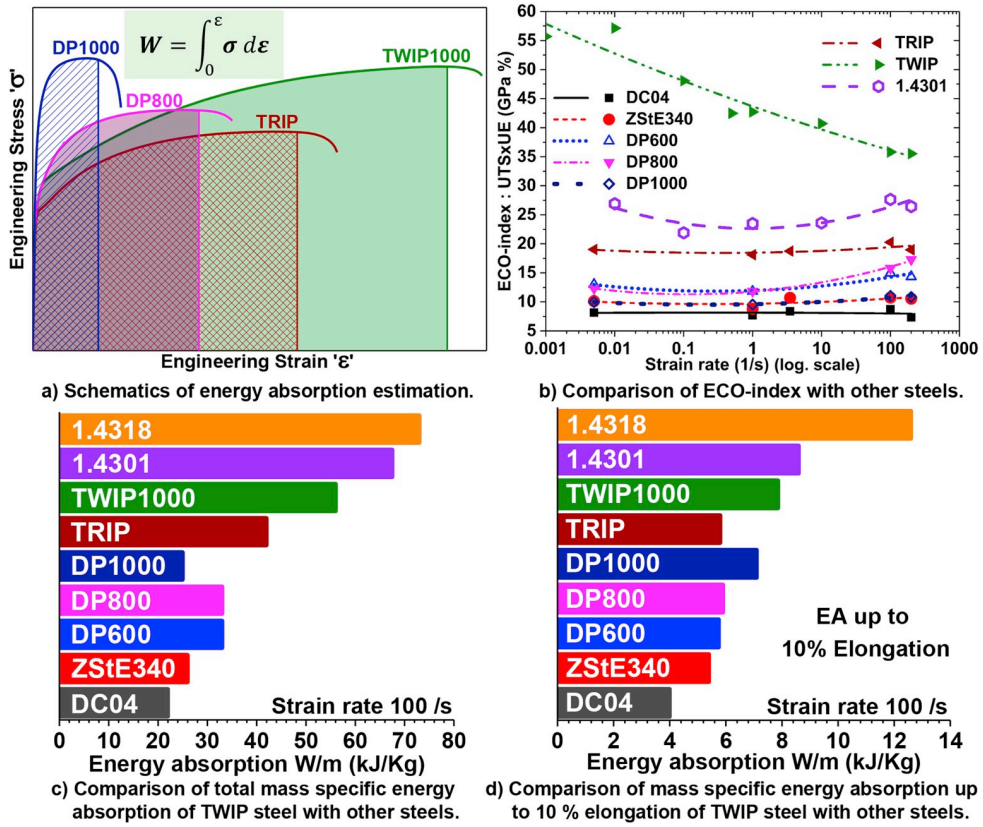

Fig. 7. Comparison of specific energy absorption capacity and ECO-index of TWIP steel with other advanced high strength steels (AHSS), ferritic steels and austenitic stainless steels. The mass specific energy absorption and mechanical properties data for all other steels were taken from Bleck and Schael (2000); The steels used for comparison are AHSS such as dual phase steels (DP600, DP800 and DP1000) and transformation induced plasticity (TRIP) steel, ferritic steels such as mild steel DC04 and the high strength steel ZStE340 and austenitic stainless steels such as 1.4301 and 1.4308. At least three repeatable tests were performed for each condition. All data are average values determined from at least three parallel experiments.

DP600, DP800 and TRIP are about 6 kJ/kg, while DP1000, TWIP1000 absorb marginally higher energy of about 7.5 kJ/kg or 7.8 kJ/kg, austenitic steels absorb the highest energy of about 9 kJ/kg (1.4301) or 13 kJ/kg (1.4318). Among all the steels considered, ferritic steel DC04 absorbs the least amount of energy of about 4 kJ/kg. Since the mechanical behavior of steels vary largely with strain rate and the active deformation mechanisms, such comparison are necessary for choosing TWIP steel for specific applications instead of other steels.

Fig. 7(b) shows the comparison of ECO-index of TWIP steel with other AHSS and conventional steels. It is shown in the diagram that ECO-index of TWIP steel decreases from ~55 GPa % to ~35 GPa %, when $\dot{\varepsilon}$ changed from quasi-static to dynamic. The ECO-index of TWIP steel is above 35 GPa % for all $\dot{\varepsilon}$, whereas for all other steel grades ECO-index values are between 5 ≤ ECO-index ≤ 25 GPa %, which are half that of the damage resistant TWIP steel. TWIP steel has high tensile strength of about 1000 MPa, ECO-index of above 35 GPa % and also excellent mass specific energy absorption of above 55 kJ/kg at all $\dot{\varepsilon}$, making them highly suitable material for all automotive safety relevant components.

3.2. Deformation mechanisms

The evolution of deformation twinning during plastic deformation plays a significant role in enhancing the hardening behavior of TWIP steel via the dynamic Hall-Petch effect (De Cooman et al., 2018). The nucleation and growth of twins in the material lead to creation of new boundaries by subdivision of original grains. Twin boundaries act as the barriers to dislocation motion thereby progressively reducing the effective mean free path of dislocations resulting in superior strain hardening of TWIP steel. The addition of vanadium to TWIP steel not only promotes grain refinement, but also increases the localized stress at the grain boundaries (GB) (Gwon et al., 2017). Larger stress at grain boundaries result in the nucleation of mechanical twins at GB as shown in Fig. 8 (black arrows). Annealing twins can also be observed in the initial stages of deformation as shown in Fig. 8(a) (light blue arrows). With small increase in macroscopic strain to ~0.05, mechanical twins can be observed in the grains oriented along $< 111 >$ (see Figs. 8(a) and Fig. 13). Increasing the deformation further lead to nucleation and growth of mechanical twins (black arrows). Some grains which are

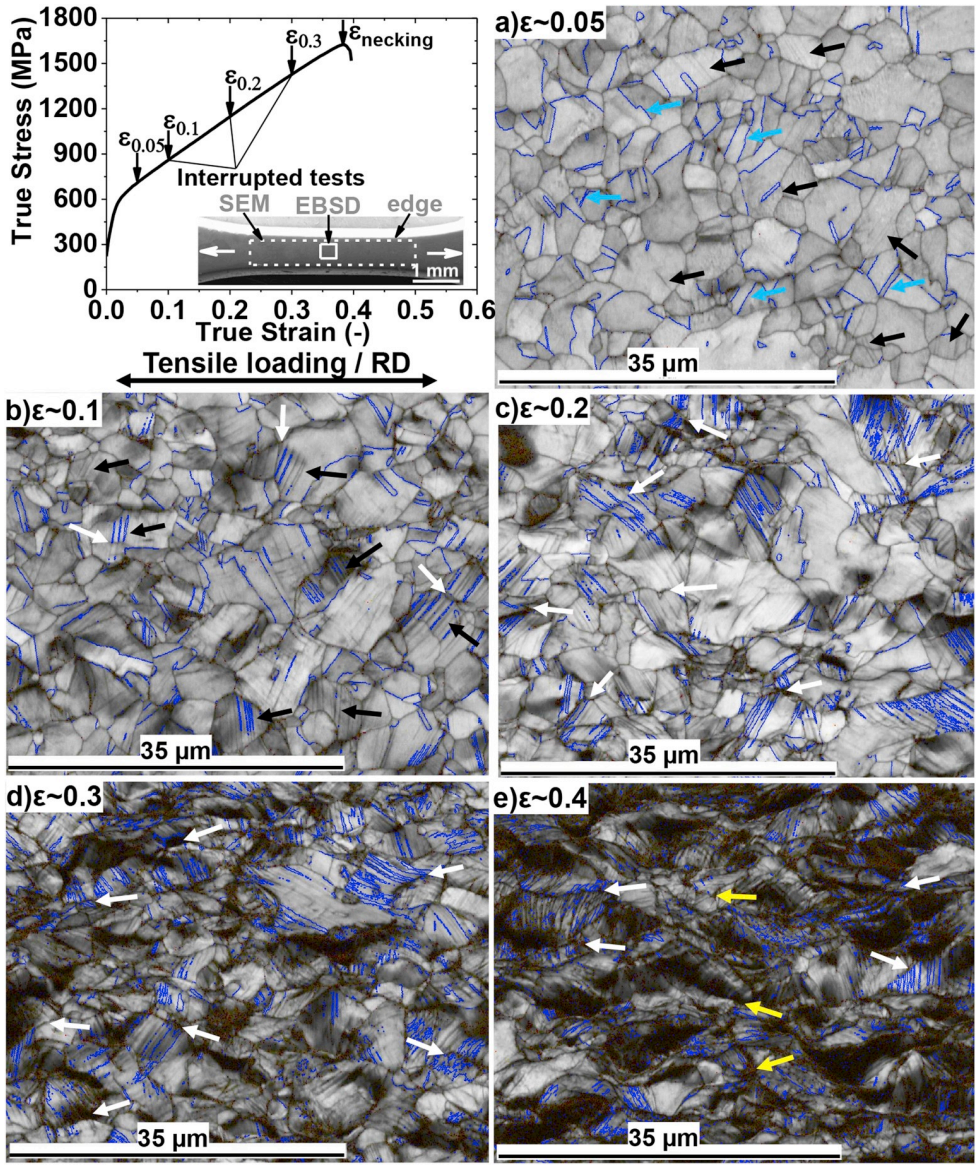

Fig. 8. Image quality (IQ) maps depicting the evolution of twinning with increasing macroscopic strain subjected to quasi-static loading: a) 0.05 b) 0.1 c) 0.2 d) 0.3 e) ~0.4; blue color in IQ maps indicates annealing twin boundaries (see a)) and detected Σ-3 deformation twin boundaries (see b), c), d), e)); blue arrows indicate annealing twin boundaries; black arrows indicate nucleation of deformation twins; white arrows indicate intercepting twins at grain boundary; yellow arrow indicate triple junctions; tensile loading direction is shown; macroscopic true strain is shown at the top right corner; pixels in black are un-indexed points. (For interpretation of the references to color in this figure legend, the reader is referred to the Web version of this article.)

oriented along the $< 101 >$ direction reorient toward the $< 111 >$ direction during deformation and twins initiate in these grains as shown in Fig. 13. In Fig. 8(b) and (c), mechanical twins can be observed in most of the grains indicating large heterogeneous deformation at micro-scale. The twin bundles can be very well identified and the increase in density of mechanical twins can be seen with increasing strain. At a strain of ~0.3 and ~0.4 (see Fig. 8(d) and (e)), the mechanical twins are saturated in the grains with no scope for further twinning. The area fraction of detected twins/twin bundles with increasing macroscopic strain is shown in Fig. 13 and twinning in the material saturates before the final failure. There are many instances in the microstructure where twinning occurs in both the neighboring grains and share a common GB (white arrow). The heavily deformed grains can also have a common junction (yellow arrow). The stress level in such grain boundaries and triple junctions is very high compared to other grains. Such high stressed regions of microstructure are prone to initiation of micro-cracks.

Strain rate has a significant effect on the temperature rise due to adiabatic heating, which leads to increase of SFE. It will result in enhancing TWIP effect up to a SFE value of 40 mJ/m^2 and there after slip is favored (see Fig. 14(a)). For all $\dot{\varepsilon}$ below 10/s, the

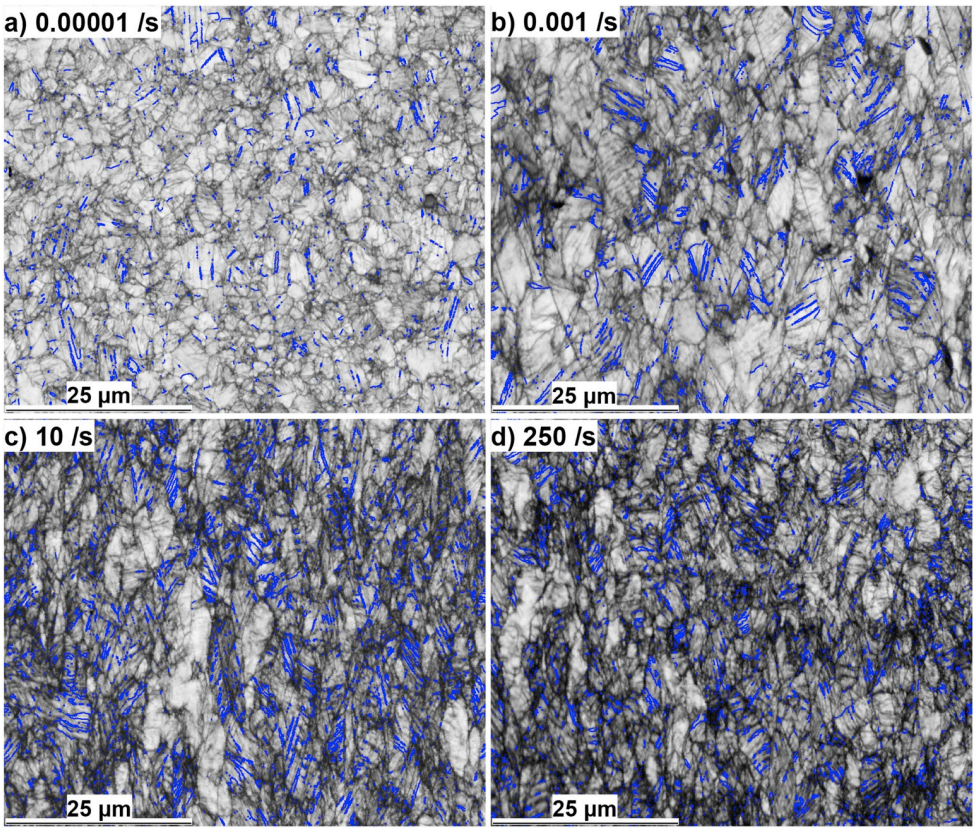

Fig. 9. Image quality (IQ) maps of the fractured samples at different strain rates depicting the deformation twinning: a) 0.00001/s b) 0.001/s c) 10/s and d) 250/s; blue color in IQ maps indicates detected Σ-3 deformation twin boundaries; pixels in black are un-indexed points. (For interpretation of the references to color in this figure legend, the reader is referred to the Web version of this article.)

temperature in the specimen could go up to 120 °C during the uniform deformation, resulting in enhanced TWIP effect in the material. For the $\dot{\varepsilon}$ above 10/s, the temperature in the specimen could go beyond 180 °C leading to twinning in combination with pronounced slip. This remarkable change in the twinning behavior can be observed in Fig. 9 as the $\dot{\varepsilon}$ increased from quasi-static to dynamic. The **Σ**-3 twin boundaries fraction (blue color) in the sample deformed to failure at low $\dot{\varepsilon}$ (0.00001/s) is quite low in comparison to other $\dot{\varepsilon}$. The fraction of **Σ**-3 twin boundaries increased with increasing $\dot{\varepsilon}$ up to 10/s and with further increase in $\dot{\varepsilon}$, slightly lower fraction of **Σ**-3 twin boundaries can be observed. This change in behavior of twinning at different $\dot{\varepsilon}$ can be correlated to temperature rise in specimen due to adiabatic heating. At lower $\dot{\varepsilon}$, many thinner twin bundles can be observed within the grains compared to few thicker twin bundles at high $\dot{\varepsilon}$. This change in twin morphology could be related to increase in SFE at high $\dot{\varepsilon}$ due to adiabatic heating.

3.3. Local deformation behavior

The σ–ε behavior extracted from the quasi-static tensile tests for a specimen along RD carried out in conjunction with DIC is shown in Fig. 10(a). The serrations can be observed on the σ–ε curve caused due to DSA. The DSA effect in TWIP steel has led to the plastic instability in the form of initiation and propagation of the shear bands during deformation. It can be seen from Fig. 10 that shear bands initiate at a strain of ~12.5% during deformation and propagate until failure. The strain at which shear bands initiate is shown in Fig. 10(a) and the region at which shear bands are active is indicated by rectangle. After a strain of ~12.5%, shear bands nucleated steadily and continuously. The plateau between the two consecutive serrations peaks corresponds to the nucleation and propagation of shear band within the gage length. The serration peak corresponds to the initiation/disappearance of the shear band outside the gage length. The local strain distribution ($\boldsymbol{\varepsilon_{local}}$) along the tensile direction at different elongations is shown in Fig. 10(b). It can be observed that over the entire gage length of the tensile specimen, the local strain distribution seems to be uniform. For the elongations above 40%, the strain starts to localize at the gripper end of the tensile specimen. With further increase in deformation, the region of strain localization has increased further, finally leading to abrupt failure. Flat fracture with slight necking on the broken tensile sample can be observed. The macroscopic failure strain ($\boldsymbol{\varepsilon_f}$) in the material is ~46%, whereas the local failure strain ($\boldsymbol{\varepsilon_{f_local}}$) is ~50%. This negligible difference between the local failure strain ($\boldsymbol{\varepsilon_{f_local}}$) and the global failure strain ($\boldsymbol{\varepsilon_f}$) indicates that there is only negligible amount of strain localization before the final failure.

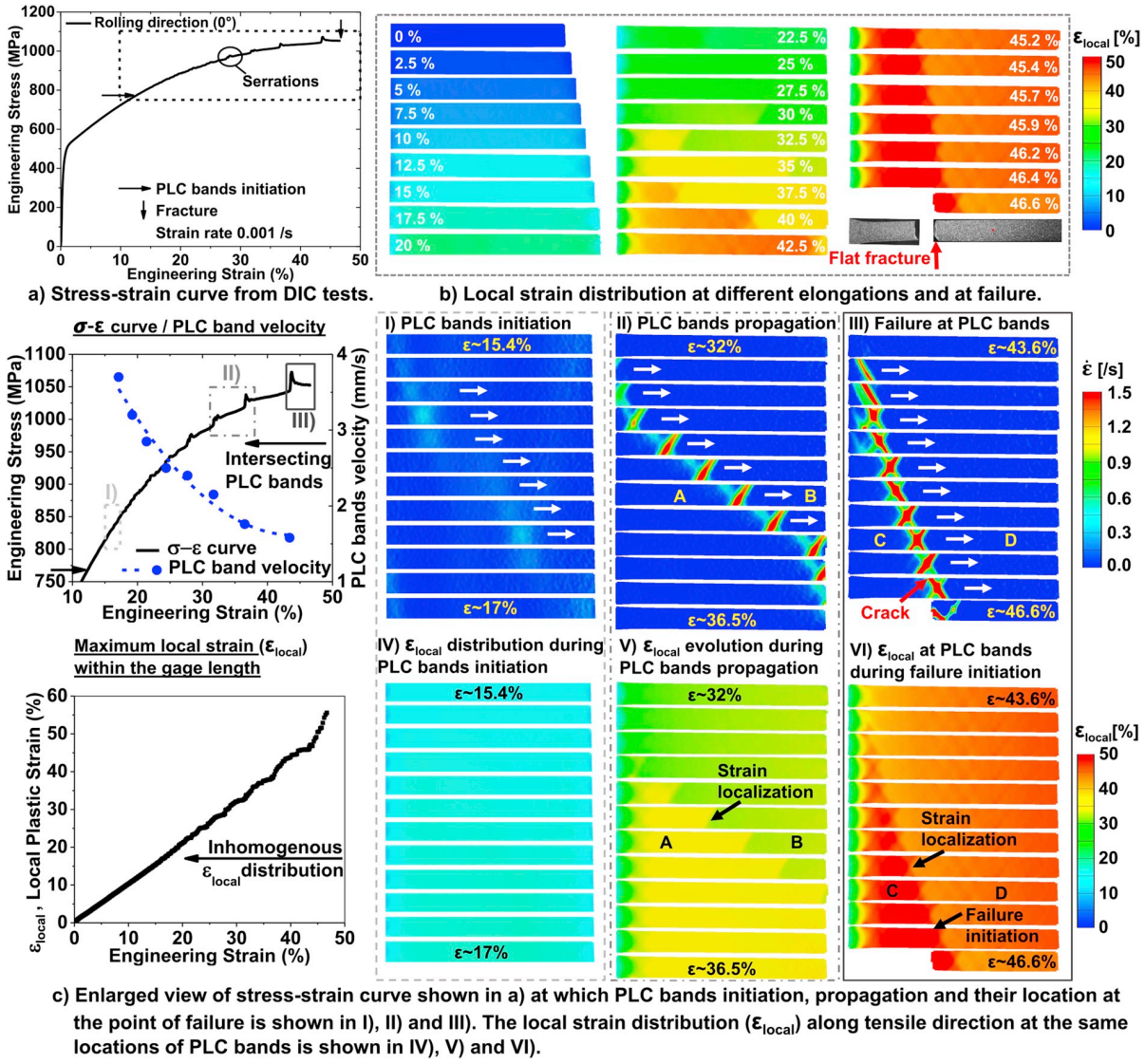

Fig. 10. Stress-strain behavior, local strain distribution and shear bands propagation for a specimen along RD extracted from the quasi-static tensile tests carried out in conjunction with DIC. The local strain distribution and PLC effect along TD and SD is same as that of RD. a) rectangle indicate the region at which shear bands initiate and propagate during the deformation. b) macroscopic strain is indicated on the plot at which local strain distribution (ε_{local}) is shown; legend for ε_{local} along tensile direction is shown on the right. c) The variation of ε_{local} with macroscopic ε within the gage length is shown (see bottom left). white arrows indicate the direction of propagation of the shear bands; the macroscopic strain at the start and end of shear band is given; The difference in strain location between the regions where shear band has already passed by and the regions where shear band has to pass through is shown by indicating with letters 'A', 'C' and 'B', 'D' respectively; images were shown in steps of ~0.4–0.6% macroscopic strain; the legend for $\dot{\varepsilon}$ and ε_{local} distribution is shown on the right. At least three repeatable tests were performed for each test condition.

The initiation and propagation of shear bands during deformation is shown in Fig. 10(c). The enlarged view of σ–ε curve from Fig. 10(a), where shear bands are active is shown in Fig. 10(c) (top left corner). It can be observed that stress jumps at serrations at the beginning are smaller compared to the final stages of deformation. Shear bands nucleated at one shoulder end or in the middle of specimen and propagated to the other end. For up to ~36% strain, only one shear band nucleated and propagated to the other end, whereas after 37% strain, two intersecting shear bands nucleated and propagated during the deformation (see Fig. 10(c) I), II) and III). From the local strain rate ($\dot{\varepsilon}$) distribution it is clear that, the deformation is localized in the shear bands, whereas it is uniform in other regions. During initiation, the local strain accumulation in shear bands is quite low, but in the subsequent shear bands, large strain localization can be observed. From Fig. 10(c) IV), V) and VI), it can be seen that during the initiation of shear bands, the distribution of local strain is uniform throughout, whereas in the later stages of deformation the strain starts to localize in the shear bands. The local strain is larger in the regions where shear band has already passed during deformation compared to the region where shear band is moving towards/yet to pass through. However, the difference in local strain between the regions where the shear band

already passed by compared to the regions where shear band moving towards is ≤ 5% strain. Thus nucleation and propagation of shear bands during deformation has resulted in inhomogeneous deformation behavior. The velocity at which shear bands propagate decrease exponentially with increasing strain as shown in Fig. 10(c). The band velocity at the beginning is ~4 mm/s, which is drastically reduced to ~1.5 mm/s in the end. The failure occurred at the intersection of shear bands when their motion is hindered significantly as shown in Fig. 10(c) III) and VI). The localization of strain within the shear bands is larger compared to the local strain distribution in other regions. Hence strain localization caused in the shear bands influence the failure initiation in TWIP steel. The local deformation behavior and the shear bands propagation along TD and SD is similar to that of RD, hence they are not included. The σ–ε curves along different directions and $\dot{\varepsilon}$ is presented in Section 3.1.1 and Section 3.1.2 respectively. The serrations which appear at lower $\dot{\varepsilon}$ disappear with increasing $\dot{\varepsilon}$ above 0.5/s, could be related to rise in the temperature of the specimen due to adiabatic heating or faster rate of shear bands propagation.

3.4. Damage development and fracture behavior

The evolution of microstructure with increasing strain is shown in Fig. 8. Twinning in combination with dislocation glide within the grains has resulted in large heterogeneous deformation. Nucleation and growth of multiple deformation twins within a single grain result in large pile up dislocations at grain boundaries (GB) or twin boundaries. Twins and slip bands in the microstructure impinge at the GB. From Fig. 8, there are many instances in microstructure, where two neighboring grains which has twins share a common GB or a grain which has twins share a GB with another grain which deform by slip or three differently deformed grains share a common junction (triple points) can be observed. Large dislocation pile up in such instances of microstructure for true strain above 0.2, result in high stress at GB. The stress level will be even higher if the GB lay ⊥ to loading direction. Micro-crack formation in such high stressed GB can be seen in Fig. 11(a),(b),(c) and (e). The micro-cracks are mainly observed at GB, triple junctions and especially in boundaries which are ⊥ to loading direction. From Fig. 11(c) it is very clear that stress concentration caused by the intersection of slip bands at GB lead to micro-crack formation at GB. Many instances of micro-cracks at triple points can also be observed. With further increase in macroscopic strain to true strain of 0.4 (just before final failure), many inter-granular micro-crack formation events can be seen. The majority of cracks observed in the microstructure are at GB and triple points. Micro-cracks formation events could also be seen at the intersection of slip bands to the GB and also at the intersection of twins with GB. The enlarged regions of microstructure in Fig. 11(d) and (f) clearly indicates the micro-crack initiation at the interception of slip bands extrusions and deformation twins at GB. It can be understood from σ–ε curve in Fig. 8 that even the micro-tensile specimen failed abruptly. From these investigations, it is very clear that there is great interplay between the deformation twins and dislocation glide at micro-scale until the saturation of hardening. The saturation of twinning in the material is the precursor to the nucleation of micro-cracks at the high stressed regions such as GB and triple junctions. Since twinning is quite uniform in almost all grains in the entire microstructure, the cracks were initiated all over the cross section. Many such micro-cracks formed coalescence together rapidly to form macro-cracks resulting in abrupt failure.

The change in local deformation behavior at different $\dot{\varepsilon}$ lead to different failure behavior of the material. The presence of large fraction of MnS in the material do play a great role on the damage initiation and fracture. The influence of anisotropy and $\dot{\varepsilon}$ on the failure behavior is shown in Fig. 12. Flat fracture surface along the width and slant fracture along the thickness can be observed on broken tensile samples as shown in Fig. 12(a) for all directions (RD, TD and SD). This indicates that rapid nucleation of micro-voids occurred in the material leading to micro-crack formation and fast crack propagation. However, the appearance of slight neck before failure in all directions shows that there is a plastic localization before the final failure. The localization of strain before the final failure is explained in Section 3.3. The role of MnS inclusions on the failure initiation can be visualized on the fracture surfaces in Fig. 12(a) (2nd row). Failure initiation at the elongated MnS inclusions when subjected to tensile loading particularly in the samples along TD has led to fracture in the material. Flat fracture surface appearance (2nd row) and the de-cohesion at the MnS inclusions (3rd and 4th rows, white arrows) clearly show that non-metallic inclusions present has triggered the damage initiation in the material. Many alternating ridges and troughs observed on the fracture surface along RD and SD (2nd row), indicate coalescence of multiple micro-cracks at different locations in the material. The presence of large elliptical or round voids (white arrows) show that coalescence of many smaller voids has occurred at the MnS inclusions, could have also played a role in failure initiation. Apart from the above mentioned differences in observations, large number of minute voids of size ≤ 1.0 μm can be seen on the fracture surfaces in all directions. From Fig. 12, it is clear that the predominant fracture mode in X60Mn22 TWIP steel is ductile failure in all directions and at all $\dot{\varepsilon}$.

The rise in temperature of the specimen during deformation due to adiabatic heating affects the material failure behavior. The fracture behavior under quasi-static tests is shown in Fig. 12(a) and under dynamic tests is shown in Fig. 12(b). It could be observed that at low $\dot{\varepsilon}$, the fracture occurs with the formation of fine and shallow dimples, whereas at high $\dot{\varepsilon}$, the dimples size increased gradually with increase in $\dot{\varepsilon}$. Large reduction of area and pronounced necking in the dynamic tensile tests shows that plastic localization is much larger compared to the quasi-static tensile tests. The fracture surface appearance is similar to quasi-static tests, except increase in size of the dimples. As explained in Section 3.2, the temperature increase of above 180 °C due to adiabatic heating could have led to the change in failure behavior and dimple size under dynamic tests.

4. Discussion

4.1. Serrated flow

Tensile tests carried out in this study over a wide range of strain rates and temperatures (Madivala et al., 2018) revealed repeated “jerks” or “serrations” during the plastic deformation at intermediate temperatures and over a range of strain rates. Serrations are

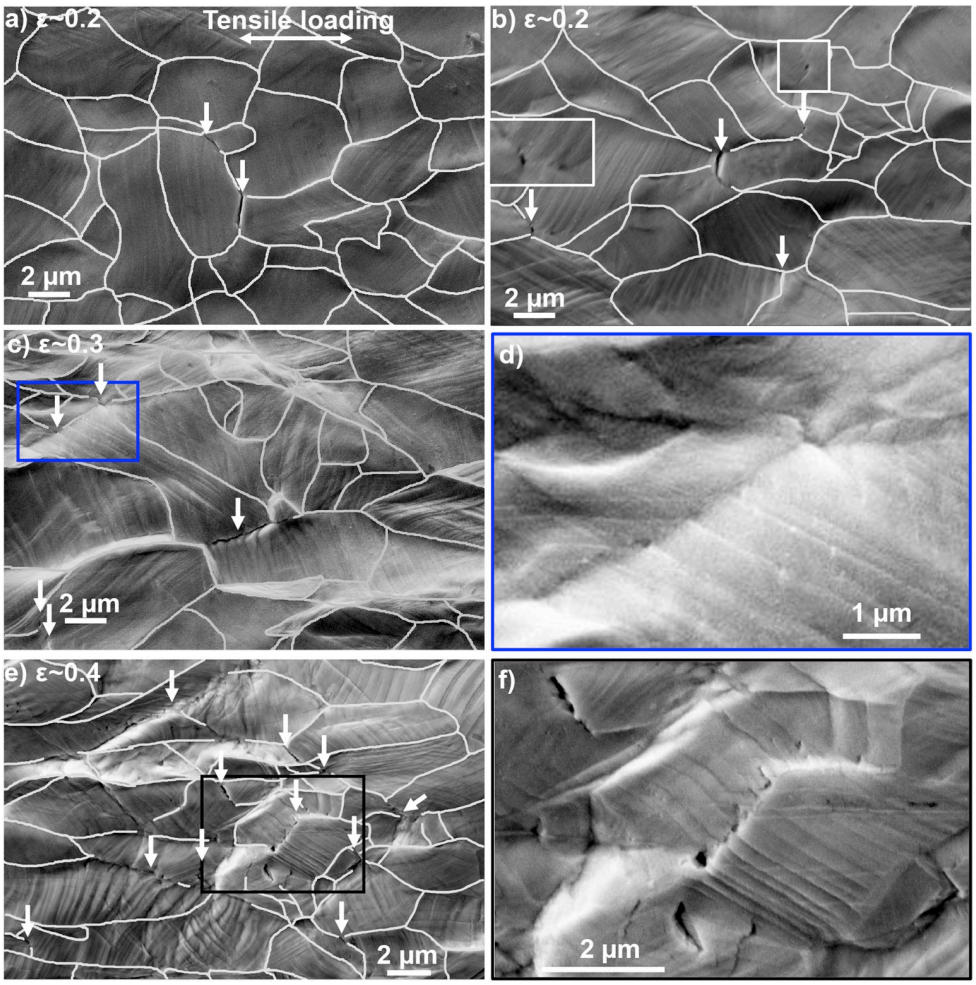

Fig. 11. Development of micro-cracks with increasing macroscopic strain subjected to quasi-static tensile loading. Cracks at a strain of $\varepsilon_{0.2}$: a) and b) inter-granular cracks nucleating at grain boundaries and triple junctions; Cracks at a strain of $\varepsilon_{0.3}$: c) and d) micro-cracks observed at the interception of twins with grain boundaries (GB); Cracks at a strain of $\varepsilon_{0.4}$: e) and f) development of inter-granular micro-cracks initiation and propagation caused by the intercepting deformation twins and slip band extrusions at GB; d) and f) are the enlarged views shown in c) and e) respectively; white arrows indicate micro-cracks.

observed on the σ–ε curves at all quasi-static strain rates and they begin to diminish with increasing strain rates above 0.5/s as shown in Fig. 5. The jerky flow behavior is quite similar in characteristics along RD, TD and 45° in tests carried out at 23 °C (see Fig. 4(a)). The periodic serrations of Type A can be seen in the temperature range between −40 °C and 200 °C in X60Mn22 TWIP steel (Madivala et al., 2018). Such serrated σ–ε behavior has also been observed in different TWIP steels by Lee et al. (2018); Lan and Zhang (2018); Yang et al. (2017). Within the temperature and strain rate regimes where serrated flow occurs, large variation in mechanical properties such as peak in UTS, a plateau in YS, reduction of ductility, more importantly negative strain rate sensitivity (SRS) and abrupt failure with negligible necking could be clearly observed (see Fig. 5). Such manifestations in mechanical behavior of material in the form of serrations, large change in mechanical properties and negative SRS is caused mainly due to DSA mechanism occurring at micro-scale. The phenomena of DSA in high Mn TWIP steels can be attributed to the formation of Mn-C short range order (SRO) or short range cluster (SRC) (Saeed-Akbari et al., 2012; Lee et al., 2011). Dastur and Leslie (1981) proposed that DSA occurs when the C atoms in the Mn-C octahedral clusters reorient themselves in the core of the dislocations, thereby locking the dislocations leading to high dislocation density. During this dynamic interaction between the mobile dislocations and the diffusing atoms during plastic flow, C atoms pins strongly to the dislocations increasing their pile up. When applied stress is sufficiently high, the dislocations overcome the obstacle in the form of SRO/SRC at once by single diffusive jump of C atoms and move to next obstacle, where they are stopped again and the process is repeated (Lee et al., 2011). According to Chen et al., the formation of Mn-C octahedral clusters result in increased lattice resistance for dislocation glide as the passage of partial dislocation will change the local position of both substitutional and interstitial atoms.

Serrated flow caused due to DSA in TWIP steels led to an instability in the form of repetitive nucleation of localized deformation bands at one end of the gage length and their continuous propagation to the other end with each load drop corresponding to

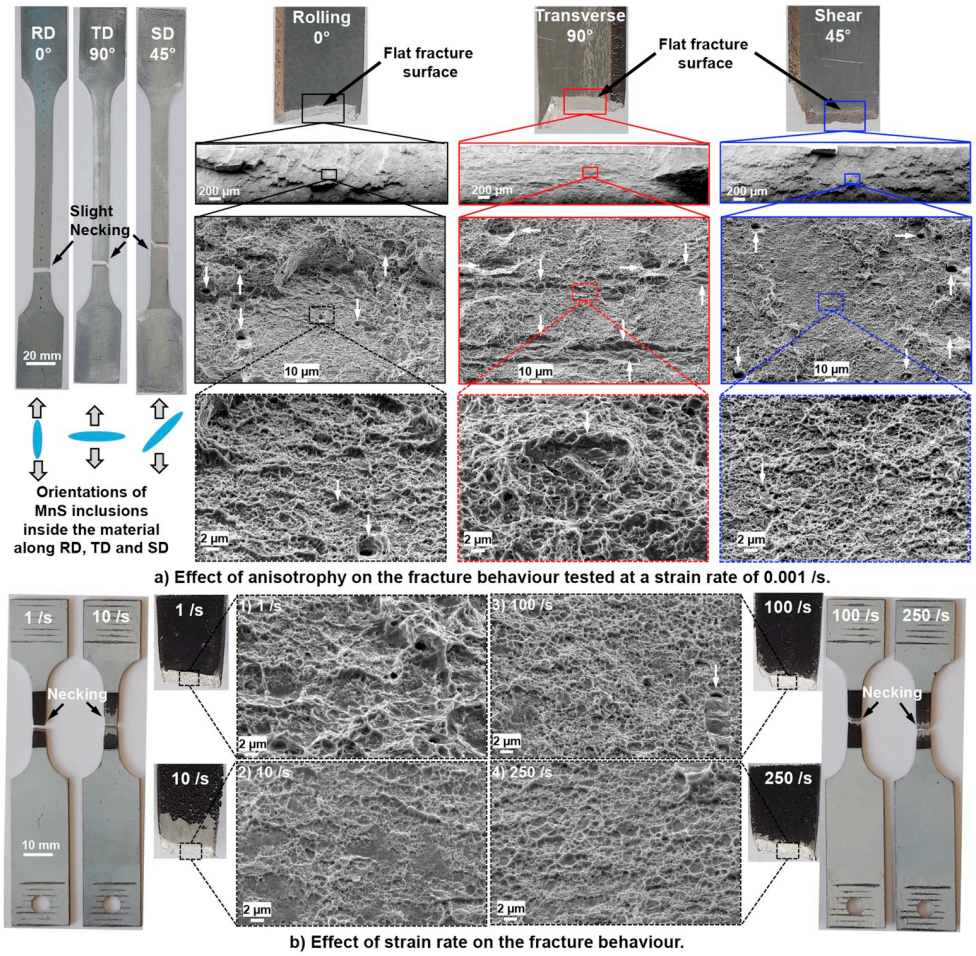

Fig. 12. Anisotropy and strain rate effect on the fracture behavior. a) Necking and fracture surface appearance (top) and SEM images of the fracture surfaces at different magnifications (middle and bottom). Average dimple size is approximately ≤ 1.0 µm. b) Necking and fracture surface appearance (left, right) and SEM images of the fracture surfaces (middle). White arrows indicate voids formed at manganese sulphide (MnS) inclusions.

nucleation of new band as shown in Fig. 10(c). The process is commonly referred to as the Portevin-LeChatelier (PLC) effect. DSA is usually not observed immediately after the start of deformation, hence shear bands or serrations can be observed only after deforming material to a critical plastic strain, $\boldsymbol{\varepsilon_c}$. This is due to the fact that sufficient vacancies must be created to enhance the solute diffusion to dislocations. The $\boldsymbol{\varepsilon_c}$, mainly depends on strain rate ($\dot{\varepsilon}$), Temperature (T), SFE and presence of additional alloying elements such as Al. The critical plastic strain, $\boldsymbol{\varepsilon_c}$ for the initiation of serrations in TWIP steels increase, with increase in SFE, increase in $\dot{\varepsilon}$, decrease in T and with increase in Al content. A relatively small magnitude of stress jump "$\boldsymbol{\Delta\sigma}$" values are associated with the initial serrations than the subsequent ones. This can be explained by the presence of transition regime, corresponding to underdeveloped serrations, before the ripples of inhomogeneous deformation transform into deformation bands, manifesting into clearly developed bands (refer Fig. 10(c) I)).

The strain localization within shear bands is slightly different over the gage length during the transition regime (see Fig. 10(c) I). After their complete development, the strain localization in them increases drastically compared to other areas (see Fig. 10(c) II, III). The distribution of local plastic strain ($\boldsymbol{\varepsilon_{local}}$) is much larger in the region where shear band has already passed by (see in Fig. 10(c) marked by 'A', 'C') compared to other region where it has to pass through (see in Fig. 10(c) marked by 'B', 'D'). Song and Houston (2018) showed by SANS experiments that the size and number density of SRO is much larger in the regions where shear band has already passed by compared to the region where it has to pass through. Also due to the fact that SRO/SRC offers higher resistance to dislocation glide there by leading to (a) aging of dislocations by C-atoms during their interaction time at obstacles (b) enhancement of diffusion coefficient by vacancies generated during plastic flow and (c) increase in mobile dislocation density with strain. The velocity of propagation of the shear bands decrease with increase in macroscopic strain. Kang et al. (2014) has reported that with increase in ε, the volume fraction of Mn-C SRO/SRC increases and the mean radius of clusters decreases. This results in increased resistance offered by the Mn-C clusters and also by the deformation twins for the shear bands propagation leading to decrease in velocity. Lan and Zhang (2018) has showed that velocity of propagation of shear bands increases with increase in $\dot{\varepsilon}$. For the $\dot{\varepsilon}$ of 0.0001, 0.001, 0.01/s, the velocity of propagation of shear bands in the beginning is 2.5, 5.0 and 35 mm/s respectively (Saeed-Akbari

et al., 2012). The strain in the shear bands also increases with increase in ε to about 0.2. This indicates that at very high $\dot{\varepsilon}$ the shear bands propagate at very high speeds of > 100 mm/s, hence shear bands disappear completely at high $\dot{\varepsilon}$.

The physical processes such as twinning and thermomechanical instabilities are very relevant for DSA under tensile deformation. With increase $\dot{\varepsilon}$, the T rises due to adiabatic heating (see Fig. 6), will in turn increase the SFE (see Fig. 14(a)). The suppression of serrations with increase in T or with increase $\dot{\varepsilon}$, indicate that the rate of diffusion of species forming the clusters will increase, allowing the clusters to multiply, and the binding energy of the cluster formation decrease due to increase in thermal fluctuations. It is possible that increase in cluster formation dominates over decrease of binding energy at lower T, whereas at higher T decrease in binding energy dominates. The occurrence of serrations in a certain temperature range and inverse $\dot{\varepsilon}$ dependence indicate that deformation twins are less likely to influence the serrated flow. Apart from this, increase in deformation T also increase SFE leading to change in deformation mechanism from predominant deformation twinning to dislocation glide, could result in smooth flow behavior at high $\dot{\varepsilon}$ or T .

4.2. Strain hradening and twinning evolution

The excellent strain hardening and ductility of TWIP steel is mainly due to the combination of deformation twinning and dislocation motion in conditions of pronounced planar glide (Kim and De Cooman, 2016; Bouaziz et al., 2011). In low SFE high Mn austenitic TWIP steels, the increased partial dislocation separation results in the ease of twin nucleation. During the deformation, the grains are progressively subdivided by the twinning process, and the internal twin boundaries increase strain hardening. Although the actual twinning strain is limited and the twin formation itself may actually cause softening, the twin boundaries reduce the effective mean free path of dislocations progressively, and promote dislocation accumulation and storage, much as grain boundaries. Such dynamic Hall-Petch effect lead to high strain hardening (Bouaziz et al., 2011). De Cooman et al. claim that mechanical twinning and the related dynamic Hall-Petch associated with TWIP effect remain the only mechanisms that can explain the high strain hardening of TWIP steel. However, the role of DSA in manifesting the strain hardening rate of TWIP steels as explained in Section 4.1 cannot be neglected, but its exact contribution to flow stress is difficult to ascertain. The ab-initio based study combined with SANS experiments by Song et al. (2018) and SANS experimental study by Kang et al. (2014) proved the presence of Mn-C octahedral clusters and their evolution during deformation in high Mn steels. Wesselmecking et al. (2018) observed the occurrence of Mn-C SRO in predeformed, annealed TWIP steel and claimed that strain aging due to presence of Mn-C SRO was solely responsible for increased yield strength and pronounced yielding of bake hardened TWIP steel. The above investigations indicates that formation of Mn-C SRO and their interactions with dislocations during deformation could influence strain hardening rate in TWIP steel, which needs further detailed investigations to determine its exact contribution.

In the current study modeling of strain rate dependent hardening behavior has not been included. However, the TWIP/TRIP model presented in Wong et al. (2016); Madivala et al. (2018) can be used for predicting the change in deformation behavior at different $\dot{\varepsilon}$. The constitutive model needs to be further improved by including adiabatic heating and DSA mechanism occurring along with other deformation mechanisms (SLIP, TWIP, TRIP) to predict the negative SRS observed in TWIP steels. The results presented in this work such as stress-strain curves at different $\dot{\varepsilon}$, initiation and propagation of shear bands during deformation, distribution of local strain and temperature with strain, temperature rise due to adiabatic heating can be used for the validation of the constitutive model and simulation results.

In this study the evolution of twinning with increasing macroscopic strain is co-related with the strain hardening rate. The plot of SHR and the evolution of twinning with macroscopic strain can be seen in Fig. 13 and the EBSD measurements carried out at different strains are shown in Fig. 8. From the evolution of microstructure with deformation as shown in Fig. 8, it is evident that twins are reasonably strong obstacles to the propagation of plastic deformation. Based on the detailed work by Gutierrez-Urrutia and Raabe (2012) the SHR of fine grained X60Mn22 TWIP steel can be divided into three distinct stages of hardening: I) continuous decrease in the SHR, which involves dynamic recovery process such as cross-slip and annihilation of screw dislocations of opposite signs; II) rapid increase in the SHR, implies that refinement of the mean free path by deformation twinning occurs at strain level slightly higher than the onset of yielding; III) steady decrease in the SHR, ascribed to the reduced additional refinement of the dislocation and twin substructures, together with the increasing strengthening effect of the individual twins as obstacles to dislocation glide, reduce the capacity for trapping more dislocations leading to decrease in SHR. The different stages of hardening along with evolution of twinning can be seen in Fig. 13. Gutierrez-Urrutia and Raabe (2012) showed that deformed microstructure during stage I) consists of loose dislocation arrangements and the twin substructure evolution in stage II) is mainly influenced by the density of nucleation sites for twins per grain boundary area, which are controlled by dislocation structure formed in stage I). The homogenous distribution of dislocations in fine grained microstructure allows large number of nucleation sites for twins at grain boundary. This results in high density of twins which promotes lamellar twin structure. The formation of lamellar twin structure has led to increased strain hardening due to the smaller twin spacing. It is observed from Fig. 13 that the twin volume fraction steadily increases from 0.015 to 0.05, for a true strain of 0.2, which corresponds to stage II) of hardening involving nucleation and growth of twin lamellae. Thereafter twin volume fraction almost remains constant until failure, which can be directly correlated with stage III) of hardening where saturation of twinning occurred in the material. At a strain of about 0.2, in almost all of the grains (see Fig. 8), twins can be observed which act as obstacles to dislocation motion leading to high strain hardening. At this stage, deformation within the grains already shows large heterogeneity and a further increase in deformation can lead to the initiation of damage in the material, mainly due to large stress concentrations at the twin and grain boundary intersections. This can lead to failure at any stage of deformation.

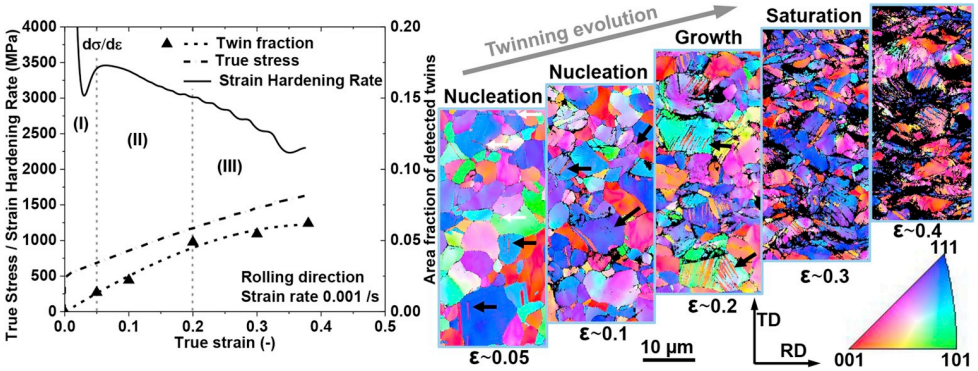

Fig. 13. Strain hardening in relation to the evolution of twinning under quasi static loading: strain hardening behavior (left) and EBSD inverse pole figure (IPF) maps with increasing macroscopic true strain (right); Annealing twins (white arrows) and mechanical twins (black arrows); pixels in black are un-indexed points.

4.3. Strain rate dependency

The measurement of temperature evolution during deformation is crucial for TWIP steel, since various temperature dependent deformation mechanisms may be activated during straining at different strain rates. During a tensile test, a portion of the applied work is converted to heat during plastic deformation of the material. High strain rate tests can have test durations in the order of milliseconds to seconds, which do not allow sufficient amount of time for heat diffusion from the interior of a sheet specimen to a free surface and subsequently transfer to surroundings. Hence adiabatic heating occurs in the material, which also depends on the sheet thickness. The larger sheet thickness lead to much higher rise of temperature. The temperature rise associated with the plastic deformation at different strain rates can have a significant softening effect on the flow stress resulting change in mechanical behavior.

The increase in T due to adiabatic heating at different strain rates at a point within the gage length for TWIP steel is shown in Fig. 14(b). It can be observed that, T increased beyond 180 °C for all tests close to fracture. However at about 30% strain the T increase is between 60 and 100 °C. The variation of SFE with temperature for chemical composition shown in Table 1 is given in Fig. 14(a). The large increase in T in the material result in increase of SFE to about 32–39 mJ/m^2 from 27 mJ/m^2. For the SFE below 40 mJ/m^2, deformation twinning is the predominant mode of deformation which occurs along with dislocation glide, thereafter dislocation slip is the predominant deformation mode. Twinning still occurs for SFE up to 60 mJ/m^2, but dislocation slip becomes the most preferred deformation mode above 40 mJ/m^2 (Madivala et al., 2018). For strain rates of 0.01, 0.5, 1 and 10/s, at about 30% strain the temperature can increase to about 60 °C from room temperature, which corresponds to SFE value of 32 mJ/m^2. This indicates that with increasing macroscopic strain the temperature rise due to adiabatic heating increases, leading to an increase in SFE preferring deformation twinning. At very high strain rates of 100 and 200/s, at about 30% strain the temperature can increase above 100 °C from room temperature, which corresponds to SFE value above 40 mJ/m^2. This large increase in SFE has led to change in prevailing deformation mode from deformation twinning to dislocation glide.

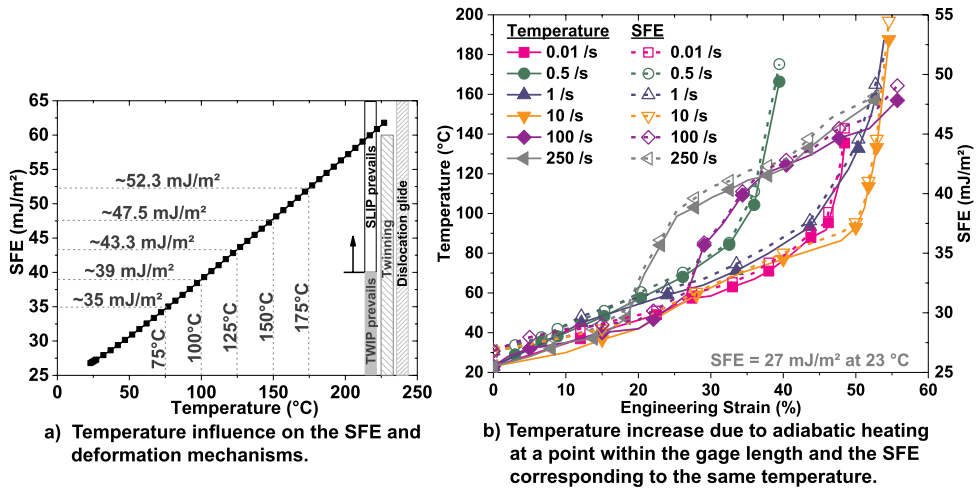

Fig. 14. Strain rate effect on adiabatic heating. Stacking fault energy (SFE) was calculated for X60Mn22 alloy using the thermodynamic approach as described in Madivala et al. (2018), assuming an interface energy ($\sigma^{\gamma/\epsilon}$) value of 10 mJ/m^2.

The strain rate effect on the work hardening behavior is shown in Fig. 5(b). It can be observed that the SHR decreases with increasing strain rate. With increasing strain rate from quasi-static to dynamic, the stage I) of hardening as explained in Section 4.2 has become wider and the initiation of stage II) has shifted to larger strains. This could be mainly attributed to the change in twin nucleation and evolution behavior. The change in deformation twinning behavior with strain rate can be seen in Fig. 9. The significant increase in Σ-3 twin boundary fraction at a strain rate of 10/s compared to 0.0001/s is mainly due to increase in SFE due to rise in temperature. It can also be seen that change in deformation rate also influenced the twin nucleation and density of twins in grains. At lower $\dot{\varepsilon}$, many thinner twin bundles can be observed within the grains compared to few thicker twin bundles at high $\dot{\varepsilon}$. The occurrence of DSA at lower $\dot{\varepsilon}$ in general result in locking of the partial dislocations leading to high dislocation density (Jung and De Cooman, 2013). The fine grain microstructure along with high density of dislocations at grain boundaries (GB) result in higher stress concentration which could assist in nucleation of twins at GB (Gwon et al., 2017). But this effect can be suppressed at high $\dot{\varepsilon}$ due to the suppression of DSA at high $\dot{\varepsilon}$. The experimental study by Yang et al. (2017) showed that number of twin nucleation sites per grain boundary area at lower $\dot{\varepsilon}$ is much larger compared to fewer twin nucleation sites at higher $\dot{\varepsilon}$. The thickness of individual twins increased from 10 nm at a $\dot{\varepsilon}$ of 0.0001/s to 40 nm at a $\dot{\varepsilon}$ of 10/s and individual twin spacing from 20 nm to 60 nm. The study also found decrease in twin area fraction with increasing $\dot{\varepsilon}$. This is mainly due to increase in average energy required for twin nucleation at high $\dot{\varepsilon}$, which led to suppressed twinning. This indicates differences in twin nucleation and growth behavior at quasi-static and dynamic loading. The synchrotron X-ray diffraction and transmission electron microscopy study by Liang et al. (2015) at low and high $\dot{\varepsilon}$ stated that the dislocations and deformation twins are suppressed at high $\dot{\varepsilon}$ deformation indicating negative strain rate sensitivity of work hardening. The detailed study by Steinmetz et al. (2013) also showed decrease of twin volume fraction with increasing rate of deformation through electron channeling contrast imaging (ECCI) measurements and crystal plasticity simulations. This change in deformation behavior could be mainly attributed to adiabatic heating associated with high $\dot{\varepsilon}$ deformation. The increase of T at $\dot{\varepsilon}$ above 1/s lead to SFE increase above 40 mJ/m^2 favoring dislocation glide above 25% strain. Hence in the stage III) of hardening, the SHR decreases more rapidly at higher $\dot{\varepsilon}$ compared to lower $\dot{\varepsilon}$. Higher T has decreased the work hardening rate by increasing the rate of dynamic recovery and the suppression of deformation twinning due to the higher SFE.

4.4. Damage and failure

High manganese TWIP steels generally exhibit ductile failure for over a wide range of temperatures and strain rates, owing to their large ductility and moderate yield strength. The activation of different deformation mechanisms such as ε-martensite, twinning and dislocation glide at various temperatures play a significant role on the fracture behavior. The fracture surface characteristics such as quasi-brittle islands along with fine dimples at low temperatures due to ε-martensite transformation, shallow dimples at moderate temperatures where DSA along with twinning occurs and larger dimples with elliptical voids at MnS inclusions at higher temperatures are the major changes due to different active deformation mechanisms (Madivala et al., 2018). Since twinning is the most dominant deformation mechanism at all quasi-static strain rates, ductile fracture with fine dimples can be commonly observed. At very high strain rates due to rise in temperature due to adiabatic heating, profuse necking and failure occurs resulting in larger dimple size (see Fig. 12). The MnS inclusions are usually elongated along RD and if the material is deformed along TD, the MnS will be subjected to tension along the minor axis as shown in Fig. 15(a). Even though MnS inclusions are deformable and ductile in nature, they have reduced toughness and ductility in TD. Thus when a material is loaded along TD, the inclusions are effective in initiating ductile cracks above a critical size range. The presence of coarser or elongated inclusions could lead to higher local stress concentrations, which cause localized rupture and micro-crack formation (see Fig. 12(a)).

The strain hardening rate ($\boldsymbol{d\sigma/d\varepsilon}$) and the $\boldsymbol{\sigma-\varepsilon}$ curves clearly indicates that failure occurs without necking for all the quasi-static strain rates whereas for dynamic tests failure occurs with necking (see Figs. 5 and 12). The serrated flow in the material due to DSA led to local plastic instability due to strain localization in the shear bands (see Fig. 10). After some deformation, shear bands nucleate and propagate from one shoulder end to the other during the entire deformation, leading to inhomogeneous deformation (see Fig. 10(c)). Since there is no prior necking before failure, there are no indications of localization of plastic strain except in the shear bands. The shear band velocity ($\mathbf{V_b}$) as a function of strain is shown in Fig. 10(c), decreases exponentially with increasing macroscopic strain. It indicates that when the band passes through the specimen, the material is strengthened and a large amount of barriers to plastic flow are generated which suppress the movement of the successive shear bands. The failure of the material occurs when the shear bands motion is retarded or when the band velocity decreases drastically approaching zero. Micro-cracks mainly initiate at the surface defects or at the edges of the tensile specimen where the intersecting shear bands are located as shown in Fig. 15(b) and propagate rapidly resulting in trans-granular ductile fracture (see Fig. 12). Experimental observations such as a flat fracture surface (see Fig. 12) on broken tensile samples and the fine dimples clearly indicate rapid nucleation of voids leading to failure (Fabrègue et al., 2013). The sudden failure in TWIP steel could be attributed due to the exponential increase of macroscopic voids during plastic deformation (Yang et al., 2017). However the interaction of various active deformation mechanisms during deformation also play a significant role in the micro-crack or voids formation in TWIP steels.

The most probable mechanisms of micro-crack formation observed in TWIP steel at micro and meso-scale is schematically described in Fig. 15. The interception of twins at GB could lead to larger stress concentration at boundaries resulting in inter-granular micro-crack formation as shown in Fig. 15(c). Numerous instances of micro-crack initiation events can be observed at GB which are $\perp$ to loading axis shared by the profusely twinned grains (see Fig. 15(c)). Triple points in the microstructure are susceptible to crack formation because each boundary shared by grains at junctions will be subjected to complex loading such as shear or tension or combination of both. There are also many instances of microstructure where a GB is shared by grains which deform by twinning and other by slip. The interception of slip band extrusions and the twins at GB result in incompatible deformation at GB which could lead

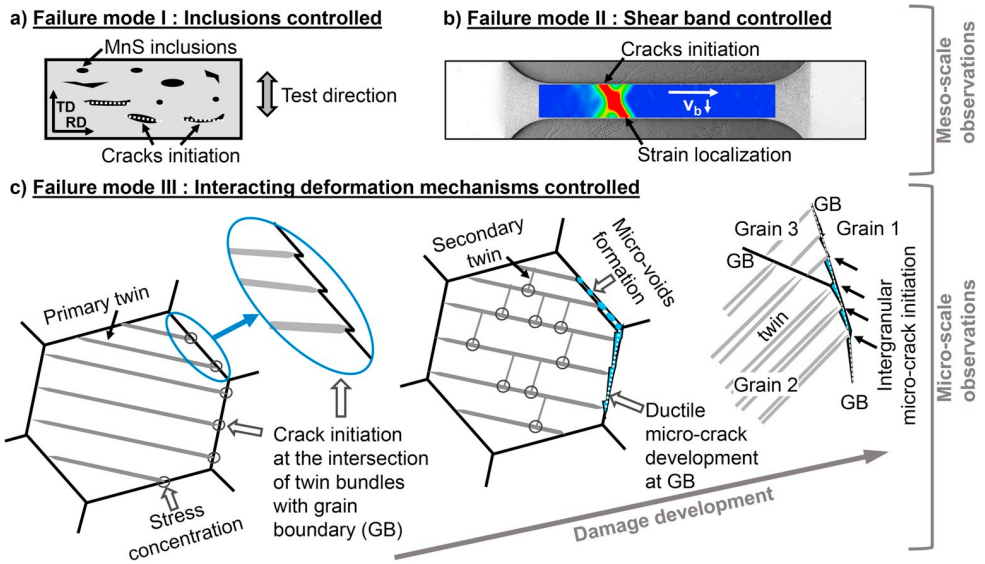

Fig. 15. Schematic description of micro-cracking mechanism in TWIP steels: a) Micro-crack formation at MnS inclusions, b) Crack initiation at shear bands, c) Stress concentration caused by the intercepting primary twins at grain boundaries (GB) and the secondary twins at primary twin boundaries, micro-voids formation at the interception of deformation twins and the slip band extrusions at GB leading to crack initiation, inter-granular micro-crack initiation at the GB due to large stress concentration caused by intercepting twins and slip band extrusions.

to micro-crack formation. The stress concentration at a) twin-grain impingement and b) intersection of slip band extrusions at GB could possibly nucleate cracking in the grain boundary. However, twin-grain impingement may not be the possible case since strain compatibility requirement at GB are rather easy to satisfy because of availability of large number of slip and twin systems (Rémy, 1981). The possible exceptions could be observed i) when either the slip or twinning systems cannot be easily activated or due to blocked slip transfer of dislocations (Knorr et al., 2015) and ii) when a cohesion margin of the boundary is reduced by the segregation of the impurities or grain boundary precipitation. However, besides the twin-grain boundary impingement, the twin boundaries can constitute nucleation sites or path for cracking (Zhang et al., 2012). Rémy stated that high stress concentrations can occur at GBs which are not all completely relieved and numerous dislocation debris resulting from interaction with matrix dislocations or eventually barriers exist in these boundaries. The predominant inter-granular fracture in tension shown in Fig. 11 suggests that it could be a problem of cohesion margin of the boundaries. Even if precipitates are not actually present in the boundaries, segregation should have occur during high temperature annealing treatment (Heo and Lee, 2011). Herbig et al. (2015) reported segregation of B, C, Si and P and traces of Cu at grain boundary in cold rolled, annealed and water quenched Fe-Mn-C TWIP steel investigated using atom probe tomography. It was also stated that neither Mn enrichment or depletion was detected at GB. An increase of C content at GB could lead to increase in local SFE values, resulting in increase of critical stress for twin formation. Thus inter-granular cracking should result while the yield strength for annealed TWIP alloy is considerably increased by high interstitial content. Grain boundary cracking thus occurs as relieving the stress concentration when a twin band impinges a grain boundary. Segregation of phosphorous at GB could lead to GB embrittlement, which could also have resulted in intergranular crack formation in TWIP steels. Thus it is supposed that the homogenous deformation of the grains by slip or twinning could not give rise to stress concentrations at grain boundaries. The relative ease of twin nucleation is supposed to relieve stress concentrations at twin impingement on grain boundaries instead of grain boundary cracking.

5. Conclusions

The X60Mn22 TWIP steel was investigated by uni-axial tensile tests under both quasi-static and dynamic conditions. For investigating the anisotropy and strain rate effects on the mechanical properties and failure behavior, various in-situ tensile testing methods were applied. The local strain evolution during deformation was monitored by carrying tests in conjunction with digital image correlation and synchronous temperature measurements using thermocamera. Interrupted tensile tests were carried out in SEM along with EBSD measurements to study the microstructure evolution and micro-cracks development. The main conclusions can be drawn for the investigated TWIP steel as follows:

- Strain hardening rate of TWIP steel is extraordinarily high under both quasi-static and dynamic tests until maximum strain/failure. It can be attributed to the deformation by dislocation glide in combination with deformation twinning. Twining is the most predominant deformation mechanism occurred along with dislocation slip under all quasi-static tests, where multiple number of thinner twin bundles within a grain was observed compared to less number of thicker twin bundles under dynamic loading. Temperature rise due to adiabatic heating led to increase in SFE, thereby resulting in a change of twinning behavior or

the promotion of dislocation glide under dynamic loading.

- The material showed similar local deformation behavior along rolling, transverse and shear (45°) directions, but slightly different mechanical properties due to the presence of inclusions. Strain rate has negligible effect on the yield and tensile strength, whereas uniform and total elongation decreased under dynamic loading. Total energy absorption capacity of TWIP steel is above 55 kJ/kg at all strain rates which is almost the double that of dual phase steel DP1000 and is slightly lower compared to austenitic stainless steels 1.4301 and 1.4318.
- Micro-cracks are observed at elongated MnS inclusions or at isolated grain boundaries at relatively small strain of ~2/3 of total strain. However, these micro-cracks showed no tendency to grow. Large heterogeneous deformation within the grains by twinning or dislocation glide has led to high stress concentration at grain boundaries (GB) due to the interception of deformation twins and slip band extrusions at GB. Hence micro-cracks in TWIP steel originated mainly at grain boundaries and triple junctions.
- Inhomogeneous flow behavior caused due to the nucleation and propagation of shear bands during deformation is mainly due to dynamic strain aging and Mn-C short range ordering. These phenomenon led to large strain localization within the shear bands and also non uniform distribution of local plastic strain in the regions behind and ahead of shear bands. The velocity of shear band motion decreased with increasing macroscopic strain due to the intersection of two shear bands. This led to local strain accumulation within the intersecting shear bands resulting in a macroscopic crack initiation close to edges of tensile specimen by the coalescence of various micro-cracks that has been previously formed at the intersection of twin bundles with GB.
- Ductile failure mode is the most predominant mode of failure in TWIP steel, mainly characterized by the formation of very fine dimples with a crack propagation along GB at all strain rates with an exception of slightly larger dimples under dynamic loading. TWIP steel showed high tendency for adiabatic heating at strain rates above 0.5/s. This changed the failure behavior from abrupt failure at shear bands without macroscopic necking to classical strain localization by pronounced necking showing larger dimples.

Acknowledgments

The authors would like to acknowledge the financial support of the German Research Foundation (DFG) within the Collaborative Research Center SFB 761 “Steel-ab initio”. The authors thank ThyssenKrupp Steel Europe AG for the material supply.

Appendix A. Supplementary data

Supplementary data to this article can be found online at https://doi.org/10.1016/j.ijplas.2018.11.015.

References

Allain, S., Cugy, P., Scott, C., Chateau, J.P., Rusinek, A., Deschamps, A., 2008. The influence of plastic instabilities on the mechanical properties of a high-manganese austenitic femnc steel. Int. J. Mater. Res. 99 (7), 734–738. https://doi.org/10.3139/146.101693.

Benzing, J.T., Poling, W.A., Pierce, D.T., Bentley, J., Findley, K.O., Raabe, D., Wittig, J.E., 2018. Effects of strain rate on mechanical properties and deformation behavior of an austenitic fe-25mn-3al-3si twip-trip steel. Mater. Sci. Eng. A 711, 78–92. https://doi.org/10.1016/j.msea.2017.11.017.

Bian, X., Yuan, F., Wu, X., 2017. Correlation between strain rate sensitivity and characteristics of portevin-lechátelier bands in a twinning-induced plasticity steel. Mater. Sci. Eng. A 696, 220–227. https://doi.org/10.1016/j.msea.2017.04.078.

Bleck, W., Schael, I., 2000. Determination of crash relevant material parameters by dynamic tensile tests. Steel Res. 71 (5), 173–178. https://doi.org/10.1002/srin.200005709.

Bouaziz, O., Allain, S., Scott, C., Cugy, P., Barbier, D., 2011. High manganese austenitic twinning induced plasticity steels: a review of the microstructure properties relationships. Curr. Opin. Solid State Mater. Sci. 15 (4), 141–168. https://doi.org/10.1016/j.cossms.2011.04.002.

Chen, L., Kim, H.S., Kim, S.K., De Cooman, B.C., 2007. Localized deformation due to portevin–lechatelier effect in 18mn–0.6c twip austenitic steel. ISIJ Int. 47 (12), 1804–1812. https://doi.org/10.2355/isijinternational.47.1804.

Curtze, S., Kuokkala, V.T., 2010. Dependence of tensile deformation behavior of twip steels on stacking fault energy, temperature and strain rate. Acta Mater. 58 (15), 5129–5141. https://doi.org/10.1016/j.actamat.2010.05.049.

Dastur, Y.N., Leslie, W.C., 1981. Mechanism of work hardening in hadfield manganese steel. Metall. Trans. A 12 (5), 749–759. https://doi.org/10.1007/BF02648339.

De Cooman, B.C., Estrin, Y., Kim, S.K., 2018. Twinning-induced plasticity (twip) steels. Acta Mater. 142, 283–362. https://doi.org/10.1016/j.actamat.2017.06.046.

Fabrègue, D., Landron, C., Bouaziz, O., Maire, E., 2013. Damage evolution in twip and standard austenitic steel by means of 3d x ray tomography. Mater. Sci. Eng. A 579, 92–98. https://doi.org/10.1016/j.msea.2013.05.013.

Gopinath, K., Gogia, A.K., Kamat, S.V., Ramamurty, U., 2009. Dynamic strain ageing in Ni-base superalloy 720Li. Acta Mater. 57 (4), 1243–1253. https://doi.org/10.1016/j.actamat.2008.11.005.

Grässel, O., Krüger, L., Frommeyer, G., Meyer, L., 2000. High strength fe–mn–(al, si) trip/twip steels development–properties–application. Int. J. Plast. 16 (10–11), 1391–1409. https://doi.org/10.1016/S0749-6419(00)00015-2.

Gutierrez-Urrutia, I., Raabe, D., 2012. Grain size effect on strain hardening in twinning-induced plasticity steels. Scripta Mater. 66 (12), 992–996. https://doi.org/10.1016/j.scriptamat.2012.01.037.

Gwon, H., Kim, J.K., Shin, S., Cho, L., De Cooman, B.C., 2017. The effect of vanadium micro-alloying on the microstructure and the tensile behavior of twip steel. Mater. Sci. Eng. A 696, 416–428. https://doi.org/10.1016/j.msea.2017.04.083.

Heo, N.H., Lee, J.K., 2011. Grain boundary segregation of phosphorus and intergranular surface cracking accompanied by decarburization in plain carbon steels. ISIJ Int. 51 (4), 673–678. https://doi.org/10.2355/isijinternational.51.673.

Herbig, M., Kuzmina, M., Haase, C., Marceau, R., Gutierrez-Urrutia, I., Haley, D., Molodov, D.A., Choi, P., Raabe, D., 2015. Grain boundary segregation in Fe–Mn–C twinning-induced plasticity steels studied by correlative electron backscatter diffraction and atom probe tomography. Acta Mater. 83, 37–47. https://doi.org/10.1016/j.actamat.2014.09.041.

Idrissi, H., Ryelandt, L., Veron, M., Schryvers, D., Jacques, P., 2009. Is there a relationship between the stacking fault character and the activated mode of plasticity of Fe–Mn-based austenitic steels? Scripta Mater. 60 (11), 941–944. https://doi.org/10.1016/j.scriptamat.2009.01.040.

Jung, I.C., De Cooman, B.C., 2013. Temperature dependence of the flow stress of fe–18mn–0.6c–xal twinning-induced plasticity steel. Acta Mater. 61 (18), 6724–6735. https://doi.org/10.1007/s12540-014-1008-y.

Kang, M., Shin, E., Woo, W., Lee, Y.K., 2014. Small-angle neutron scattering analysis of mn–c clusters in high-manganese 18mn–0.6c steel. Mater. Char. 96, 40–45. https://doi.org/10.1016/j.matchar.2014.07.010.

Kang, M., Park, J., Sohn, S.S., Kim, H.S., Kim, N.J., Lee, S., 2017. Interpretation of quasi-static and dynamic tensile behavior by digital image correlation technique in twinning induced plasticity (twip) and low-carbon steel sheets. Mater. Sci. Eng. A 693, 170–177. https://doi.org/10.1016/j.msea.2017.03.076.
Kim, J.K., De Cooman, B.C., 2016. Stacking fault energy and deformation mechanisms in fe-xmn-0.6c-yal twip steel. Mater. Sci. Eng. A 676, 216–231. https://doi.org/10.1016/j.msea.2016.08.106.
Kim, J.K., Kwon, M.H., De Cooman, B.C., 2017. On the deformation twinning mechanisms in twinning-induced plasticity steel. Acta Mater. 141, 444–455. https://doi.org/10.1016/j.actamat.2017.09.043.
Knorr, A.F., Marx, M., Schaefer, F., 2015. Crack initiation at twin boundaries due to slip system mismatch. Scripta Mater. 94, 48–51. https://doi.org/10.1016/j.scriptamat.2014.09.015.
Koyama, M., Sawaguchi, T., Tsuzaki, K., 2013. TWIP effect and plastic instability condition in an Fe-Mn-C austenitic steel. ISIJ Int. 53 (2), 323–329. https://doi.org/10.2355/isijinternational.53.323.
Lan, P., Zhang, J., 2018. Serrated flow and dynamic strain aging in Fe-Mn-C TWIP steel. Metall. Mater. Trans. A 49 (1), 147–161. https://doi.org/10.1007/s11661-017-4421-2.
Lee, S.J., Kim, J., Kane, S.N., De Cooman, B.C., 2011. On the origin of dynamic strain aging in twinning-induced plasticity steels. Acta Mater. 59 (17), 6809–6819. https://doi.org/10.1016/j.actamat.2011.07.040.
Lee, S.J., Han, J., Lee, S., Kang, S.H., Lee, S.M., Lee, Y.K., 2017. Design for fe-high mn alloy with an improved combination of strength and ductility. Sci. Rep. 7 (1), 3573. https://doi.org/10.1038/s41598-017-03862-y.
Lee, S.Y., Lee, S.I., Hwang, B., 2018. Effect of strain rate on tensile and serration behaviors of an austenitic fe-22mn-0.7c twinning-induced plasticity steel. Mater. Sci. Eng. A 711, 22–28. https://doi.org/10.1016/j.msea.2017.10.074.
Liang, Z.Y., Wang, X., Huang, W., Huang, M.X., 2015. Strain rate sensitivity and evolution of dislocations and twins in a twinning-induced plasticity steel. Acta Mater. 88, 170–179. https://doi.org/10.1016/j.actamat.2015.01.013.
Lorthios, J., Nguyen, F., Gourgues, A.F., Morgeneyer, T.F., Cugy, P., 2010. Damage observation in a high-manganese austenitic TWIP steel by synchrotron radiation computed tomography. Scripta Mater. 63 (12), 1220–1223. https://doi.org/10.1016/j.scriptamat.2010.08.042.
Madivala, M., Schwedt, A., Wong, S.L., Roters, F., Prahl, U., Bleck, W., 2018. Temperature dependent strain hardening and fracture behavior of TWIP steel. Int. J. Plast. https://doi.org/10.1016/j.ijplas.2018.02.001.
Mosecker, L., Pierce, D.T., Schwedt, A., Beighmohamadi, M., Mayer, J., Bleck, W., Wittig, J.E., 2015. Temperature effect on deformation mechanisms and mechanical properties of a high manganese c + n alloyed austenitic stainless steel. Mater. Sci. Eng. A 642, 71–83. https://doi.org/10.1016/j.msea.2015.06.047.
Park, J., Kang, M., Sohn, S.S., Kim, S.H., Kim, H.S., Kim, N.J., Lee, S., 2017. Quasi-static and dynamic deformation mechanisms interpreted by microstructural evolution in twinning induced plasticity (twip) steel. Mater. Sci. Eng. A 684, 54–63. https://doi.org/10.1016/j.msea.2016.12.037.
Pierce, D.T., Jiménez, J.A., Bentley, J., Raabe, D., Wittig, J.E., 2015. The influence of stacking fault energy on the microstructural and strain-hardening evolution of fe–mn–al–si steels during tensile deformation. Acta Mater. 100, 178–190. https://doi.org/10.1016/j.actamat.2015.08.030.
Rahman, K.M., Vorontsov, V.A., Dye, D., 2014. The dynamic behaviour of a twinning induced plasticity steel. Mater. Sci. Eng. A 589, 252–261. https://doi.org/10.1016/j.msea.2013.09.081.
Rémy, L., 1981. The interaction between slip and twinning systems and the influence of twinning on the mechanical behavior of fcc metals and alloys. Metall. Trans. A 12 (3), 387–408. https://doi.org/10.1007/BF02648536.
Renard, K., Jacques, P.J., 2012. On the relationship between work hardening and twinning rate in TWIP steels. Mater. Sci. Eng. A 542, 8–14. https://doi.org/10.1016/j.msea.2012.01.123.
Saeed-Akbari, A., Mosecker, L., Schwedt, A., Bleck, W., 2012. Characterization and prediction of flow behavior in high-manganese twinning induced plasticity steels: Part i. mechanism maps and work-hardening behavior. Metall. Mater. Trans. A 43 (5), 1688–1704. https://doi.org/10.1007/s11661-011-0993-4.
Seol, J., Kim, J., Na, S., Park, C., Kim, H., 2017. Deformation rate controls atomic-scale dynamic strain aging and phase transformation in high mn trip steels. Acta Mater. 131, 187–196. https://doi.org/10.1016/j.actamat.2017.03.076.
Shen, Y.F., Jia, N., Misra, R., Zuo, L., 2016. Softening behavior by excessive twinning and adiabatic heating at high strain rate in a fe–20mn–0.6c twip steel. Acta Mater. 103, 229–242. https://doi.org/10.1016/j.actamat.2015.09.061.
Song, W., Houston, J., 2018. Local deformation and mn-c short-range ordering in a high-mn fe-18mn-0.6c steel. Metals 8 (5), 292. https://doi.org/10.3390/met8050292.
Song, W., Bogdanovski, D., Yildiz, A., Houston, J., Dronskowski, R., Bleck, W., 2018. On the Mn–C short-range ordering in a high-strength high-ductility steel: small angle neutron scattering and ab initio investigation. Metals 8 (1), 44. https://doi.org/10.3390/met8010044.
Steinmetz, D.R., Jäpel, T., Wietbrock, B., Eisenlohr, P., Gutierrez-Urrutia, I., Saeed-Akbari, A., Hickel, T., Roters, F., Raabe, D., 2013. Revealing the strain-hardening behavior of twinning-induced plasticity steels: theory, simulations, experiments. Acta Mater. 61 (2), 494–510. https://doi.org/10.1016/j.actamat.2012.09.064.
Wesselmecking, S., Song, W., Ma, Y., Roesler, T., Hofmann, H., Bleck, W., 2018. Strain aging behavior of an austenitic high-Mn steel. Steel Res. Int. 88, 1700515. https://doi.org/10.1002/srin.201700515.
Wong, S.L., Madivala, M., Prahl, U., Roters, F., Raabe, D., 2016. A crystal plasticity model for twinning- and transformation-induced plasticity. Acta Mater. 118, 140–151. https://doi.org/10.1016/j.actamat.2016.07.032.
Yang, C.L., Zhang, Z.J., Zhang, P., Zhang, Z.F., 2017. The premature necking of twinning-induced plasticity steels. Acta Mater. 136, 1–10. https://doi.org/10.1016/j.actamat.2017.06.042.
Yu, H.Y., Lee, S.M., Nam, J.H., Lee, S.J., Fabrègue, D., Park, Mh, Tsuji, N., Lee, Y.K., 2017. Post-uniform elongation and tensile fracture mechanisms of fe-18mn-0.6c-xal twinning-induced plasticity steels. Acta Mater. 131, 435–444 0.1016/j.actamat.2017.04.011.
Zavattieri, P.D., Savic Jr., V., LGH Fekete, J.R., Tong, W., Xuan, Y., 2009. Spatio-temporal characteristics of the portevin–le châtelier effect in austenitic steel with twinning induced plasticity. Int. J. Plast. 25 (12), 2298–2330. https://doi.org/10.1016/j.ijplas.2009.02.008.
Zhang, Z.J., Zhang, P., Li, L.L., Zhang, Z.F., 2012. Fatigue cracking at twin boundaries: effects of crystallographic orientation and stacking fault energy. Acta Mater. 60 (6–7), 3113–3127. https://doi.org/10.1016/j.actamat.2012.02.016.

3.3 Research Paper 3

Title:Strain hardening, damage and fracture behavior of Al added high Mn TWIP Steels

Manjunatha Madivala, Alexander Schwedt, Ulrich Prahl, and Wolfgang Bleck. Strain hardening, damage and fracture behavior of al added high mn twip steels. *Metals*, 8(12), 2019. ISSN 2075-4701. doi: 10.3390/met8121014. URL http://www.mdpi.com/2075-4701/8/12/1014
© 2018 MDPI. Reprinted with permission. The original publication is available at Metals–Open Access Journal.

Highlights:

- The strain hardening and damage behavior of Al-added TWIP steels.
- The evolution of microstructure, deformation mechanisms and micro-cracks development with increasing deformation.
- Local strain distribution and its evolution during deformation.
- Adiabatic heating and its effect on deformation mechanisms.
- Mechanism of micro-crack formation in X60MnAl17-1 and X30MnAl23-1 TWIP steels.

metals

MDPI

Article

Strain Hardening, Damage and Fracture Behavior of Al-Added High Mn TWIP Steels

Manjunatha Madivala [1,*], Alexander Schwedt [2], Ulrich Prahl [3] and Wolfgang Bleck [1]

1 Steel Institute (IEHK), RWTH Aachen University, Intzestraße 1, 52072 Aachen, Germany; bleck@iehk.rwth-aachen.de
2 Central Facility for Electron Microscopy (GFE), RWTH Aachen University, Ahornstraße 55, 52074 Aachen, Germany; schwedt@gfe.rwth-aachen.de
3 Institute of Metal Forming (imf), TU Bergakademie Freiberg, Bernhard-von-Cotta-Straße 4, 09599 Freiberg, Germany; Ulrich.Prahl@imf.tu-freiberg.de
* Correspondence: manjunatha.madivala@iehk.rwth-aachen.de; Tel.: +49-241-80-90137

Received: 15 February 2019; Accepted: 19 March 2019; Published: 21 March 2019

Abstract: The strain hardening and damage behavior of Al-added twinning induced plasticity (TWIP) steels were investigated. The study was focused on comparing two different alloying concepts by varying C and Mn contents with stacking fault energy (SFE) values of 24 mJ/m^2 and 29 mJ/m^2. The evolution of microstructure, deformation mechanisms and micro-cracks development with increasing deformation was analyzed. Al-addition has led to the decrease of C diffusivity and reduction in tendency for Mn-C short-range ordering resulting in the suppression of serrated flow caused due to dynamic strain aging (DSA) in an alloy with 0.3 wt.% C at room temperature and quasi-static testing, while DSA was delayed in an alloy with 0.6 wt.% C. However, an alloy with 0.6 wt.% C showing DSA effect exhibited enhanced strain hardening and ductility compared to an alloy with 0.3 wt.% C without DSA effect. Twinning was identified as the most predominant deformation mode in both the alloys, which occurred along with dislocation glide. Al-addition has increased SFE thereby delaying the nucleation of deformation twins and prolonged saturation of twinning, which resulted in micro-cracks initiation only just prior to necking or failure. The increased stress concentration caused by the interception of deformation twins or slip bands at grain boundaries (GB) has led to the development of micro-cracks mainly at GB and triple junctions. Deformation twins and slip bands played a vital role in assisting inter-granular crack initiation and propagation. Micro-cracks that developed at manganese sulfide and aluminum nitride inclusions showed no tendency for growth even after large deformation indicating the minimal detrimental effect on the tensile properties.

Keywords: TWIP steel; deformation twinning; serrated flow; dynamic strain aging; damage; fracture

1. Introduction

Through many years of development and application, advanced high strength steels (AHSS), aluminum, magnesium and titanium alloys have proved themselves to be versatile and effective materials for automotive parts [1–6]. However, the demand for safety and cost-effectiveness of the components have raised enormously [7]. Thus it is necessary to develop new materials focusing on the special requirements. Through careful control of chemistry and processing, materials can be tailored to provide optimum performance, keeping an aim on specific applications. By choosing different alloying elements and careful processing, the required microstructural constituents with unique mechanical behavior can be obtained resulting in many types of materials for automotive applications [8]. Thus variations in chemistry, microstructure, and deformation mechanisms are crucial aspects in the design and performance of metallic materials. The current work reveals the

mechanical behavior of the Al-added high Mn twinning induced plasticity (TWIP) steels designed for safety-relevant automotive parts and other applications.

TWIP steels exhibit extraordinary mechanical properties such as exceptional strength (>1000 MPa), high ductility (>50%) and excellent energy absorption capacity (>55 kJ/kg) making them highly suitable for automotive applications [9–15]. The sustained and high strain hardening rate (SHR) of TWIP steels can be ascribed to their deformation mechanisms such as dislocation glide, deformation twinning, and ε-martensite transformation. The materials behavior strongly dependent on their chemical composition, microstructure and deformation conditions [15–19]. The unique characteristic behavior of these steels is the nucleation and propagation of deformation bands during deformation, which results in serrations on the σ–ε curves, known as Portevin-Le Chatelier (PLC) effect [20–22]. The serrations in TWIP steels are classified as Type A, depending on their morphology. They are known as locking serrations because of repeated locking and unlocking of dislocations by solute atoms commonly known as dynamic strain aging (DSA) [16,22–24]. It was stated that DSA effectively modified the SHR but its influence on the SHR is limited due to the lower activation energy attained in these steels [21]. Many authors stated that mechanical twinning and its associated dynamic Hall-Petch effect remain the only mechanisms that can be responsible for sustained and high SHR of TWIP steels [10,13,21,25]. However, the influence of DSA on the deformation behavior and its role in manifesting the SHR cannot be ignored. Thus in this study, an alloy showing DSA effect is compared with an alloy without DSA effect. The SHRs of the alloys were correlated to the evolution of twin volume fraction (TVF) with increasing deformation.

The appearance of serrations on the σ–ε curves requires the material to be plastically deformed to a certain deformation known as critical strain (ε_c). A detailed study on the X60Mn22 alloy revealed repeated serrations on the σ–ε curves at different strain rates and temperatures. With an increase in temperature or grain size, the ε_c for the initiation of serrations decreased and with the increase of strain rate ($\dot{\varepsilon}$), the ε_c increased [14,19]. In Fe-Mn-C alloys, it was shown that with the increase in C content from 0.0 wt.% to 1.1 wt.% C, the ε_c for triggering serrations has decreased [26]. A comparative study on Fe-Mn-C-x alloys with and without Al showed that with Al-addition the ε_c has increased [27]. It was also shown that with increasing Al content from 0.0 to 3.0 wt.%, the initiation of serrated flow shifted to higher strains or completely suppressed [28]. A similar study also revealed severe serrated flow in an X60Mn22 alloy at different $\dot{\varepsilon}$, whereas in an X60MnAl22-1.5 alloy serrations appeared only at quasi-static $\dot{\varepsilon}$ and the initiation of serrations shifted to high strains [29]. It was shown in X60MnAl18-x alloys with 0.0, 1.5 and 2.5 wt.% Al contents, that severe serrated flow also occurred in Al-containing alloys at elevated temperatures [16]. Thus, it can be clearly understood that ε_c for the initiation of the serrations in Fe-Mn-C-Al alloys is mainly influenced by stacking fault energy (SFE), the alloying elements such as C and Al, deformation temperature, $\dot{\varepsilon}$ and microstructure of the material. From the experimental observations in the literature, it can be stated that in the alloys of Fe-Mn-C and Fe-Mn-C-Al with different chemical compositions the serrated σ–ε behavior can be observed but the range of temperature, $\dot{\varepsilon}$ regimes, microstructure states and the strain ε_c at which serrations appears could be different. In the current study, an X60MnAl17-1 and X30MnAl23-1 alloys were investigated in detail to study the influence of alloying elements such as C and Al on the serrated flow behavior.

Macroscopic observations revealed an abrupt failure in TWIP steels without any strain localization or necking, which occurred at the intersection of two deformation bands close to the specimen edges. It was claimed that the increased stress concentration caused by the intercepting deformation twins and the slip band extrusions at grain boundary (GB) has led to micro-crack formation. Inter-granular micro-crack initiation and propagation events were observed in the microstructure at GBs and triple junctions along with the rapid nucleation of minute voids [14]. A similar study also showed micro-cracks at the intersection of deformation bands mainly at the edge and side surfaces of the tensile specimen. The cracks were observed at GB junctions and the mechanical twin boundaries [30]. It was claimed that the exponential increase of the macroscopic void volume fraction led to the sudden failure or decrease of SHR in TWIP steels [31]. A detailed study on the evolution of damage in TWIP

steel by 3D X-ray tomography experiments has shown that the average void diameter and the stress triaxiality remained constant throughout the deformation until failure. It was claimed that the damage development process involved rapid nucleation of minute voids combined with substantial growth of the largest voids [32]. The distribution of tiny voids with few elongated cavities close to the fracture surface in shear tests clearly indicated localized failure [33]. The above-mentioned studies were on TWIP steels showing DSA effect, where an abrupt failure occurred in the material. However, the addition of Al not only increases ductility but also changes the local deformation and fracture behavior. Thus in this study damage and failure behavior of Al-added TWIP steels were investigated both at the micro- and macro-scale. The current work focuses on the relationship between the deformation mechanisms and the mechanism of micro-crack formation.

In the current study, the strain hardening, damage and fracture behavior of Al-added TWIP steels with different chemical compositions were investigated. To ascertain the role of the interstitial C atoms on the interaction between Mn-C short-range ordering (SRO) and dislocations in causing DSA phenomena, two alloys with different C contents were studied. By analyzing the local plastic strain (ε_{local}) evolution, the serrated flow behavior caused due to the nucleation and propagation of deformation bands and their subsequent influence on the failure initiation during the deformation was investigated. The measurement of a rise in temperature during deformation aided in the accurate estimation of SFE, which enabled the prediction of change in deformation mechanisms. The evaluated TVF and the predicted SFE was used to explain the SHR, the mechanical behavior of alloys. The evolution of microstructure, the mechanism of micro-crack initiation and their development with increasing strain were studied in detail. The influence of non-metallic inclusions on the mechanical properties and micro-crack formation was also investigated.

2. Materials and Experimental Methods

The materials investigated in this study are Al-added high Mn TWIP steels produced in the laboratory, designated as X60MnAl17-1 and X30MnAl23-1. The electron backscatter diffraction (EBSD) technique was used to characterize the initial microstructure such as the grain size and the evolution of twinning with increasing strain. The optical and field-emission scanning electron microscope (SEM) with energy dispersive X-ray spectroscopy (EDS/EDX) was used to qualitatively and quantitatively analyze the inclusions type, size, and distribution. Interrupted micro-tensile tests were carried out in SEM to study the evolution of microstructure and micro-cracks development during deformation. Tensile tests were carried out in conjunction with the digital image correlation (DIC) to investigate the macroscopic material behavior. An infrared thermography camera along with video extensometer was used to measure the temperature rise due to adiabatic heating (AH) during deformation. The elastic properties of the material were determined by the ultrasonic method. The fracture behavior of the macroscopic tensile specimens was analyzed in the SEM.

2.1. Materials Processing

The materials were produced by ingot-casting using a vacuum induction furnace. The cast ingots (each ∼30 kg) were homogenized in a muffle furnace at 1150 °C for 5 h, in order to reduce the segregation of alloying elements, especially Mn. The homogenized ingots (140 mm in height) were then forged at 1150 °C to a height of 55 mm, followed by another homogenization and then hot rolled at 1150 °C to a sheet thickness of 2.8 mm. The hot rolled sheets were cold-rolled to 50% reduction to get a final sheet thickness of 1.4 mm. Finally, annealing heat treatment was carried out in a salt bath furnace at 900 °C for 20 min, followed by quenching in water to obtain a completely recrystallized microstructure. The major differences in alloy compositions are C and Mn contents. The alloy X60MnAl17-1 has 0.6 wt.% C, 17.17 wt.% Mn, whereas alloy X30MnAl23-1 has 0.3 wt.% C, 22.43 wt.% Mn. The chemical compositions and SFE values of the alloys are presented in Table 1. The chemical composition was determined using optical emission spectroscopy. The Mn content from 0.001 to 20 wt.% with an accuracy of ±0.05, C from 0.001 to 1.2 wt.% with an accuracy of ±0.01

and Al from 0.001 to 2 wt.% with an accuracy ±0.01 can be determined. The Mn content above 20 wt.% is verified by melt extraction analysis. The SFE was calculated using the sub-regular solution thermodynamic model of Saeed-Akbari et al. [11]. The interface energy ($\sigma^{\gamma/\varepsilon}$) value of 10 mJ/m^2 as recommended in [11,34] was used for calculating the SFE. The model is implemented as a MATLAB® program to evaluate the SFE as explained in [19]. Based on their chemical composition, the evaluated SFE value of X60MnAl17-1 and X30MnAl23-1 are 29 and 24 mJ/m^2 respectively.

Table 1. Chemical compositions (in wt.%) and the stacking fault energy (SFE) values (in mJ/m^2) of the investigated alloys.

Alloy	C	Si	Mn	P	S	Cr	Ni	Cu	Al	V	N	Fe	SFE
X60MnAl17-1	0.60	0.06	17.17	<0.009	<0.006	0.05	0.04	0.03	1.50	0.07	0.015	Bal.	29
X30MnAl23-1	0.30	0.04	22.43	<0.009	<0.005	0.05	0.04	0.02	1.39	0.10	0.013	Bal.	24

2.2. Microstructure Characterization

2.2.1. Micro-Tensile Tests

The un-deformed and deformed microstructures were analyzed by using EBSD on the RD-TD plane (RD/TD: rolling/transverse direction). The micro-tensile test specimens with a gauge length of 2 mm, a width of 1 mm and having a thickness of 1.4 mm as shown in Figure 1 were obtained by wire erosion cutting from the cold-rolled and annealed sheet. The samples were initially mechanically ground and then polished up to 1 µm using diamond suspension. They were further electro-polished by applying a voltage potential of 35 V for 15 s using an electrolyte consisting of 95% acetic acid and 5% perchloric acid. A field-emission JEOL JSM-7000F SEM equipped with an EDAX-TSL Hikari detector operating at a voltage of 20 kV and a probe current of about 20–30 nA was used for the measurements. The data was analyzed using TSL OIM® Analysis 7 software. A step size of 100 nm was chosen for the measurements and all the scanned points with a confidence index (CI) value of below 0.1 were not considered for the analysis. The measurements were carried out in the middle of the sample as shown in Figure 1c and at a true strain of 0.0, 0.1, 0.2, 0.3, 0.4 and $\varepsilon_{necking}$. The procedure used for processing EBSD data to identify the grains and twins is described in [14,19]. The TVF was evaluated based on the relative fraction of the pixel areas of Σ-3 twins to the measurement areas at different macroscopic strains [19].

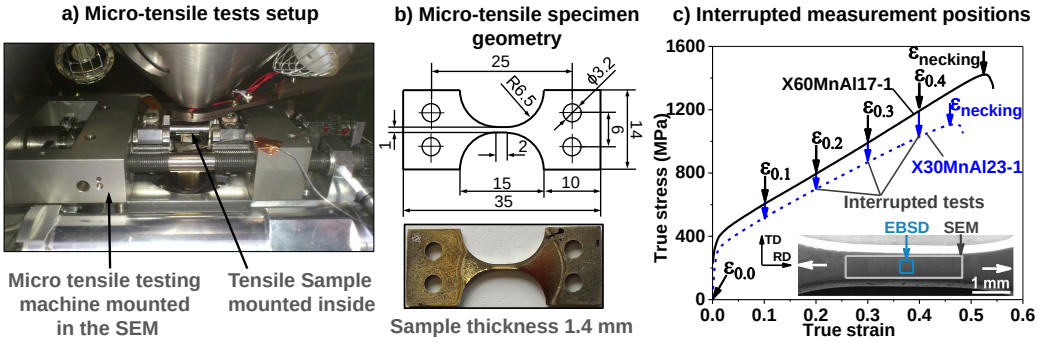

Figure 1. In-situ micro-tensile tests in conjunction with scanning electron microscope (SEM) and electron backscatter diffraction (EBSD) : (**a**) test setup, (**b**) specimen geometry, (**c**) true stress-strain curves obtained for X60MnAl17-1 and X30MnAl23-1; tests were carried out with a crosshead displacement rate of 0.2 mm/min, which corresponds to a quasi-static $\dot{\varepsilon}$ of about 0.001 s^{-1} and interrupted at different strains as pointed to observe the microstructure and micro-crack development; EBSD measurement area and the region of SEM investigations on the micro-tensile specimen is shown; white arrows indicate tensile loading direction.

The micro-tensile tests were carried out in a field emission SEM to investigate the mechanisms of micro-crack formation. The tests were interrupted at different strains to observe the micro-crack initiation and their development as shown in Figure 1. The tests were performed at room temperature (RT) and by applying a crosshead displacement rate of 0.2 mm/min which corresponds to a quasi-static $\dot{\varepsilon}$ of 0.001 s^{-1} using an in-situ micro-tensile testing device mounted in the SEM. The macroscopic fractured samples were also analyzed in SEM to study the failure behavior of the alloys. To observe the changes in dimple size and morphology at the inclusions several SEM images were taken at different locations. The average dimple size was determined by image processing as explained in [19].

2.2.2. Inclusions and Fracture Surface Analysis

The specimens of size 20 × 20 mm^2 (RD-TD plane) were embedded in an epoxy resin, ground and mechanically polished with a diamond suspension up to 1 µm for inclusions analysis. They were characterized quantitatively to determine the size and area fraction according to DIN EN 10247 standard by optical microscopy in conjunction with an image-analysis software. Due to the inherent high-contrast ratio between non-metallic inclusions and the matrix, inclusions were accurately determined by image-analysis and quantitative data was extracted. The inclusions were analyzed qualitatively based on their chemical composition by SEM/EDS technique.

2.3. Mechanical Tests

2.3.1. Macro-Tensile Tests with Digital Image Correlation (DIC)

Macroscopic tensile tests were carried out according to DIN EN ISO 6892 standard. A sample geometry of gauge length 75 mm, a width of 12.5 mm and having a thickness of 1.4 mm as shown in Figure A1 was used. The samples were obtained by water-jet cutting along the RD and the machined edges were polished up to a surface roughness of 0.125 µm. The tests were performed at RT in conjunction with DIC or video extensometer using a Zwick/Roell Z100 machine with a crosshead displacement rate of 1.8 mm/min, which corresponds to a quasi-static $\dot{\varepsilon}$ of about 0.001 s^{-1}. A force transducer was used to measure force and a video extensometer was used to measure the elongation. The GOM Aramis 12M 2D DIC system (see Figure A1) was used for evaluating the ε_{local}distribution and to investigate the initiation and propagation of deformation bands during straining. A high contrast black and white stochastic pattern was prepared on the samples for the measurements. The images were captured at a rate of 1 Hz during the test and a facet size of 100 µm was set for the ε_{local} evaluation. The force data was imported into the ARAMIS DIC software for calculating the σ–ε curves. The mechanical properties were evaluated following the ASTM E517, ASTM E646, and DIN ISO 10275 standards. The properties evaluated using video extensometer and DIC were almost similar. The SHR curves were evaluated from the smoothened σ–ε curves.

2.3.2. Macro-Tensile Tests with High-Speed Thermocamera

The rise in temperature due to adiabatic heating during deformation was measured by high-speed infrared thermography camera of type varioCAM® hr along with video extensometer as shown in Figure A2. The temperature measurement of the camera is from −40 °C to 1200 °C. The overall accuracy of temperature measurement within the range of calibration is ±1 °C. A tensile sample with a gauge length of 30 mm and a width of 6 mm as shown in Figure A2 was tested using a Zwick/Roell Z100 machine at a $\dot{\varepsilon}$ of 0.001 s^{-1}. The emissivity was also calibrated before the measurements and the specimen was coated with black lacquer to minimize the reflections from the surroundings. The images were acquired at a frequency of 1 Hz in full-frame-mode with a maximum of 384 × 288 pixels resolution using the IRBIS® online software. The data was analyzed to extract the temperature variation within the gauge length and co-related with the strain measured from the video extensometer.

2.3.3. Elastic Constants Measurement

Elastic properties of the alloys were determined by using the GE USM35 ultrasonic testing machine. Longitudinal and transversal pulses were measured by using normal incident 20 MHz (CLF4) longitudinal and 10 MHz (K7KY) shear transducers respectively. The presence of air can disrupt the propagation of the acoustic waves into the material, therefore a viscous liquid such as oil (longitudinal)/honey (transversal) was applied as contact material between the transducer and the sample surface. With the accurate measurement of the sample thickness (l) and the transit time (t) between the peaks of consecutive echoes, the longitudinal (v_l) and transversal (v_t) sound velocities of the material was calculated by using $v_{l/t} = l/(\frac{t}{2})$. The density ($\rho$) of the alloys was determined by using AccuPyc 1330 pycnometer. The elastic properties of the alloys such as Young's modulus (E), shear modulus (G) and Poisson's ratio (ν) were calculated using the relations given by [35]

$$E = 3\rho v_t^2(v_l^2 - \frac{4}{3}v_t^2)/(v_l^2 - v_t^2), \qquad G = \rho v_t^2, \qquad \nu = \frac{1}{2}(v_l^2 - 2v_t^2)/(v_l^2 - v_t^2) \tag{1}$$

3. Results

3.1. Microstructure Analysis

The initial microstructure of both alloys X60MnAl17-1 and X30MnAl23-1 consisted of fully austenitic (γ) grains with an average grain size of 16.0 µm and 12.0 µm respectively. The inverse pole figure (IPF) maps with respect to the RD depicting the grain sizes and the crystal orientation distribution are shown in Figure 2a,b. It can be observed from Figure 2d that for an alloy X30MnAl23-1, the grain size varies within a range of about 1–40 µm, with small fractions of grains larger than 25 µm, whereas for an alloy X60MnAl17-1 shown in Figure 2c, the grain size varies with a large range of about 1–50 µm, with small fractions of grains larger than 35 µm. The initial texture is rather weak for both alloys with a texture index value of 1.33 for X60MnAl17-1 and 1.18 for X30MnAl23-1, as shown in Figure 2a,b.

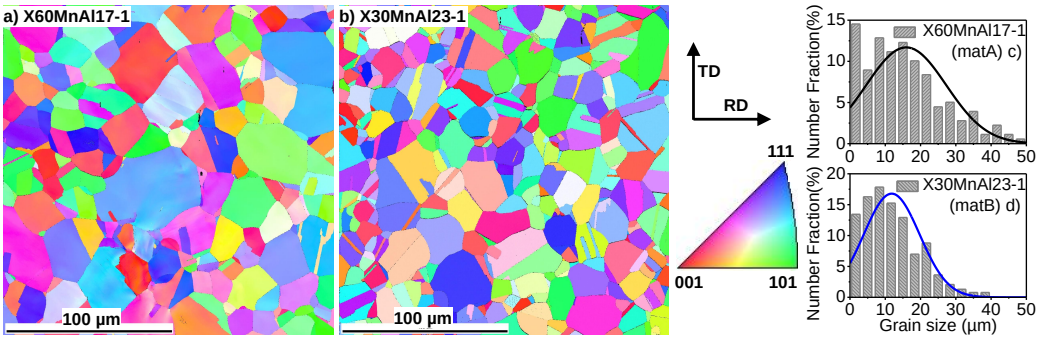

Figure 2. The EBSD inverse pole figure (IPF) maps of the undeformed samples showing grain size and orientations: (**a**) X60MnAl17-1, (**b**) X30MnAl23-1. Grain size fitted using normal distribution function shown in: (**c**) X60MnAl17-1, (**d**) X30MnAl23-1; microstructures of both alloys is completely austenite (γ); the average grain size of X60MnAl17-1 is 16.0 µm and X30MnAl23-1 is 12.0 µm.

The estimated area fraction and the size of inclusions present in the materials are presented in Table 2. The measured area fraction of inclusions in both alloys is ~0.1%. The average size of the inclusions in X60MnAl17-1, X30MnAl23-1 is about 1.2 µm and 1.5 µm respectively. The distribution of different type of inclusions present in the materials is shown in Figure 3. EDS analysis performed on the inclusions at different locations indicate the presence of manganese sulfides (MnS) and aluminum nitrides (AlN), both in globular and elongated shapes as shown in Figure 2. The globular MnS inclusions have slightly high fractions of Mn and S contents compared to the base material, whereas the elongated MnS contains a higher fraction of Mn and S.

Table 2. Cleanliness analysis: area fraction, average and largest size of the inclusions. Size of the smallest inclusions found in both alloys is ∼0.5 µm. The scatter was estimated by analyzing four to five images taken at different locations.

Alloy	Area Fraction (%)	Average Size (µm)	Largest Size (µm)
X60MnAl17-1	0.10 ± 0.01	1.23 ± 0.05	8.0 ± 1.5
X30MnAl23-1	0.11 ± 0.02	1.50 ± 0.10	12.0 ± 2.0

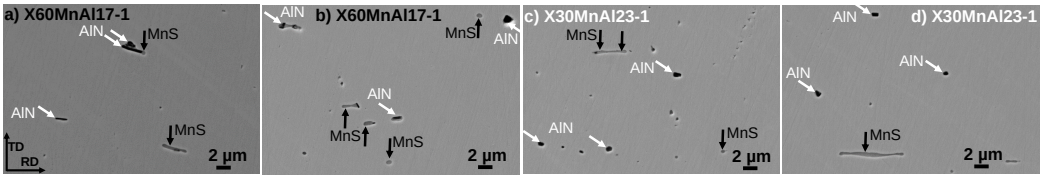

Figure 3. SEM micrographs depicting non-metallic inclusions present in the investigated alloys: X60MnAl17-1 (**a**,**b**); X30MnAl23-1 (**c**,**d**); manganese sulphide (MnS) (black arrows) and aluminium nitride (AlN) (white arrows).

3.2. Mechanical Properties

The mechanical properties of the TWIP steels vary with chemical composition due to change in SFE resulting in different deformation behavior. The stress-strain curves and the SHR for X60MnAl17-1 and X30MnAl23-1 obtained by uni-axial tensile tests at RT are shown in Figure 4. The σ–ε curve of X30MnAl23-1 exhibit homogenous flow behavior throughout the deformation, whereas periodic serrations of type A can be observed in the flow curve of X60MnAl17-1. Both X60MnAl17-1 and X30MnAl23-1 show linear flow behavior and slight necking just before the final failure. Initially, strain hardening for both alloys is characterized by a sharp drop of the SHR and then it increases to reach a constant value with small increase in deformation. Thereafter, both alloys show a general drop with a pronounced multistage character at different strains. The first marked inflection in SHR after the sudden drop occurs at ∼0.04 true strain for X60MnAl17-1 and at ∼0.03 true strain for X30MnAl23-1 to attain the highest point of strain hardening. The peak value of SHR for X60MnAl17-1 is about 2460 MPa and X30MnAl23-1 is about 2360 MPa and after that SHR started to decrease steadily for both alloys. The second marked inflection in SHR occurs at ∼0.15 true strain for X60MnAl17-1 and at ∼0.18 true strain for X30MnAl23-1. The SHR increases at second inflection for X60MnAl17-1 compared to a steady decrease in SHR for X30MnAl23-1 until failure. The SHR of X60MnAl17-1 attains another maximum between 0.3 and ∼0.4 true strain, and then it decreases continuously until failure. The SHR for both alloys at the beginning of the deformation is above 2350 MPa and it decreases to about 1400 MPa at failure. Since the SHR of both alloys shows multistage hardening behavior with increasing macroscopic strain indicating a change in active deformation mechanisms at different strains. The serrated flow caused due to DSA in X60MnAl17-1 alloy after a strain of ∼0.15 could have played a crucial role in enhancing the strain hardening and ductility of the material.

The variation in the mechanical properties of X60MnAl17-1 and X30MnAl23-1 are presented in Table 3. The X60MnAl17-1 with 0.6 wt.% C has a higher yield strength of about 294 MPa compared to 246 MPa of X30MnAl23-1 with 0.3 wt.% C. Similarly, the tensile strength of X60MnAl17-1 and X30MnAl23-1 are very different, which are about 844 MPa and 693 MPa respectively. The TE of X60MnAl17-1 is 70%, which is larger compared to 63% of X30MnAl23-1. The density of X60MnAl17-1 is slightly lower and E, G are much larger compared to X30MnAl23-1. The mechanical properties of X60MnAl17-1 and X30MnAl23-1 presented in Table 3 are very different even though both the designed alloys are very similar in terms of SFE values, heat treatment, and microstructure.

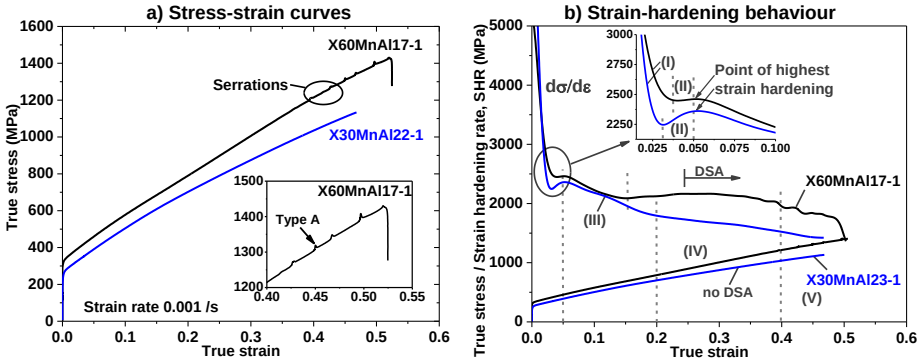

Figure 4. Macroscopic material response: (**a**) True stress-strain curves (**left**,**b**) Strain-hardening behavior (**right**).

Table 3. Mechanical properties of Al-added TWIP steels: Yield/ultimate tensile strength (YS/UTS), uniform/total elongation (UE/TE), Lankford coefficient (r-value), strain hardening exponent (n-value), density (ρ), Young's modulus (E), shear modulus (G) and Poisson's ratio (ν). All data are average values determined from at least three parallel experiments.

Alloy	YS	UTS	UE	TE	r-Value	n-Value	ρ	E	G	ν
Unit	MPa	MPa	%	%	-	-	kg/m^3	GPa	GPa	-
X60MnAl17-1	294 ± 10	844 ± 15	65 ± 5	70 ± 5	0.90 ± 0.01	0.35 ± 0.01	7700 ± 10	188 ± 2	75 ± 1	0.267 ± 0.01
X30MnAl23-1	246 ± 10	693 ± 15	62 ± 2	63 ± 2	0.83 ± 0.01	0.37 ± 0.01	7715 ± 5	161 ± 1	63 ± 1	0.274 ± 0.01

3.3. Deformation Mechanisms

The chemical composition of an alloy has a significant influence on the SFE, which controls the activation of different deformation mechanisms during deformation. Hence SFE of an alloy plays a crucial role in the evolution of microstructure and its phases. The SFE value of 29 mJ/m^2 for X60MnAl17-1 and 24 mJ/m^2 for X30MnAl23-1, indicate that both alloys are designed to exhibit twinning induced plasticity in combination with dislocation glide as a major deformation mechanism. Activation of DSA in an X60MnAl17-1 alloy can be observed from Figure 4, whereas in an X30MnAl23-1 alloy DSA is not activated.

The evolution of microstructure and deformation mechanisms is shown in Figure 5. Annealing twins can be observed in the initial stages of deformation as shown in Figure 5a,e (black arrows). Mechanical twins or twin bundles could not be observed in EBSD image quality maps in both alloys at a strain of ∼0.1. However, an advanced technique such as transmission electron microscopy is essential for observing the initiation of twins. With the small increase in macroscopic strain to ∼0.2, mechanical twins can be observed in the grains oriented along <111> (see Figures 5b,f and 13). It could be observed that the fraction of twinned grains or twin area fraction in an X60MnAl17-1 alloy is much high compared to an X30MnAl23-1 alloy. Increasing the deformation further to ∼0.3 lead to further nucleation and growth of mechanical twins (white arrows). More intense twinning can be observed in grains of an X60MnAl17-1 alloy compared to an X30MnAl23-1 alloy. The grains which are oriented along the <101> direction reorient toward the <111> direction during deformation and twins initiate in these grains as shown in Figure 13. At a macroscopic strain of ∼0.4, both primary and secondary twins can be observed in both alloys. In Figure 5d,h, mechanical twins can be observed in most of the grains indicating large deformation at micro-scale. The twin bundles can be very well identified and the increase in density of mechanical twins can be seen with increasing macroscopic strain. At a strain of ∼0.4, the mechanical twins are saturated in the grains in both alloys with no scope for further twinning. The area fraction of detected twins or twin bundles with increasing macroscopic strain is shown in Figure 13. The intense twinning in the grains can be observed before the failure initiation. High TVF in an X60MnAl17-1 alloy has led to better SHR and increased ductility compared to an X30MnAl23-1 alloy. There are many instances in the microstructure where twinning occurs in both the

neighboring grains and share a common GB (light blue arrows). The heavily deformed grains can also have a common junction (yellow arrow). The stress level in such GBs and triple junctions is very high compared to other grains. Such high stressed regions of the microstructure are prone to initiation of micro-cracks.

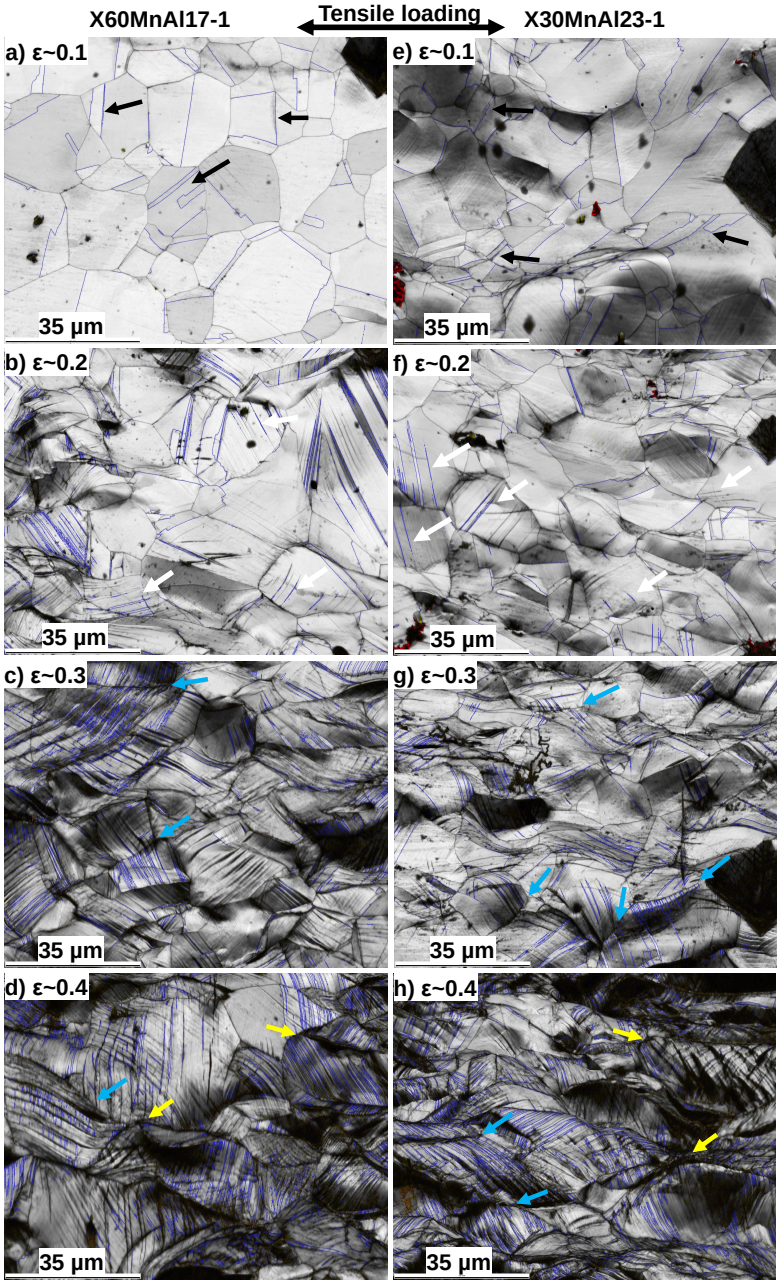

Figure 5. EBSD image quality (IQ) maps depicting the evolution of twinning with increasing macroscopic strain: X60MnAl17-1 (**a**) $\varepsilon_{\sim 0.1}$ (**b**) $\varepsilon_{\sim 0.2}$ (**c**) $\varepsilon_{\sim 0.3}$ (**d**) $\varepsilon_{\sim 0.4}$ (left column), X30MnAl23-1 (**e**) $\varepsilon_{\sim 0.1}$ (**f**) $\varepsilon_{\sim 0.2}$ (**g**) $\varepsilon_{\sim 0.3}$ (**h**) $\varepsilon_{\sim 0.4}$ (right column); blue color in IQ maps in (**a**,**e**) indicates annealing twin boundaries and detected Σ-3 deformation twin boundaries in (**b**–**d**,**f**–**h**); The arrows indicate annealing twin boundaries (black), nucleation of deformation twins (white), intercepting twins at grain boundary (light blue) and triple junctions (yellow); pixels in black are unindexed points.

3.4. Local Deformation Behavior

The chemical composition of the alloy mainly C content, has a significant influence on the local deformation behavior. The σ–ε behavior extracted from the quasi-static tensile tests at RT carried out in conjunction with DIC is shown in Figure 6a. The serrations can be observed on the σ–ε curve caused due to DSA in an X60MnAl17-1 alloy, whereas smooth σ–ε curve without any serrations in an X30MnAl23-1 alloy. The DSA in X60MnAl17-1 alloy has led to the plastic instability in the form of initiation and propagation of the deformation bands. The deformation bands initiated at a macroscopic strain of ∼24% during deformation propagate until failure. The strain at which deformation bands initiated is shown in Figure 7I and the region at which deformation bands were active is indicated by a rectangle in Figure 6a. After a strain of ∼24%, deformation bands nucleated steadily and continuously. The plateau between the two consecutive serrations peaks corresponds to the nucleation and propagation of deformation band within the gage length. The serration peak corresponds to the initiation/disappearance of the deformation band outside the gage length. The initiation and propagation of deformation bands during deformation for X60MnAl17-1 is shown in Figure 7i–k. The enlarged view of σ–ε curve from Figure 6a, where deformation bands were active is shown in Figure 7I. It can be observed that stress jumps at serrations at the beginning are smaller compared to the final stages of deformation. The deformation bands nucleated at one shoulder end or in the middle of the specimen propagate to the other end. For up to ∼28% strain, only one deformation band nucleated and propagated, whereas after 28% strain, two intersecting deformation bands nucleated and propagated during the deformation (see Figure 7j,k). It is clear from the local strain rate ($\dot{\varepsilon}_{\text{local}}$) distribution in Figure 7i–k that, the deformation is localized in the deformation bands, whereas it is uniform in other regions. During initiation of deformation bands, the $\varepsilon_{\text{local}}$ accumulation in deformation bands is quite low, but in the subsequent bands, large strain localization can be observed (see Figure 7l–n). The $\varepsilon_{\text{local}}$ is larger in the regions where deformation band has already passed compared to the region where deformation band is moving towards or yet to pass through. However, the difference in $\varepsilon_{\text{local}}$ between the regions where the deformation band already passed by compared to the regions where the deformation band moving towards is $\leq$5% strain. Thus nucleation and propagation of deformation bands during deformation has resulted in inhomogeneous deformation behavior in X60MnAl17-1 alloy. The velocity at which deformation bands propagate decrease exponentially with increasing strain as shown in Figure 7II. The band velocity at the beginning is ∼2 mm/s, which is drastically reduced to ∼0.5 mm/s in the end. The failure in X60MnAl17-1 alloy occurred at the intersection of deformation bands when their motion is hindered significantly as shown in Figure 7k,n. The localization of strain within the deformation bands is larger compared to the $\varepsilon_{\text{local}}$ distribution in other regions. Hence strain localization caused at the deformation bands influenced the failure initiation in X60MnAl17-1 alloy. For X30MnAl23-1 alloy, the $\dot{\varepsilon}_{\text{local}}$ distribution is shown in Figure 7u–w and $\varepsilon_{\text{local}}$ distribution is shown in Figure 7x–z. It could be observed that the $\varepsilon_{\text{local}}$ and $\dot{\varepsilon}_{\text{local}}$ is quite uniform until the beginning of necking. The necking begins at a macroscopic strain of ∼60% and with further straining failure occurs due to strain localization. Even though both alloys deform by twinning in combination with dislocation glide, the local deformation behavior in X30MnAl23-1 alloy is homogenous compared to inhomogeneous behavior in X60MnAl17-1 alloy due to the activation of DSA.

The rise in temperature due to adiabatic heating could influence the local deformation behavior. The temperature distribution over the entire gage length of the specimen at different elongations is shown in Figure 8b,d and the temperature variation in the middle of the specimen is shown in Figure 8a,c. From Figure 8, it can be observed that the temperature of the specimen rises due to adiabatic heating (AH) with increasing strain. The temperature distribution is inhomogeneous in X60MnAl17-1 alloy due to the propagation of deformation bands compared to the homogenous temperature distribution in X30MnAl23-1 alloy. The temperature increased above RT by 14 °C in an X60MnAl17-1 alloy and by 12 °C in an X30MnAl23-1 alloy. Thus AH has resulted in an increase of SFE from 24 to 25 mJ/m^2 in an X30MnAl23-1 alloy and from 29 to 31.5 mJ/m^2 in an X60MnAl17-1 alloy. However, the SFE increase due to AH is not significant for the change in deformation mechanisms.

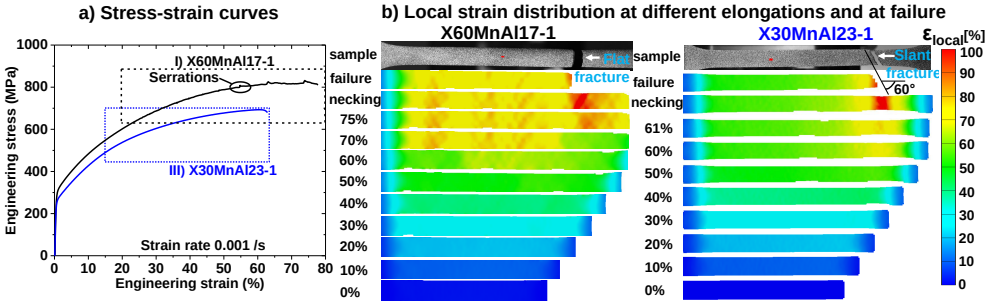

Figure 6. (**a**) Stress-strain behavior extracted from the macroscopic tensile tests carried out in conjunction with digital image correlation (DIC). (**b**) Local strain distribution: X60MnAl17-1—Failure at the intersection of deformation bands with large strain localization (see also Figure 7k), X30MnAl23-1—Failure due to diffuse necking and large strain localization; rectangles indicate regions chosen to investigate deformation bands; left: macroscopic strain; right: legend for local von Mises effective plastic strain (ε_{local}) distribution.

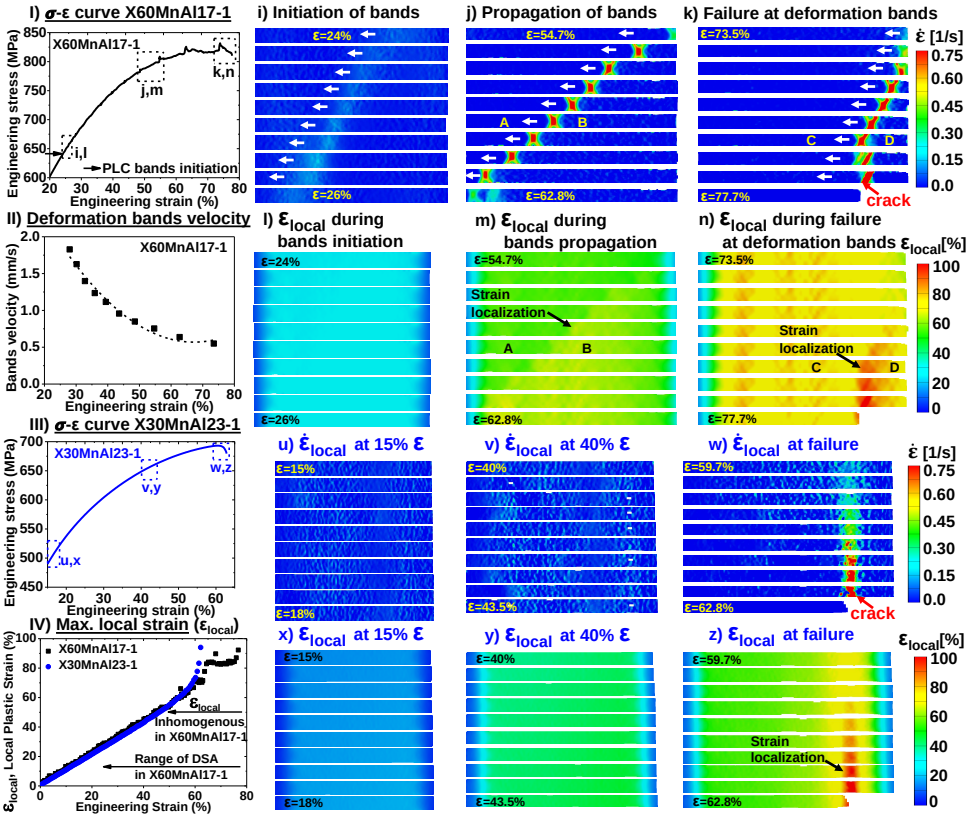

Figure 7. Deformation bands initiation, propagation and their location at the point of failure obtained from the tensile tests in conjunction with DIC: (**I**) X60MnAl17-1: enlarged view of σ–ε curve depicting the initiation of deformation bands (**i**,**l**), propagation of deformation bands (**j**,**m**) and failure at deformation bands (**k**,**n**), (**II**) plot of the deformation bands velocity versus strain, (**III**) X30MnAl23-1: enlarged view of σ–ε curve depicting no deformation bands initiation and propagation (**u**,**v**,**x**,**y**) and failure due to diffuse necking and strain localization (**w**,**z**), (**IV**) plot of the maximum local plastic strain versus strain; (**i**–**k**,**u**–**w**) shows local strain rate ($\dot{\varepsilon}_{local}$) distribution; (**l**–**n**,**x**–**z**) shows local strain (ε_{local}) distribution; the legend for $\dot{\varepsilon}_{local}$ and ε_{local} distribution (**right**); white arrows indicate the direction of propagation of the deformation bands; the macroscopic strain at the start and end of deformation band is given; images were shown in steps of ~0.4–0.6% macroscopic strain.

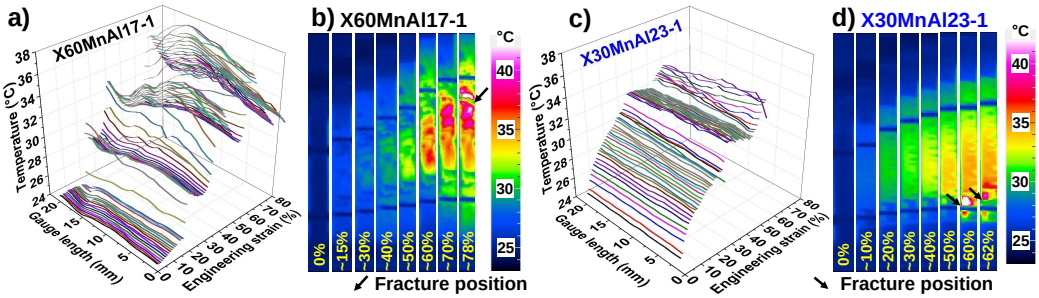

Figure 8. Temperature increase due to adiabatic heating in the macroscopic tensile tests carried out in conjunction with infrared thermography camera and video extensometer: (**a**,**c**) Rise in surface temperature during deformation, (**b**,**d**) Distribution of local temperature at different elongations and at failure.

The ε_{local} distribution along the tensile direction at different elongations is shown in Figure 6b. It can be observed that over the entire gage length of the tensile specimen, the ε_{local} distribution is uniform until 50% elongation. In an X60MnAl17-1 alloy, inhomogeneous distribution of ε_{local} can be observed due to deformation bands propagation. The failure initiated at the point of intersection of deformation bands close to the edges of the tensile specimen. In an X30MnAl23-1 alloy for the elongations above 50%, the strain starts to localize within the gage length of the tensile specimen. The region of strain localization has increased further with the increase in deformation and then finally leading to abrupt failure in the localized region.

Slant fracture with pronounced necking can be observed on the broken tensile sample. The macroscopic failure strain (ε_f) in an X60MnAl17-1 alloy is ~77%, whereas the local failure strain (ε_{f_local}) in the deformation band is ~98%. Similarly in an X30MnAl23-1 alloy ε_f is ~64% and the ε_{f_local} is ~98%. This large difference between the ε_{f_local} and the ε_f indicates that a large amount of strain localization occurred before the final failure. The major differences in failure initiation can be observed in the alloys with and without DSA effect. In an X60MnAl17-1 alloy with DSA effect, failure occurred at the intersection of deformation bands close to edges, whereas in an X30MnAl23-1 alloy without any DSA effect, failure occurred by classical necking and strain localization.

3.5. Mechanisms of Damage and Failure

The damage initiation is mainly influenced by the active deformation mechanisms and the presence of non-metallic inclusions in the material. The evolution of microstructure with increasing strain is shown in Figure 9. The micro-crack formation events in the microstructure are shown in Figure 10 and at inclusions is shown in Figure 11. The damage development in both the alloys could be explained in three stages namely damage incubation stage ($\varepsilon_{0.10-0.3}$), damage nucleation stage ($\varepsilon_{0.3-necking}$) and damage growth stage ($\varepsilon_{necking-failure}$). In an X60MnAl17-1 alloy, the major active deformation mechanisms were twinning and slip, activation of DSA and occurrence of intense twinning can be observed at lower strains, hence the damage nucleation begins at earlier stages of deformation. Whereas in an X30MnAl23-1 alloy, only twinning and slip were the active deformation mechanisms and the occurrence of intense twinning can be observed at later stages of deformation close to necking, which could have delayed the beginning of damage nucleation.

During the damage incubation stage, the interaction of the various active deformation mechanisms with the microstructure constituents and non-metallic inclusions play a significant role. Twinning in combination with dislocation slip within the grains has resulted in large local deformation as shown in Figure 9a,d. With further increase in deformation (see Figure 9b,e), nucleation and growth of multiple deformation twins within a single grain result in a large pileup of dislocations at GBs or twin boundaries. It can be observed from Figure 9 that, there are many instances in microstructure, where two neighboring grains which deform by twinning share a common GB or a grain which deform

by twinning share a GB with another grain which deforms by slip or three differently deformed grains share a common junction (triple points) can be observed. A large pileup of dislocations in such instances of microstructure could be observed at $\varepsilon_{>0.2}$, which could result in high stress at GBs. The stress level will be even higher if the GB lay $\perp$ to the loading direction. Such instances of microstructure could be prone to damage nucleation. The presence of inclusions such as MnS and AlN as shown in Figure 3 could also play a role at this stage. Micro-crack formation events at the MnS inclusions can be observed at $\varepsilon_{0.3}$ in Figure 9d. Many such instances of micro-cracks were also observed in AlN and MnS inclusions at very early stages of deformation at $\varepsilon_{0.10-0.3}$.

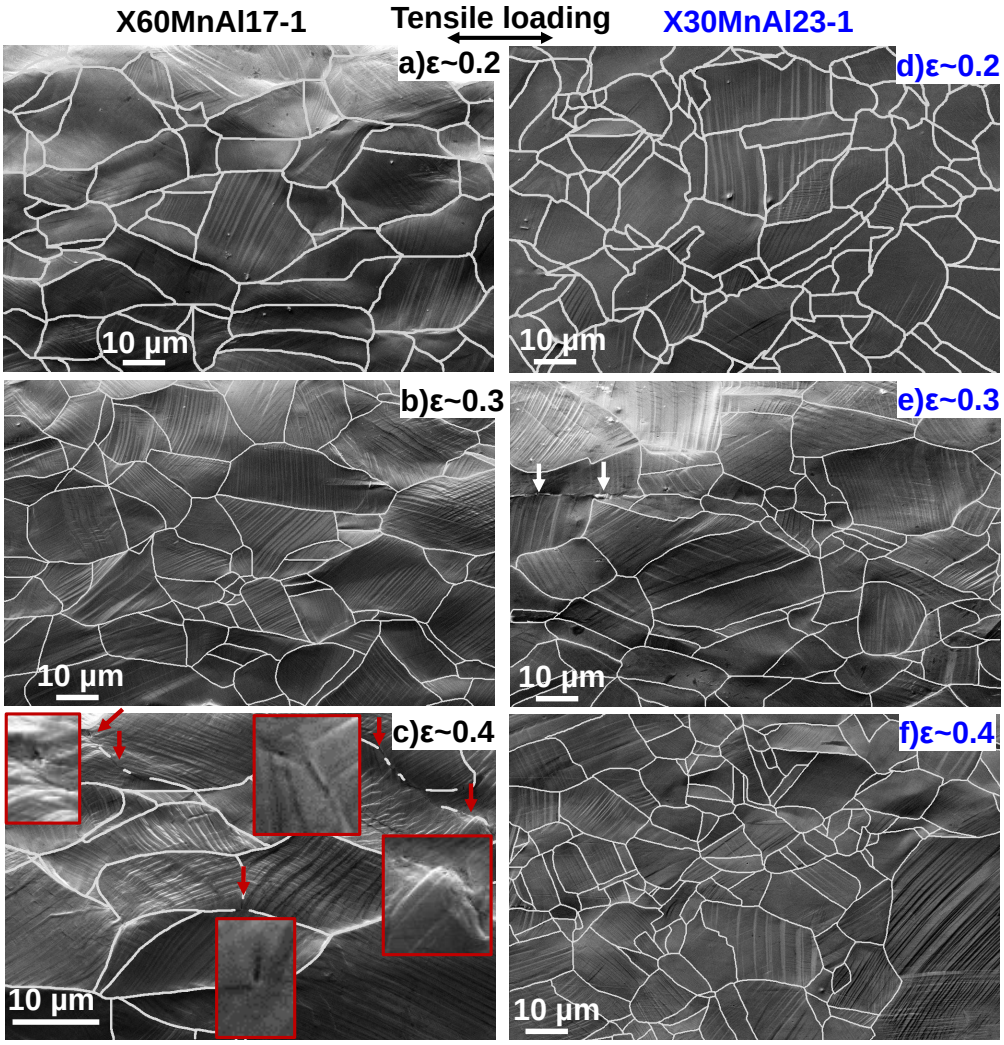

Figure 9. Evolution of microstructure and micro-crack formation with deformation. X60MnAl17-1: (**a**) $\varepsilon_{\sim 0.2}$ (**b**) $\varepsilon_{\sim 0.3}$ (**c**) $\varepsilon_{\sim 0.4}$ (left column), X30MnAl23-1: (**d**) $\varepsilon_{\sim 0.2}$ (**e**) $\varepsilon_{\sim 0.3}$ (**f**) $\varepsilon_{\sim 0.4}$ (right column); red arrows indicate micro-cracks; white arrows indicate cracks in MnS inclusions at grain boundary (GB); macroscopic true strain is indicated at the top right corner.

The saturation of the twinning within the microstructure is the precursor to the initiation of damage nucleation stage. Both the alloys deform by dislocation slip and twinning as shown in Figures 5 and 9. However, more pronounced twinning can be observed at earlier strains in X60MnAl17-1 alloy compared to an X30MnAl23-1 alloy. From Figure 5, it is very clear that at $\varepsilon_{0.3}$ large deformation due to slip and twinning within the grains can be observed in X60MnAl17-1 alloy, which

increases stress at the GB. In such high stressed GBs shown in Figure 9c micro-voids nucleate and coalesce together leading to micro-crack formation. The micro-cracks are mainly observed at GBs, triple junctions and especially in boundaries which are $\perp$ to loading direction as shown in Figure 10a,b. Thus it is very clear that stress concentration caused by the intersection of slip bands at GB lead to intergranular micro-crack formation. Many instances of micro-cracks at triple points can also be observed. However, in X30MnAl23-1 alloy the nucleation of micro-cracks did not start at $\varepsilon_{\sim 0.4}$, but at $\varepsilon_{necking}$. Many instances of inter-granular micro-crack formation events can be observed as shown in Figure 10c,d. The majority of cracks observed in the microstructure are at GB and triple points. The enlarged regions of microstructure in Figure 10 clearly indicates that micro-cracks initiated at the interception of slip bands and deformation twins at GB. From Figure 10a–d, it can be observed that the mechanism of micro-crack nucleation in both the alloys is the same. The micro-cracks which nucleated at the MnS and AlN inclusions did not grow much even after deforming to $\varepsilon_{>0.4}$ and does not propagate to the matrix (see Figure 11). Such micro-cracks can be observed in the AlN inclusions present at GB in an X60MnAl17-1 alloy as shown in Figure 11a. Similarly, in an X30MnAl23-1 alloy, micro-cracks were also observed at the MnS inclusion present at GB shown in Figure 11b and within the grain in Figure 11c. These micro-cracks were within the inclusion even after large deformation. Thus it can be stated that, micro-cracks nucleated in all inclusions present in the material, much before the beginning of the necking in both the alloys. The coalescence of micro-cracks at the inclusions present at different locations in the material could play a vital role in macroscopic failure initiation. The micro-cracks in X60MnAl17-1 alloy initiated earlier compared to X30MnAl23-1 alloy. The activation of DSA in an X60MnAl17-1 alloy could have led to an early start of damage nucleation.

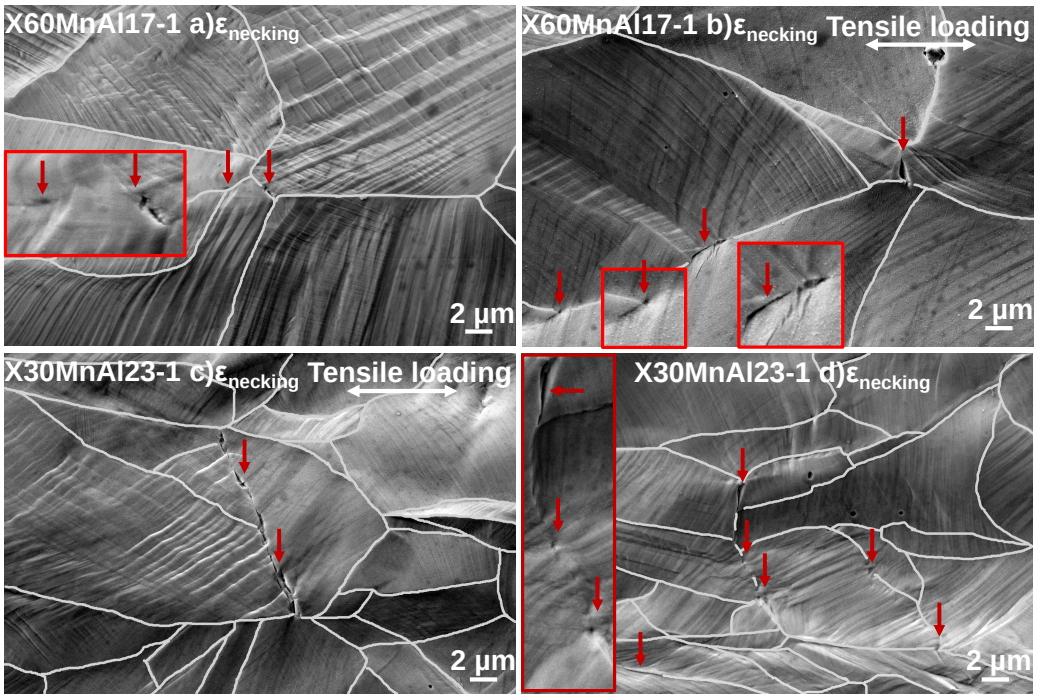

Figure 10. Mechanism of micro-cracks development at a strain of $\varepsilon_{necking}$. X60MnAl17-1 (**a**) Micro-crack initiation at triple junction and crack propagation into the neighboring grains assisted by the intercepting deformation twins, (**b**) Intergranular cracks nucleating at GB, X30MnAl23-1: (**c**) Micro-cracks initiation at GB and their propagation, (**d**) Intergranular cracks nucleation at grain boundaries and triple junctions; red arrows indicate micro-cracks.

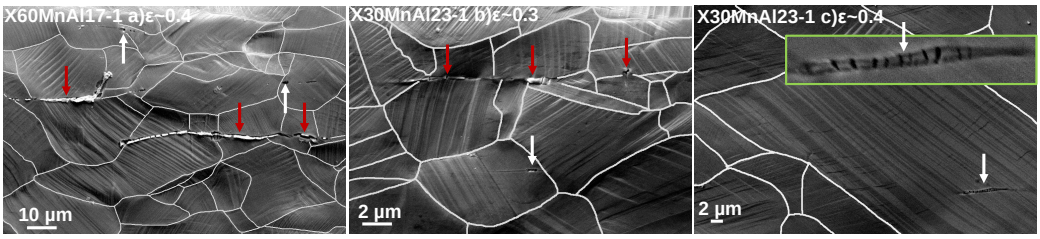

Figure 11. Micro-cracks at inclusions. X60MnAl17-1: (**a**) Micro-cracks in AlN inclusions at GB and in MnS inclusions close to GB and also inside the grains, X30MnAl23-1: (**b**) Micro-cracks in MnS inclusion at GB, (**c**) Micro-cracks in MnS inclusion inside a grain; red arrows indicates cracks in inclusions at GB; white arrows indicate cracks in inclusions inside the grains.

The damage growth stage starts with the coalescence of micro-cracks at various constituents of the microstructure in the material leading to macroscopic failure initiation. From the observations shown in Figures 10 and 11, it is very clear that there is a great interplay between the deformation twins and slip bands at micro-scale until the saturation of twinning. The saturation of twinning within the microstructure has led to the nucleation of micro-cracks at the high stressed GB and triple junctions. Since deformation by twinning and slip is quite uniform in almost all grains in the entire microstructure, the cracks were initiated all over the cross-section. The micro-cracks formed at MnS and AlN inclusions in the material also play a significant role in the damage growth. The variety of micro-cracks formed at different microstructure constituents coalescence together rapidly to develop macro-cracks leading to localized necking. It can be understood from the σ–ε curve in Figures 4 and 6 that in both alloys large strain localization in the material occurred resulting in necking and failure. The appearance of localized necking before the failure shows that there is a plastic localization before the final failure as shown in Figure 12. This indicates that nucleation of micro-voids in the material is followed by the coalescence and growth of many micro-voids leading to micro-crack formation. The role of MnS and AlN inclusions on the failure initiation can be visualized on the fracture surfaces. The presence of large elliptical or round voids (white arrows) shows that coalescence of many smaller voids has occurred at the MnS or AlN inclusions. The large number of minute voids of size $\leq$2.5 µm can be seen on the fracture surfaces for both alloys. Thus it is clear that the predominant fracture mode in both alloys is a ductile failure with the formation of fine dimples.

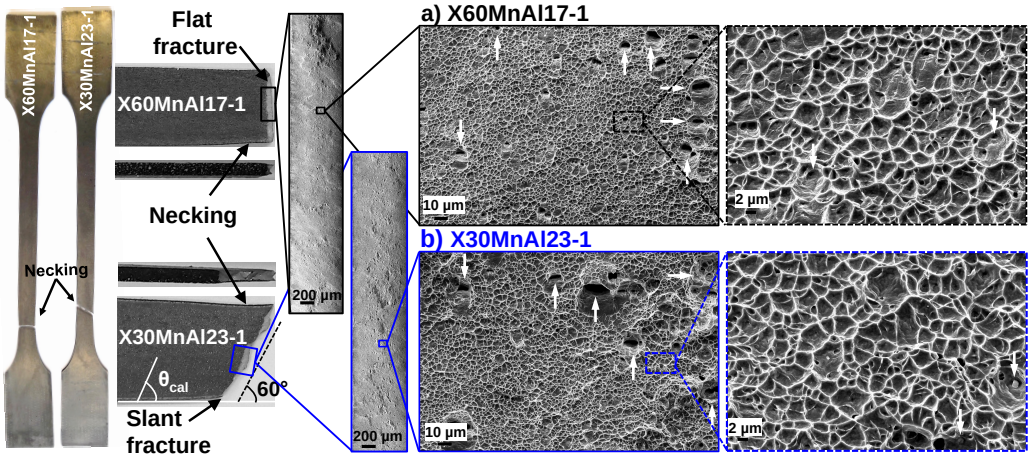

Figure 12. Fracture behavior of tensile specimens. Diffuse necking and fracture surface appearance (**left**) and SEM images of the fracture surfaces at different magnifications (**right**). Average dimple size of both X60MnAl17-1 and X30MnAl23-1 is approximately $\leq$2.5 µm. White arrows indicate large elliptical voids at MnS and AlN inclusions.

4. Discussion

4.1. Serrated Flow and PLC Effect

In an X60MnAl17-1 alloy repeated serrations can be observed on the σ–ε curves during the plastic deformation, whereas in an X30MnAl23-1 alloy, no serrations can be observed at RT and quasi-static $\dot{\varepsilon}$ (see Figure 4). The manifestations in σ–ε behavior in the form of serrations such as a change in mechanical properties and negative SRS is mainly due to DSA. The mechanism of DSA in C containing high Mn TWIP steels can be attributed to the formation of Mn-C short-range order or short-range cluster (SRO/SRC) [11,22,24]. It is proposed that DSA occurs when the C atoms in the Mn-C octahedral clusters reorient themselves in the core of the dislocations, thereby locking the dislocations leading to high dislocation density [36]. During this dynamic interaction between the diffusing atoms and the mobile dislocations during plastic flow, C atoms pin strongly to the dislocations increasing their pile up. When the applied stress is sufficiently high, the dislocations overcome the obstacles in the form of SRO/SRC at once by a single diffusive jump of C atoms and move to next obstacle, where they are stopped again and the process is repeated [22]. The formation of Mn-C octahedral clusters result in increased lattice resistance for dislocation glide as the passage of partial dislocation will change the local position of both substitutional and interstitial atoms [20].

The serrations were initiated at a ε_c of ~12.5% in an X60Mn22 alloy without Al [14], whereas in alloys with 1.5 wt.% Al-addition, the serrations appeared at a ε_c of ~24% in X60MnAl17-1 and serrations are completely suppressed in X30MnAl23-1 at RT and quasi-static $\dot{\varepsilon}$ (see Figures 6 and 7). In the Fe–Mn–Al–C alloys, the serrations are reported to occur mainly in the steels with C content above 0.6 wt.% at RT tensile testing [14,24,27–29,37]. It was stated that with the addition of Al, the diffusivity of the carbon will be reduced and the serrated flow will be shifted to higher temperatures [38]. The addition of Al has suppressed the DSA phenomena by increasing the activation energy for C diffusion and reducing the interaction time between stacking faults and the Mn-C SRO [16]. However, even in Al-added alloys, the DSA could occur at elevated temperatures because of the increased defect mobility resulting in serrated σ–ε curves.

Twinning behavior in both Al-added alloys are quite similar, except for the initiation and saturation of twinning and TVF (see Figures 5 and 13). Even though twinning occurs in both alloys, the serrated σ–ε flow is observed only in X60MnAl17-1 alloy and not in X30MnAl23-1 alloy. The local deformation behavior is inhomogeneous in an X60MnAl17-1 alloy due to the initiation and propagation of deformation bands during deformation commonly known as Portevin-LeChatelier (PLC) effect, whereas in an X30MnAl23-1 alloy homogenous σ–ε behavior can be observed. The nucleation and propagation of deformation bands result in serrations on the σ–ε curves which can be ascribed to the DSA. Kang et al. showed that the number of Mn-C SRO clusters increases with increasing macroscopic strain in X60Mn18 alloy [23]. Song and Houston reported that with an increase in ε, the volume fraction of Mn-C SRO/SRC increases and the mean radius of clusters decreases [24]. Madivala et al. investigated an X60Mn22 alloy and showed that serrations disappear at elevated temperatures and at high strain rates. It was also stated that twinning occurs at these temperatures and at high strain rate tests [14,19]. Koyama et al. also indicated that the deformation twinning and martensitic transformation did not cause the serrations [39]. Lebedkina et al. suggested that twinning starting at some point in the specimen will initiate twins in the neighboring grains and advance into the unoccupied regions of the specimen. However, they claimed that twinning cannot alone responsible for the entire strain accumulation during strain jumps due to low TVF observed in TWIP Steel [40]. Recently, Sevsek et al. proposed a multi-scale-bridging model for the formation and propagation of the deformation bands and the resulting occurrence of the serrated flow in high Mn TWIP steels. However, they also stated that neither the SRO-based theory nor the deformation twinning based theory proposed could explain the experimental observations completely [37]. Based on the experimental observations from this study and the from the literature, it can be clearly stated that deformation twinning and ε-martensite

transformation cannot be responsible for causing serrations in Fe-Mn-C-Al alloys. Thus, DSA is the dominant factor for causing the serrations in an X60MnAl17-1 alloy.

The strain localization within the deformation bands in X60MnAl17-1 alloy is slightly different over the gauge length during the transition regime (see Figure 7l–n). After their complete development, the strain localization in them increases drastically compared to other areas (see Figure 7n). The ε_{local} is much larger in the region where deformation band has already passed by (see in Figure 7m,n marked by 'B', 'D') compared to another region where the deformation bands has to pass through (see in Figure 7m,n marked by 'A', 'C'). The velocity of propagation of the deformation bands decreases with increase in macroscopic strain. Song and Houston showed by SANS experiments that the size and number density of SRO is much larger in the regions where deformation band has already passed by compared to the region where it has to pass through [24]. Also due to the fact that SRO/SRC offers higher resistance to dislocation glide thereby leading to (a) aging of dislocations by C-atoms during their interaction time at obstacles (b) enhancement of diffusion coefficient by vacancies generated during plastic flow and (c) increase in mobile dislocation density with strain. This results in increased resistance offered by the Mn-C clusters and also by the deformation twins for the bands propagation leading to decrease in velocity and difference local deformation behavior.

4.2. Strain Hardening and Twinning Evolution

Deformation twinning during plastic deformation plays a significant role in enhancing the strain hardening behavior of materials through the creation of new boundaries thereby subdividing the original grains commonly known as dynamic Hall-Petch effect [10,13,39]. Twin boundaries act as the barriers to dislocation motion thereby progressively reducing the effective mean free path (MFP) of dislocations resulting in enhanced strain hardening. Bouaziz et al., De Cooman et al., Koyama et al. claim that mechanical twinning and the related dynamic Hall-Petch effect associated with TWIP effect remain the only mechanisms that can explain the high strain hardening of TWIP steel [10,13,39]. However, the role of DSA in manifesting the SHR of TWIP steels as explained in Section 4.1 cannot be neglected.

An X60MnAl17-1 alloy, where DSA can be observed shows enhanced strain hardening and ductility compared to an X30MnAl23-1 alloy, where DSA does not occur (see Figure 13). Such sustained and high work hardening rates can also be seen in austenitic steels with high C content because of DSA [41]. The ab-initio based study combined with SANS experiments by Song et al. [42] and SANS experimental study by Kang et al. proved the presence of Mn-C octahedral clusters and their evolution, indicating the occurrence of DSA during deformation in high Mn steels. The occurrence of static strain aging due to the presence of Mn-C SRO was stated to be responsible for increased yield strength and pronounced yielding of annealed TWIP steel [43]. It was stated that deformation twinning in TWIP steels is promoted by thermally activated nature of dislocation slip due to dynamic interactions between solute C atoms and dislocations that inhibit dislocation slip due to lattice friction effects [44]. It was proposed that the trapping of slowly moving partial dislocations by C atoms results in increased inter-granular stress and reduction of MFP [37,39]. The increased localized stress near the GB facilitate grain boundary nucleation of deformation twins [45]. DSA is also showed to be crystallographic orientation dependent, could occur at elevated temperatures and is enhanced by increasing C content [39]. Thus in an X60MnAl17-1 alloy, the occurrence of DSA has led to increased stresses at GBs. This led to triggering of the nucleation of multiple deformation twins in the preferably oriented grains. Whereas in X30MnAl23-1 alloy, conventional twinning mechanisms occurs in combination with dislocation glide at RT (see Figure 5). Thus the yield strength increase by static strain aging and the indirect promotion of the mechanical twinning during deformation in an X60MnAl17-1 alloy, could have led to high SHR and enhanced ductility.

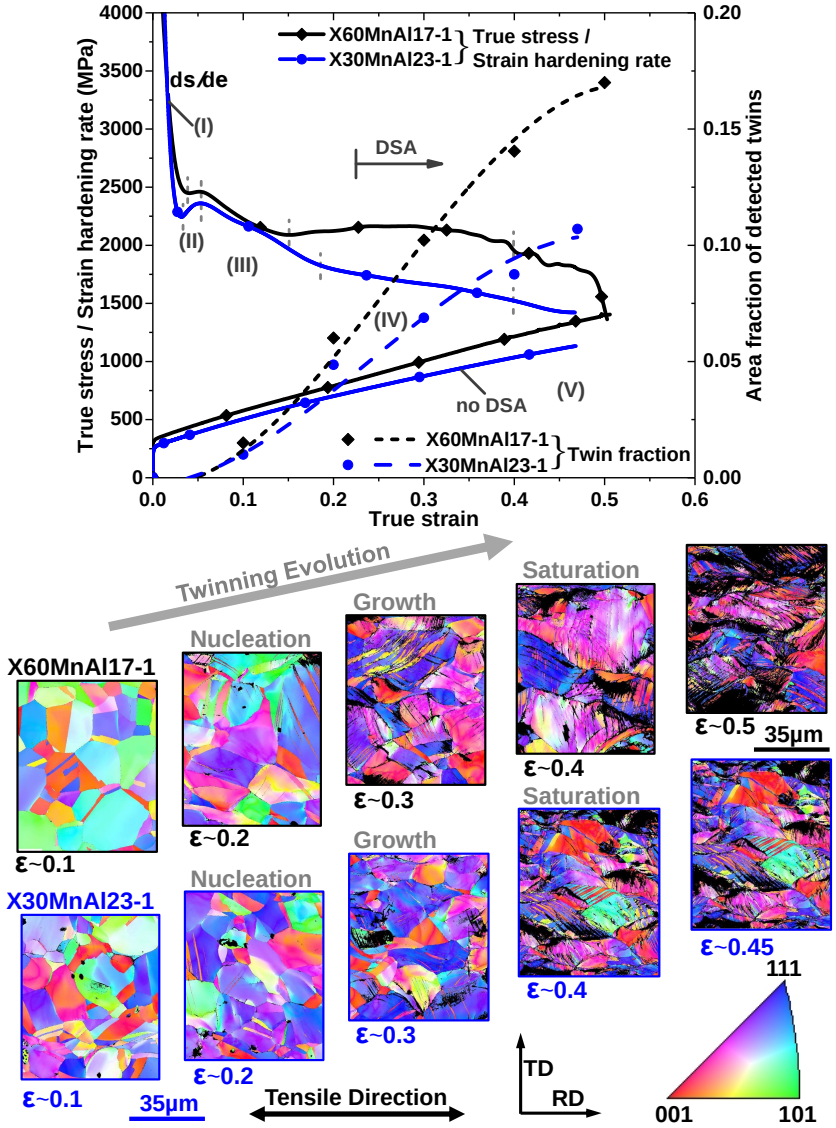

Figure 13. Strain hardening in relation to the evolution of twinning; strain hardening behavior (**top**) and EBSD IPF maps with increasing macroscopic true strain (**bottom**).

The evolution of twinning with increasing macroscopic strain is correlated with the SHR as shown in Figure 13. The RD-IPF maps at different strains are also shown. Based on the detailed work by De Cooman et al., Gutierrez-Urrutia and Raabe, the SHR in the current study is divided into five stages [13,46]. Stage (I) is the initial strain hardening stage controlled by the dislocation density evolution without the initiation of twins. The initial downfall of SHR is characterized by a continuously decreasing rate of dislocation storage and an increasing rate of dynamic recovery. The dislocation reactions in this stage are responsible for the nucleation of twins. Stage (II) is characterized by an increase of SHR in both alloys and is referred to as the primary twinning stage. It begins slightly above yielding and at a strain of ~0.03 in an X30MnAl23-1 alloy and at a strain of ~0.04 in an X60MnAl17-1 alloy (see Figure 4). The stress at the beginning of stage II is referred to as the twin initiation stress. It is about 345 MPa in an X30MnAl23-1 alloy and is about 435 MPa in X60MnAl17-1 alloy. The evolution of dislocation structures and the initiation of primary twins are supposed to be responsible for the rise of SHR in this stage. The maximum SHR for both the alloys occurs at ~0.05 strain at the end of stage II.

Stage (III) is characterized by a decrease in SHR with increasing macroscopic strain. It can be attributed to the reduced rate of primary twins initiation. It was also stated that the initial twins subdivide the original grains thereby reducing the MFP of dislocations, which results in increased stress for twin nucleation. At the end of this stage, twins can be clearly observed in the preferably oriented grains as shown in Figure 13 at a strain of 0.2. Stage (IV) and (V) are quite different in both the alloys. Stage (IV) and (V) in an X30MnAl23-1 alloy marked by a continuous decrease in SHR, ascribed to the reduced additional refinement of the dislocation and twin substructures, together with the increasing strengthening effect of the individual twins as obstacles to dislocation glide, reduce the capacity for trapping more dislocations. Stage (IV) in an X60MnAl17-1 alloy can be distinguished by again increase in SHR and reaching maximum between a strain of 0.3 and 0.4. This stage is characterized by the activation of the secondary twin systems and the formation of the multiple twin-twin interactions. This results in a further subdivision of grains and thus reduces the MFP of the dislocations considerably leading to increasing or constant SHR. During stage (V) in X60MnAl17-1 alloy, the SHR decreases continuously. In this stage TVF increases significantly and the twin bundles get thicker and denser. This can be observed in the microstructure at a strain of 0.4 and 0.5. The major difference in SHR between two alloys can be observed at stage (III), at which DSA gets activated in X60MnAl17-1 alloy which has indirectly led to significant increase in TVF, whereas in X30MnAl23-1 alloy, the TVF increase was marginal.

4.3. Damage and Fracture

Heterogeneous deformation twinning and dislocation slip could be observed in the microstructure in the early stages of deformation (see Figures 5 and 13). Micro-cracks could be observed in the MnS and AlN inclusions at strain below 0.2 (see Figure 11). The nucleation and propagation of deformation bands due to DSA has resulted in localization of strain within the bands leading to failure initiation (see Figure 7). Thus twins, slip bands, deformation bands, and non-metallic inclusions play a significant role in the fracture phenomena in TWIP steels.

In both alloys, dislocation glide and deformation twinning are the major active deformation mechanisms. Even though both these deformation mechanisms did not induce damage directly, but they acted as a source for increasing the stress concentration within the microstructure, which is a precursor step for damage initiation. A schematic diagram illustrating the mechanism of micro-crack formation in TWIP steels based on the experimental observations is depicted in Figure 14. The development of large inter-granular regions with high dislocation density within the microstructure due to the subdivision of grains due to twinning and also deformation by slip resulted in pronounced inter-granular stress. Deformation by twinning and dislocation slip can be observed in the microstructure in the preferably oriented grains leading to the localization of the plastic strain. It could be observed that <111> tensile orientation is the preferential orientation for the deformation twinning and <100> is the non-preferential tensile orientation for twinning. Many bundles of primary and secondary deformation twins can be observed in <111>-oriented grains and slip bands in <100>-oriented grains (see Figure 13). Largest plastic strain concentration can occur in the <111>-oriented grains, which are preferred for the deformation twinning and the second largest strain concentration could occur in the <100>-oriented grains, which are preferred for the dislocation slip. The large plastic localization associated to accommodate the plasticity within the grains results in high-stress concentration at the GB. This results in the initiation of voids which combine together leading to initiation of inter-granular micro-cracks (see Figures 10 and 14). Even though micro-cracks initiated at inclusions at an early stage, their growth during deformation was limited (see Figure 11). Thus at a micro-scale, stress concentration caused by the interception of deformation twins and slip bands at GB lead to damage initiation. This results in the intergranular crack propagation with a fracture surface characterized by shallow dimples (see Figure 12).

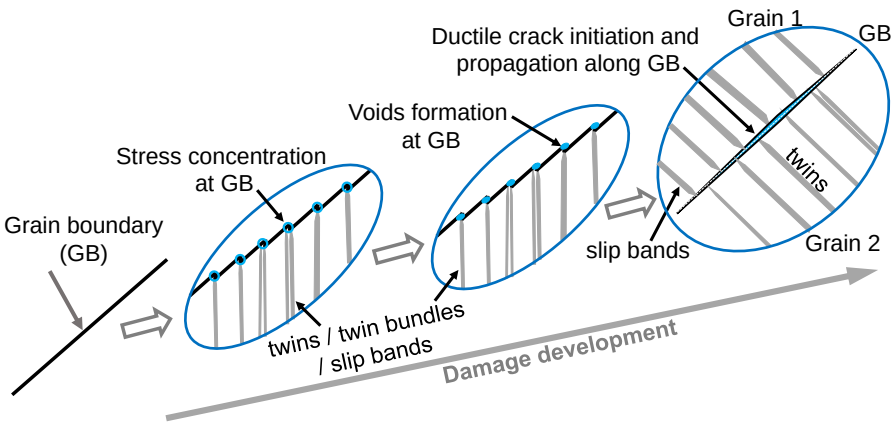

Figure 14. A schematic illustration of micro-cracking mechanisms in TWIP steels based on the experimental observations from interrupted micro-tensile tests carried out in the SEM. Stress concentration caused by the intercepting deformation twins at GB. Void formation and their growth leading to inter-granular micro-crack initiation at GBs.

5. Conclusions

The Al-added TWIP steels X60MnAl17-1 and X30MnAl23-1 were investigated by carrying out uni-axial tensile tests. The local plastic strain (ε_{local}) and temperature evolution during deformation were monitored in conjunction with digital image correlation and synchronous temperature measurements using thermocamera. Interrupted tensile tests were carried out in SEM along with EBSD measurements to study the microstructure evolution and micro-cracks development. The main conclusions can be drawn as follows:

- Strain hardening rate of an X60MnAl17-1 alloy is extraordinarily high compared to an X30MnAl23-1 alloy. An X60MnAl17-1 alloy showed higher yield strength, tensile strength and elongation compared to an X30MnAl23-1 alloy. The enhanced mechanical properties of the X60MnAl17-1 alloy is mainly due to the enhanced deformation twinning in addition to dislocation glide and also activation of dynamic strain aging (DSA). DSA is completely suppressed in an X30MnAl23-1 alloy at room temperature and quasi-static strain rate due to lower carbon content.
- Twining is the most predominant deformation mechanism occurred along with dislocation slip in both the alloys. The addition of Al has led to increased stacking fault energy thereby delaying nucleation of deformation twins and prolonged the saturation of twinning.
- Micro-cracks are observed at elongated MnS inclusions or at AlN inclusions at a relatively small strain of $\sim 2/3$ of total strain. However, these micro-cracks showed no tendency to grow.
- Large heterogeneous deformation within the grains by twinning or dislocation slip has led to a high-stress concentration at grain boundaries (GBs) due to the interception of deformation twins and slip band extrusions at GBs. Hence micro-cracks in Al-added TWIP steels originated mainly at grain boundaries and triple junctions.
- In an X60MnAl17-1 alloy, the occurrence of DSA has led to inhomogeneous flow behavior due to the nucleation and propagation of deformation bands during deformation. This resulted in large strain localization within the deformation bands and the velocity of band motion decreased with increasing strain due to the intersection of two bands. The ε_{local} accumulation within the intersecting bands resulted in a macroscopic crack initiation close to the edges of the tensile specimen. In an X30MnAl23-1 alloy, homogenous ε_{local} distribution throughout the gauge length could be observed until the beginning of necking. Thereafter failure in the material occurred by classical necking and strain localization.
- The ductile failure mode is the most predominant mode of failure in Al-added TWIP steels, mainly characterized by the formation of very fine dimples with a crack propagation along GBs.

Author Contributions: M.M. designed, performed and analyzed the experimental data such as SEM, tensile tests and mechanical properties. A.S. performed the EBSD measurements and analyzed the data. W.B. and U.P. contributed with ideas and intensive discussions. M.M. wrote the initial draft version. All authors contributed equally to the interpretation of results and writing the final version of the manuscript.

Funding: This research was funded by the German Research Foundation (DFG) within the framework of the SFB 761 "Steel-ab initio".

Acknowledgments: This work was carried out within the framework of the SFB 761 "Steel-ab initio" under the sub-project C6: Damage and failure. We would like to thank all the members of the SFB 761 "Steel-ab initio" project for their valuable cooperation and tremendous support.

Conflicts of Interest: The authors declare no conflict of interest.

Appendix A. Macro-Tensile Tests Setup for the Local Strain Analysis Using Digital Image Correlation

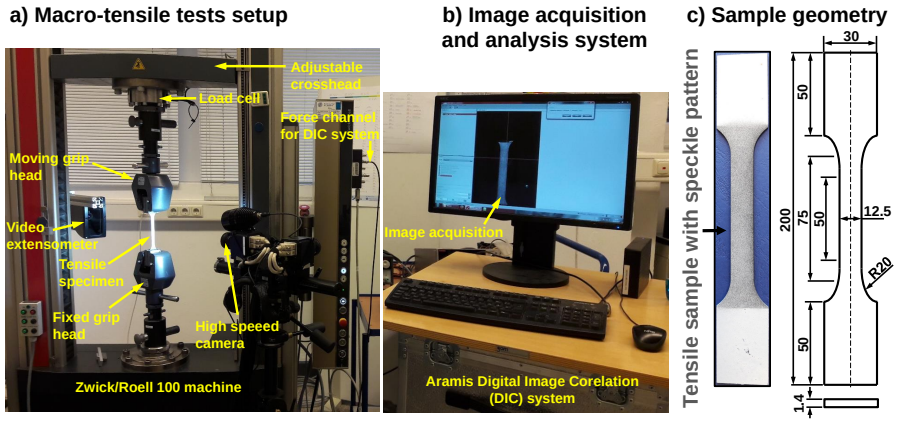

Figure A1. Macro-Tensile tests carried out in conjunction with DIC for investigating the local plastic strain (ε_{local}) evolution, nucleation, and propagation of deformation bands with increasing strain. (**a**) Tensile testing machine depicting the adjustable crosshead, grips for clamping, load cell, video extensometer and high-speed camera for image acquisition, (**b**) Aramis DIC system used for analysis, (**c**) Tensile sample with black and white speckle pattern prepared for ε_{local} measurement.

Appendix B. Macro-Tensile Tests Setup for Temperature Measurement using High Resolution Thermocamera

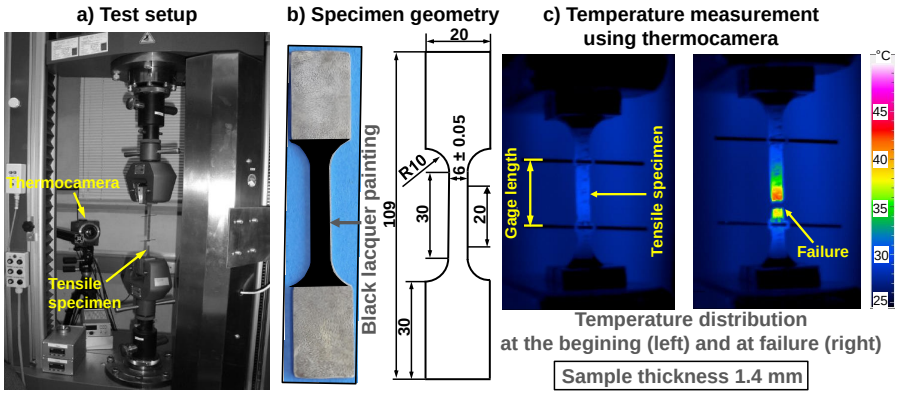

Figure A2. Temperature measurement setup using Macro-Tensile tests carried out in conjunction with high-resolution thermocamera for investigating the rise in temperature due to adiabatic heating. (**a**) Tensile testing machine depicting the thermocamera, tensile sample, (**b**) sample painted with black lacquer painting to minimize the reflections from the surroundings, (**c**) Image acquisition and analysis using IRBIS® online software.

References

1. Horvath, C.D. Advanced steels for lightweight automotive structures. In *Materials, Design and Manufacturing for Lightweight Vehicles*; Elsevier: Amsterdam,The Netherlands, 2010; pp. 35–78, doi:10.1533/9781845697822.1.35.
2. Hirsch, J. Aluminium in Innovative Light-Weight Car Design. *Mater. Trans.* **2011**, *52*, 818–824, doi:10.2320/matertrans.L-MZ201132.
3. Hirsch, J.; Al-Samman, T. Superior light metals by texture engineering: Optimized aluminum and magnesium alloys for automotive applications. *Acta Mater.* **2013**, *61*, 818–843, doi:10.1016/j.actamat.2012.10.044.
4. Sherman, A.M.; Sommer, C.J.; Froes, F.H. The use of titanium in production automobiles: Potential and challenges. *JOM* **1997**, *49*, 38–41, doi:10.1007/BF02914682.
5. Luo, A.; Sachdev, A. 12—Applications of magnesium alloys in automotive engineering. In *Advances in Wrought Magnesium Alloys*; Bettles, C., Barnett, M., Eds.; Woodhead Publishing Series in Metals and Surface Engineering; Woodhead Publishing: Cambridge, UK, 2012; pp. 393–426, doi:10.1533/9780857093844.3.393.
6. Kantanen, P.; Somani, M.; Kaijalainen, A.; Haiko, O.; Porter, D.; Kömi, J. Microstructural Characterization and Mechanical Properties of Direct Quenched and Partitioned High-Aluminum and High-Silicon Steels. *Metals* **2019**, *9*, 256.
7. Hall, J.N.; Fekete, J.R. Steels for auto bodies. In *Automotive Steels: Design, Metallurgy, Processing and Applications*; Woodhead Publishing: Cambridge, UK, 2017; pp. 19–45.
8. Krauss, G. Physical metallurgy of steels. In *Automotive Steels: Design, Metallurgy, Processing and Applications*; Woodhead Publishing: Cambridge, UK, 2017; pp. 95–111.
9. Grässel, O.; Krüger, L.; Frommeyer, G.; Meyer, L. High strength Fe–Mn–(Al, Si) TRIP/TWIP steels development–properties–application. *Int. J. Plast.* **2000**, *16*, 1391–1409, doi:10.1016/S0749-6419(00)00015-2.
10. Bouaziz, O.; Allain, S.; Scott, C.; Cugy, P.; Barbier, D. High manganese austenitic twinning induced plasticity steels: A review of the microstructure properties relationships. *Curr. Opin. Solid State Mater. Sci.* **2011**, *15*, 141–168, doi:10.1016/j.cossms.2011.04.002.
11. Saeed-Akbari, A.; Mosecker, L.; Schwedt, A.; Bleck, W. Characterization and Prediction of Flow Behavior in High-Manganese Twinning Induced Plasticity Steels: Part I. Mechanism Maps and Work-Hardening Behavior. *Metall. Mater. Trans. A* **2012**, *43*, 1688–1704, doi:10.1007/s11661-011-0993-4.
12. Lee, S.J.; Han, J.; Lee, S.; Kang, S.H.; Lee, S.M.; Lee, Y.K. Design for Fe-high Mn alloy with an improved combination of strength and ductility. *Sci. Rep.* **2017**, *7*, 3573, doi:10.1038/s41598-017-03862-y.
13. De Cooman, B.C.; Estrin, Y.; Kim, S.K. Twinning-induced plasticity (TWIP) steels. *Acta Mater.* **2018**, *142*, 283–362, doi:10.1016/j.actamat.2017.06.046.
14. Madivala, M.; Schwedt, A.; Prahl, U.; Bleck, W. Anisotropy and strain rate effects on the failure behavior of TWIP steel: A multiscale experimental study. *Int. J. Plast.* **2019**, 115, 178–199, doi:10.1016/j.ijplas.2018.11.015.
15. Madivala, M.; Bleck, W. Strain Rate Dependent Mechanical Properties of TWIP Steel. *JOM* **2019**, 71, 1291–1302.
16. Jung, I.C.; De Cooman, B.C. Temperature dependence of the flow stress of Fe–18Mn–0.6C–xAl twinning-induced plasticity steel. *Acta Mater.* **2013**, *61*, 6724–6735, doi:10.1007/s12540-014-1008-y.
17. Pierce, D.T.; Jiménez, J.A.; Bentley, J.; Raabe, D.; Wittig, J.E. The influence of stacking fault energy on the microstructural and strain-hardening evolution of Fe–Mn–Al–Si steels during tensile deformation. *Acta Mater.* **2015**, *100*, 178–190, doi:10.1016/j.actamat.2015.08.030.
18. Kim, J.K.; Kwon, M.H.; De Cooman, B.C. On the deformation twinning mechanisms in twinning-induced plasticity steel. *Acta Mater.* **2017**, *141*, 444–455, doi:10.1016/j.actamat.2017.09.043.
19. Madivala, M.; Schwedt, A.; Wong, S.L.; Roters, F.; Prahl, U.; Bleck, W. Temperature dependent strain hardening and fracture behavior of TWIP steel. *Int. J. Plast.* **2018**, *104*, 80–103, doi:10.1016/j.ijplas.2018.02.001.
20. Chen, L.; Kim, H.S.; Kim, S.K.; De Cooman, B.C. Localized Deformation due to Portevin–LeChatelier Effect in 18Mn–0.6C TWIP Austenitic Steel. *ISIJ Int.* **2007**, *47*, 1804–1812, doi:10.2355/isijinternational.47.1804.
21. Allain, S.; Cugy, P.; Scott, C.; Chateau, J.P.; Rusinek, A.; Deschamps, A. The influence of plastic instabilities on the mechanical properties of a high-manganese austenitic FeMnC steel. *Int. J. Mater. Res.* **2008**, *99*, 734–738.
22. Lee, S.J.; Kim, J.; Kane, S.N.; De Cooman, B.C. On the origin of dynamic strain aging in twinning-induced plasticity steels. *Acta Mater.* **2011**, *59*, 6809–6819, doi:10.1016/j.actamat.2011.07.040.
23. Kang, M.; Shin, E.; Woo, W.; Lee, Y.K. Small-angle neutron scattering analysis of Mn–C clusters in high-manganese 18Mn–0.6C steel. *Mater. Charact.* **2014**, *96*, 40–45, doi:10.1016/j.matchar.2014.07.010.

24. Song, W.; Houston, J. Local Deformation and Mn-C Short-Range Ordering in a High-Mn Fe-18Mn-0.6C Steel. *Metals* **2018**, *8*, 292, doi:10.3390/met8050292.
25. Koyama, M.; Sawaguchi, T.; Tsuzaki, K. TWIP Effect and Plastic Instability Condition in an Fe-Mn-C Austenitic Steel. *ISIJ Int.* **2013**, *53*, 323–329, doi:10.2355/isijinternational.53.323.
26. Koyama, M.; Sawaguchi, T.; Tsuzaki, K. Overview of Dynamic Strain Aging and Associated Phenomena in Fe–Mn–C Austenitic Steels. *ISIJ Int.* **2018**, *58*, 1383–1395, doi:10.2355/isijinternational.ISIJINT-2018-237.
27. Kim, J.; Estrin, Y.; De Cooman, B.C. Application of a Dislocation Density-Based Constitutive Model to Al-Alloyed TWIP Steel. *Metall. Mater. Trans. A* **2013**, *44*, 4168–4182, doi:10.1007/s11661-013-1771-2.
28. Kim, J.K.; De Cooman, B.C. Stacking fault energy and deformation mechanisms in Fe-xMn-0.6C-yAl TWIP steel. *Mater. Sci. Eng. A* **2016**, *676*, 216–231, doi:10.1016/j.msea.2016.08.106.
29. Yang, H.K.; Zhang, Z.J.; Dong, F.Y.; Duan, Q.Q.; Zhang, Z.F. Strain rate effects on tensile deformation behaviors for Fe–22Mn–0.6C–(1.5Al) twinning-induced plasticity steel. *Mater. Sci. Eng. A* **2014**, *607*, 551–558.
30. Yu, H.Y.; Lee, S.M.; Nam, J.H.; Lee, S.J.; Fabrègue, D.; Park, M.h.; Tsuji, N.; Lee, Y.K. Post-uniform elongation and tensile fracture mechanisms of Fe-18Mn-0.6C-xAl twinning-induced plasticity steels. *Acta Mater.* **2017**, *131*, 435–444, doi:0.1016/j.actamat.2017.04.011.
31. Yang, C.L.; Zhang, Z.J.; Zhang, P.; Zhang, Z.F. The premature necking of twinning-induced plasticity steels. *Acta Mater.* **2017**, *136*, 1–10, doi:10.1016/j.actamat.2017.06.042.
32. Fabrègue, D.; Landron, C.; Bouaziz, O.; Maire, E. Damage evolution in TWIP and standard austenitic steel by means of 3D X ray tomography. *Mater. Sci. Eng. A* **2013**, *579*, 92–98, doi:10.1016/j.msea.2013.05.013.
33. Lorthios, J.; Nguyen, F.; Gourgues, A.F.; Morgeneyer, T.F.; Cugy, P. Damage observation in a high-manganese austenitic TWIP steel by synchrotron radiation computed tomography. *Scr. Mater.* **2010**, *63*, 1220–1223.
34. Allain, S.; Chateau, J.P.; Bouaziz, O.; Migot, S.; Guelton, N. Correlations between the calculated stacking fault energy and the plasticity mechanisms in Fe–Mn–C alloys. *Mater. Sci. Eng. A* **2004**, *387–389*, 158–162.
35. Ledbetter, H.M.; Frederick, N.V.; Austin, M.W. Elastic–constant variability in stainless–steel 304. *J. Appl. Phys.* **1980**, *51*, 305–309, doi:10.1063/1.327371.
36. Dastur, Y.N.; Leslie, W.C. Mechanism of work hardening in Hadfield manganese steel. *Metall. Trans. A* **1981**, *12*, 749–759, doi:10.1007/BF02648339.
37. Sevsek, S.; Brasche, F.; Haase, C.; Bleck, W. Combined deformation twinning and short-range ordering causes serrated flow in high-manganese steels. *Mater. Sci. Eng. A* **2019**, *746*, 434–442, doi:10.1016/j.msea.2019.01.042.
38. Shun, T.; Wan, C.M.; Byrne, J.G. A study of work hardening in austenitic Fe-Mn-C and Fe-Mn-Al-C alloys. *Acta Metall. Mater.* **1992**, *40*, 3407–3412, doi:10.1016/0956-7151(92)90054-I.
39. Koyama, M.; Sawaguchi, T.; Tsuzaki, K. Deformation Twinning Behavior of Twinning-Induced Plasticity Steels with Different Carbon Concentrations. *Tetsu-to-Hagane* **2014**, *100*, 1253–1260.
40. Lebedkina, T.A.; Lebyodkin, M.A.; Chateau, J.P.; Jacques, A.; Allain, S. On the mechanism of unstable plastic flow in an austenitic FeMnC TWIP steel. *Mater. Sci. Eng. A* **2009**, *519*, 147–154, doi:10.1016/j.msea.2009.04.067.
41. Ogawa, T.; Koyama, M.; Tasan, C.C.; Tsuzaki, K.; Noguchi, H. Effects of martensitic transformability and dynamic strain age hardenability on plasticity in metastable austenitic steels containing carbon. *J. Mater. Sci.* **2017**, *52*, 7868–7882, doi:10.1007/s10853-017-1052-3.
42. Song, W.; Bogdanovski, D.; Yildiz, A.; Houston, J.; Dronskowski, R.; Bleck, W. On the Mn–C Short-Range Ordering in a High-Strength High-Ductility Steel: Small Angle Neutron Scattering and Ab Initio Investigation. *Metals* **2018**, *8*, 44, doi:10.3390/met8010044.
43. Wesselmecking, S.; Song, W.; Ma, Y.; Roesler, T.; Hofmann, H.; Bleck, W. Strain Aging Behavior of an Austenitic High-Mn Steel. *Steel Res. Int.* **2018**, *88*, 1700515, doi:10.1002/srin.201700515.
44. Allain, S.; Bouaziz, O.; Lebedkina, T.; Lebyodkin, M. Relationship between relaxation mechanisms and strain aging in an austenitic FeMnC steel. *Scr. Mater.* **2011**, *64*, 741–744, doi:10.1016/j.scriptamat.2010.12.039.
45. Gwon, H.; Kim, J.K.; Shin, S.; Cho, L.; De Cooman, B.C. The effect of vanadium micro-alloying on the microstructure and the tensile behavior of TWIP steel. *Mater. Sci. Eng. A* **2017**, *696*, 416–428.
46. Gutierrez-Urrutia, I.; Raabe, D. Grain size effect on strain hardening in twinning-induced plasticity steels. *Scr. Mater.* **2012**, *66*, 992–996, doi:10.1016/j.scriptamat.2012.01.037.



© 2019 by the authors. Licensee MDPI, Basel, Switzerland. This article is an open access article distributed under the terms and conditions of the Creative Commons Attribution (CC BY) license (http://creativecommons.org/licenses/by/4.0/).

3.4 Research Paper 4

Title: Strain Rate Dependent Mechanical Properties of TWIP Steel

Manjunatha Madivala and Wolfgang Bleck. Strain rate dependent mechanical properties of twip steel. *JOM*, Sep 2018. ISSN 1543-1851. doi: https://doi.org/10.1007/s11837-018-3137-0
© 2018 The Minerals, Metals & Materials Society. With kind permission from Springer Nature. The original publication is available at SpringerLink.

Highlights:

- The strain rate effect on the strain hardening behavior X60Mn22 TWIP steel.
- The mechanical properties of X60Mn22 TWIP steel compared with AHSS under both quasi-static and dynamic tensile tests.
- Energy absorption capacity of TWIP steel compared with AHSS.
- Adiabatic heating and its effect on deformation mechanisms.

JOM
https://doi.org/10.1007/s11837-018-3137-0
© 2018 The Minerals, Metals & Materials Society

Strain Rate Dependent Mechanical Properties of TWIP Steel

MANJUNATHA MADIVALA[1,2] and WOLFGANG BLECK[1]

1.—Institut für Eisenhüttenkunde (IEHK), RWTH Aachen University, Intzestraße 1, 52072 Aachen, Germany. 2.—e-mail: mmadivala@iehk.rwth-aachen.de

The effect of strain rate on the work-hardening behavior of high-manganese twinning-induced plasticity (TWIP) steel has been investigated. The influence of adiabatic heating and deformation rate on the mechanical properties was studied by quasi-static and dynamic tensile tests with synchronous temperature and strain measurements. TWIP steel has excellent strain-hardening behavior under both quasi-static and dynamic loading conditions. Strain rate has negligible effects on yield and tensile strength, but the uniform and total elongation decreases under dynamic tests. TWIP steel has excellent energy absorption (EA) capacity of above 55 kJ/kg at all strain rates compared to dual-phase steels, transformation-induced plasticity steel and ferritic steels. However, the EA of TWIP steel is slightly lower compared to austenitic stainless steels. A rise in temperature due to adiabatic heating has led to the increase of stacking fault energy, thereby resulting in a change of twinning behavior or the promotion of dislocation glide under dynamic loading.

Key words: TWIP steel, AHSS, Strain rate, Dynamic tests, Energy absorption

INTRODUCTION

Many years of research and development have made advanced high-strength steels (AHSS) versatile and effective materials for the construction of structural parts in modern automobiles. The high demand for safety, durability and cost effectiveness has driven steel producers and engineers to develop new grades that are lighter, stronger and better formable with improved mechanical properties.[1] These applications have ranged from increased strength for performance and weight reduction to zinc coatings for improved corrosion resistance to bake-hardenable grades for closure panel dent resistance.[2] Steels for automotive applications in general require greater formability for styling body panels to great strength for crash performance. The components not only have to be stronger to resist crushing in the passenger compartment but should also provide energy absorption in the front and rear crumple zones.[3] High-manganese twinning-induced plasticity (TWIP) steels are such a class of steels characterized by high work-hardening capacity along with exceptional strength and ductility.[4–6] The high-energy absorption capacity enables their use in the production of high-performance structural parts in automobiles with superior crash performance and lightweight structural reinforcements.[7] To describe the overall performance of steels combining both strength and elongation, the most commonly used material characteristic parameter is the ECO-index, expressed as the product of ultimate tensile strength (UTS) and uniform elongation (UE). The ECO-index value for conventional AHSS is limited to about 20 GPa %, but for high-Mn TWIP steels, it can go beyond 50 GPa %.[8] However, evaluating the material performance based solely on quasi-static tensile test properties, such as strength and ductility, and judging their suitability for structural parts may be inadequate since, during the crash of automobiles, the parts are not deformed until failure and the deformation rates are much larger.[9] The most commonly used techniques to characterize dynamic tensile properties are the servo-hydraulic (SH) system, the split Hopkinson pressure bar (SHB) system, the single bar (SB) system and the drop weight system, with each test method providing a specific strain rate ($\dot{\varepsilon}$) range. The bar systems (SBH and SB) are able to offer very high $\dot{\varepsilon}$ range (>1000/s) compared with the SH

Published online: 25 September 2018

system, yet the SH system is more reliable for relatively lower $\dot{\varepsilon}$ (< 500/s).[10] Thus, to check the crash-worthiness of TWIP steels, it is necessary to determine the mechanical properties and energy absorption capacity under dynamic loading conditions. In addition, it is also important to compare TWIP steel properties with other AHSS steel grades to check its suitability for different components.

The current study focuses on the influence of strain rate on the strain-hardening behavior of X60Mn22 TWIP steel. Uni-axial tensile tests were carried out at different strain rates ranging from 0.00001/s to 250/s to investigate the mechanical behavior under both quasi-static and dynamic conditions. Synchronous temperature measurements during deformation at various strain rates aid in the accurate estimation of stacking fault energy (SFE) at different strain rates, enabling the prediction of deformation mechanisms. The correlation of predicted deformation mechanisms with the mechanical behavior was also verified. Strain rate effect on the yield strength (YS), ultimate tensile strength (UTS), uniform elongation (UE), total elongation (TE) and energy absorption (EA) capacity of TWIP steel were compared with other AHSS, ferritic and austenitic stainless steels under both quasi-static and dynamic loading conditions. The temperature increase due to adiabatic heating and its subsequent effect on the mechanical properties at different strain rates has been presented in detail.

MATERIAL AND EXPERIMENTAL METHODS

Material

The material investigated in this study was industrially produced, cold-rolled and annealed sheet steel with a thickness of 1.4 mm. The chemical composition of the alloy was determined by using optical emission spectroscopy, and the SFE of the material was calculated using the sub-regular solution thermodynamic model of Ref. 11, as described in Ref. 12, and both are shown in Table I. The interface energy ($\sigma^{\gamma/\varepsilon}$) value of 10 mJ/m^2 was assumed for calculating the SFE.

The microstructure of the material consisted of fine equiaxed austenitic grains (γ) with an average grain size of about 3.0 μm. Figure 1a shows the inverse pole figure (IPF) map with respect to the rolling direction, depicting the grain sizes and the crystal orientation distribution. Figure 1b provides the grain size distribution function, where it can be observed that the grain size varied from 0.5 μm to 10 μm, with only a small fraction of grains being larger than 5 μm.

The materials used for the comparison of mechanical properties are mild steel DC04, high-strength steel ZStE340 with completely ferritic microstructure, dual-phase (DP) steels consisting of a dispersed martensite (M) in ferrite (F) matrix (DP600, DP800 and DP1000), transformation-induced plasticity (TRIP) steel consisting of ferrite, bainite and a small amount of retained austenite (A) and austenitic stainless steels (1.4301 and 1.4308) with fully austenitic microstructures. The grain size of DC04–22 μm, ZStE340–7 μm, DP600–5.5(F) + 4.1(M) μm, DP800–4.4(F) + 4.0(M) μm, DP1000–2.8(F) + 2.0(M) μm, TRIP–9.0(F) + A(< 1.5) μm, 1.4301–60 μm and 1.4308–60 μm. All the investigated steels are industrially melted, hot- and cold-rolled, annealed and temper-rolled to a final sheet thickness between 1.0 and 2.0 mm. More details about them can be found in Ref. 9. All the materials were tested in the as-delivered condition as explained in section "Mechanical Tests".

Mechanical Tests

Macroscopic tensile tests were carried out according to the DIN EN ISO 6892 standard with a specimen geometry consisting of a gage length of 20 mm and a width of 6 mm, as shown in Fig. 2a. The samples for all the tests were obtained using water-jet cutting along the rolling direction. The cut edges of the samples were polished up to a surface roughness of 0.125 μm. Tensile tests in conjunction with a thermocamera were performed at room temperature (RT) using a Zwick/Roell Z100 tensile testing machine. To study the influence of $\dot{\varepsilon}$ under quasi-static loading, different cross-head displacement rates, such as 0.018 mm/min, 0.18 mm/min, 1.8 mm/min, 18 mm/min, 180 mm/min and 900 mm/min, were set to achieve the strain rates of 0.00001/s, 0.0001/s, 0.001/s, 0.01/s, 0.1/s and 0.5/s, respectively. A video-extensometer was used to measure the change in length of the samples, which facilitates the recording of the actual elongation. Young's modulus, shear modulus and Poisson's ratio of the material were determined by an ultrasonic method, as described in Ref. 13.

To investigate the TWIP steel behavior under crash loading conditions, dynamic tensile tests were carried out at RT using a servo-hydraulic high-speed Roell/Amsler HTM2012 tensile testing machine equipped with an electro-optical extensometer and a thermocamera. Tensile tests with the

Table I. Chemical composition (in wt.%) and the SFE value (in mJ/m^2) of the investigated TWIP steel

C	Si	Mn	P	S	Cr	Ni	Cu	Al	V	N	Fe	SFE
0.59	0.21	22.26	0.013	< 0.001	0.08	0.02	0.02	0.01	0.27	0.019	Bal.	27

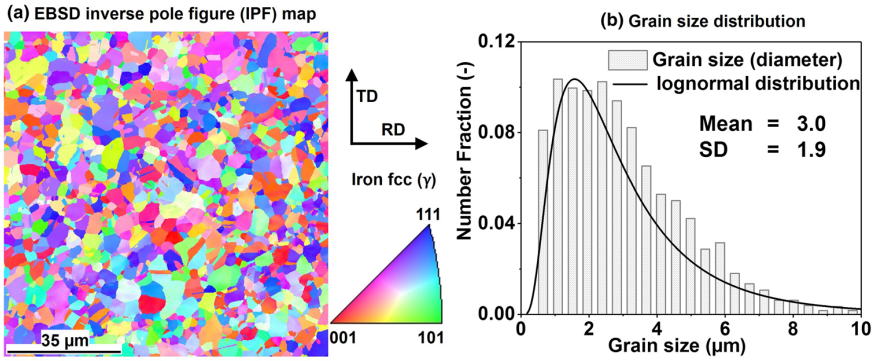

Fig. 1. Microstructure and grain size distribution of the investigated TWIP steel. (a) EBSD IPF map of undeformed sample showing variation in grain size and orientation; microstructure is fully austenitic (γ); *RD* rolling direction; *TD* transverse direction. (b) Grain size distribution obtained from EBSD measurements fitted with a log-normal distribution function; average grain size is 3.0 µm and standard deviation (*SD*) is 1.9 µm.

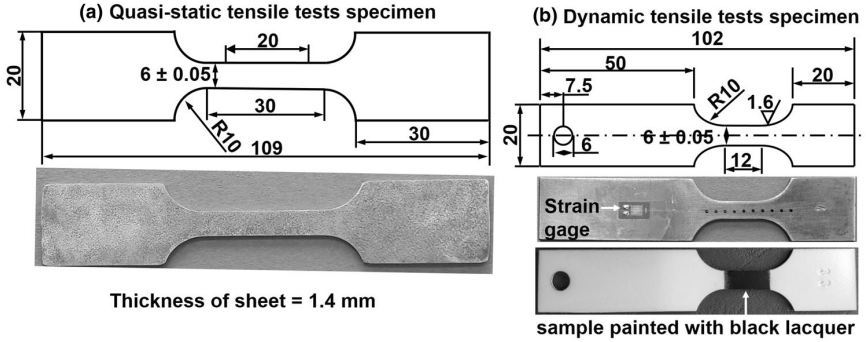

Fig. 2. Geometries used for the quasi-static and dynamic tensile tests.

ram speeds in the range from 0.01 mm/s to 5000 mm/s can be performed with the geometry shown in Fig. 2b. The speeds used in the current work were 12 mm/s, 120 mm/s, 1200 mm/s and 3000 mm/s, which correspond to the strain rates of 1/s, 10/s, 100/s and 250/s, respectively. The tensile force was measured by a standard piezo-electric load cell up to a $\dot{\varepsilon}$ of 10/s, and at high strain rates using a titanium load cell with strain gages attached to the sample shoulder (as shown in the middle of Fig. 2b). The strain was measured by an inductive displacement sensor for the piston stroke, and the results were verified by using an electro-optical extensometer. The storage of test data was carried out using a 4-channel transient recorder. The sample was painted with black lacquer to achieve the optimum contrast for the elongation measurements using an extensometer of type Zimmer 200×.

Temperature variation in the specimen during deformation was investigated by carrying out tensile tests in conjunction with a high-speed infrared thermography camera (JADE III MWIR S MTC; InfraTec). A sample geometry shown in Fig. 2b was used for all tests. A Zwick/Roell Z100 machine was used for the quasi-static tests and Roell/Amsler HTM2012 for the dynamic tests. Each specimen was coated with a black lacquer to minimize the reflections from the surroundings. The temperature measurement range of the camera is from −40°C to 600°C. The temperature measurement was carried out as a function of strain rate and maximum image acquisition rate in different photography modes. The data was acquired and analyzed using IRBIS® online software to extract the temperature variation within the gage length of the specimen. The temperature data were correlated with the strain measured from the extensometer. For all the quasi-static tests, images were acquired at a frame rate of 1 Hz in full-frame-mode with a maximum of 384 × 288 pixels and with a temperature calibration range from 30°C to 130°C. At the strain rates of 1/s and 10/s, images were acquired in quarter-frame-mode at a frame rate of 888 Hz with a maximum of 80 × 60 pixels and a calibration range from 30°C to 170°C. For strain rates above 10/s, images were captured using line-mode at a frame rate of 6578 Hz with a maximum of 320 × 1 pixels and a calibration range from 30°C to 150°C. The major difference between line-mode and the others is that only a single line in the center of the sample over the entire gage length will be scanned during deformation, whereas full/half/quarter images will

be captured in the other modes. The overall accuracy of the temperature measurements within the range of calibration was ± 1°C.

RESULTS

The strain rate-dependent properties of TWIP steel are of crucial importance for evaluating the crash performance of the material, and they also play a large role in selecting the optimal forming processes for the manufacturing of components. Understanding the mechanical behavior under both quasi-static and dynamic conditions will aid in choosing TWIP steel for a particular application.

Mechanical Properties

The σ–ε curves and the strain-hardening rate (SHR) obtained by uni-axial tensile tests at RT at different $\dot{\varepsilon}$ are shown in Fig. 3, where periodic serrations of type A can be observed, caused mainly by dynamic strain aging (DSA). At a $\dot{\varepsilon}$ of 0.001/s, the material shows almost linear flow behavior throughout the deformation and an abrupt failure at the end. Initially, hardening is characterized by a sharp drop of the SHR, which then increases to reach a constant value with small increase in deformation. The first marked inflexion in SHR occurs at $\sim$ 0.05 true strain, where it started to decrease steadily. Thereafter, SHR shows a general drop until the final failure, indicating no additional active deformation mechanisms. The SHR at the beginning of the deformation for a $\dot{\varepsilon}$ of 0.001/s is above 3000 MPa, and it decreases to about 2000 MPa at failure.

The mechanical properties of TWIP steel, such as YS, UTS, UE, TE, Lankford coefficient (r-value), strain hardening exponent (n-value), density (ρ), Young's modulus (E), shear modulus (G), Poisson's ratio (ν) and ECO-index tested at a $\dot{\varepsilon}$ of 0.001/s, are presented in Table II. The material has a YS of 500 MPa along RD and a UTS of above 1100 MPa. TE or the macroscopic failure strain (ε_f) of the material is about 45%. The ECO-index of TWIP steel is about 52 GPa % and the strain-hardening exponent (n-value) is $\sim$ 0.33. The material has a Young's modulus of 165 GPa, shear modulus of 63 GPa and a Poisson's ratio of 0.31.

Effect of Strain Rate

The σ–ε curves of quasi-static and dynamic tensile tests are shown in Fig. 3a and c. Serrations can be observed on the σ–ε curves depicted in Fig. 3a for all $\dot{\varepsilon}$ except at 0.5/s. With an increase in $\dot{\varepsilon}$ from 0.00001/s to 0.5/s, the serrations start to disappear and the failure behavior changes from abrupt failure to necking and failure. Under the dynamic loading conditions, as shown in Fig. 3c, smooth flow behavior without any serrations can be observed along with the pronounced necking and failure at the end. The serrations observed on the σ–ε curves for $\dot{\varepsilon}$ of 100/s and 250/s in Fig. 3c are not due to DSA, but mainly due to the force measurement.

The SHR ($d\sigma/d\varepsilon$) plotted as a function of quasi-static and dynamic $\dot{\varepsilon}$ are shown in Fig. 3b and d, respectively. The hardening for all $\dot{\varepsilon}$ is characterized by a sharp drop in the SHR, followed by its increase to a constant value with further increase in deformation. The first inflexion in SHR occurs at $\sim$ 0.05 true strain for a $\dot{\varepsilon}$ of 0.00001/s and it shifts to the right with increasing $\dot{\varepsilon}$. The inflexion in SHR for $\dot{\varepsilon}$ above 0.5/s occurs at $\sim$ 0.1 true strain, where it started to decrease steadily. The SHR for a $\dot{\varepsilon}$ of 0.00001/s is about 3500 MPa at the beginning of the deformation and decreases to about 2000 MPa at failure. With the increase in $\dot{\varepsilon}$ from 0.00001/s to 0.5/s, the SHR decreases from 3500 MPa to 2800 MPa at the beginning of the deformation. The SHR of TWIP steel decreases with increasing $\dot{\varepsilon}$ and shows a general drop for all quasi-static tests until the final failure, indicating no additional active deformation mechanisms. The SHR is above 2500 MPa for all dynamic tests up to a true strain of $\sim$ 0.2. With further increase in deformation, the SHR decreases steadily for all dynamic tests, suggesting a slight change in the deformation behavior of the material.

The variation of mechanical properties with increasing $\dot{\varepsilon}$ is plotted in Fig. 3e. The YS of the material remains almost constant for all quasi-static tests, and starts to increase linearly when the $\dot{\varepsilon}$ changed to dynamic. The UTS of the material is above 1000 MPa until a $\dot{\varepsilon}$ of 0.5/s, and it started to decrease slightly by about 50 MPa with the further increase in $\dot{\varepsilon}$. The uniform/total elongation (UE/TE) of the material is almost the same for the quasi-static tests, but with increasing $\dot{\varepsilon}$, the UE decreased almost linearly, whereas the TE is almost constant at high $\dot{\varepsilon}$ as well.

The strain rate influence on the YS, UTS and UE/TE of TWIP steel compared with other steels [AHSS (DP steels and TRIP steel), austenitic stainless steel (1.4301) and ferritic steels (mild steel–DC04 and extra deep drawable steel–ZStE340)] is shown in Fig. 4. The results show significant strain rate dependencies for TWIP steel and also for all other steels considered for comparison. The YS of all steels increase continuously with increasing $\dot{\varepsilon}$, as shown in Fig. 4a; however, TWIP and TRIP steels have smaller slopes compared to ferritic, DP steels and austenitic stainless steel. Strain rate has a remarkable effect on YS in DP steels, where YS increases drastically for DP1000 and marginally for DP600 and DP800 with increasing $\dot{\varepsilon}$. The UTS of TWIP steel decreases slightly with increasing $\dot{\varepsilon}$ compared to increases in UTS in all other steels, as plotted in Fig. 4b. The increase in tensile strength is smaller in the cases of DP1000 and TRIP steel, whereas in other steels the effect is more substantial. The UE of the TWIP steel decreases with increasing $\dot{\varepsilon}$ similar to ferritic steels, as shown in Fig. 4c. The austenitic stainless steel, DP600 and DP800 show slight decreases in UE initially and

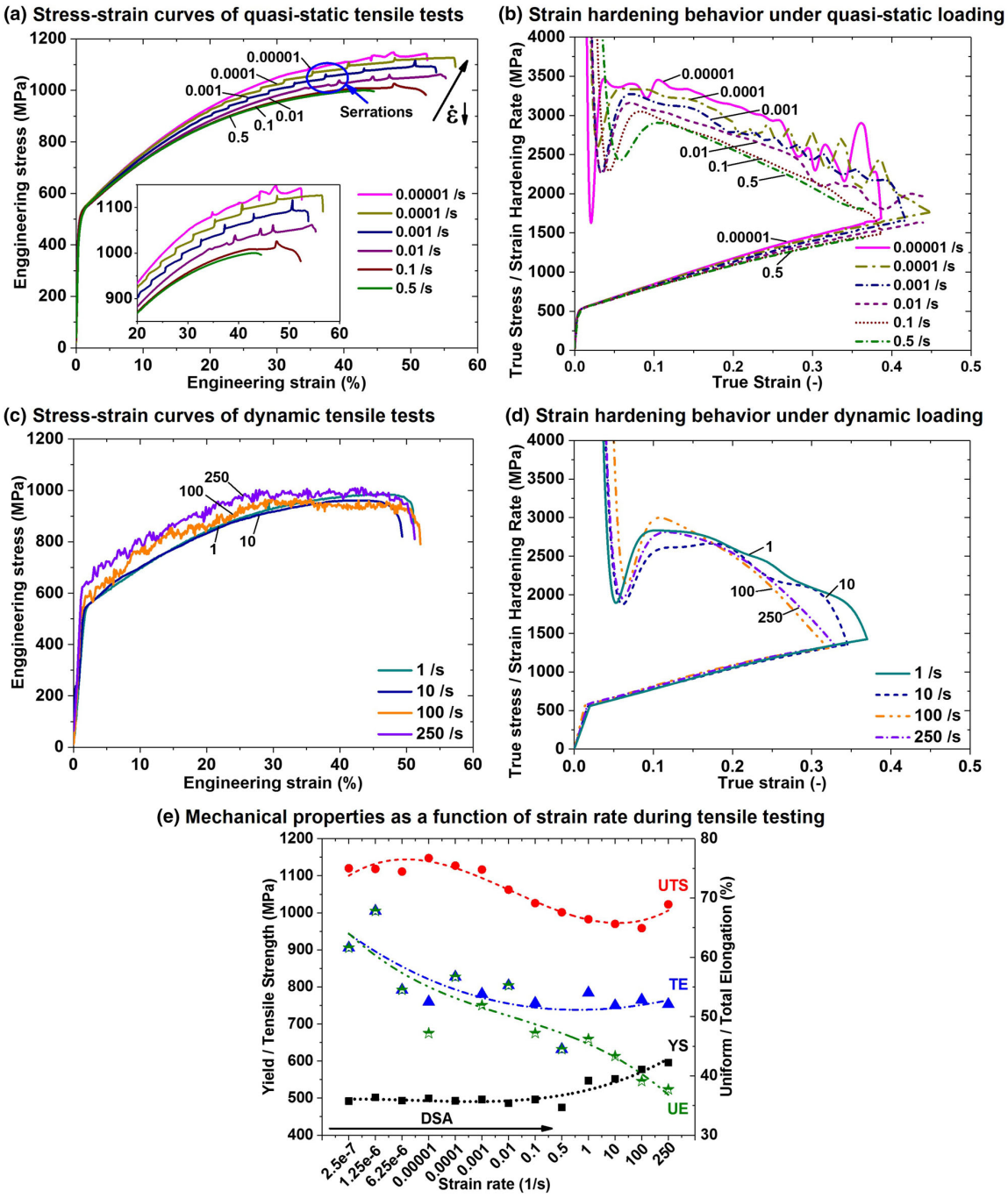

Fig. 3. Strain rate effect on the mechanical properties.The strain-hardening curves are smoothened for strain rates of 100/s and 250/s. *YS* yield strength, *UTS* ultimate tensile strength, *UE* uniform elongation, *TE* total elongation.

thereafter increases for very high $\dot{\varepsilon}$. Strain rate has a negligible effect on the UE of TRIP steel and DP1000. From Fig. 4d, it can be observed that the TE values of TWIP steel, austenitic stainless steel and TRIP steel first decrease up to moderate strain rates followed by an increase up to the highest strain rates, obtaining the same values as measured under quasi-static conditions. The TE of ferritic

Table II. Mechanical properties of X60Mn22 TWIP steel: yield/ultimate tensile strength (*YS*/*UTS*), uniform/total elongation (*UE*/*TE*), Lankford coefficient (*r* value), strain hardening exponent (*n* value), Young's modulus (*E*), shear modulus (*G*), Poisson's ratio (*v*) and ECO-index

Direction	YS MPa	UTS MPa	UE %	TE %	*r* value –	*n* value –	E GPa	G GPa	*v* –	ECO-index GPa %
RD	501	1139	45.7	45.7	0.81	0.33	165.7	62.9	0.316	52

All data are average values determined from at least three parallel experiments. *RD* rolling direction.

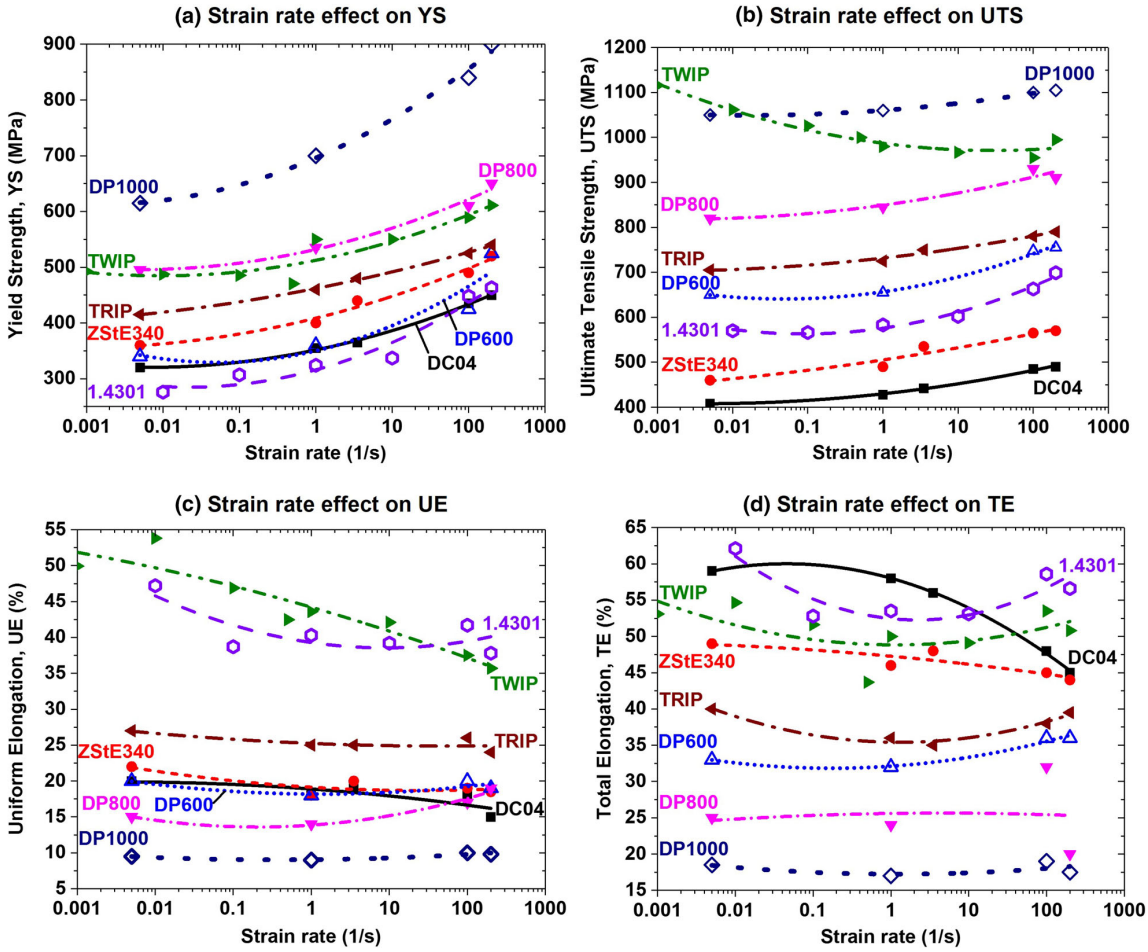

Fig. 4. Comparison of the mechanical properties of TWIP steel with other advanced high strength steels (AHSS) and conventional steels. The mechanical properties data for ferritic steels, DP steels and TRIP steel were taken from Ref. 9. The data for austenitic stainless steel 1.4301 were taken from Ref. 14. All data are average values determined from at least three repeated experiments.

steels also decreases with increasing $\dot{\varepsilon}$, similar to the UE, as illustrated in Fig. 4c.

The strain rate effect on UTS, UE and TE is negligible for TRIP and DP1000, whereas the YS increase in DP1000 is fairly large compared to TRIP steel. In the case of TWIP steel, the strain rate effect on YS, UTS and TE is marginal compared to the huge influence on UE. The strain rate dependency of the elongation values, shown in Fig. 4c and d, indicate the largest difference between UE and TE for ferritic steels, whereas for all other steels both the elongation values were found to be similar. The ferritic steels DC04 and ZStE340, show decreases in elongation values over the whole range of $\dot{\varepsilon}$, whereas

the ductility of 1.4301, TWIP, TRIP and DP600 steels is minimum at intermediate $\dot{\varepsilon}$. The elongation values at high strain rates are almost the same or even higher as those of quasi-static conditions. This behavior of the materials can be correlated to local temperature increases in the specimens due to adiabatic heating.

The local temperature increase in the material during deformation due to adiabatic heating is shown in Fig. 5. For tensile tests at different $\dot{\varepsilon}$, the temperature distribution over the entire gage length of the specimen with increasing strain is shown in Fig. 5a, and the temperature variation in the middle of the specimen is shown in Fig. 5b. It can be observed from Fig. 5a that, with the increase in macroscopic strain, the temperature in the specimen rises due to adiabatic heating. As the $\dot{\varepsilon}$ increases from quasi-static to dynamic, the temperature raises quite rapidly in the specimen during deformation. The localized deformation in the material after reaching uniform elongation will also lead to a rise in temperature locally. At the $\dot{\varepsilon}$ of 0.01/s and 0.5/s, the maximum localized temperature

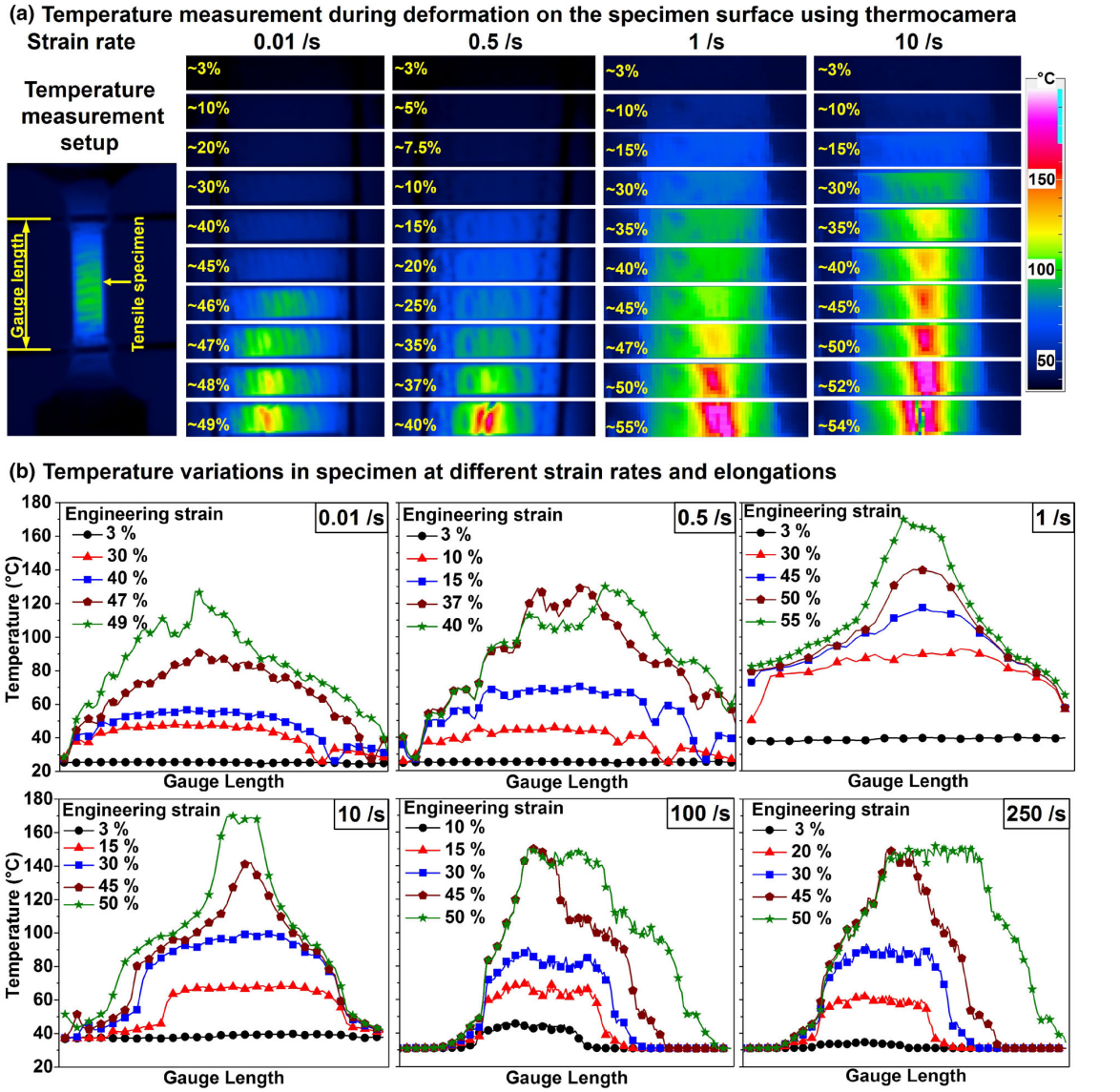

Fig. 5. Strain rate influence on the adiabatic heating during deformation. (a) Left measurement setup illustration; middle temperature distribution at different strain rates and macroscopic strains over the entire gage length; right legend for local temperature distribution. (b) Thermocamera temperature calibration range: from 30–130°C for strain rates of 0.01/s and 0.5/s; from 30–170°C for 1/s and 10/s; from 30–150°C for 100/s and 250/s.

just before the failure is $\sim$ 120°C, whereas under dynamic tests, the temperature rises even higher to $\sim$ 180°C and above. However, at the point before the uniform elongation, the average temperature is between 60°C and 100°C. At $\sim$ 30% strain, the temperature distribution in the specimen is uniform throughout and the average values are about 40°C, 80°C, 90°C, 100°C, and 110°C at a $\dot{\varepsilon}$ of 0.01/s, 0.5/s, 1/s, 10/s and 100/s, respectively. After 30% strain, the temperature distribution is localized and increases further close to necking. Just before failure, the temperature raises above 200°C locally, which is also beyond the range of temperature measurements in high-speed testing. It can be seen from Fig. 5b that, as the $\dot{\varepsilon}$ is increased from quasi-static to dynamic, localization of the temperature increases due to necking at high $\dot{\varepsilon}$, whereas the temperature distribution is more uniform over the gage length until failure at low $\dot{\varepsilon}$. The rise in temperature above 180°C due to adiabatic heating could influence the deformation mechanisms active at different $\dot{\varepsilon}$, leading to change in the material failure behavior.

Energy Absorption

The important property which characterize the crash behavior of the material is the specific energy absorption (EA), defined as the deformation energy per unit volume at a given temperature (23°C) and at the $\dot{\varepsilon}$ of 100/s to 1000/s, determined by high-speed tensile tests. Similarly, ECO-index parameter defined as the product of UTS and UE is also an indicator of the overall performance of the material.

Energy absorption values for different steels are determined by integrating the area under the σ–ε curve until the start of the decrease in stress, as shown in Fig. 6a, and alternatively until 10% elongation. The area under the σ–ε curve for TWIP steel is quite large compared with all other AHSS, indicating high energy absorbed per volume (W). In order to exclude the influence of the specimen geometry, particularly the different thickness values, the total energy values were converted to mass-specific values. The bar diagram in Fig. 6c shows the total specific EA capacity of the TWIP steel in comparison with other AHSS (DP steels and TRIP steel), ferritic steels (DC04 and ZStE340) and austenitic stainless steels (1.4301 and 1.4318).[9] EA values of TWIP steel are double or even higher than those of DP steels (DP600, DP800 and DP1000) and ferritic steels. TWIP steel absorbs 1.5 times more energy than that of the TRIP steel and also more than twice that of DP1000 at all $\dot{\varepsilon}$. However, both austenitic stainless steels (1.4301 and 1.4318) show slightly higher EA compared to TWIP steel under crash conditions. At a $\dot{\varepsilon}$ above 100/s, specific EA values of TWIP steels are above 55 kJ/kg and all other AHSS and ferritic steels possess energy values between $22 \leq W \leq 35$ kJ/kg, which absorb 60–35% less energy compared to that of the crash-resistant TWIP steel.

Higher EA is achieved by the TWIP steel for all $\dot{\varepsilon}$. However, the absorption is slightly lower for the dynamic tests, since there is a sharp drop in UTS and UE with increasing $\dot{\varepsilon}$. Similarly, TRIP steel also absorbs high energy for all $\dot{\varepsilon}$, but the absorption is maximum for the dynamic tensile tests ($\dot{\varepsilon}$ = 100/s or 250/s), since the YS and UTS increases with increasing $\dot{\varepsilon}$ with no significant effect on the UE. The energy values of austenitic stainless steels are nearly twice that of TRIP steel and also slightly higher than that of TWIP steel. The EA is even higher ($\sim$ thrice) when compared to ferritic and DP steels. At a $\dot{\varepsilon}$ of 200/s, the energy values of TRIP steel are 1.5 times that of DP800, DP1000 and slightly higher compared to DP600. At $\dot{\varepsilon} = 200$/s, EA values of DP600 are high compared to DP800, DP1000 and also ferritic steels. At lower $\dot{\varepsilon}$ up to 1/s, EA values are similar for all DP steels. DP800 shows high energy only at 100/s, whereas at all other $\dot{\varepsilon}$, EA is less and also lower values at higher $\dot{\varepsilon}$. Similar trends can also be seen in DP1000. The EA of DC04 is nearly constant for all $\dot{\varepsilon}$ because the decrease in UE/TE is compensated by the increase in YS/UTS. Energy values are similar for ZStE340 in quasi-static tests, but show increased values for dynamic tests, since the ductility decrease with increasing $\dot{\varepsilon}$ is smaller.

It can be understood from Figs. 6c and 4c, that for all steels the change in EA at different $\dot{\varepsilon}$ is mainly influenced by elongation values. Considering the fact that parts subjected to crash loading will never be deformed until failure, it is reasonable to compare EA values of steels up to 10% elongation. This procedure also eliminates the adiabatic heating effects and also statistical errors arising in estimating elongation values. Figure 6d shows the EA comparison up to 10% elongation. It can be observed that TWIP steel absorbs more energy compared to all other AHSS and ferritic steels for up to 10% elongation. However, the austenitic stainless steels still absorbs more energy compared to all other steels considered for the comparison. Total EA of DP800 and DP1000 under crash conditions ($\dot{\varepsilon} = 100$/s) is less than that of DP600 and TRIP steel, whereas for up to 10% elongation they both absorb more energy compared to DP600 and TRIP steel. The EA values for TRIP steel are higher even if the value at $\dot{\varepsilon} = 100$/s is slightly lower than that of DP800 and DP1000. EA values for ferritic steels look almost similar to the behavior shown in Fig. 6c, especially for ZStE340, whereas for DC04 the values increases slightly with increasing $\dot{\varepsilon}$, but the energy values are still lowest compared to all other steels considered.

Figure 6b shows the comparison of the ECO-index of TWIP steel with other AHSS and conventional steels. It is shown in the diagram that the ECO-index of TWIP steel decreases from $\sim$ 55 GPa % to $\sim$ 35 GPa %, when $\dot{\varepsilon}$ changed from quasi-static to dynamic. The ECO-index of TWIP steel is above 35 GPa % for all $\dot{\varepsilon}$, whereas for all other steel grades,

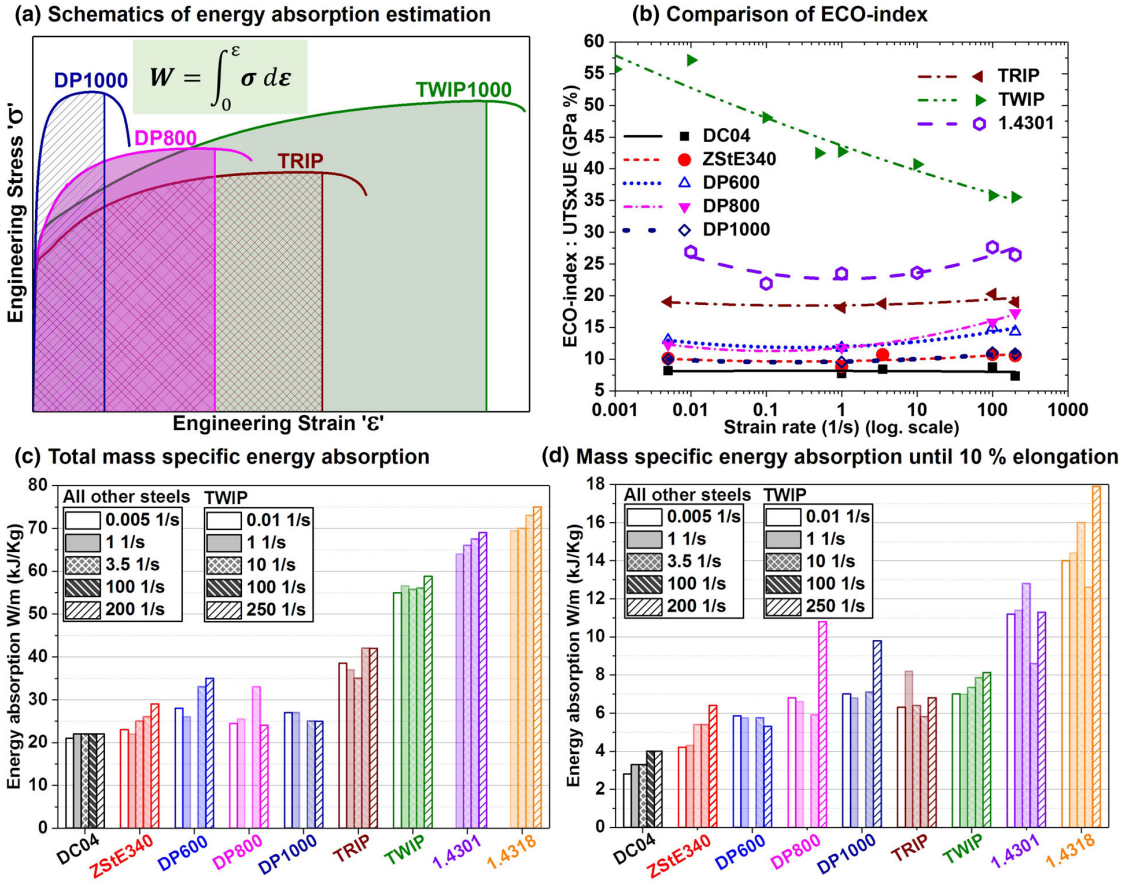

Fig. 6. Comparison of ECO-index and specific energy absorption capacity of TWIP steel with other AHSS and conventional steels. The mass specific energy absorption data for AHSS, ferritic and austenitic stainless steels were taken from Ref. 9. The strain rates used for TWIP steel are slightly different from other steels.

the ECO-index values are between $5 \leq$ ECO-index ≤ 25 GPa %, which are half that of the damage-resistant TWIP steel. TWIP steel has high tensile strength of about 1000 MPa, an ECO-index of above 35 GPa % and also excellent specific EA of about 55 kJ/kg at all $\dot{\varepsilon}$ up to 250/s, making it a highly suitable material for all automotive safety relevant parts subjected to both frontal and side crashes.

DISCUSSION

The measurement of temperature evolution during deformation is crucial for TWIP steel, since various temperature-dependent deformation mechanisms may be activated during straining at different strain rates. During a tensile test, a portion of the applied work is converted to heat during plastic deformation of the material. High strain rate tests can have test durations in the order of milliseconds to seconds, which do not allow sufficient amounts of time for heat diffusion from the interior of a sheet specimen to a free surface and subsequent transfer to the surroundings. Hence, adiabatic heating occurs in the material, which also depends on the sheet thickness. The larger sheet thickness leads to much higher increase of temperature. The temperature rise associated with the plastic deformation at different $\dot{\varepsilon}$ can have a significant softening effect on the flow stress, resulting in change in mechanical behavior.

The increase in temperature due to adiabatic heating at different $\dot{\varepsilon}$ at a point within the gage length for TWIP, TRIP and austenitic stainless steel is shown in Fig. 7c. It can be observed that for TWIP steel, the temperature increased beyond 180°C for all tests close to fracture. However, at about 30% strain, the temperature increase is between 60 and 100°C. Such a large increase in temperature in the material results in the increase of SFE from 27 mJ/m^2 to about 32–39 mJ/m^2. The variation of SFE with temperature for chemical composition shown in Table I is given in Fig. 7b. For the SFE below 40 mJ/m^2, mechanical twinning is the predominant deformation mode which occurs along with

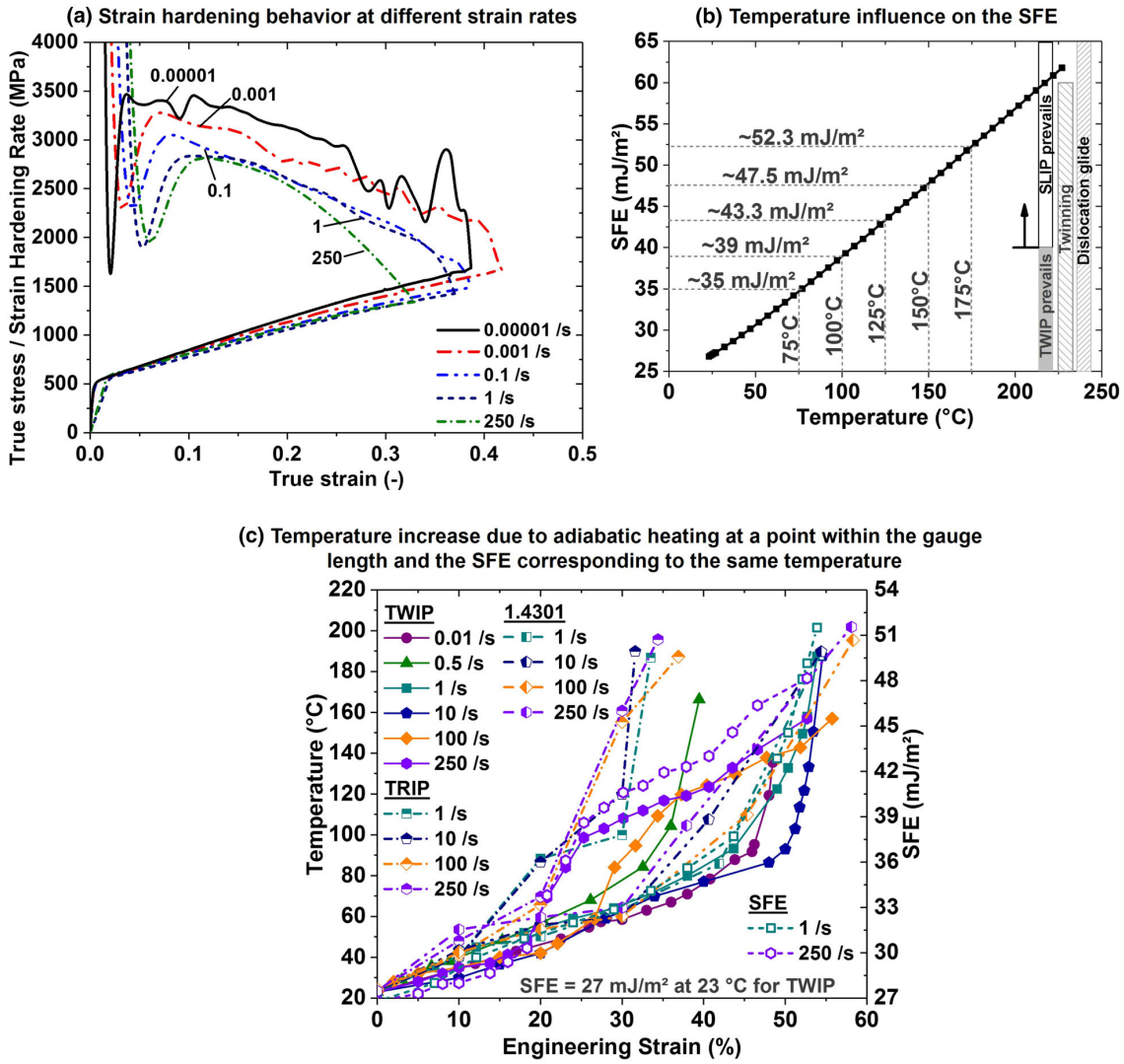

Fig. 7. Strain rate effect on work hardening and adiabatic heating. Stacking fault energy (*SFE*) was calculated for X60Mn22 alloy using the thermodynamic approach, as described in Ref. 12, assuming an interface energy ($\sigma^{\gamma/\varepsilon}$) value of 10 mJ/m^2. The temperature increase due to adiabatic heating for TRIP steel and austenitic stainless steel 1.4301 are taken from Ref. 14.

dislocation glide; thereafter, dislocation slip becomes the most predominant deformation mode. Twinning still occurs for SFE up to 60 mJ/m^2, but dislocation slip becomes the most preferred deformation mode above 40 mJ/m^2.[12] For $\dot{\varepsilon}$ of 0.01/s, 0.5/s, 1/s and 10/s, at about 30% strain, the temperature can increase to about 60°C from RT, which corresponds to a SFE value of 32 mJ/m^2. This indicates that, with increasing macroscopic strain, the temperature rises due to adiabatic heating leading to an increase in SFE preferring deformation twinning. At very high $\dot{\varepsilon}$ of 100/s and 200/s, at about 30% strain, the temperature can increase above 100°C from RT, which corresponds to a SFE value above 40 mJ/m^2. This large increase in SFE has led to change in the prevailing deformation mode from deformation twinning to dislocation glide.

The $\dot{\varepsilon}$ effect on the work-hardening behavior is shown in Fig. 7a. It can be observed that the SHR decreases with increasing $\dot{\varepsilon}$. Based on the detailed work described in Ref. 15, the SHR of fine-grained X60Mn22 TWIP steel can be divided into three distinct stages of hardening: (1) continuous decrease in the SHR, which involves dynamic recovery process such as cross-slip and annihilation of screw dislocations of opposite signs; (2) rapid increase in

the SHR, implies that refinement of the mean free path by deformation twinning at strain level slightly higher than the onset of yielding; and (3) steady decrease in the SHR, ascribed to the reduced additional refinement of the dislocations and twin substructures, together with the increasing strengthening effect of the individual twins as obstacles to dislocation glide, reduce the capacity for trapping more dislocations leading to a decrease in SHR. With increasing $\dot{\varepsilon}$ from quasi-static to dynamic, the stage 1 of hardening has become wider and the initiation of stage 2 has shifted to larger strains. This could be mainly attributed to the change in twinning behavior.

The change in the rate of deformation could influence twin nucleation and twin density. The occurrence of DSA at lower $\dot{\varepsilon}$ in general results in locking of the partial dislocations leading to high dislocation density.[16] The fine grain microstructure along with the high density of dislocations at grain boundaries (GB) result in higher stress concentration which could assist in nucleation of twins at GB.[17] But this effect can be suppressed at high $\dot{\varepsilon}$ due to the suppression of DSA at high $\dot{\varepsilon}$. The experimental study by Ref. 18 showed that the number of twin nucleation sites per grain boundary area at lower $\dot{\varepsilon}$ is much larger compared to fewer twin nucleation sites at higher $\dot{\varepsilon}$. The thickness of individual twins increased from 10 nm at a $\dot{\varepsilon}$ of 0.0001/s to 40 nm at a $\dot{\varepsilon}$ of 10/s, and individual twin spacing from 20 nm to 60 nm. The study also found decrease in the twin area fraction with increasing $\dot{\varepsilon}$. This is mainly due to the increase in the average energy required for twin nucleation at high $\dot{\varepsilon}$, which led to suppressed twinning.[18] This indicates differences in twin nucleation and growth behavior at quasi-static and dynamic loading. The synchrotron x-ray diffraction and transmission electron microscopy study by Ref. 19 at low and high $\dot{\varepsilon}$ stated that the dislocations and deformation twins are suppressed at high $\dot{\varepsilon}$ deformation, indicating negative strain rate sensitivity of work hardening. The detailed study by Ref. 20 also showed a decrease of twin volume fraction with increasing rate of deformation through electron channeling contrast imaging measurements and crystal plasticity simulations. This change in deformation behavior could be mainly attributed to adiabatic heating associated with high $\dot{\varepsilon}$ deformation. The increase of temperature at $\dot{\varepsilon}$ above 1/s lead to SFE increase above 40 mJ/m^2 favoring dislocation glide above 25% strain. Hence, in stage 3 of hardening, the SHR decreases more rapidly at higher $\dot{\varepsilon}$ compared to lower $\dot{\varepsilon}$. Higher temperature has decreased the work-hardening rate by increasing the rate of dynamic recovery and the suppression of deformation twinning due to the higher SFE.[16]

Similar to TWIP steel, the increase in $\dot{\varepsilon}$ led to significant rise in temperature due to adiabatic heating for TRIP steel and austenitic stainless steel 1.4301. The temperature rise in austenitic stainless steel is almost the same as that of TWIP steel at different strains, but in TRIP steel, the temperature rises above 60°C at about 20% elongation. By comparing adiabatic heating in three different steels at high $\dot{\varepsilon}$, it is clear that TWIP steel shows significantly different behavior compared to TRIP steel. To compare the effect of adiabatic heating, total mass specific EA and EA up to 10% elongation of TWIP steel is compared with different AHSS, ferritic and austenitic stainless steels at a $\dot{\varepsilon}$ of 100/s tested under similar conditions, as shown in Fig. 6c and d. It is evident that TWIP steel absorbs much more energy compared to AHSS and ferritic steels, but slightly less energy than austenitic stainless steels. Even for up to 10% elongation TWIP steel absorbs slightly more energy compared to DP1000. However, at a fixed elongation value of 10%, EA values of ferritic steel ZStE340, DP600, DP800 and TRIP are about 6 kJ/kg, while DP1000 and TWIP1000 absorb marginally more energy, of about 7.5 kJ/kg or 7.8 kJ/kg, while austenitic stainless steels absorb the highest energy of about 9 kJ/kg (1.4301) to 13 kJ/kg (1.4318). Among all the steels considered, ferritic steel DC04 absorbs the least amount of energy. Since the mechanical behavior of steels and the active deformation mechanisms vary largely with $\dot{\varepsilon}$, such comparisons are necessary for choosing TWIP steel for specific applications instead of others.

CONCLUSION

The X60Mn22 TWIP steel was investigated by uni-axial tensile tests under both quasi-static and dynamic conditions. For investigating the strain rate effect on the mechanical behavior, various in situ tensile testing methods were applied. The synchronous temperature measurements during deformation was monitored by carrying out tests in conjunction with a thermocamera. The main conclusions can be drawn for the investigated TWIP steel as follows:

- Strain-hardening rate of TWIP steel is extraordinarily high under both quasi-static and dynamic tests until maximum strain/failure. This can be attributed to the deformation by dislocation glide in combination with deformation twinning. A rise in temperature due to adiabatic heating has led to increases of SFE, thereby resulting in a change of twinning behavior or the promotion of dislocation glide under dynamic loading.
- Adiabatic heating has led to an increase in the temperature of the sample to about 35–50°C under quasi-static tests (0.01–0.5/s) up to 30% elongation, whereas under dynamic tests (1–250/s), it rose to about 85–100°C from room temperature (23°C). At the point of fracture, the temperature increased beyond 100°C under quasi-static tests and 180°C under dynamic tests. The increase in temperature during defor-

mation has led to an SFE increase from 27 mJ/m^2 at 23°C to about 30–32 mJ/m^2 for a $\dot{\varepsilon}$ in the range from 0.01/s to 0.5/s and 38–40 mJ/m^2 for the $\dot{\varepsilon}$ above 10/s. The SFE increase under quasi-static conditions has negligible effects on mechanical properties, whereas under dynamic loading, reduced strength and necking were observed.

– The strain rate has negligible effects on the yield and tensile strength, whereas the uniform and total elongation decreases under dynamic loading. The tensile strength of the material is above 1000 MPa for all quasi-static $\dot{\varepsilon}$ and it decreases slightly when the $\dot{\varepsilon}$ increased to dynamic. Total elongation is above 50% for all $\dot{\varepsilon}$, whereas uniform elongation decreased mainly under dynamic loading due to necking and adiabatic heating.
– TWIP steel has excellent energy absorption capacity compared to other AHSS such as DP steels, TRIP steel and also ferritic steels. At all $\dot{\varepsilon}$ energy absorption of TWIP steel is above 55 kJ/kg, which is almost double that of DP steel DP1000. However, the energy absorption of TWIP steel is slightly lower compared to austenitic stainless steels 1.4301 and 1.4318. TWIP steel has a very high ECO-index value of 52 GPa % which decreases to about 35 GPa % under very high $\dot{\varepsilon}$ compared to the constant ECO-index values of AHSS which lie below 20 GPa % at all $\dot{\varepsilon}$.

ACKNOWLEDGEMENTS

The authors would like to acknowledge the financial support of the German Research Foundation (DFG) within the Collaborative Research Center SFB 761 “Steel-ab initio”. The authors thank ThyssenKrupp Steel Europe AG for the material supply.

REFERENCES

1. C.D. Horvath, *Advanced steels for lightweight automotive structures* (Elsevier, 2010).
2. X. Sun (ed.), *Failure mechanisms of advanced welding processes* (Woodhead Pub. Ltd, 2010).
3. J.N. Hall and J.R. Fekete, *Steels for auto bodies* (Elsevier, 2017).
4. O. Grässel, L. Krüger, G. Frommeyer, and L. Meyer, *International Journal of Plasticity***16**(10–11), 1391 (2000).
5. O. Bouaziz, S. Allain, C. Scott, P. Cugy, and D. Barbier, *Current Opinion in Solid State and Materials Science***15**(4), 141 (2011).
6. S.J. Lee, J. Han, S. Lee, S.H. Kang, S.M. Lee, and Y.K. Lee, *Scientific Reports***7**(1), 3573 (2017).
7. B.C. De Cooman, Y. Estrin, and S.K. Kim, *Acta Materialia***142**, 283 (2018).
8. C. Haase, T. Ingendahl, O. Gven, M. Bambach, W. Bleck, D.A. Molodov, and L.A. Barrales-Mora, *Materials Science and Engineering: A***649**, 74 (2016).
9. W. Bleck and I. Schael, *Steel Research***71**(5), 173 (2000).
10. G. Huang, Y. Benda, H. Zhu, and J. Chintamani, *The Strain Rate Effect on Tensile Properties and Fracture Strain of Advanced High Strength Steels* (John Wiley & Sons, 2011).
11. A. Saeed-Akbari, J. Imlau, U. Prahl, and W. Bleck, *Metallurgical and Materials Transactions A***40**(13), 3076 (2009).
12. M. Madivala, A. Schwedt, S.L. Wong, F. Roters, U. Prahl, and W. Bleck, *International Journal of Plasticity* (2018).
13. L. Mosecker, D.T. Pierce, A. Schwedt, M. Beighmohamadi, J. Mayer, W. Bleck, and J.E. Wittig, *Materials Science and Engineering: A***642**, 71 (2015).
14. K. Dahmen, Numerische Fließkurvenmodellierung von Feinblechstählen unter besonderer Berücksichtigung von Dehnrate, Temperatur und Phasenzusammensetzung. PhD thesis, RWTH Aachen University, Aachen (2014).
15. I. Gutierrez-Urrutia and D. Raabe, *Scripta Materialia***66**(12), 992 (2012).
16. I.C. Jung and B.C. De Cooman, *Acta Materialia***61**(18), 6724 (2013).
17. H. Gwon, J.K. Kim, S. Shin, L. Cho, and B.C. De Cooman, *Materials Science and Engineering: A***696**, 416 (2017).
18. H.K. Yang, Z.J. Zhang, Y.Z. Tian, and Z.F. Zhang, *Materials Science and Engineering: A***690**, 146 (2017).
19. Z.Y. Liang, X. Wang, W. Huang, and M.X. Huang, *Acta Materialia***88**, 170 (2015).
20. D.R. Steinmetz, T. Jäpel, B. Wietbrock, P. Eisenlohr, I. Gutierrez-Urrutia, A. Saeed-Akbari, T. Hickel, F. Roters, and D. Raabe, *Acta Materialia***61**(2), 494 (2013).

4 General discussion

4.1 Serrated flow and dynamic strain aging

4.1.1 Influence of temperature, strain rate and anisotropy

Tensile tests carried out in this study over a wide range of strain rates and temperatures Fig. 4.1 [1] revealed repeated "jerks" or "serrations" during the plastic deformation at intermediate temperatures and over a range of strain rates. Serrations are observed on the σ–ε curves at all quasi-static strain rates and they begin to diminish with increasing strain rates above 0.5 /s. The jerky flow behavior is quite similar in characteristics along RD, TD and 45° in tests carried out at 23 °C. The periodic serrations of Type A can be seen in the temperature range between -40 °C and 200 °C in X60Mn22 TWIP steel [1]. Such serrated σ–ε behavior has also been observed in different TWIP steels by [77, 80, 81]. Within the temperature and strain rate regimes where serrated flow occurs, large variation in mechanical properties such as peak in UTS, a plateau in YS, reduction of ductility, more importantly negative strain rate sensitivity (SRS) and abrupt failure with negligible necking could be clearly observed. Such manifestations in mechanical behavior of material in the form of serrations, large change in mechanical properties and negative SRS is caused mainly due to DSA mechanism occurring at micro-scale. The phenomena of DSA in high Mn TWIP steels can be attributed to the formation of Mn-C short range order (SRO) or short range cluster (SRC) [29, 39]. Dastur and Leslie proposed that DSA occurs when the C atoms in the Mn-C octahedral clusters reorient themselves in the core of the dislocations, thereby locking the dislocations leading to high dislocation density. During this dynamic interaction between the mobile dislocations and the diffusing atoms during plastic flow, C atoms pins strongly to the dislocations increasing their pile up. When applied stress is sufficiently high, the dislocations overcome the obstacle in the form of SRO/SRC at once by single diffusive jump of C atoms and move to next obstacle, where they are stopped again and the process is repeated [39]. According to Chen et al., the formation of Mn-C octahedral clusters result in increased lattice resistance for dislocation glide as the passage of partial dislocation will change the local position of both substitutional and interstitial atoms.

Serrations are observed in the experimental flow curves at temperatures above 298 K, however they begin to diminish with increasing temperatures up to 473 K. This behavior in the flow curves has also been observed in other TWIP steels [13, 44, 83]. It has been primarily attributed to the Portevin–Le Chatelier effect, a type of dynamic strain aging mechanism, which describes the dynamic interaction between mobile dislocations and the obstacles in the form of twin boundaries. When dislocations meet obstacles (twins) they are temporarily arrested. During this time solutes such as interstitial atoms diffuse to the dislocations further strengthening the obstacles. Eventually, when the applied stress is sufficiently high, dislocations will overcome these obstacles and will quickly move to the next obstacle, where they are stopped again and the process is repeated. With increasing temperature the SFE increases, leading to the suppression of twinning in the material, thereby reducing the number of twin boundaries resulting in the suppression of serrations. Serrations are completely suppressed above 473 K, due to the change in deformation mode from twinning along with dislocation glide to only dislocation glide. The diffusivity of the solute atoms decreases with decreasing temperature, which suppresses the DSA below 298 K [32].

Serrated flow caused due to DSA in TWIP steels led to an instability in the form of repetitive

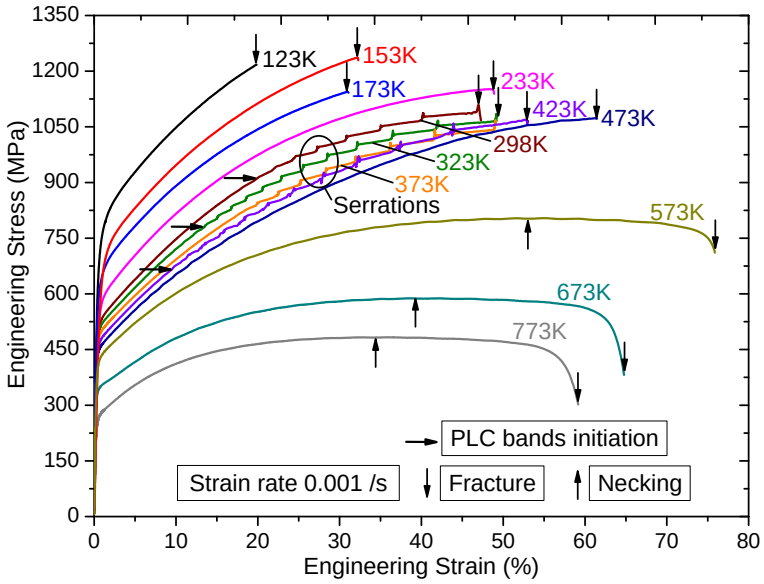

Figure 4.1: Stress-strain curves at different deformation temperatures for X60Mn22 TWIP Steel; serrations are observed in a temperature range from 298 K to 473 K; diffuse necking is observed for temperatures between 573 K and 773 K, which is indicated by upward arrows; downward arrows indicate fracture in the specimen [1].

nucleation of localized deformation bands at one end of the gage length and their continuous propagation to the other end with each load drop corresponding to nucleation of new band. The process is commonly referred to as the Portevin-LeChatelier (PLC) effect. DSA is usually not observed immediately after the start of deformation, hence shear bands or serrations can be observed only after deforming material to a critical plastic strain, ε_c. This is due to the fact that sufficient vacancies must be created to enhance the solute diffusion to dislocations. The ε_c, mainly depends on strain rate ($\dot{\varepsilon}$), Temperature (T), SFE and presence of additional alloying elements such as Al. The critical plastic strain, ε_c for the initiation of serrations in TWIP steels increase, with increase in SFE, increase in $\dot{\varepsilon}$, decrease in T and with increase in Al content. A relatively small magnitude of stress jump "$\Delta\sigma$" values are associated with the initial serrations than the subsequent ones. This can be explained by the presence of transition regime, corresponding to underdeveloped serrations, before the ripples of inhomogeneous deformation transform into deformation bands, manifesting into clearly developed bands.

4.1.2 Influence of C and Al alloying

In an X60MnAl17-1 alloy repeated serrations can be observed on the σ–ε curves during the plastic deformation, whereas in an X30MnAl23-1 alloy, no serrations can be observed at RT and quasi-static $\dot{\varepsilon}$. The manifestations in σ–ε behavior in the form of serrations such as a change in mechanical properties and negative SRS is mainly due to DSA. The serrations were initiated at a ε_c of ~12.5% in an X60Mn22 alloy without Al [2], whereas in alloys with 1.5 wt.% Al-addition, the serrations appeared at a ε_c of ~24% in X60MnAl17-1 and serrations are completely suppressed in X30MnAl23-1 at RT and quasi-static $\dot{\varepsilon}$. In the Fe-Mn-Al-C alloys, the serrations are reported to occur mainly in the steels with C content above 0.6 wt.% at RT tensile

testing [2, 19, 41, 57, 58, 84]. It was stated that with the addition of Al, the diffusivity of the carbon will be reduced and the serrated flow will be shifted to higher temperatures [85]. The addition of Al has suppressed the DSA phenomena by increasing the activation energy for C diffusion and reducing the interaction time between stacking faults and the Mn-C SRO [30]. However, even in Al-added alloys, the DSA could occur at elevated temperatures because of the increased defect mobility resulting in serrated σ–ε curves. Twinning behavior in both Al-added alloys are quite similar, except for the initiation and saturation of twinning and TVF. Even though twinning occurs in both alloys, the serrated σ–ε flow is observed only in X60MnAl17-1 alloy and not in X30MnAl23-1 alloy. The local deformation behavior is inhomogeneous in an X60MnAl17-1 alloy due to the initiation and propagation of deformation bands during deformation commonly known as Portevin-LeChatelier (PLC) effect, whereas in an X30MnAl23-1 alloy homogenous σ–ε behavior can be observed. The nucleation and propagation of deformation bands result in serrations on the σ–ε curves which can be ascribed to the DSA. Kang et al. showed that the number of Mn-C SRO clusters increases with increasing macroscopic strain in X60Mn18 alloy [40]. Song and Houston reported that with an increase in ε, the volume fraction of Mn-C SRO/SRC increases and the mean radius of clusters decreases [41]. Madivala et al. investigated an X60Mn22 alloy and showed that serrations disappear at elevated temperatures and at high strain rates. It was also stated that twinning occurs at these temperatures and at high strain rate tests [1, 2]. Koyama et al. also indicated that the deformation twinning and martensitic transformation did not cause the serrations [86]. Lebedkina et al. suggested that twinning starting at some point in the specimen will initiate twins in the neighboring grains and advance into the unoccupied regions of the specimen. However, they claimed that twinning cannot alone responsible for the entire strain accumulation during strain jumps due to low TVF observed in TWIP Steel [45]. Recently, Sevsek et al. proposed a multi-scale-bridging model for the formation and propagation of the deformation bands and the resulting occurrence of the serrated flow in high Mn TWIP steels. However, they also stated that neither the SRO-based theory nor the deformation twinning based theory proposed could explain the experimental observations completely [84]. Based on the experimental observations from this study and the from the literature, it can be clearly stated that deformation twinning and ε-martensite transformation cannot be responsible for causing serrations in Fe-Mn-C-Al alloys. Thus, DSA is the dominant factor for causing the serrations in an X60MnAl17-1 alloy.

4.2 Strain hardening

Deformation twinning during plastic deformation plays a significant role in enhancing the strain hardening behavior of materials through the creation of new boundaries thereby subdividing the original grains commonly known as dynamic Hall-Petch effect [13, 22, 86]. Twin boundaries act as the barriers to dislocation motion thereby progressively reducing the effective mean free path (MFP) of dislocations resulting in enhanced strain hardening. Bouaziz et al., De Cooman et al., Koyama et al. claim that mechanical twinning and the related dynamic Hall-Petch effect associated with TWIP effect remain the only mechanisms that can explain the high strain hardening of TWIP steel [13, 22, 86]. However, the role of DSA in manifesting the SHR of TWIP steels as explained in Section 4.1 cannot be neglected.

4.2.1 Effect of temperature

TWIP steel exhibit high strain hardening at all temperatures below 473 K and the failure occurs abruptly without necking. The excellent strain hardening behavior is mainly due to dislocation glide in combination with twinning and ε-martensite transformation [19, 51, 87]. The strain

hardening behavior of the TWIP steel at 298 K and the evolution of twinning with strain can be seen in [1]. Based on the detailed work by Gutierrez-Urrutia and Raabe the SHR of fine grained X60Mn22 TWIP steel can be divided into three distinct stages of hardening: I) continuous decrease in the SHR, which involves dynamic recovery process such as cross-slip and annihilation of screw dislocations of opposite signs; II) rapid increase in the SHR, implies that refinement of the mean free path by deformation twinning occurs at strain level slightly higher than the onset of yielding; III) steady decrease in the SHR, ascribed to the reduced additional refinement of the dislocation and twin substructures, together with the increasing strengthening effect of the individual twins as obstacles to dislocation glide, reduce the capacity for trapping more dislocation leading to decrease in SHR. The different stages of hardening along with evolution of twinning can be seen in Fig. 4.2 [4]. Gutierrez-Urrutia and Raabe showed that deformed microstructure during stage I) consists of loose dislocation arrangements and the twin substructure evolution in stage II) is mainly influenced by the density of nucleation sites for twins per grain boundary area, which are controlled by dislocation structure formed in stage I). The homogenous distribution of dislocations in fine grained microstructure allows large number of nucleation sites for twins at grain boundary. This results in high density of twins which promotes lamellar twin structure. The formation of lamellar twin structure has led to increased strain hardening due to the smaller twin spacing. It is observed from Fig. 4.2 [4] that the twin volume fraction steadily increases from 0.015 to 0.05, for a true strain of 0.2, which corresponds to stage II) of hardening involving nucleation and growth of twin lamellae. Thereafter twin volume fraction almost remains constant until failure, which can be directly correlated with stage III) of hardening where saturation of twinning occurred in the material. At a strain of about 0.2, in almost all of the grains, twins can be observed which act as obstacles to dislocation motion leading to high strain hardening. At this stage, deformation within the grains already shows large heterogeneity and a further increase in deformation can lead to the initiation of damage in the material, which can lead to failure at any stage of deformation.

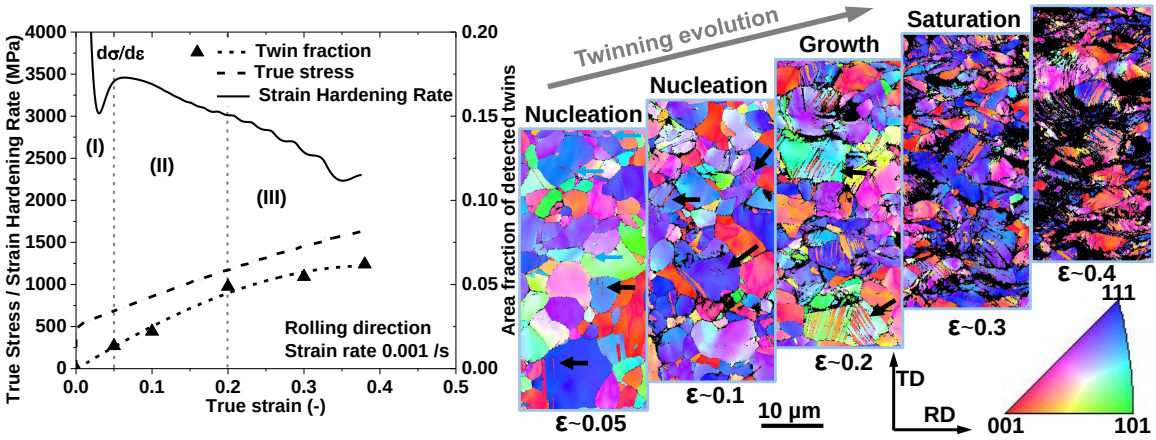

Figure 4.2: Strain hardening in relation to the evolution of twinning under quasi static loading: strain hardening behavior (left) and EBSD inverse pole figure (IPF) maps with increasing macroscopic true strain (right); Annealing twins (white arrows) and mechanical twins (black arrows); pixels in black are un-indexed points [4].

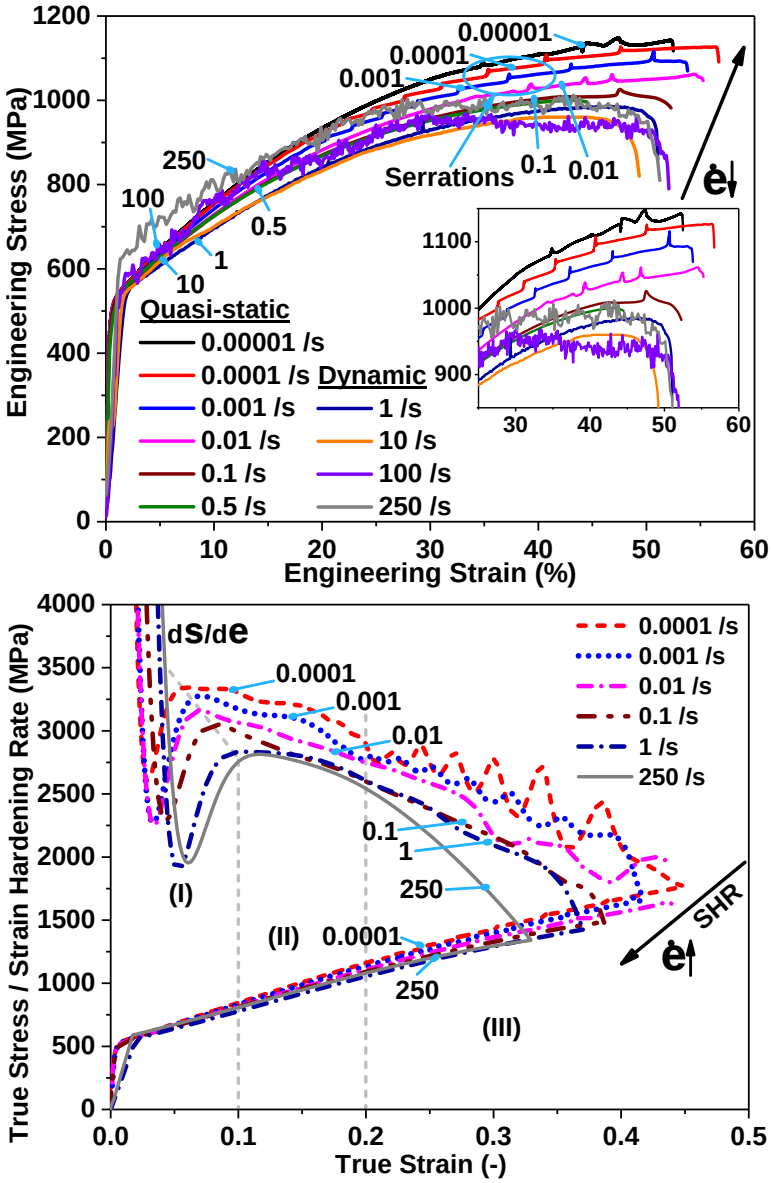

Figure 4.3: Strain rate effect on the mechanical behavior of the investigated X60Mn22 TWIP steel. At least three repeatable tests were performed for each condition. All data are average values determined from at least three parallel experiments [2, 4].

4.2.2 Effect of strain rate

The strain rate effect on the work hardening behavior is shown in Fig. 4.3 [2, 4]. It can be observed that the SHR decreases with increasing strain rate. With increasing strain rate from quasi-static to dynamic, the stage I) of hardening has become wider and the initiation of stage II) has shifted to larger strains. This could be mainly attributed to the change in twin nucleation and evolution behavior. The significant increase in Σ-3 twin boundary fraction at a strain rate

of 10 /s compared to 0.0001 /s is mainly due to increase in SFE due to rise in temperature due to adiabatic heating. It can also be seen that change in deformation rate also influenced the twin nucleation and density of twins in grains. At lower $\dot{\varepsilon}$, many thinner twin bundles can be observed within the grains compared to few thicker twin bundles at high $\dot{\varepsilon}$. The occurrence of DSA at lower $\dot{\varepsilon}$ in general result in locking of the partial dislocations leading to high dislocation density [30]. The fine grain microstructure along with high density of dislocations at grain boundaries (GB) result in higher stress concentration which could assist in nucleation of twins at GB [89]. But this effect can be suppressed at high $\dot{\varepsilon}$ due to the suppression of DSA at high $\dot{\varepsilon}$. The experimental study by [77] showed that number of twin nucleation sites per grain boundary area at lower $\dot{\varepsilon}$ is much larger compared to fewer twin nucleation sites at higher $\dot{\varepsilon}$. The thickness of individual twins increased from 10 nm at a $\dot{\varepsilon}$ of 0.0001 /s to 40 nm at a $\dot{\varepsilon}$ of 10 /s and individual twin spacing from 20 nm to 60 nm. The study also found decrease in twin area fraction with increasing $\dot{\varepsilon}$. This is mainly due to increase in average energy required for twin nucleation at high $\dot{\varepsilon}$, which led to suppressed twinning. This indicates differences in twin nucleation and growth behavior at quasi-static and dynamic loading. The synchrotron X-ray diffraction and transmission electron microscopy study by [90] at low and high $\dot{\varepsilon}$ stated that the dislocations and deformation twins are suppressed at high $\dot{\varepsilon}$ deformation indicating negative strain rate sensitivity of work hardening. The detailed study by [91] also showed decrease of twin volume fraction with increasing rate of deformation through electron channeling contrast imaging (ECCI) measurements and crystal plasticity simulations. This change in deformation behavior could be mainly attributed to adiabatic heating associated with high $\dot{\varepsilon}$ deformation. The increase of T at $\dot{\varepsilon}$ above 1 /s lead to SFE increase above 40 mJ/m^2 favoring dislocation glide above 25 % strain. Hence in the stage III) of hardening, the SHR decreases more rapidly at higher $\dot{\varepsilon}$ compared to lower $\dot{\varepsilon}$. Higher T has decreased the work hardening rate by increasing the rate of dynamic recovery and the suppression of deformation twinning due to the higher SFE.

4.2.3 Effect of Al-addition

An X60MnAl17-1 alloy, where DSA can be observed shows enhanced strain hardening and ductility compared to an X30MnAl23-1 alloy, where DSA does not occur. Such sustained and high work hardening rates can also be seen in austenitic steels with high C content because of DSA [92]. The ab-initio based study combined with SANS experiments by Song et al. and SANS experimental study by Kang et al. proved the presence of Mn-C octahedral clusters and their evolution, indicating the occurrence of DSA during deformation in high Mn steels. The occurrence of static strain aging due to the presence of Mn-C SRO was stated to be responsible for increased yield strength and pronounced yielding of annealed TWIP steel [94]. It was stated that deformation twinning in TWIP steels is promoted by thermally activated nature of dislocation slip due to dynamic interactions between solute C atoms and dislocations that inhibit dislocation slip due to lattice friction effects [95]. It was proposed that the trapping of slowly moving partial dislocations by C atoms results in increased inter-granular stress and reduction of MFP [84, 86]. The increased localized stress near the GB facilitate grain boundary nucleation of deformation twins [89]. DSA is also showed to be crystallographic orientation dependent, could occur at elevated temperatures and is enhanced by increasing C content [86]. Thus in an X60MnAl17-1 alloy, the occurrence of DSA has led to increased stresses at GBs. This led to triggering of the nucleation of multiple deformation twins in the preferably oriented grains. Whereas in X30MnAl23-1 alloy, conventional twinning mechanisms occurs in combination with dislocation glide at RT. Thus the yield strength increase by static strain aging and the indirect promotion of the mechanical twinning during deformation in an X60MnAl17-1 alloy, could

have led to high SHR and enhanced ductility.

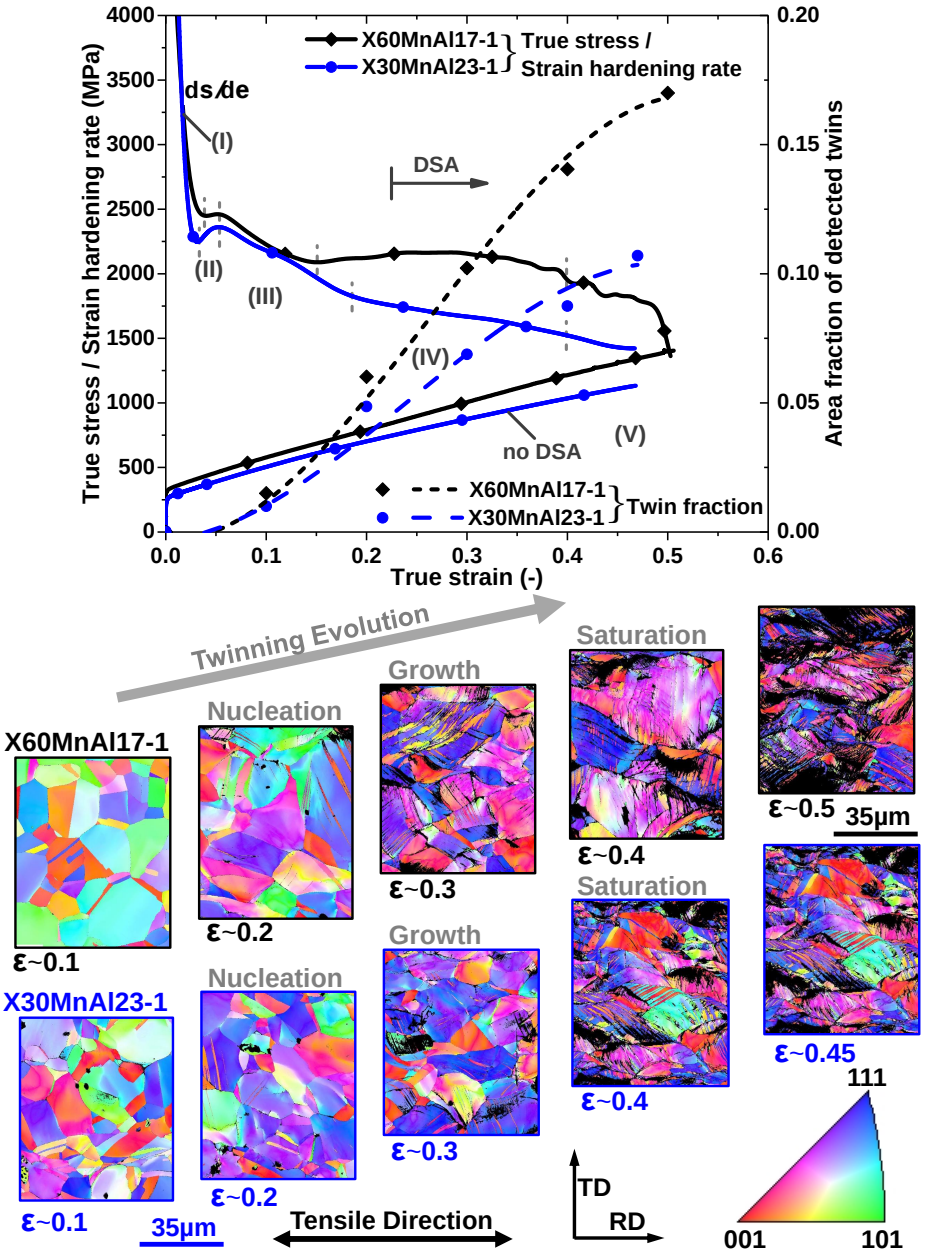

Figure 4.4: Strain hardening in relation to the evolution of twinning; strain hardening behavior (top) and EBSD IPF maps with increasing macroscopic true strain (bottom) [3].

The evolution of twinning with increasing macroscopic strain is correlated with the SHR and The RD-IPF maps at different strains are shown in Fig. 4.4 [3]. Based on the detailed work by De Cooman et al., Gutierrez-Urrutia and Raabe, the SHR in Al-added aloys is divided into five stages [22, 88]. Stage I) is the initial strain hardening stage controlled by the dislocation den-

sity evolution without the initiation of twins. The initial downfall of SHR is characterized by a continuously decreasing rate of dislocation storage and an increasing rate of dynamic recovery. The dislocation reactions in this stage are responsible for the nucleation of twins. Stage II) is characterized by an increase of SHR in both alloys and is referred to as the primary twinning stage. It begins slightly above yielding and at a strain of $\sim$0.03 in an X30MnAl23-1 alloy and at a strain of $\sim$0.04 in an X60MnAl17-1 alloy. The stress at the beginning of stage II is referred to as the twin initiation stress. It is about 345 MPa in an X30MnAl23-1 alloy and is about 435 MPa in X60MnAl17-1 alloy. The evolution of dislocation structures and the initiation of primary twins are supposed to be responsible for the rise of SHR in this stage. The maximum SHR for both the alloys occurs at $\sim$0.05 strain at the end of stage II. Stage III) is characterized by a decrease in SHR with increasing macroscopic strain. It can be attributed to the reduced rate of primary twins initiation. It was also stated that the initial twins subdivide the original grains thereby reducing the MFP of dislocations, which results in increased stress for twin nucleation. At the end of this stage, twins can be clearly observed in the preferably oriented grains at a strain of 0.2. Stage IV) and V) are quite different in both the alloys. Stage IV) and V) in an X30MnAl23-1 alloy marked by a continuous decrease in SHR, ascribed to the reduced additional refinement of the dislocation and twin substructures, together with the increasing strengthening effect of the individual twins as obstacles to dislocation glide, reduce the capacity for trapping more dislocations. Stage IV) in an X60MnAl17-1 alloy can be distinguished by again increase in SHR and reaching maximum between a strain of 0.3 and 0.4. This stage is characterized by the activation of the secondary twin systems and the formation of the multiple twin-twin interactions. This results in a further subdivision of grains and thus reduces the MFP of the dislocations considerably leading to increasing or constant SHR. During stage V) in X60MnAl17-1 alloy, the SHR decreases continuously. In this stage TVF increases significantly and the twin bundles get thicker and denser. This can be observed in the microstructure at a strain of 0.4 and 0.5. The major difference in SHR between two alloys can be observed at stage III), at which DSA gets activated in X60MnAl17-1 alloy which has indirectly led to significant increase in TVF, whereas in X30MnAl23-1 alloy, the TVF increased was marginal.

4.3 Damage and failure

4.3.1 Role of extrinsic parameters

High manganese TWIP steels generally exhibit ductile failure for over a wide range of temperatures and strain rates, owing to their large ductility and moderate yield strength. The activation of different deformation mechanisms such as ε-martensite, twinning and dislocation glide at various temperatures play a significant role on the fracture behavior. The fracture surface characteristics such as quasi-brittle islands along with fine dimples at low temperatures due to ε-martensite transformation, shallow dimples at moderate temperatures where DSA along with twinning occurs and larger dimples with elliptical voids at MnS inclusions at higher temperatures are the major changes due to different active deformation mechanisms. Since twinning is the most dominant deformation mechanism at all quasi-static strain rates, ductile fracture with fine dimples can be commonly observed. At very high strain rates due to rise in temperature due to adiabatic heating, profuse necking and failure occurs resulting in larger dimple size.

4.3.2 Role of deformation bands

The strain hardening rate ($d\sigma/d\varepsilon$) and the $\sigma - \varepsilon$ curves for X60Mn22 and X60MnAl17-1 TWIP steels clearly indicates that failure occurs without necking for all the quasi-static strain rates

whereas for dynamic tests failure occurs with necking. The serrated flow in the material due to DSA led to local plastic instability due to strain localization in the deformation bands. After some deformation, deformation bands nucleate and propagate from one shoulder end to the other during the entire deformation, leading to inhomogeneous deformation. Since there is no prior necking before failure, there are no indications of localization of plastic strain except in the shear bands. The deformation band velocity (V_b) decreases exponentially with increasing macroscopic strain. It indicates that when the band passes through the specimen, the material is strengthened and a large amount of barriers to plastic flow are generated which suppress the movement of the successive deformation bands. The failure of the material occurs when the deformation bands motion is retarded or when the band velocity decreases drastically approaching zero. Micro-cracks mainly initiate at the surface defects or at the edges of the tensile specimen where the intersecting deformation bands are located and propagate rapidly resulting in trans-granular ductile fracture. Experimental observations such as a flat fracture surface on broken tensile samples and the fine dimples clearly indicate rapid nucleation of voids leading to failure [78]. The sudden failure in TWIP steel could be attributed due to the exponential increase of macroscopic voids during plastic deformation [77]. However the interaction of various active deformation mechanisms during deformation also play a significant role in the micro-crack or voids formation in TWIP steels.

4.3.3 Role of inclusions

The MnS inclusions are usually elongated along RD and if the material is deformed along TD, the MnS will be subjected to tension along the minor axis. Even though MnS inclusions are deformable and ductile in nature, they have reduced toughness and ductility in TD. Thus when a material is loaded along TD, the inclusions are effective in initiating ductile cracks above a critical size range. The presence of coarser or elongated inclusions could lead to higher local stress concentrations, which cause localized rupture and micro-crack formation in TWIP steels.

4.3.4 Role of deformation mechanisms

In TWIP steels, dislocation glide and deformation twinning are the major active deformation mechanisms above RT. These deformation mechanisms did not induce damage directly but they acted as a source for increasing the stress concentration within the microstructure, which is a precursor step for damage initiation. A schematic diagram illustrating the mechanism of micro-crack formation in TWIP steels based on the experimental observations is depicted in Fig. 4.5. The development of large inter-granular regions with high dislocation density within the microstructure due to the subdivision of grains due to slip and twinning resulted in high inter-granular stress. Deformation by twinning and dislocation slip can be observed in the microstructure in the preferably oriented grains leading to the localization of the plastic strain. It could be observed that <111> tensile orientation is the preferential orientation for the deformation twinning and <100> is the non-preferential tensile orientation for twinning. Many bundles of primary and secondary deformation twins can be observed in <111>-oriented grains and slip bands in <100>-oriented grains. Largest plastic strain concentration can occur in the <111>-oriented grains, which are preferred for the deformation twinning and the second largest strain concentration could occur in the <100>-oriented grains, which are preferred for the dislocation slip. The large plastic localization associated to accommodate the plasticity within the grains results in high-stress concentration at the GB. The slip/twins within the grains could also lead to the generation of ledges at GB and with further increase in deformation subsequent unaccommodating GB sliding can occurs. This results in the initiation of voids at GB or triple points. The voids formed coalesce together leading to initiation of inter-granular micro-cracks. The

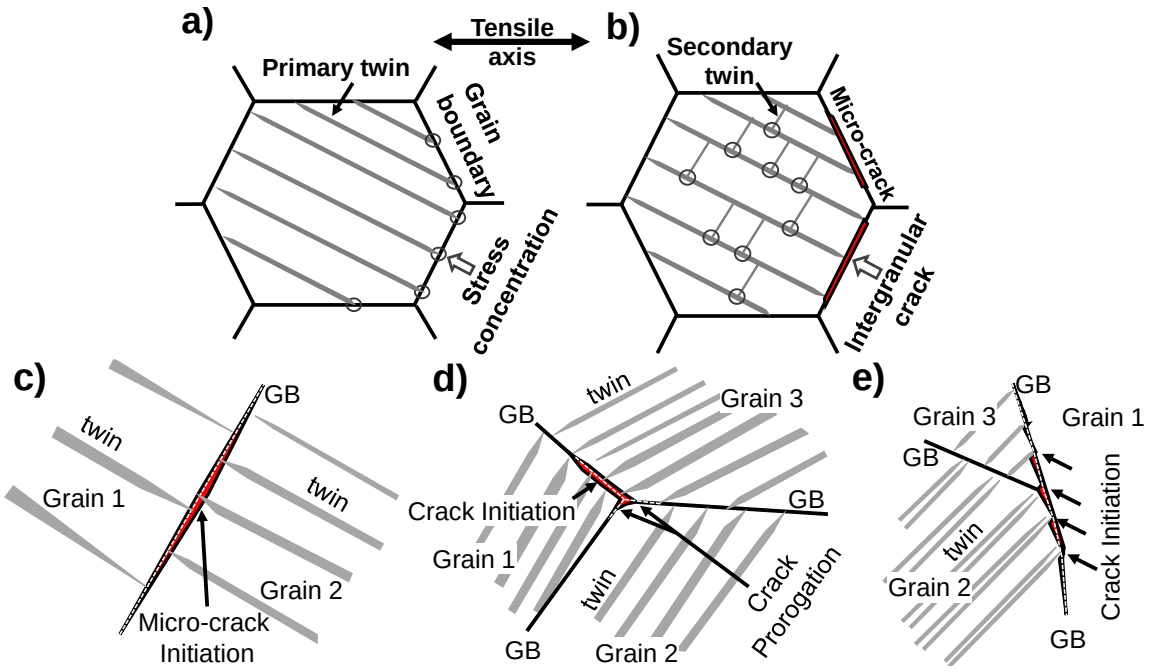

Figure 4.5: A schematic illustration of micro-cracking mechanisms in TWIP steels based on the experimental observations from interrupted micro-tensile tests carried out in the SEM. a) Stress concentration caused by the intercepting deformation twins at GB. b) and c) Void formation and their growth leading to inter-granular micro-crack initiation at GBs. d) Initiation of voids or micro-cracks at triple junction. e) The mechanism of void formation due to unconstrained plastic deformation at GB due to deformation by slip or twinning.

micro-cracks are also formed at the triple junctions due to void formation/growth and also due to partially unconstrained ligaments that deform plastically. Thus at a micro-scale, stress concentration caused by the interception of deformation twins and slip band extrusions at GB lead to damage initiation. However, the interaction and coalescence of micro-cracks at inclusions, GBs and triple points etc. result in the localization of strain and beginning of necking in the material. This will finally lead to ductile failure with the formation of fine dimples on the fracture surface.

5 Conclusions

TWIP steels was investigated by uni-axial tensile tests under both quasi-static and dynamic conditions. For investigating the mechanical properties and damage behavior, various in-situ tensile testing methods were applied. The local strain evolution during deformation was monitored by carrying tests in conjunction with digital image correlation and synchronous temperature measurements using thermocamera. X-ray diffraction and EBSD measurements were carried out on the interrupted tensile samples to study the evolution of deformation mechanisms and micro-cracks development. Crystal plasticity based constitutive model was developed for predicting deformation mechanisms and stress-strain behavior. The main conclusions can be drawn for the investigated TWIP steel as follows:

- The deformation mechanisms of X60Mn22 TWIP steel strongly depend on temperature. At temperatures below 298 K, the $\gamma \rightarrow \varepsilon$-martensite transformation occurs and its volume fraction increases as the temperature decreases. A small fraction of twins is present even at these low temperatures. Twinning and dislocation glide are the dominant deformation mechanisms at 298 K and the twin fraction increases with temperature up to the transition temperature of 473 K, above which the deformation mode changes from both deformation twinning and dislocation glide to only dislocation glide due to the increasing stacking fault energy (SFE).
- Strain hardening rate of X60Mn22 TWIP steel is extraordinarily high under both quasi-static and dynamic tests until maximum strain/failure. Twining is the most predominant deformation mechanism occurred along with dislocation slip under all quasi-static tests, where multiple number of thinner twin bundles within a grain was observed compared to less number of thicker twin bundles under dynamic loading. Temperature rise due to adiabatic heating led to increase in SFE, thereby resulting in a change of twinning behavior or the promotion of dislocation glide under dynamic loading.
- The X60Mn22 TWIP steel has excellent energy absorption capacity compared to other AHSS such as dual phase steels, TRIP steel and also ferritic steels. At all $\dot{\varepsilon}$ energy absorption of TWIP steel is above 55 kJ/Kg which is almost double that of dual phase steel DP1000.
- Strain hardening rate of an X60MnAl17-1 alloy is extraordinarily high compared to an X30MnAl23-1 alloy. The enhanced mechanical properties of the X60MnAl17-1 alloy is mainly due to the enhanced deformation twinning in addition to dislocation glide and also activation of dynamic strain aging (DSA). In an X30MnAl23-1 alloy, DSA is completely suppressed at room temperature and quasi-static strain rate due to lower carbon content. The addition of Al has led to increased SFE thereby delaying nucleation of deformation twins and prolonged the saturation of twinning.
- Micro-cracks are observed at elongated MnS inclusions, AlN inclusions or at isolated grain boundaries at relatively small strain of $\sim 2/3$ of total strain. However, these micro-cracks showed no tendency to grow. Large heterogeneous deformation within the grains by twinning or dislocation glide has led to high stress concentration at grain boundaries (GB) due to the interception of deformation twins and slip band extrusions at GB. Thus micro-cracks in TWIP steels originated mainly at grain boundaries and triple junctions.

- The ductile failure mode is the most predominant mode of failure in TWIP steels, mainly characterized by the formation of fine shallow dimples with a crack propagation along GBs.
- Inhomogeneous flow behavior caused due to the nucleation and propagation of deformation bands is mainly due to DSA. The occurrence of DSA has led to large strain localization within the deformation bands and also non uniform distribution of local plastic strain ($\varepsilon_{\text{local}}$) in the regions behind and ahead of shear bands in both X60Mn22 and X60MnAl17-1 alloys. The velocity of shear band motion decreased with increasing macroscopic strain due to the intersection of two deformation bands. This led to local strain accumulation within the intersecting deformation bands resulting in a macroscopic crack initiation close to edges of tensile specimen by the coalescence of various micro-cracks that has been previously formed at the intersection of twin bundles with GB. However, in an X30MnAl23-1 alloy, homogenous $\varepsilon_{\text{local}}$ distribution throughout the gauge length could be observed until the beginning of necking. Thus the failure in an X30MnAl23-1 alloy occurred by classical necking and strain localization, whereas in X60Mn22 and X60MnAl17-1 alloys failure occurred at the intersection of deformation bands due to strain localization.
- A dislocation density based crystal plasticity model incorporating dislocation glide, twinning and ε-martensite phase transformation can be used for the modeling of the flow behavior and the evolution of twin and ε-martensite volume fraction. Based on the temperature dependent SFE and Gibbs free energy, the model predicts the activation of ε-martensite transformation at low temperatures, twinning at intermediate temperatures and dislocation glide only at high temperatures. Quantitative comparisons were made between the experiments and simulations based on the RVE simulations using the FFT-based solver implemented in the DAMASK framework. The excellent correspondence of simulation and experimental results suggest that, this technique can be applied to the design and testing of new advanced high strength steels (AHSS) and in particular austenitic TWIP/TRIP steels of Fe-Mn-C, Fe-Mn-C-Al, Fe-Mn-C-Al-Cr, and Cr-Mn-Ni alloys.

Bibliography

[1] Manjunatha Madivala, Alexander Schwedt, Su Leen Wong, Franz Roters, Ulrich Prahl, and Wolfgang Bleck. Temperature dependent strain hardening and fracture behavior of twip steel. *International Journal of Plasticity*, 104:80 – 103, 2018. ISSN 0749-6419. doi: https://doi.org/10.1016/j.ijplas.2018.02.001.

[2] Manjunatha Madivala, Alexander Schwedt, Ulrich Prahl, and Wolfgang Bleck. Anisotropy and strain rate effects on the failure behavior of twip steel: A multiscale experimental study. *International Journal of Plasticity*, 2018. ISSN 0749-6419. doi: https://doi.org/10.1016/j.ijplas.2018.11.015.

[3] Manjunatha Madivala, Alexander Schwedt, Ulrich Prahl, and Wolfgang Bleck. Strain hardening, damage and fracture behavior of al added high mn twip steels. *Metals*, 8(12), 2019. ISSN 2075-4701. doi: 10.3390/met8121014. URL `http://www.mdpi.com/2075-4701/8/12/1014`.

[4] Manjunatha Madivala and Wolfgang Bleck. Strain rate dependent mechanical properties of twip steel. *JOM*, Sep 2018. ISSN 1543-1851. doi: https://doi.org/10.1007/s11837-018-3137-0.

[5] C. D. Horvath. Advanced steels for lightweight automotive structures. In *Materials, Design and Manufacturing for Lightweight Vehicles*, pages 35–78. Elsevier, 2010. ISBN 9781845694630. doi: 10.1533/9781845697822.1.35.

[6] Jürgen Hirsch. Aluminium in innovative light-weight car design. *MATERIALS TRANSACTIONS*, 52(5):818–824, 2011. doi: 10.2320/matertrans.L-MZ201132.

[7] A. M. Sherman, C. J. Sommer, and F. H. Froes. The use of titanium in production automobiles: Potential and challenges. *JOM*, 49(5):38–41, May 1997. ISSN 1543-1851. doi: https://doi.org/10.1007/BF02914682.

[8] A.A. Luo and A.K. Sachdev. 12 - applications of magnesium alloys in automotive engineering. In Colleen Bettles and Matthew Barnett, editors, *Advances in Wrought Magnesium Alloys*, Woodhead Publishing Series in Metals and Surface Engineering, pages 393 – 426. Woodhead Publishing, 2012. ISBN 978-1-84569-968-0. doi: https://doi.org/10.1533/9780857093844.3.393.

[9] Pekka Kantanen, Mahesh Somani, Antti Kaijalainen, Oskari Haiko, David Porter, and Jukka KÃ¶mi. Microstructural characterization and mechanical properties of direct quenched and partitioned high-aluminum and high-silicon steels. *Metals*, 9(2), 2019. ISSN 2075-4701. doi: http://www.mdpi.com/2075-4701/9/2/256.

[10] Xin Sun, editor. *Failure mechanisms of advanced welding processes*. Woodhead Publishing Series in Welding and Other Joining Technologies. Woodhead Pub. Ltd, Boca Raton, Fla and Oxford, 2010. ISBN 9781439831724. doi: 10.1016/B978-1-84569-536-1.50003-2.

[11] J. N. Hall and J. R. Fekete. Steels for auto bodies. In *Automotive Steels*, pages 19–45. Elsevier, 2017. ISBN 9780081006382. doi: 10.1016/B978-0-08-100638-2.00002-X.

[12] G. Krauss. Physical metallurgy of steels. In *Automotive Steels*, pages 95–111. Elsevier, 2017. ISBN 9780081006382. doi: http://dx.doi.org/10.1016/B978-0-08-100638-2.00004-3.

[13] O. Bouaziz, S. Allain, C.P. Scott, P. Cugy, and D. Barbier. High manganese austenitic twinning induced plasticity steels: A review of the microstructure properties relationships. *Current Opinion in Solid State and Materials Science*, 15(4):141 – 168, 2011. ISSN 1359-0286. doi: 10.1016/j.cossms.2011.04.002.

[14] Bruno C. De Cooman, Yuri Estrin, and Sung Kyu Kim. Twinning-induced plasticity (TWIP) steels. *Acta Materialia*, 2017. doi: http://doi.org/10.1016/j.actamat.2017.06.046.

[15] M. Linderov, C. Segel, A. Weidner, H. Biermann, and A. Vinogradov. Deformation mechanisms in austenitic TRIP/TWIP steels at room and elevated temperature investigated by acoustic emission and scanning electron microscopy. *Materials Science and Engineering: A*, 597:183–193, 2014. doi: http://dx.doi.org/10.1016/j.msea.2013.12.094.

[16] Stefan Martin, Steffen Wolf, Ulrich Martin, Lutz Krüger, and David Rafaja. Deformation Mechanisms in Austenitic TRIP/TWIP Steel as a Function of Temperature. *Metallurgical and Materials Transactions A*, 47(1):49–58, 2016. doi: http://dx.doi.org/10.1007/s11661-014-2684-4.

[17] Jin-Kyung Kim, Min-Hyeok Kwon, and Bruno C. De Cooman. On the deformation twinning mechanisms in twinning-induced plasticity steel. *Acta Materialia*, 141:444–455, 2017. doi: http://dx.doi.org/10.1016/j.actamat.2017.09.043.

[18] D.T. Pierce, J.A. Jiménez, J. Bentley, D. Raabe, C. Oskay, and J.E. Wittig. The influence of manganese content on the stacking fault and austenite/ε-martensite interfacial energies in Fe-Mn-(Al-Si) steels investigated by experiment and theory. *Acta Materialia*, 68:238 – 253, 2014. ISSN 1359-6454. doi: http://dx.doi.org/10.1016/j.actamat.2014.01.001.

[19] Jin-Kyung Kim and Bruno C. De Cooman. Stacking fault energy and deformation mechanisms in fe-xmn-0.6c-yal twip steel. *Materials Science and Engineering: A*, 676:216–231, 2016. ISSN 09215093. doi: 10.1016/j.msea.2016.08.106.

[20] O Grässel, L Krüger, G Frommeyer, and L.W Meyer. High strength fe-mn-(al,si) trip/twip steels development-properties-application. *International Journal of Plasticity*, 16(10–11):1391 – 1409, 2000. ISSN 0749-6419. doi: 10.1016/S0749-6419(00)00015-2.

[21] Seung-Joon Lee, Jeongho Han, Sukjin Lee, Seok-Hyeon Kang, Sang-Min Lee, and Young-Kook Lee. Design for fe-high mn alloy with an improved combination of strength and ductility. *Scientific reports*, 7(1):3573, 2017. ISSN 2045-2322. doi: 10.1038/s41598-017-03862-y.

[22] Bruno C. De Cooman, Yuri Estrin, and Sung Kyu Kim. Twinning-induced plasticity (twip) steels. *Acta Materialia*, 142:283–362, 2018. ISSN 13596454. doi: 10.1016/j.actamat.2017.06.046.

[23] Christian Haase, Tobias Ingendahl, Onur GÃ¼venÃ§, Markus Bambach, Wolfgang Bleck, Dmitri A. Molodov, and Luis A. Barrales-Mora. On the applicability of recovery-annealed twinning-induced plasticity steels: Potential and limitations. *Materials Science and Engineering: A*, 649:74 – 84, 2016. ISSN 0921-5093. doi: 10.1016/j.msea.2015.09.096.

[24] Wolfgang Bleck and Ingo Schael. Determination of crash relevant material parameters by dynamic tensile tests. *Steel Research*, 71(5):173–178, 2000. doi: 10.1002/srin.200005709.

[25] Gang Huang, Yan Benda, Hong Zhu, and Jayanth Chintamani. The strain rate effect on tensile properties and fracture strain of advanced high strength steels. In *Materials Science & Technology 2011 Conference & Exhibition, October 16-20, 2011, Columbus, Ohio*. John Wiley & Sons, October 2011.

[26] Seung-Joon Lee, Jeongho Han, Sukjin Lee, Seok-Hyeon Kang, Sang-Min Lee, and Young-Kook Lee. Design for fe-high mn alloy with an improved combination of strength and ductility. *Scientific reports*, 7(1):3573, 2017. ISSN 2045-2322. doi: 10.1038/s41598-017-03862-y.

[27] D. T. Pierce, J. A. Jiménez, J. Bentley, D. Raabe, and J. E. Wittig. The influence of stacking fault energy on the microstructural and strain-hardening evolution of fe–mn–al–si steels during tensile deformation. *Acta Materialia*, 100:178–190, 2015. ISSN 13596454. doi: 10.1016/j.actamat.2015.08.030.

[28] Jin-Kyung Kim, Min-Hyeok Kwon, and Bruno C. De Cooman. On the deformation twinning mechanisms in twinning-induced plasticity steel. *Acta Materialia*, 141:444–455, 2017. ISSN 13596454. doi: 10.1016/j.actamat.2017.09.043.

[29] A. Saeed-Akbari, L. Mosecker, A. Schwedt, and W. Bleck. Characterization and prediction of flow behavior in high-manganese twinning induced plasticity steels: Part i. mechanism maps and work-hardening behavior. *Metallurgical and Materials Transactions A*, 43(5):1688–1704, 2012. ISSN 1073-5623. doi: 10.1007/s11661-011-0993-4.

[30] Il-Chan Jung and Bruno C. De Cooman. Temperature dependence of the flow stress of fe–18mn–0.6c–xal twinning-induced plasticity steel. *Acta Materialia*, 61(18):6724–6735, 2013. doi: 10.1007/s12540-014-1008-y.

[31] S. Allain, J.-P. Chateau, O. Bouaziz, S. Migot, and N. Guelton. Correlations between the calculated stacking fault energy and the plasticity mechanisms in fe–mn–c alloys. *Materials Science and Engineering: A*, 387-389:158–162, 2004. doi: 10.1016/j.msea.2004.01.059.

[32] H. Idrissi, L. Ryelandt, M. Veron, D. Schryvers, and P.J. Jacques. Is there a relationship between the stacking fault character and the activated mode of plasticity of fe-mn-based austenitic steels. *Scripta Materialia*, 60(11):941 – 944, 2009. ISSN 1359-6462. doi: http://dx.doi.org/10.1016/j.scriptamat.2009.01.040.

[33] K. Renard and P. J. Jacques. On the relationship between work hardening and twinning rate in twip steels. *Materials Science and Engineering: A*, 542:8–14, 2012. doi: http://dx.doi.org/10.1016/j.msea.2012.01.123.

[34] D. T. Pierce, J. A. Jiménez, J. Bentley, D. Raabe, and J. E. Wittig. The influence of stacking fault energy on the microstructural and strain-hardening evolution of Fe–Mn–Al–Si steels during tensile deformation. *Acta Materialia*, 100:178–190, 2015. doi: http://dx.doi.org/10.1016/j.actamat.2015.08.030.

[35] S. Curtze and V.-T. Kuokkala. Dependence of tensile deformation behavior of twip steels on stacking fault energy, temperature and strain rate. *Acta Materialia*, 58(15):5129 – 5141, 2010. ISSN 1359-6454. doi: http://dx.doi.org/10.1016/j.actamat.2010.05.049.

[36] Vadim Shterner, Ilana B. Timokhina, and Hossein Beladi. On the work-hardening behaviour of a high manganese TWIP steel at different deformation temperatures. *Materials Science and Engineering: A*, 669:437–446, 2016. ISSN 09215093. doi: http://dx.doi.org/10.1016/j.msea.2016.05.104.

[37] Lei Chen, Han-Soo Kim, Sung-Kyu Kim, and B. C. De Cooman. Localized deformation due to portevin–lechatelier effect in 18mn–0.6c twip austenitic steel. *ISIJ International*, 47(12): 1804–1812, 2007. ISSN 0915-1559. doi: http://dx.doi.org/10.2355/isijinternational.47.1804.

[38] Sébastien Allain, Philippe Cugy, C. Scott, J. P. Chateau, Alexis Rusinek, and Alexis Deschamps. The influence of plastic instabilities on the mechanical properties of a high-manganese austenitic femnc steel. *International Journal of Materials Research*, 99(7):734–738, 2008. doi: 10.3139/146.101693.

[39] Seok-Jae Lee, Jinkyung Kim, Shashank N. Kane, and Bruno Charles De Cooman. On the origin of dynamic strain aging in twinning-induced plasticity steels. *Acta Materialia*, 59(17): 6809–6819, 2011. ISSN 13596454. doi: 10.1016/j.actamat.2011.07.040.

[40] Mihyun Kang, Eunjoo Shin, Wanchuck Woo, and Young-Kook Lee. Small-angle neutron scattering analysis of mn–c clusters in high-manganese 18mn–0.6c steel. *Materials Characterization*, 96:40–45, 2014. ISSN 10445803. doi: 10.1016/j.matchar.2014.07.010.

[41] Wenwen Song and Judith Houston. Local deformation and mn-c short-range ordering in a high-mn fe-18mn-0.6c steel. *Metals*, 8(5):292, 2018. ISSN 2075-4701. doi: 10.3390/met8050292.

[42] Motomichi Koyama, Takahiro Sawaguchi, and Kaneaki Tsuzaki. TWIP Effect and Plastic Instability Condition in an Fe-Mn-C Austenitic Steel. *ISIJ International*, 53(2):323–329, 2013. ISSN 0915-1559. doi: 10.2355/isijinternational.53.323.

[43] Lei Chen, Han-Soo Kim, Sung-Kyu Kim, and B. C. De Cooman. Localized deformation due to portevin–lechatelier effect in 18mn–0.6c twip austenitic steel. *ISIJ International*, 47(12): 1804–1812, 2007. ISSN 0915-1559. doi: http://dx.doi.org/10.2355/isijinternational.47.1804.

[44] P. D. Zavattieri, V. Savic, L. G. Hector Jr., J. R. Fekete, W. Tong, and Y. Xuan. Spatio-temporal characteristics of the portevin–le châtelier effect in austenitic steel with twinning induced plasticity. *International Journal of Plasticity*, 25(12):2298 – 2330, 2009. ISSN 0749-6419. doi: 10.1016/j.ijplas.2009.02.008.

[45] T. A. Lebedkina, M. A. Lebyodkin, J.-Ph. Chateau, A. Jacques, and S. Allain. On the mechanism of unstable plastic flow in an austenitic femnc twip steel. *Materials Science and Engineering: A*, 519(1-2):147–154, 2009. ISSN 09215093. doi: 10.1016/j.msea.2009.04.067.

[46] A. Roth, T. A. Lebedkina, and M. A. Lebyodkin. On the critical strain for the onset of plastic instability in an austenitic femnc steel. *Materials Science and Engineering: A*, 539:280–284, 2012. ISSN 09215093. doi: http://dx.doi.org/10.1016/j.msea.2012.01.094.

[47] Motomichi Koyama, Takahiro Sawaguchi, and Kaneaki Tsuzaki. TWIP Effect and Plastic Instability Condition in an Feˆ—ˆndash;Mnˆ—ˆndash;C Austenitic Steel. *ISIJ International*, 53(2):323–329, 2013. ISSN 0915-1559. doi: http://dx.doi.org/10.2355/isijinternational.53.323.

[48] H. K. Yang, Z. J. Zhang, Y. Z. Tian, and Z. F. Zhang. Negative to positive transition of strain rate sensitivity in Fe-22Mn-0.6C-x(Al) twinning-induced plasticity steels. *Materials Science and Engineering: A*, 690:146–157, 2017. doi: http://dx.doi.org/10.1016/j.msea.2017.02.014.

[49] Xiangde Bian, Fuping Yuan, and Xiaolei Wu. Correlation between strain rate sensitivity and characteristics of portevin-lechátelier bands in a twinning-induced plasticity steel. *Materials Science and Engineering: A*, 696:220–227, 2017. ISSN 09215093. doi: 10.1016/j.msea.2017.04.078.

[50] Minju Kang, Jaeyeong Park, Seok Su Sohn, Hyoung Seop Kim, Nack J. Kim, and Sunghak Lee. Interpretation of quasi-static and dynamic tensile behavior by digital image correlation technique in twinning induced plasticity (twip) and low-carbon steel sheets. *Materials Science and Engineering: A*, 693:170–177, 2017. ISSN 09215093. doi: 10.1016/j.msea.2017.03.076.

[51] Motomichi Koyama, Takahiro Sawaguchi, Taekyung Lee, Chong Soo Lee, and Kaneaki Tsuzaki. Work hardening associated with epsilon-martensitic transformation, deformation twinning and dynamic strain aging in fe–17mn–0.6c and fe–17mn–0.8c twip steels. *Materials Science and Engineering: A*, 528(24):7310–7316, 2011. ISSN 09215093. doi: http://dx.doi.org/10.1016/j.msea.2011.06.011.

[52] J. T. Benzing, W. A. Poling, D. T. Pierce, J. Bentley, K. O. Findley, D. Raabe, and J. E. Wittig. Effects of strain rate on mechanical properties and deformation behavior of an austenitic fe-25mn-3al-3si twip-trip steel. *Materials Science and Engineering: A*, 711:78–92, 2018. ISSN 09215093. doi: 10.1016/j.msea.2017.11.017.

[53] Jaeyeong Park, Minju Kang, Seok Su Sohn, Sang-Heon Kim, Hyoung Seop Kim, Nack J. Kim, and Sunghak Lee. Quasi-static and dynamic deformation mechanisms interpreted by microstructural evolution in twinning induced plasticity (twip) steel. *Materials Science and Engineering: A*, 684:54–63, 2017. ISSN 09215093. doi: 10.1016/j.msea.2016.12.037.

[54] Y. F. Shen, N. Jia, R.D.K. Misra, and L. Zuo. Softening behavior by excessive twinning and adiabatic heating at high strain rate in a fe–20mn–0.6c twip steel. *Acta Materialia*, 103:229–242, 2016. ISSN 13596454. doi: 10.1016/j.actamat.2015.09.061.

[55] K. M. Rahman, V. A. Vorontsov, and D. Dye. The dynamic behaviour of a twinning induced plasticity steel. *Materials Science and Engineering: A*, 589:252–261, 2014. ISSN 09215093. doi: 10.1016/j.msea.2013.09.081.

[56] Motomichi Koyama, Takahiro Sawaguchi, and Kaneaki Tsuzaki. Overview of dynamic strain aging and associated phenomena in fe-mn-c austenitic steels. *ISIJ International*, 58(8):1383–1395, 2018. doi: 10.2355/isijinternational.ISIJINT-2018-237.

[57] Jinkyung Kim, Yuri Estrin, and Bruno Charles De Cooman. Application of a dislocation density-based constitutive model to al-alloyed twip steel. *Metallurgical and Materials Transactions A*, 44(9):4168–4182, Sep 2013. ISSN 1543-1940. doi: https://doi.org/10.1007/s11661-013-1771-2.

[58] H. K. Yang, Z. J. Zhang, F. Y. Dong, Q. Q. Duan, and Z. F. Zhang. Strain rate effects on tensile deformation behaviors for fe–22mn–0.6c–(1.5al) twinning-induced plasticity steel. *Materials Science and Engineering: A*, 607:551–558, 2014. ISSN 09215093. doi: 10.1016/j.msea.2014.04.043.

[59] O Bouaziz and N Guelton. Modelling of {TWIP} effect on work-hardening. *Materials Science and Engineering: A*, 319–321:246 – 249, 2001. ISSN 0921-5093. doi: http://dx.doi.org/10.1016/S0921-5093(00)02019-0.

[60] S. Allain, J.-P. Chateau, and O. Bouaziz. A physical model of the twinning-induced plasticity effect in a high manganese austenitic steel. *Materials Science and Engineering: A*, 387–389:143 – 147, 2004. ISSN 0921-5093. doi: http://dx.doi.org/10.1016/j.msea.2004.01.060. 13th International Conference on the Strength of Materials.

[61] Jinkyung Kim, Yuri Estrin, Hossein Beladi, Ilana Timokhina, Kwang-Geun Chin, Sung-Kyu Kim, and Bruno C. De Cooman. Constitutive Modeling of the Tensile Behavior of Al-TWIP Steel. *Metallurgical and Materials Transactions A*, 43(2):479–490, 2012. doi: http://dx.doi.org/10.1007/s11661-011-0898-2.

[62] D. R. Steinmetz, T. Jäpel, B. Wietbrock, P. Eisenlohr, I. Gutierrez-Urrutia, A. Saeed-Akbari, T. Hickel, F. Roters, and D. Raabe. Revealing the strain-hardening behavior of twinning-induced plasticity steels: Theory, simulations, experiments. *Acta Materialia*, 61(2):494 – 510, 2013. doi: http://dx.doi.org/10.1016/j.actamat.2012.09.064.

[63] F. Roters, D. Raabe, and G. Gottstein. Work hardening in heterogeneous alloys—a microstructural approach based on three internal state variables. *Acta Materialia*, 48(17):4181–4189, 2000. ISSN 13596454. doi: http://dx.doi.org/10.1016/S1359-6454(00)00289-5.

[64] S. Mahajan and G.Y. Chin. Formation of deformation twins in f.c.c. crystals. *Acta Metallurgica*, 21(10):1353 – 1363, 1973. ISSN 0001-6160. doi: http://dx.doi.org/10.1016/0001-6160(73)90085-0.

[65] S. R. Kalidindi. Modeling the strain hardening response of low {SFE} {FCC} alloys. *International Journal of Plasticity*, 14(12):1265 – 1277, 1998. ISSN 0749-6419. doi: http://dx.doi.org/10.1016/S0749-6419(98)00054-0.

[66] A. Staroselsky and L. Anand. Inelastic deformation of polycrystalline face centered cubic materials by slip and twinning. *Journal of the Mechanics and Physics of Solids*, 46(4):671 – 696, 1998. ISSN 0022-5096. doi: http://dx.doi.org/10.1016/S0022-5096(97)00071-9.

[67] I Karaman, H Sehitoglu, A.J Beaudoin, Y.I Chumlyakov, H.J Maier, and C.N Tomé. Modeling the deformation behavior of hadfield steel single and polycrystals due to twinning and slip. *Acta Materialia*, 48(9):2031 – 2047, 2000. ISSN 1359-6454. doi: http://dx.doi.org/10.1016/S1359-6454(00)00051-3.

[68] S. R. Kalidindi. Modeling anisotropic strain hardening and deformation textures in low stacking fault energy fcc metals. *International Journal of Plasticity*, 17(6):837 – 860, 2001. ISSN 0749-6419. doi: http://dx.doi.org/10.1016/S0749-6419(00)00071-1.

[69] M. Shiekhelsouk, V. Favier, K. Inal, and M. Cherkaoui. Modelling the behaviour of polycrystalline austenitic steel with twinning-induced plasticity effect. *International Journal of Plasticity*, 25(1):105–133, 2009. doi: http://doi.org/10.1016/j.ijplas.2007.11.004.

[70] S. Dancette, L. Delannay, K. Renard, M. A. Melchior, and P. J. Jacques. Crystal plasticity modeling of texture development and hardening in TWIP steels. *Acta Materialia*, 60(5):2135–2145, 2012. doi: http://doi.org/10.1016/j.actamat.2012.01.015.

[71] C.Y. Sun, N. Guo, M.W. Fu, and S.W. Wang. Modeling of slip, twinning and transformation induced plastic deformation for TWIP steel based on crystal plasticity. *International Journal of Plasticity*, 76:186 – 212, 2016. ISSN 0749-6419. doi: http://dx.doi.org/10.1016/j.ijplas.2015.08.003.

[72] N. Jia, F. Roters, P. Eisenlohr, C. Kords, and D. Raabe. Non-crystallographic shear banding in crystal plasticity FEM simulations: Example of texture evolution in α-brass. *Acta Materialia*, 60(3):1099 – 1115, 2012. ISSN 1359-6454. doi: http://dx.doi.org/10.1016/j.actamat.2011.10.047.

[73] F. Roters, P. Eisenlohr, C. Kords, D.D. Tjahjanto, M. Diehl, and D. Raabe. Damask: the düsseldorf advanced MAterial simulation kit for studying crystal plasticity using an FE based or a spectral numerical solver. *Procedia IUTAM*, 3:3 – 10, 2012. ISSN 2210-9838. doi: http://dx.doi.org/10.1016/j.piutam.2012.03.001.

[74] Su Leen Wong, Manjunatha Madivala, Ulrich Prahl, Franz Roters, and Dierk Raabe. A crystal plasticity model for twinning- and transformation-induced plasticity. *Acta Materialia*, 118:140–151, 2016. doi: http://dx.doi.org/10.1016/j.actamat.2016.07.032.

[75] Julie Lorthios, Matthieu Mazière, Xavier Lemoine, Philippe Cugy, Jacques Besson, and Anne-Françoise Gourgues-Lorenzon. Fracture behaviour of a Fe–22Mn–0.6C–0.2V austenitic TWIP steel. *International Journal of Mechanical Sciences*, 101-102:99–113, 2015. doi: http://dx.doi.org/10.1016/j.ijmecsci.2015.07.029.

[76] Ha-Young Yu, Sang-Min Lee, Jae-Hoon Nam, Seung-Joon Lee, Damien Fabrègue, Myeong-heom Park, Nobuhiro Tsuji, and Young-Kook Lee. Post-uniform elongation and tensile fracture mechanisms of fe-18mn-0.6c-xal twinning-induced plasticity steels. *Acta Materialia*, 131:435–444, 2017. ISSN 13596454. doi: 0.1016/j.actamat.2017.04.011.

[77] H. K. Yang, Z. J. Zhang, Y. Z. Tian, and Z. F. Zhang. Negative to positive transition of strain rate sensitivity in Fe-22Mn-0.6C-x(Al) twinning-induced plasticity steels. *Materials Science and Engineering: A*, 690:146–157, 2017. ISSN 09215093. doi: 10.1016/j.msea.2017.02.014.

[78] D. Fabrègue, C. Landron, O. Bouaziz, and E. Maire. Damage evolution in twip and standard austenitic steel by means of 3d x ray tomography. *Materials Science and Engineering: A*, 579:92–98, 2013. doi: 10.1016/j.msea.2013.05.013.

[79] J. Lorthios, F. Nguyen, A.-F. Gourgues, T. F. Morgeneyer, and P. Cugy. Damage observation in a high-manganese austenitic TWIP steel by synchrotron radiation computed tomography. *Scripta Materialia*, 63(12):1220–1223, 2010. doi: 10.1016/j.scriptamat.2010.08.042.

[80] Seung-Yong Lee, Sang-In Lee, and Byoungchul Hwang. Effect of strain rate on tensile and serration behaviors of an austenitic fe-22mn-0.7c twinning-induced plasticity steel. *Materials Science and Engineering: A*, 711:22–28, 2018. ISSN 09215093. doi: 10.1016/j.msea.2017.10.074.

[81] Peng Lan and Jiaquan Zhang. Serrated Flow and Dynamic Strain Aging in Fe-Mn-C TWIP Steel. *Metallurgical and Materials Transactions A*, 49(1):147–161, 2018. ISSN 1073-5623. doi: 10.1007/s11661-017-4421-2.

[82] Y. N. Dastur and W. C. Leslie. Mechanism of work hardening in hadfield manganese steel. *Metallurgical Transactions A*, 12(5):749–759, 1981. doi: 10.1007/BF02648339.

[83] Jin-Kyung Kim, Lei Chen, Han-Soo Kim, Sung-Kyu Kim, Y. Estrin, and B. C. Cooman. On the tensile behavior of high-manganese twinning-induced plasticity steel. *Metallurgical and Materials Transactions A*, 40(13):3147–3158, 2009. ISSN 1543-1940. doi: http://dx.doi.org/10.1007/s11661-009-9992-0.

[84] Simon Sevsek, Frederike Brasche, Christian Haase, and Wolfgang Bleck. Combined deformation twinning and short-range ordering causes serrated flow in high-manganese steels. *Materials Science and Engineering: A*, 746:434 – 442, 2019. ISSN 0921-5093. doi: https://doi.org/10.1016/j.msea.2019.01.042.

[85] Taotsung Shun, C. M. Wan, and J. G. Byrne. A study of work hardening in austenitic Fe-Mn-C and Fe-Mn-Al-C alloys. *Acta Metallurgica et Materialia*, 40(12):3407–3412, 1992. ISSN 09567151. doi: 10.1016/0956-7151(92)90054-I.

[86] Motomichi Koyama, Takahiro Sawaguchi, and Kaneaki Tsuzaki. Deformation twinning behavior of twinning-induced plasticity steels with different carbon concentrations. *Tetsu-to-Hagane*, 100(10):1253–1260, 2014. doi: 10.2355/tetsutohagane.100.1253.

[87] I. Gutierrez-Urrutia and D. Raabe. Dislocation and twin substructure evolution during strain hardening of an fe-22wt.% mn-0.6wt.% c twip steel observed by electron channeling contrast imaging. *Acta Materialia*, 59(16):6449–6462, 2011. doi: http://dx.doi.org/10.1016/j.actamat.2011.07.009.

[88] I. Gutierrez-Urrutia and D. Raabe. Grain size effect on strain hardening in twinning-induced plasticity steels. *Scripta Materialia*, 66(12):992–996, 2012. ISSN 13596462. doi: 10.1016/j.scriptamat.2012.01.037.

[89] Hojun Gwon, Jin-Kyung Kim, Sunmi Shin, Lawrence Cho, and Bruno C. De Cooman. The effect of vanadium micro-alloying on the microstructure and the tensile behavior of twip steel. *Materials Science and Engineering: A*, 696:416–428, 2017. ISSN 09215093. doi: 10.1016/j.msea.2017.04.083.

[90] Z. Y. Liang, X. Wang, W. Huang, and M. X. Huang. Strain rate sensitivity and evolution of dislocations and twins in a twinning-induced plasticity steel. *Acta Materialia*, 88:170–179, 2015. ISSN 13596454. doi: 10.1016/j.actamat.2015.01.013.

[91] David R. Steinmetz, Tom Jäpel, Burkhard Wietbrock, Philip Eisenlohr, Ivan Gutierrez-Urrutia, Alireza Saeed-Akbari, Tilmann Hickel, Franz Roters, and Dierk Raabe. Revealing the strain-hardening behavior of twinning-induced plasticity steels: Theory, simulations, experiments. *Acta Materialia*, 61(2):494–510, 2013. ISSN 13596454. doi: 10.1016/j.actamat.2012.09.064.

[92] Takuro Ogawa, Motomichi Koyama, Cemal Cem Tasan, Kaneaki Tsuzaki, and Hiroshi Noguchi. Effects of martensitic transformability and dynamic strain age hardenability on plasticity in metastable austenitic steels containing carbon. *Journal of Materials Science*, 52 (13):7868–7882, Jul 2017. ISSN 1573-4803. doi: https://doi.org/10.1007/s10853-017-1052-3.

[93] Wenwen Song, Dimitri Bogdanovski, Ahmet Yildiz, Judith Houston, Richard Dronskowski, and Wolfgang Bleck. On the Mn–C Short-Range Ordering in a High-Strength High-Ductility Steel: Small Angle Neutron Scattering and Ab Initio Investigation. *Metals*, 8(1):44, 2018. ISSN 2075-4701. doi: 10.3390/met8010044.

[94] Sebastian Wesselmecking, Wenwen Song, Yan Ma, Thorsten Roesler, Harald Hofmann, and Wolfgang Bleck. Strain Aging Behavior of an Austenitic High-Mn Steel. *steel research international*, 88:1700515, 2018. ISSN 16113683. doi: 10.1002/srin.201700515.

[95] S. Allain, O. Bouaziz, T. Lebedkina, and M. Lebyodkin. Relationship between relaxation mechanisms and strain aging in an austenitic femnc steel. *Scripta Materialia*, 64(8):741 – 744, 2011. ISSN 1359-6462. doi: https://doi.org/10.1016/j.scriptamat.2010.12.039.